Carbon-nanotube-based membranes for water desalination by membrane distillation

By

Ludovic Francis Dumée (Ludo)

Master of material engineering - ENSISA - France

A thesis submitted to Victoria University, Melbourne - Australia

for the degree of Doctor in Philosophy

with the support of the

Commonwealth Scientific and Industrial Research Organisation, Division of Materials Science and Engineering

&

The Institute for Sustainability and Innovation at Victoria University

Melbourne Australia

March 2011

Statement of originality

"I, **Ludovic Dumée**, declare that the PhD thesis entitled **Carbon-nanotube-based membranes for water desalination by membrane distillation** is no more than 100,000 words in length including quotes and exclusive of tables, figures, appendices, bibliography, references and footnotes. This thesis contains no material that has been submitted previously, in whole or in part, for the award of any other academic degree or diploma. Except where otherwise indicated, this thesis is my own work".

Signature Date 28th of March 2011

Ludo Dumée, PhD candidate

Melbourne, Victoria - Australia

Disclaimer

This work is a co-operative research project involving the author, the Victoria University (Victoria, Australia) and the Commonwealth Science Industrial and Research Organisation of Australia. All parties have agreed to pursue this project in an Agreement made in September 2007 commencing 25th of January 2008. Information disclosed in this project is subject to this agreement.

Acknowledgements

Merci beaucoup…

As per her support, fair judgement and advice over the past 3 years, I would like to heart fully thank Dr. **Kallista Sears**. Despite my tremendous character and wild imagination she managed to focus my brain on the main task to achieve, namely my PhD. Her advice, moral support and occasional cakes greatly helped me explore undiscovered features of the wondrous world of carbon nanotubes.

My most sincere gratitude goes to my academic supervisors and mentors, A/Prof **Mikel Duke** and Prof. **Stephen Gray** from Victoria University, for their professional advice and moral encouragement during my PhD research. Their comments, advice and ideas certainly greatly helped me focus and organize my experiments and thoughts over the past 3 years.

My appreciation and gratitude extends to those who, with their expert assistance, allowed me to work at the CSIRO, namely Dr. **Jürg Schütz** and Dr. **Niall Finn**. Their confidence, help and open-mindness gave me such a stunning opportunity to let my imagination flourish and my skills develop. To give me a chance to work and express myself in this wonderful facilities and laboratory, they are granted my eternal gratitude.

I would also like to express my gratitude to the Commonwealth Scientific Industrial and Research Organisation (CSIRO) for financial support of my scholarship and for funding, equipment, laboratory supply and travel during my PhD. This experience at the CSIRO has been very fruitful and certainly did extend the scope of my skills and open my mind on a different cultural research experience.

My thanks also go to the following people that either helped me with their advice or so kindly accepted to teach or direct me on the right track over my journey:

• Marta Redrado Notivoli, Chi Huynh and Dr. Stephen Hawkins for their considerable work on the growth of carbon nanotubes and for providing us with such a high quality material to fabricate our membranes (CSIRO MSE);
• Mark Hickey, Jacinta Poole, Dr Yuan Gao and Dr. Mustafa Musameh for their numerous advice on technical matters and for giving me tricks on how to efficiently improve my writing skills (CSIRO MSE);
• Robin Cranston, Dr. Ron Denning, Dr. Geoff Naylor and Dr. Bill Humphries for their professional and financial support, and for giving me the opportunity to stay and work within their division and groups at the CSIRO over those past 3 years. Nothing would have worked out so well without funding and they have been very supportive and helpful in that regard;
• Mark Greaves and Dr. John Ward (CSIRO) … Dr. Sergey Rubanov (Bio 21) for their expert advice and help on SEM and TEM imaging;
• The CSIRO Belmont workshop staff, for their professionalism helpful advice and high quality workmanship;
• The CSIRO HSE committee for allowing me to work with carbon nanotubes in a safe environment;
• My colleagues in the Nanofibrous material group, Dr. Yen Truong, for granting me access to her goniometer and her porometer… Dr. Louis Kyriatzis for letting me use his electrospinning rigs… the CSIRO staff for their warm welcome and help over the past 3 years;
• Dr. Aaron Thornton for sharing a night shift on the Synchrotron and his advice on modelling… Dr. Paolo Falcaro and Dr. Dario Buso for fascinating ideas and discussions… Dr. Anita Hill for fruitful discussions and general advice on my PhD project… Zongli Xie and Lisa Wong for their help on the BET tests…Dr. Matthew Hill for his moral help, great discussions on gas adsorption, full support, and for granting access to his gas adsorption device;
• Dr. Jianhua Zhang and Prof. Jun-de Li from Victoria University for fruitful discussions on thermal behaviours and membrane distillation process;
• Dr. Shane Cox and Dr. Pierre Le-Clech (UNSW), for granting me the access to their porometer in the early stage of my PhD and for wise advice over the end of it;
• Dr. Leonora Velleman and Joe Shapter (Flinders University) for the use of their laboratory and their technical advice on the plating of gold;

• Dr. Mary She and Dr. Lingxue Kong (Deakin University) for their help on the TEM 3D reconstruction and time in taking the micrographs at various tilt angle;
• Jos Campbell and Prof. Kourosh Kalantaar-Zadeh (RMIT) for access to their PTFE sputtering device;
• Steven Spoljaric and Prof. Robert Shanks (RMIT) for doing mt-Tm thermal expansion tests;
• Zach Sears for giving me a 6 month well deserved break;
• Stephen Wright (CSIRO PSE) for teaching me how to use his Anter laser flash thermal expansion device;
• The board of the Membrane Society of Australasia for granting me a travel award to attend AMS5 in Kobe, Japan in 2009; the European Union, through the Marie Curie funding scheme for financial support to attend the 2010 NanoMemPro course on Nano-structured materials and Membranes for Health and Sustainable Water;
• The board of the conferences I attended as presenter: ICOM08, AMS5, AMS6, the Australian Water desalination summit 2010, the AWA membrane specialty conference 09, ICONN10, the 1st Student Symposium of the MSA 2010…for giving me a chance to present my work and share with my fellow researchers;
• Prof Iijima for his work on carbon nanotubes in the 90'; Dr. Mainak Majumder, Prof Jason Holt and Prof Bruce Hinds for being pioneers in CNT membrane science and inspiring this project; the people I cite in my literature review as this work would not have been possible without their efforts over the past century and more…
• To the ones I forgot…
• Séda, my wife for cooking such great cakes. Pluche the cat for hugs and moral support;

To **Gabrielle Aïko Mary**, my daughter born the month I finalize these lines.

Publications from this research

Published journal papers

[1] Sears, K., L. **Dumée**, J. Schütz, M. She, C. Huynh, S. Hawkins, M. Duke, and S. Gray, *Recent Developments in Carbon Nanotube Membranes for Water Purification and Gas Separation.* **Materials**, 2009. 3(1): p. 127-149.

[2] **Dumée**, L.F., K. Sears, J. Schütz, N. Finn, C. Huynh, S. Hawkins, M. Duke, and S. Gray, *Characterization and evaluation of carbon nanotube Bucky-Paper membranes for direct contact membrane distillation.* **Journal of Membrane Science**, 2010. 351(1-2): p. 36-43.

[3] **Dumée**, L., K. Sears, J. Schutz, N. Finn, M. Duke, and S. Gray, *Carbon nanotube based composite membranes for water desalination by membrane distillation.* **Desalination and Water treatment**, 2010. 17(1-3): p. 72-79.

[4] **Dumee**, L., L. Velleman, K. Sears, M. Hill, J. Schutz, N. Finn, M. Duke, and S. Gray, *Control of Porosity and Pore Size of Metal Reinforced Carbon Nanotube Membranes.* **Membranes**, 2010. 1(1): p. 25-36.

[5] **Dumée**, L., V. Germain, K. Sears, J. Schutz, N. Finn, M. Duke, D. Cornu and S. Gray, *Enhanced durability and hydrophobic property of carbon nanotube bucky paper membranes by alkoxy-silanisation surface modification.* **Accepted by Desalination, March 2011**

[6] **Dumée**, L., K. Sears, J. Campbell, J. Schutz, N. Finn, M. Duke, and S. Gray, *Impact of the hydrophobicity and porosity of PTFE coated carbon nanotube bucky-paper membranes on their performance in membrane distillation.* **Accepted by Journal of Membrane Science, March 2011**

[7] **Dumée**, L.F., Kallista Sears, Jürg Schütz, Niall Finn, Mikel Duke and Stephen Gray**,** *A Preliminary Study on the Effect of Macro Cavities Formation on Properties of Carbon Nanotube Bucky-Paper Composites*. **Materials** 2011, *4*(3), 553-561

Papers submitted or under writing process

[8] **Dumée**, L.F., Matthew Hill, Mikel Duke, Leonora Velleman, Kallista Sears, Jürg Schütz, Niall Finn, Stephen Gray, *A route to the fabrication and activation of gold nanoparticles within carbon nanotube porous structures for gas storage application*.

[9] **Dumée**, L., K. Sears, S. Wright, J. Schutz, N. Finn, M. Duke, and S. Gray, *Thermal properties of carbon nanotube self-supporting bucky-papers.*

[10] **Dumée,** L.F., Kallista Sears, Jürg Schütz, Niall Finn, Mikel Duke and Stephen Gray**,** *Impact of the temperature of sonication on the dispersion of CVD grown multi-walled CNTs.*

[11] **Dumée**, L., Thornton, A., L.F., Kallista Sears, Jürg Schütz, Niall Finn, Mikel Duke and Stephen Gray**,** *The Orientation of Carbon Nanotube in macro structures: a Small Angle X-ray Scattering analysis of CNT yarns, bucky-paper, webs and forests.*

[12] **Dumée**, L., Thornton, A., L.F., Kallista Sears, Jürg Schütz, Niall Finn, Mikel Duke and Stephen Gray, *Thermal expansion of carbon nanotube based structures determined by Small Angle X-ray Scattering.*

Selected presentations and talks

November 2010 Sydney, New South Wales - AUSTRALIA – International Membrane Science and Technology Conference - **IMSTEC 10** in conjunction with the Aseanian Membrane Society 6 - **AMS 6**. Talk on the *Properties of high gas adsorption capacity gold reinforced carbon nanotube bucky-paper hybrid membranes* - **Prize for the best student oral presentation**

Poster on *Functionalised carbon nanotube membranes for desalination: impact of hydrophobicity on the membrane performance*

July 2010 New London, NH – USA – **Gordon Research Conference** (GRC): on Membrane: Materials and processes. Poster presentation on *Alkoxysilane modified carbon nanotubes for increased hydrophobicity bucky-papers used as membranes in membrane distillation*

July 2010 Melbourne, Victoria - AUSTRALIA – **Australian desalination summit** 2010. Talk in plenary session on a *Review of the use of carbon nanotube for separation and water purification*

April 2010 Twente, the NETHERLANDS – European Union **Marie Curie scholarship** (**2000AUD)** to attend the **NanoMemCourse** on "Health and sustainable water". Poster on the *Performance of carbon nanotube based membranes for seawater desalination - a review*

February 2010 Sydney, New South Wales - AUSTRALIA – **International Congress on Nanotechnology and Nanosciences** 2010 (ICONN10), talk on the *Thermal properties of carbon nanotube macro-structures* and poster on *tuning the porosity of composite material carbon nanotube based membranes for water desalination*

February 2010 Wollongong, New South Wales - AUSTRALIA – First Membrane Society of Australasia Student Symposium (MSASS1) talk on *Performance of PTFE/carbon nanotube composites for water desalination by membrane distillation* - **Prize for Best Student Presentation**

September 2009 Melbourne, Victoria - AUSTRALIA – Victoria University student symposium 2009, talk on a *Review of my PhD work on integrating carbon nanotubes into membranes* - **Prize for Best Presentation**

July 2009 Kobe, JAPAN **– Aseanian Membrane Society conference 5**, Co-winner of the **Membrane Society of Australasia – Millipore travel grant** (500AUD) to attend AMS5. Poster entitled *Carbon Nanotube based composite membranes for water desalination by membrane distillation* - **Prize for Best Student Presentation**

February 2009 Sydney, New South Wales - AUSTRALIA - Australian Water Association conference on Desalination and Membrane Technologies, Talk in plenary session at the on *Advanced carbon nanotube membranes for direct contact membrane distillation*

July 2008 Honolulu, Hawaii - USA – **International Congress on Membranes 2008** (ICOM08), Poster presentation on *Pure Carbon Nanotube Bucky-paper membrane fabrication and use in Direct Contact Membrane Distillation – preliminary results*

Abstract

"What makes the desert beautiful is that somewhere it hides a well."

~Antoine de Saint-Exupery

More than 70% of the global community sources its fresh water from rivers, lakes and aquifers.. As the worldwide population approaches 9 billion by 2050 and the standard of living of fast developing countries, including Australia, increases, so does the demand for fresh water. Excessive exploitation of our finite fresh water resources has already impacted both eco-systems and global water reserves that are highly dependent on rainfall to regenerate and on geological hydrodynamics for storage.

To avoid further damaging and exploiting these dwindling natural resources, desalination appears to be a promising solution. Amongst the major processes that are commercially available on the market, the most common techniques are Multi-Stage Flash distillation and Reverse Osmosis (RO). Although commonly used, these two processes remain highly expensive because of both (i) the energy input required for either evaporating the water or overcoming its osmotic pressure and (ii) their high operating costs associated with maintenance and stress induced on the systems in harsh alkaline media.

Other less energy consuming techniques based on membrane separation are being sought to reduce both the carbon footprint and operating costs. Re-emerging in the 90's, Membrane Distillation (MD) is an alternative technique that involves the evaporation of a hot feed by creating a water vapor pressure difference across the thickness of a porous, hydrophobic membrane. The main advantage of MD over its counterparts resides (i) in the reduction of membrane and module stress, as no trans-membrane pressure is being applied, (ii) the decreased impact of contaminant fouling, since only water vapor is transported and (iii) low grade or waste heat from the industry can be used to generate the required difference of temperature across the membrane. Several attempts to commercialize large MD modules have been

made in Singapore and Amsterdam. Although the performance of these units, including commercial PVDF membranes were found satisfactory improved performance could be obtained for other membrane materials and module structures. Thus, to become competitive with other techniques, advanced membranes need to be designed that fit MD requirements.

Amongst the possible candidates, carbon nanotubes (CNTs) have shown interesting fluid transport characteristics and their intrinsic and semi 1D dimensional properties make them promising candidates for many separation and purification applications. Work has already demonstrated their potential for nanofiltration, bacteria removal, pervaporation and capacitive deionisation. Natural CNT properties, such as high hydrophobicity, chemical and thermal stability, make of them promising candidates for MD.

In this work, CNT Bucky-Papers (BPs), mats of entangled nanotubes, were processed and tested both as gas adsorption support and membranes for MD. The BPs exhibited very high porosities (up to 90%), can be easily functionalised to enhance the natural hydrophobicity of the CNTs, used as a template for advanced composite processing, and offer low thermal conductivity in assemblies. BPs were fabricated by vacuum filtrating CNTs suspended in solution and further processed into porous composite membranes by different approaches: (i) sandwiched with porous polymeric layers, (ii) infiltrated with polymers to enhance their stiffness and improve their lifespan; (iii) coated with a thin, active polymer layers to benefit from both the polymer properties and properties of the BP; or (iv) coated with metal nanoparticles. Work was carried out to tune their surface hydrophobicity, porosity and pore size to fabricate high performance membranes. The composite membranes were tested in Direct Contact Membrane Distillation and compared with materials commonly used in MD, namely commercial poly(vinyl-difluoride) and poly(tetra-fluoro-ethylene) membranes.

Introduction

'Experience is the name everyone gives to their mistakes.'

~Mr Dumby in *Lady Windermere's Fan*, Act III, 1892 – Oscar Wilde

Water is the key to life on Earth. A biological, economical and social asset, it represents 70 % of the mass of our bodies, is required to grow crops and foster livestock, and an essential fluid in industries for cooling, lubricating, or use as solvent for chemical reactions. However, despite it's prevalence in our life and its abundance on Earth, our society is facing global water stress. Population growth, increased standards of living and changing water distribution due to climate change are fast forcing us to change our habits and to adapt to new sources of clean fresh water. Furthermore, the energy crisis linked to the end of the oil era, and mankind's desire to limit its carbon footprint on our environment, have changed people's attitude and sustainability is now a key, long term societal development strategy. New methods to produce fresh water that require less energy and that can be applied over a large range of scales and under various economic conditions have to be developed.

As 97 % of water is salty, desalination of seawater appears as an infinite source of fresh water, able to provide people anywhere on Earth. Current desalination processes and methods can achieve high yields and salt rejection but rely on systems expensive to run and maintain. Therefore, new desalination routes that can be either substitutes or complementary to well established methods are being sought. Issues related to brine treatment and highly concentrated brine discharge also arose over the past decade with the implementation of desalination plants, and techniques that could either increase the water recovery or diminish the discharge impact on the environment must be investigated. Expensive pre-treatments, bio-fouling and membrane durability are real challenges for the sustainable water production of more than 7 billion people.

Therefore, new desalination technologies are promising candidates to complement and assist existing techniques. New methods have to be able to benefit from low grade energy, be less sensitivity to fouling with reduced reliance on pre-treatments while being operable with less energy input or by combining them with existing energy systems thus making them free or cheap to run. Several techniques such as forward osmosis, relying solely on the using the osmotic pressure across a semi-dense membrane, capacitive deionisation where the ions are adsorbed into highly porous, conductive structures, or membrane distillation where water is evaporated at low temperature by creating a water vapor pressure gradient across a porous membrane, are promising candidates to be used either on small scale desalination or as complementary processes to existing reverse osmosis or thermal desalination plants.

Membrane distillation (MD) particularly has attracted interest from researchers and industries over the past 30 years and several pilot plants have been commissioned in Amsterdam and Singapore to assess their efficiency for seawater desalination (MemStill). A German Company (MemSys) also commercialized small units that can be implemented on existing waste heat sources to save on energy costs. MD is a thermal technique based on the evaporation of a water feed in contact with a porous, hydrophobic membrane. A temperature gradient is generated across the membrane and vapor transported across its air-gap before condensing on the other side. As only vapor is transported, the theorical salt rejection is higher than 99.99%, and high flux, comparable with reverse osmosis, have been reported across highly porous, hydrophobic membranes. Membrane distillation also offers several advantages over current techniques, as the water does not need to be either pressurized or boiled, thus limiting the risks of fouling on the membrane surface due to clogging and/or organic compound degradation. The trans-membrane pressure is kept low, in the order of the vapor pressure which limits the need for pre-treatment and reduces the risk of membrane ageing. Furthermore, as only vapor is transported, the process is also less affected by salt concentration and highly concentrated brines can be treated, thus allowing increased net water recovery. It can operate in different

configurations depending on the need for feed organic or volatile compounds recovery.

Despite those promising results, specific membranes need to be designed for MD to become more competitive and complementary with current techniques. As the diffusion regime across the air-gap largely depends on the pore size distribution, porosity and thickness of the membranes, a thorough control of these parameters is required to achieve high flux and selectivity. Several critical parameters such as the hydrophobicity, thermal conductivity and chemical stability must also be controlled to ensure long term stability of the material. In fact, to become more competitive over its desalination technologies counterparts, MD requires specifically engineered membranes with improved properties for enhanced performance.

Amongst the new and versatile materials that can be processed, nano-materials and nanotubes especially have already shown to be promising candidates in many separation applications. Intrinsic properties of nanotubes such as their frictionless surface properties, their low thermal conductivity in bundles, their very high thermal and chemical stability, as well as the opportunity to form very high porosity materials could be assets in MD and used to process improved membranes.

Macro-structures made of CNTs can be processed in a large range of morphologies. CNT can be aligned in forest-like fashion to form a network of parallel and aligned tubes, drawn from a forest to form a mat of aligned fibres or dispersed to form an anisotropic mat, similar to a non-woven structure. Each structure offers advantages over its counterpart and specific properties of the CNTs might be better used when specifically oriented or dispersed in a certain way. Aligning the CNT in a forest fashion has been demonstrated to form advanced nanofiltration membranes with enhanced flux, while webs of CNTs exhibit extremely high thermal and electrical conductivity making them promising substrates in nano-electronics and sensing. Yarns can also be drawn and twisted from drawable forests to form very thin and strong structures to be used in aerospace, automotive or composite material industries. On the other hand, random mats of CNTs, called Bucky-papers (BPs), exhibit very high porosities, far larger than conventional polymeric membranes, while being flexible structures that can undertake further

chemical or mechanical modifications to fit the needs of specific applications. The very high specific surface area of the CNTs can be, in the case of the BPs, preserved and used to make high adsorption and exchange capacity materials. Furthermore, as per the anisotropic CNT properties, thermal and electrical exchanges are made more difficult, thus making BPs promising low conductivity structures as opposed to their forests, webs or yarns counterparts. Processing BPs is usually performed by vacuum filtrating suspensions of CNTs and requires a deal of control over the CNT dispersion and suspension stability. It is however, a cheap and reliable method to process large surface areas with small amounts of CNTs, thus making BPs one of the most promising techniques to use CNTs on an industrial scale.

This work investigates ways to fabricate composite macro-structures made of carbon nanotubes in combination with polymers and metals to enhance membrane lifespan and performance. Carbon nanotube Bucky-papers were used as a template to engineer composite structures. The new materials have been thoroughly characterized for their thermal, structural and performance characteristics. The permeation and adsorption of gas and water vapor, as well as the membranes' performance in desalination by direct contact membrane distillation, were tested and compared with polymeric benchmarks.

This thesis is structured into 6 chapters and 5 appendixes. A brief summary of each chapter is given in the following:

Chapter 1

Literature review

The purpose of this chapter is to introduce the rationale behind the work undertaken over the past 3 years. The main advantages and drawbacks of current desalination techniques are reviewed to show where improvements can still be made. The membrane distillation process is reviewed and the opportunities promised over classic desalination techniques identified. Furthermore, an introduction to nano-particles and nano-tubes will be presented to highlight the latest breakthroughs and improvements that nanotechnologies can bring to separation science.

Chapter 2

Experimental techniques

This chapter covers all the experimental setups and techniques used in this research. Carbon nanotube growth and dispersion techniques are first described. Then the bucky-paper membrane characterisation techniques will be presented, including the investigation of their intrinsic properties (pore size, bubble point, porosity, thickness, BET surface area, contact angle…), and mechanical and thermal properties. Finally, the gas permeation and the Direct Contact Membrane Distillation setups, built for this work, are described.

Chapter 3

Carbon nanotube dispersion and bucky-paper processing

The rationale behind the technique used to disperse the chemical vapor deposition grown CNTs, as well as characterisation results of the suspension lifespan and quality will be given. The protocol for fabrication of the Bucky-paper membranes will also be described.

Chapter 4

Commercial membranes and self-supporting Bucky-paper membrane: setting up a benchmark

Commercial poly(vinyl-difluoride) and poly(tetra-fluoro ethylene) membranes were tested as a benchmark for the DCMD performance experiments. Preliminary results of water vapor permeation and salt rejection will also be presented for self-supporting carbon nanotube structures. This work was the starting point for the composite material processing undertaken in chapter 5.

Chapter 5

Composite BP membranes: improving the properties of self-supporting BPs for higher separation and adsorption efficiency

The processing of polymeric / carbon nanotube and metal / carbon nanotube membranes is described and their performance for gas permeation, gas adsorption and water vapor permeation is presented and compared.

Chapter 6

Discussion on the membrane distillation results

In this final chapter the outcomes of the work on the direct contact membrane distillation results and the benefits from the carbon nanotube membranes will be discussed.

General conclusions

The outcomes of this thesis will be summarized and the main breakthrough and novel work identified. Some issues related to the use of CNTs are discussed while future opportunities for carbon nanotubes in separation technologies and other applications are described.

Appendix

Appendix 1 - Dispersion and CNT/solvent interaction

Supplementary materials on the CNT dispersion and information on a related study where isoporous membranes fabricated from carbon nanotube forests were processed.

Appendix 2 - Pore and surface characterisation

Supplementary materials on the surface and pore characterisation are provided in this section.

Appendix 3 – Direct Contact Membrane Distillation

Supplementary materials on the polymeric membranes characterisation and membrane distillation results as well as surface SEM images are displayed.

Appendix 4 – Bucky-paper thermal properties

Extra information on the bucky-paper thermal properties are provided.

Appendix 5 – Small Angle X-ray Scattering analysis

Example of preliminary results of the SAXS results obtained at the Australian Synchrotron are presented.

Appendix 6 – Tortuosity calculations

Calculations and explanations on the tortuosity calculations based on the experimental values of porosity and of average carbon nanotube diameter are shown.

Table of Contents

Table of figures

Table of tables

List of common abbreviations

Carbon nanotube	CNT
Single Walled CNT	SWNT
Chemical Vapor Deposition	CVD
Catalyst Continuous Injection	CCI
Nano-particle	NP
Bucky-paper	BP
Bucky-Ribbon	BR
Membrane Distillation	MD
Direct Contact Membrane Distillation	DCMD
Reverse Osmosis	RO
Nano-filtration	NF
Electrodialysis	ED
Electroless plating	ES
Poly(tetra-fluoro-ethylene)	PTFE
Pall commercial 20 nm PTFE membrane	PTFE20
Pall commercial 220 nm PTFE membrane	PTFE220
Pall commercial 450 nm PTFE membrane	PTFE450
Poly(vynil-difluorure)	PVDF
Poly(styrene)	PS
Poly(propylene)	PP
Poly(ethylene)	PE
Dimethylformamide	DMF
Carbon dioxide	CO_2
Hydrogen	H_2
Methane	CH_4
Nitrogen	N_2
Nanometre	nm
Micrometre	µm
Microlitre	µL
Weight percent	w%

Volume percent	v%
Scanning Electron Microscopy	SEM
Transmission Electron Microscopy	TEM
Photo-Electron Spectroscopy in Air	PESA
Thermo-gravimetric Analysis	TGA
Fourier Transform Infra-Red	FTIR
Electron Dispersion Spectroscopy	EDS
Liquid Entry Pressure	LEP
Kilo electron volt	keV
Watts	W

Commonwealth Scientific Industrial and Research Organisation	CSIRO
Materials Science and Engineering	MSE
Institute for Sustainability and Innovation	ISI
Victoria University	VU
The University of New South Wales	UNSW
The Royal Melbourne Institute of Technology	RMIT

List of common symbols

Bolltzman Constant	R
Molar mass	M
Temperature	T
Area (surface)	A
Pressure variation	ΔP
Density (greek RHO)	ρ
Tortuosity (greek TAU)	τ
Thickness	t
Porosity (greek EPSILON)	ε
Pore radius	r
Pore diameter	d
Permeation prefactor	P
Flux	J
Permeance	f
Permeability	k
Power (greek PIE)	Π
Thermal conductivity (greek LAMBDA)	λ
Surface tension	γ

Chapter 1

1 Literature Review: desalination techniques, membrane distillation and nano-materials in separation

1.1 Introduction

"Thousands have lived without love, but not one has lived without water."
W.H. Auden

From the clouds of the sky to the tides on the shores, from the drops in the rain to the aquifers in the ground water lies everywhere on Earth. An impressive amount of ~1,400,000,000 km^3 of water that boils, drops, flows and freezes. Water can be found in various forms: vapor in the clouds and atmosphere, liquid in the oceans, rivers, lakes and aquifers and solid in both glaciers and ice caps. But is it really that much? If one made a sphere out of this volume, it would have a diameter of only 1390 km and would not even entirely cover Europe or Australia (Figure 1-1) [1].

Figure 1-1 Water volume on the Earth compared to the planet size

Furthermore only ~3% of this water is naturally fresh enough to sustain non marine life. On every continent a race is on between social and biological needs, between men and nature to get control over the main sources of fresh water. Life is sometimes at stake and only wise use of resources will lead to sustainability. In fact, fresh water can be produced by three different main methods. It can be either directly extracted from rivers, lakes or aquifers, collected from the rain, or transformed from seawater Figure 1-2 [2].

Nowadays, fresh water is being produced and extracted for ~70% of human beings from rivers, lakes or aquifers. Population growth may reach 9 billion in 2050 [3] and the increasing standard of living of the various developing countries will require further development of fresh water production before reaching peak water use. Water stress, as emphasized in Figure 1-3 is a critical global issue. Entire parts of the world are being affected and more and more urban area might be subject to climate change effects [4].

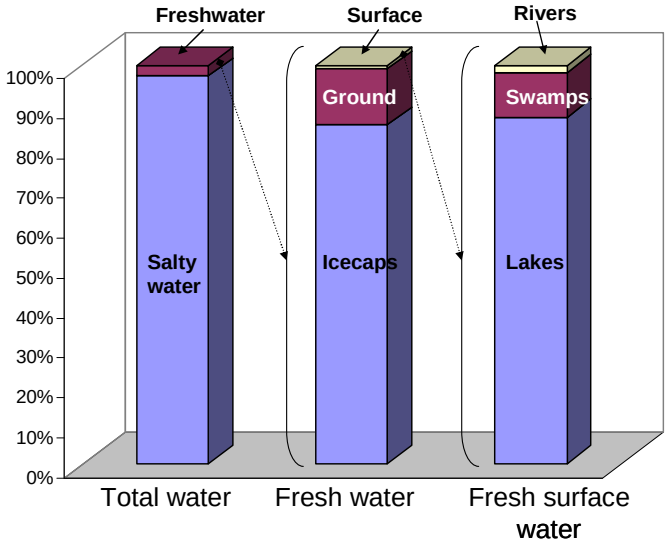

Figure 1-2 Breakdown of the water on Earth

Outrageous exploitation of our finite fresh water resources has already impacted both eco-systems and global water reserves that are highly dependent on rainfall to regenerate and on geological hydrodynamics. Entire parts of the world are drawing down their water reserves because of excessive extraction of the ground resources or collection from our rivers [5, 6]. Fresh water is vital for our societies either for irrigation in agriculture, cooling, cleaning or as a reactive media in industry and of course for health purposes [7]. Furthermore, for each application the water needs to match specific requirements of composition, purity and salinity to perform at its best.

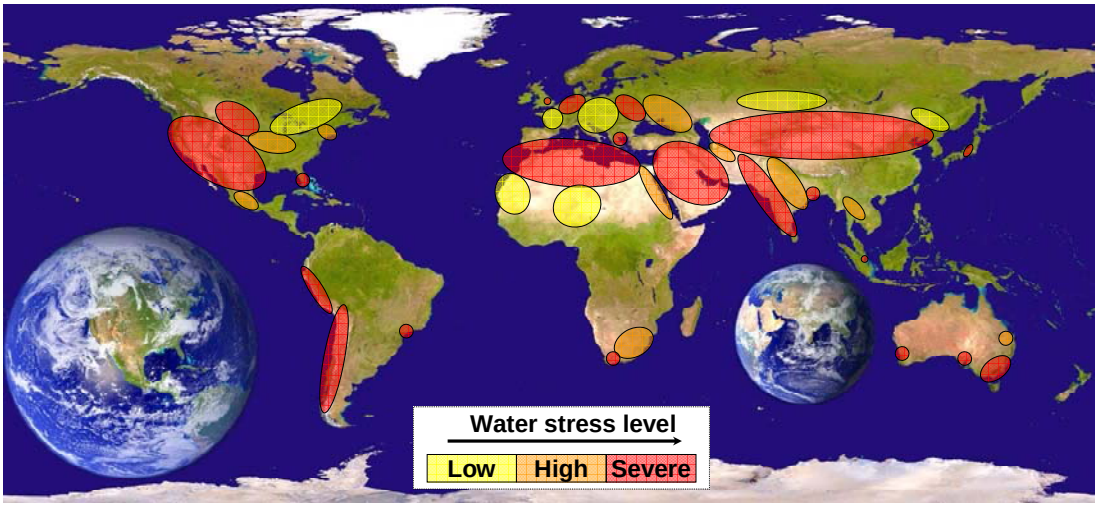

Figure 1-3 Global water stress level-extracted from the IDA website – accessed 14th of May 2010; Un-labelled areas are considered to not be under water stress

The scope of this PhD covers various fields of research and a comprehensive review was required to present its various dimensions. The general aim of this PhD was to engineer membranes for separations applications based on Carbon Nanotubes (CNT). The main focus of this work was to fabricate advanced composite membranes for membrane distillation as an alternative technique to desalinate water. The review will be divided up into three sections.

The first section focused on the major techniques available to desalinate water. Two very different approaches are currently being used: (i) thermal or (ii) membrane based techniques. The different techniques will be introduced and compared to present their main advantages and drawbacks. Membrane based desalination techniques, i.e. reverse osmosis, electrodialysis and membrane distillation will be presented and several examples of their performance and potential complementarities depicted. The properties of the membrane structures for the different techniques will be described to show where improvements are still required in membrane science.

Membrane distillation stands as a complementary and alternative technique where waste heat can be used as cheap energy to desalinate water and this is of high interest in our times of global energy crisis and to reduce

our carbon dioxide emissions. The theory behind membrane distillation will be developed and both the limitations and the optimal properties that an adequate membrane for MD should have will be presented. To become more competitive and complementary over other desalination techniques, new membranes are required to offer a low energy route, high salt rejection and permeability for improved performance.

Eventually, the latest breakthroughs in nanomaterial based membranes for separation and water treatment will be presented. Several nanomaterials and nanostructures have shown to enhance either selectivity or permeability of membranes for separation. CNTs especially have shown fascinating fluidic properties and their frictionless and semi 1D dimensions make them promising candidates for many separation and purification applications. Work has already demonstrated their potential for nanofiltration, bacteria removal, desalination and membrane distillation. In this part, we will briefly present various forms and structures of nano-materials. A review on CNTs and on their incorporation into macrostructures will be presented to underline the applications in which they could play a leading role in the future.

1.2 Main desalination techniques

1.2.1 General facts

Desalination of seawater appears today to be the most obvious solution to respond to fresh water stress and shortage. It does not impact highly on ecosystems and preserves natural resources. Desalination refers de facto to the removal of excess salts or minerals from soil or water [8]. In fact ,over 203 countries recognized by the UN 79% have open access to seawater which represents ~93% of the human population [9]. Despite the fact that most of the population is close by the sea and that research has been done on it over the last 50 years, desalination is still a costly and high energy consuming technique. Research is being carried out to reduce costs and new techniques are emerging to produce fresh water of high quality with less energy.

The most commonly used techniques worldwide [10] are thermally driven techniques where the feed of water to desalinate is evaporated, thus concentrating the salts in a brine waste stream while the water vapor is condensed in a separated cooling system. These techniques were developed in the 1940's and present many conveniences, such as the simplicity of these systems and/or the quality of the final product. The installations are generally considered to be expensive to run as they require a lot of maintenance. This is the reason why alternative techniques requiring less energy and achieving better separation are being investigated.

At the moment, one the most popular technique is the Multi-Stage Flash distillation that covers 35 % of the worldwide production [10-12]. This non-membrane based technique relies on vacuum distillation of seawater by evaporating hot water at a pressure lower than atmospheric pressure. Vapor compression desalination (VC) [13-15] is another technique that uses the steam generated in power production as the heat source. Mechanical energy through a compressor needs to be input and the maintenance costs of such

systems in very alkaline solutions remain very high [10, 16]. Multiple-effect distillation (MED/ME) is another technique, where water and steam circuits are fed in parallel to each other, and steam generated in one stage is used to heat up the water in the next stage. Even though energy recovery improves the efficiency the energy costs remain high if free or waste heat is not available [17-19].

All those methods remain highly expensive because of their energy consumption, if no excess heat is input [20-22], and their high operating costs [23] linked to both maintenance and thermal stress induced in those working conditions [10]. Thus, alternative techniques based on membrane separation are being sought [24].

The second set of techniques can be either pressure, concentration, thermally or electrically driven. They are based on the separation of at least two streams of fluids by a third medium. These media, called membranes, are used as separation barriers between the streams. The membranes have different geometries and properties depending upon the application. Various desalination techniques where a membrane is involved are presented and compared.

The major breakthrough over the past 50 years in membrane based desalination came through pressure driven techniques where a membrane is used in cross flow mode. About 60 % of the current desalination plants are based on Reverse Osmosis (RO) [25]. In RO [10, 26] the water is pressurized onto a semi-dense membrane to a pressure greater than the osmotic pressure of the solution [27]. Salt ions are rejected and water is transported across the membrane. RO's efficiency is high and energy recovery is also possible leading to lower operating costs. However, because of the sensitivity of the membranes to contaminants [28-31], surface charge [32] and pH [33-35], extensive pre-treatments are required to sustain both the lifetime and the performance of the membranes [36-38]. Amongst the other pressure driven processes, Nanofiltration (NF) is also used to separate low molecular weight polymers or inorganic salts from a solvent by pressurizing a feed on a membrane and forcing part of species present through the membrane. NF relies on both size and Donnan exclusion [10] (surface charge) for separation,

similar to RO that also requires size and charge for separation of species. Generally NF and RO membranes are used at pressures ranging respectively between 10 and 20 bars, and 20 and 70 bars. The structure of the membranes varies from porous (pore range between 0.5 and 2 nm) in the case of NF to semi-dense (<0.5 nm) for RO membranes. The material properties also impact the performance, and most RO membranes are asymmetric with a bi-layer structure where a thin, dense, 100 nm layer is deposited onto a strong supporting layer. NF membranes can be either symmetric or asymmetric and present mono-disperse pore size distribution. RO membranes are classically polymeric and need to be hydrophilic to facilitate the water diffusion. These membranes, made of for example cellulose acetate, aromatic polyamides or polyimides and offer low solute permeability and high rejection factors.

A second technique called Electro-dialysis (ED), relies on an electrically driven potential difference where the feed flows between series of alternating anion and cation selective ion exchange membranes [10]. An electric field is applied across the stack of alternating cationic/anionic ion exchange membranes, and ions are transported across the membranes. In electrically driven membrane processes, an ion exchange membrane acts as a charged barrier where ions of a specific charge are either repelled or transported through it. Ions get attracted to the ion exchange membranes via the applied electric field, and diffuse across the membrane towards their corresponding electrode [39]. In the ED reversal process, the membrane polarity is reversed periodically to reduce scaling. Pre-treatments are once again required to avoid fouling of the membranes but in general this technique is less sensitive to suspended solids and can treat more concentrated solutions than RO. In this case the amount of ions transported through the membrane is directly proportional to their valence and to the applied electrical current. Ion exchange membranes are divided into anion exchange membranes, or positively charged membranes and cation exchange membranes or negatively charged membranes. Anion exchange membranes contain positively charged groups, such as quaternary ammonium ions while cation exchange membranes contain sulphonic or carboxylic groups.

Desalination efficiency and permeability are limited and the membranes tend to be more selective to monovalent ions.

Pervaporation is a concentration based technique where the feed is in direct contact with one side of the membrane while the other side is composed solely of the fluid vapor. A low vapor pressure is created on the permeate side and selectivity is achieved by a difference in the components vapor pressures by the solubility of components in the membrane and its desorption into a carrier medium (sweep gas or vacuum for example). Pervaporation is in fact more selective than MD because of the membrane characteristics [39-41]. A dense membrane acts as a barrier between the liquid and the vapor phase. The limiting factor is thus the solubility/diffusivity of the vapor in the membrane. Polymers classically used for desalination have to be hydrophilic and offer high solute permeability. In the case of water desalination, poly(vinyl-acetate) or polyamides are classically used and present good solubility/diffusivity ratios.

Amongst the thermally driven techniques, Membrane Distillation (MD) is one of the complementary techniques for RO. MD processes rely on the vapor pressure gradients created across a porous membrane. In Direct Contact MD (DCMD), two solutions at different temperatures are separated by a non-wettable porous membrane. The temperature difference between both streams induces a liquid vapor pressure gradient thus evaporating the hot liquid in contact with the membrane, transporting vapor across the pores to the cold surface where it is eventually condensed. In the case of water desalination MD relies on the evaporation of a hot brine feed in contact with a porous, hydrophobic membrane and the condensation of the pure water vapor on the other side of the membrane. A water vapor pressure gradient is generated across the membrane by the temperature difference between both feed and permeate. MD can be configured in 4 different setups, which includes Direct Contact (DCMD), Vacuum (VMD) Air-gap and Sweep-gas membrane distillation. MD is a less mechanical stressful technique since the the membrane is pressurized at much lower pressure than in conventional methods such as RO. However, condensation and collection of the permeate and its transport as water vapor can be costly. These techniques will be developed in the 3rd section of this review.

Other techniques, such as capacitive deionisation [42-47] and forward osmosis [48-54] are being developed and offer interesting alternative technologies but there is no large commercial development of these techniques on the market yet.

The global desalination market split over those techniques is dominated by Multi-stage Flash desalination (thermal technique) and Reverse Osmosis (membrane technique) as shown in Figure 1-4.

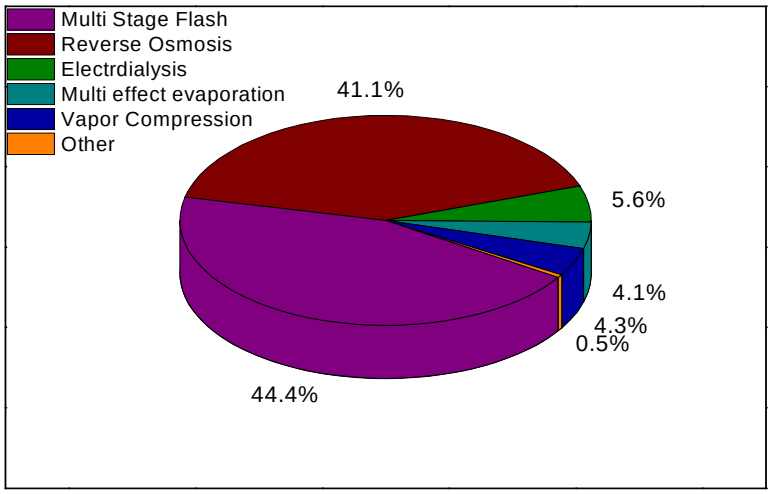

Figure 1-4 Desalination capacity classified by technique used. More than 99.5% of the water being desalinated is being treated either by Multi Stage Flash desalination, Reverse Osmosis, Electrodyalisis, Multi-effect evaporation, or Vapor compression – data 2006. www.worldwater.org – accessed 16th of May 2010

The Middle East (Saudi Arabia, United Arab Emirates, Kuwait, Israel, Algeria, and Bahrain) and the USA are the two main areas where most of the major plants have been installed over the last 55 years (Figure 1-5). These countries are heavily touched by drought and water stress and need huge amounts of water to sustain their growth. The energy is generally provided by oil or coal power plants.

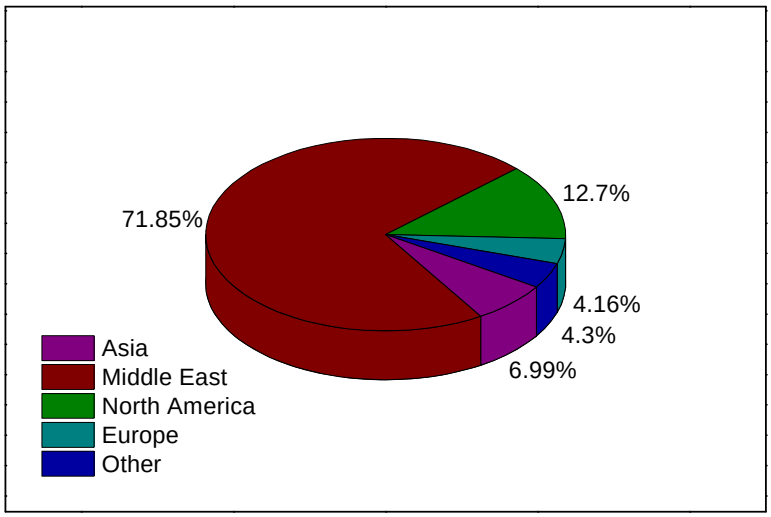

Figure 1-5 Main desalination plants classified by geographic area from 1960 to 2005 IDA website; www.worldwater.org – accessed 16th of May 2010

To face the new challenges that arise from developing and growing societies new complementary techniques need to be combined to address the rising energy consumption and environment concerns while sustaining the production of high water quality. One of the previously quoted techniques, Membrane Distillation offer several advantages, such as the possibility to work at low pressure and at very high salt concentration, over its counterparts and research is focused on establishing synergies between techniques to treat the water.

1.2.2 Statistics on desalination techniques

Over the past 35 years desalination research has been mostly focused on the improvement in the engineering of the modules as well as addressing the increasing cost of energy. Research has been carried out on thermally driven techniques mostly in the Middle East, where energy costs are much smaller than in America or Europe (Figure 1-6). Europe is very active in MD and ED, while North America as a strong focus on RO. The number of publication reflects well the global desalination market trends by geographical areas. Most of the membrane manufacturers and RO desalination plants are located in America, Europe or Asia, while most of the thermal based plants are based in the Middle East and North Africa.

Furthermore, even though the average desalination plants treatment capacity is between 100,000 and 300,000 m^3/day (Figure 1-7) the current trend is to build either much bigger plants to fulfil the needs of the major cities or smaller plants for remote small communities. This trend is particularly visible in Australia, where many small community projects are being funded in parallel to massive plants to provide water for the capital cities. Similarly, America has an average RO treatment capacity of only of 85,000 m^3/day.

Better processes consuming less energy for the same output were required, which gave its chance to emerging technologies such as RO or ED. Both started to grow rapidly in the 1960's exceeding thermal based techniques in the early 2000's [25]. Both methods have been commercialised in either small portable units or large plants in the case of both RO and ED.

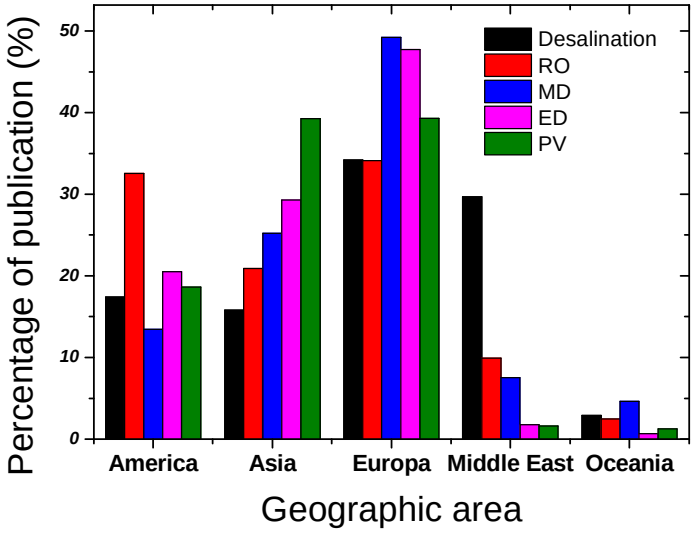

Figure 1-6 Publications in various fields sorted out by geographic area; Data obtained from Science direct website publication analyser 2010

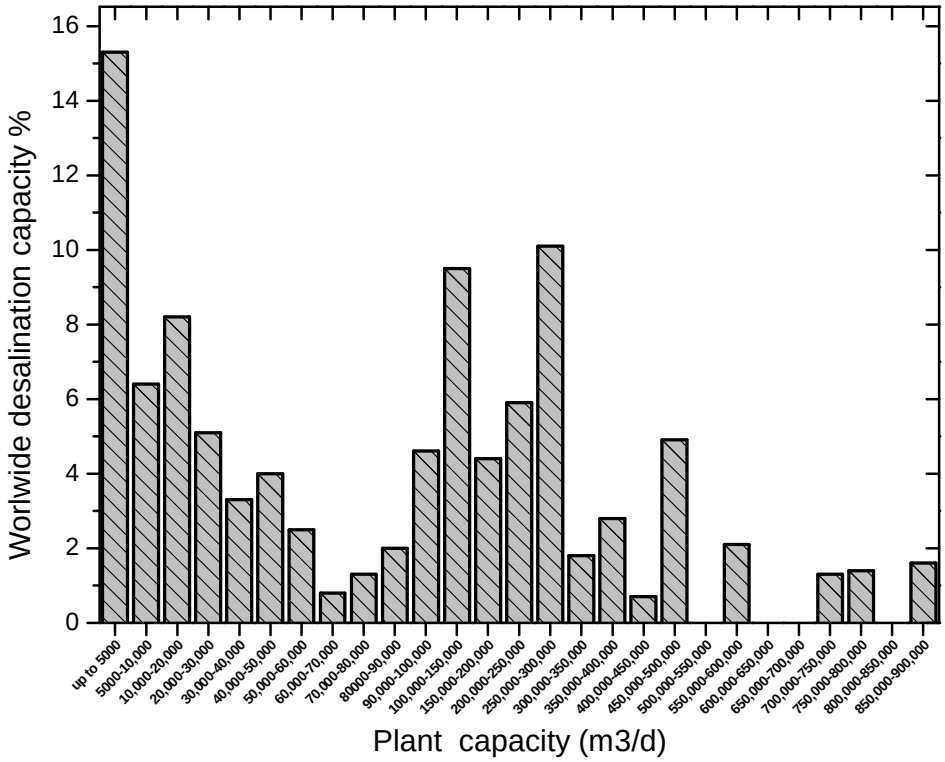

Figure 1-7 Worldwide desalination capacity sorted by plant size; Data obtained from Science direct website publication analyser 2010

Furthermore, grafted onto these two techniques, alternative and complementary methods such as pervaporation and membrane distillation started to emerge. The number of publication from 1985 to 2010 shows clearly this diversification trend (Figure 1-8). Pilot plants using the membrane distillation setup have been built and are run in Amsterdam (the Netherlands) and Singapore [55-57]. It was proposed to benefit from the fact that MD is less sensitive to the salt concentration to post treat RO brine and benefit, by energy recovery of “free” energy from the RO plants. Studies showed that lost heat generated by plants could supply the energy to heat the water in MD, offering an alternate route to desalination at very low cost.

However to stay competitive with thermally based desalination plants, even though energy cost is the main factor, membrane based techniques had to reach higher efficiency than the thermally based processes. Most of the work published over the past 50 years has focused either on chemical engineering or polymer science (Figure 1-9).

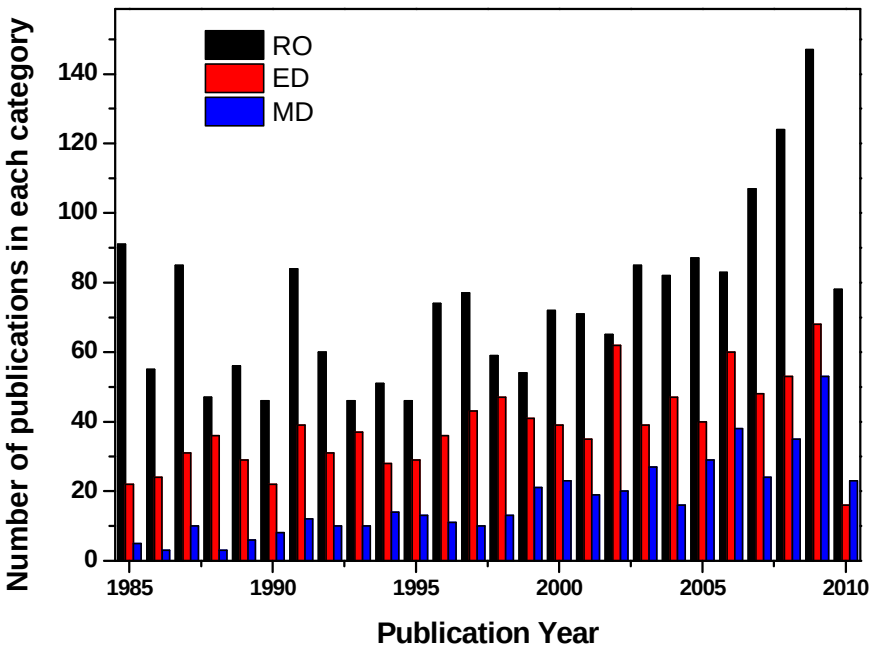

Figure 1-8 Number of publications since 1985 on Reverse Osmosis (RO), Electrodialysis (ED) and Membrane Distillation (MD) - obtained from an analysis on Science Direct 2010

This fact shows how important is the control and the modification of membrane properties. Membrane based techniques had to become economically sustainable only if the separation barrier was efficient and appropriate enough. Most of the work has then been focused on the membrane module design and on the chemistry of the active layers of the membranes to enhance their properties (Figure 1-9).

A summary table of the main properties of the membrane used for the various techniques previously quoted are given in Table 1-1. This shows the diversity of the membrane material, structure and properties.

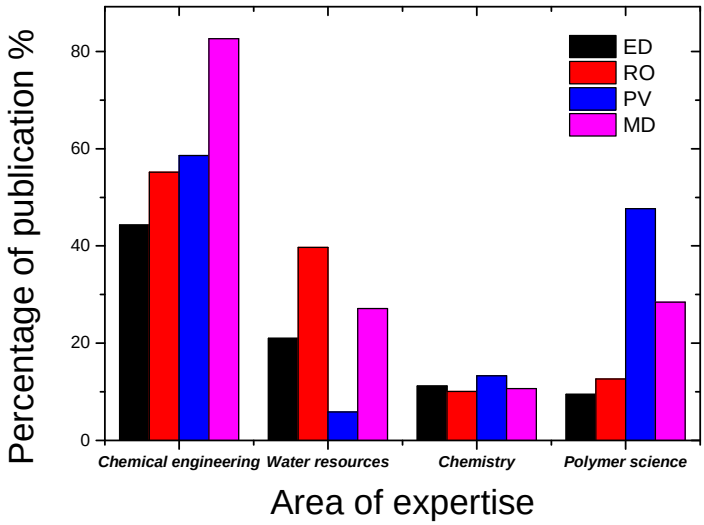

Figure 1-9 Scientific fields where membrane research is being pursued – obtained from an analysis on Science Direct 2010

Table 1-1 Properties of the membranes used in the previous techniques

Technique	*Density*	*Pore size*	*Material*	*Cost*
RO	Semi dense	<0.5 nm	Resins (i.e. polyamide (PA), cellulose acetate)	High
NF	Porous	<1-2 nm	PA	High
ED	Dense	N/A	Ion exchange resins (Nafion, PE)	Medium to high
Pervaporation	Dense	N/A	PVA	Low
MD	Porous	<1 μm	PTFE, PVDF, PP, PE	Low to Medium

1.2.3 Conclusions

There is a clear need for improved desalination technologies offering enhanced flux at lower prices. Several techniques seem today to be possible candidates and MD is certainly amongst them. The low pressure and high feed salt concentration make of MD systems interesting complementary techniques to RO or ED plants. However to become more competitive the membrane properties (pore size, porosity, and thermal conductivity) need to be engineered and improved to tackle the performance of the actual leading techniques.

1.3 Membrane Distillation

1.3.1 Introduction

Direct Contact Membrane Distillation (DCMD) is a separation technique where a non-wettable porous membrane is used as a separation barrier between two independent streams [58-60]. The streams are circulating on both sides of the membrane at different temperatures creating a vapor pressure gradient. MD is a non-pressure driven separation technique since only liquid vapor is transported across the membrane due to differences in vapor pressure across the membrane (Figure 1-10).

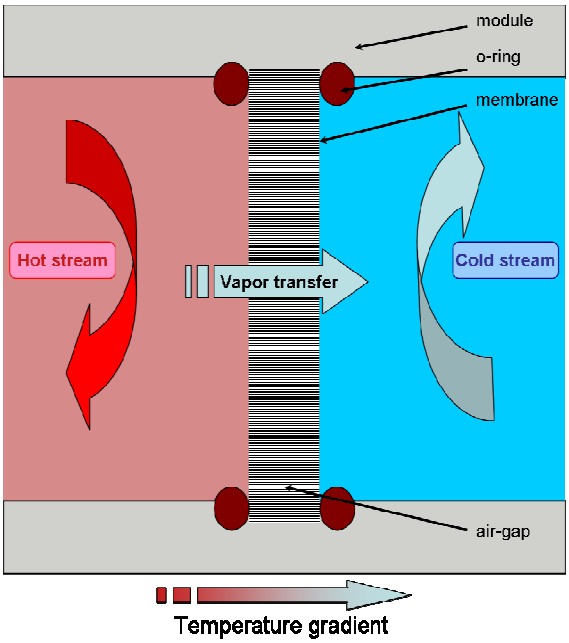

Figure 1-10 MD concept; A membrane is used as a separation barrier between two independent streams

MD membranes need to match specific properties to achieve high performance in both permeation and selectivity. According to the 'Terminology for membrane distillation', MD membranes should match the following criteria [61]:

- be porous (present an air gap)
- should not be wetted by the process fluids (hydrophobicity criteria)

- must not alter the vapor liquid equilibrium of the different components in the process fluids
- no capillary condensation should take place within its structure
- one side of the membrane at least should be in direct contact with the process fluid and
- the driving force of the operation should be the partial pressure difference in the vapor phase

Industrially, MD is used for chemical separation in the pharmaceutical industry, degassing and volatile fluid removal in the mining industry and proteins or sugar concentration in the food industry. Amongst the possible applications where MD might bring benefits, fruit juice concentration [62, 63], de-nitrification of mining extracts and ammonium removal [64], alcohol-water and liquid mixtures separation [65-68], proteins concentration [69] and water desalination [70-80] have been demonstrated either in laboratory or pilot plant trials.

1.3.2 Membrane morphology

The shape of the pores and the material composition of the membrane may differ greatly depending on the material constituting the membrane, the processing conditions and the kind of properties sought [81]. The membrane material and structure has to be carefully chosen to both achieve high permeability and selectivity. It is generally admitted that permeability is controlled by the membrane pore size and porosity, while selectivity is obtained because of differences in the vapor pressures of the compounds being separated [82-85]. Generally, as shown in Figure 1-11, various kinds of pore structures can be found. The characterisation of the pore morphology, tortuosity and pore density can be done using various techniques, including BET [77, 84, 86-92], AFM [87] and/or SEM [81]. The pore size distribution can be determined by porometry [93-96] while the porosity of the membrane can be estimated by using pycnometers [77, 97, 98]. Other techniques such as air permeability tests can also be used to evaluate and predict the performance of membranes in MD [99, 100].

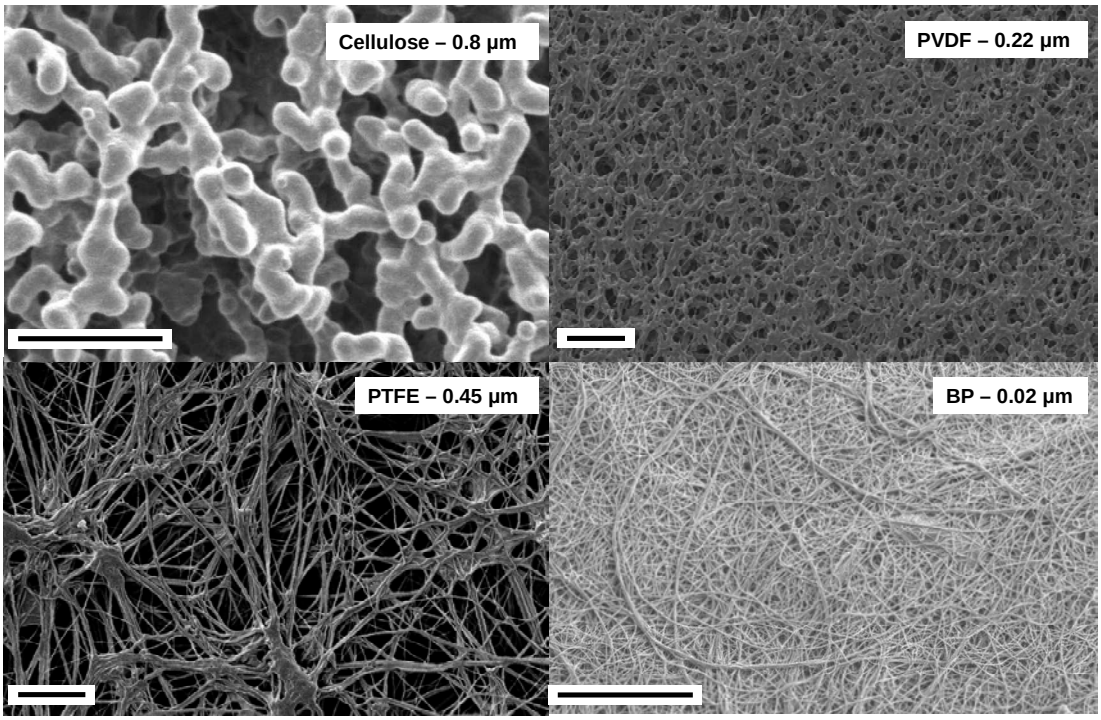

Figure 1-11 Various membrane morphologies. Top left: cellulose acetate membrane 0.8 µm pore size. Top right: PVDF membrane 0.22 µm pore size membrane; Bottom left: PTFE 0.45 µm pore size membrane; Bottom right: CNT BP 0.02 µm pore size membrane

It is generally recognized that determining a real pore size is difficult and indirect measurements are often preferred through Liquid Entry Pressure (LEP) or porometry [61, 101, 102]. The most critical parameter in MD is the surface energy of the membrane as pore wetting by the processed liquids must be avoided. The Laplace equation gives us a relationship between the membrane's largest available (non-closed) pore size (r_{max}) and the operating conditions (Equation 1). To work efficiently the LEP of the membrane, calculated from the Laplace equation, must remain higher than the gradient of pressure applied on the interface pore/liquid:

$$LEP > \Delta P_{interface} = \frac{-2B\gamma_L \cos\theta}{r_{max}} \qquad (1\text{-}1)$$

where *B* is a geometric factor determined by the pore structure, γ_L the liquid surface tension and θ is the liquid/solid contact angle and r_{max} the largest pores in the structure.

The diffusion mechanisms across the membrane are considered to follow gas diffusion theory and highly depend on its average pore size. Three different regimes can rule the diffusion mechanism depending on the mean free path of the molecules within the pores [58, 103-107] (Equation 2). A general law ruling gas diffusion is given in Equation 2. Typically diffusion is proportional to the average pore size distribution and porosity while inversely proportional to the thickness and tortuosity of the membrane.

$$f = K(T) \times \left(\frac{r \times \varepsilon}{\tau \times t} \right)^{\alpha} \qquad (1\text{-}2)$$

where f is the permeance of the membrane, K(T) is a function of temperature and molecular gas of the gas; r is the average radius of the pores, ε the porosity, t the thickness and τ the tortuosity of the membrane.

Furthermore, the power α will vary with the ratio of the mean free path, λ, with the average pore size of the membrane with three different scenarios:

- if λ/r > 1 then the mechanism is said to follow Knüdsen diffusion
- if 0.5 < λ/r < 1 the regime is called transition regime
- if λ/r < 0.5 the regime is called molecular diffusion

The mean free path is defined in Equation 3 as:

$$\lambda = \frac{k_B \times T}{\sqrt{2}\Pi \times d^2 \times P} \qquad (1\text{-}3)$$

where k_B the Boltzmann constant, T the temperature (K), d the average kinetic diameter of the molecule and P the pressure.

As shown in Equation 1 the likelihood for wetting across the membrane decreases with smaller pores. On the other hand, as shown in Equation 2, the permeance is directly proportional to the average pore size and to the porosity of the membrane. Large pores are thus needed to achieve high permeability.

A trade off is necessary and the pore size distribution needs to be narrow enough to address the wetting criterion while large enough to facilitate efficient vapor transport.

Both flat-sheet and hollow fibre membranes can be operated in MD [82, 86, 95, 108]. Figure 1-12 presents some geometrical differences between poly(vinyl-difluorure) (PVDF) flat sheet and hollow fibre 0.2 micron pore size membranes. Appropriate MD Membranes can be either symmetric or asymmetric with, respectively, one single thick active layer or a thin active layer reinforced on a support layer.

The active layer needs to be as thin as possible to enhance the permeance while presenting a low tortuosity path to the gas molecules (Equation 2). Membranes for MD generally have pore size distributions lying between 0.05 and 1 µm [59, 84, 109]. Typically, the porosity of commercially available membranes is often around 70% while the thickness of their active layer can vary from a few dozen up to a hundred microns.

Previous publications have shown that multi-layer approaches with gradients of hydrophobicity / hydropillicity can lead to high performance MD membranes [110-112]. This suggests that hybrid structures where a highly hydrophobic surface is put in contact with the feed, while an hydrophilic surface is in contact with the permeate may provide improvements in MD performance. The wetting is more favourable on the permeate side which was shown to reduce the temperature polarisation and helps condensation of the water vapor. Wetting can however enhance the chances of fouling and work to understand the process behind multi-layer MD membranes and their potential has been conducted [110, 113, 114].

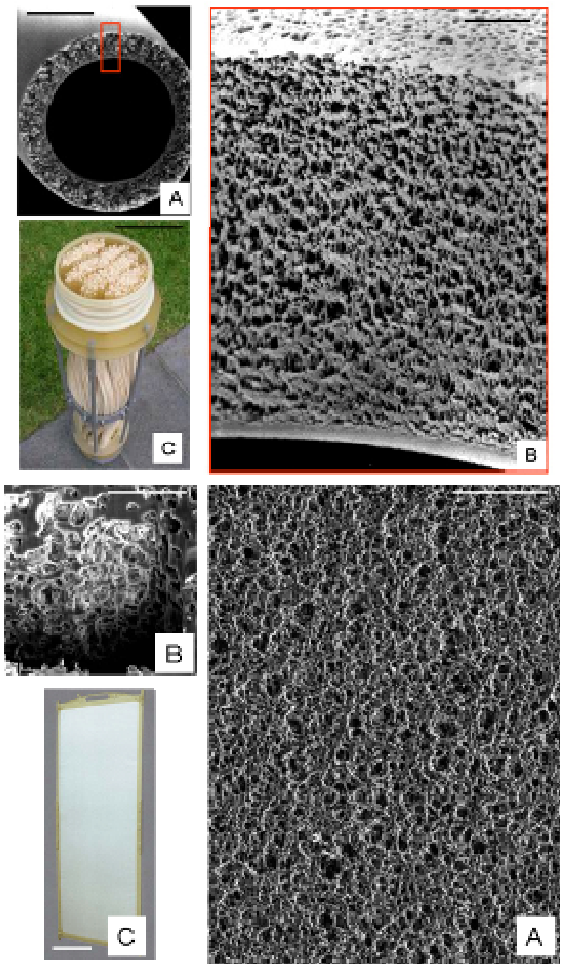

Figure 1-12 Hollow fibre (left) and flat sheet (right) membranes [115-117]

1.3.3 Membrane distillation configurations

In MD, both feed and permeate come in contact with the membrane and infiltrate the surface of the pores [84, 109, 114]. The vapor pressure difference generates the driving force and water vapor is transferred across the membrane.

The vapor can be either condensed directly on the other side of the membrane, (Direct Contact Membrane Distillation - DCMD) [109, 118, 119], or on a cold trap located further away in the module. In this late case three different approaches can be chosen: either by using a carrier gas on the permeate side (Sweep gas - SGMD) [120-123], by applying a vacuum (Vacuum MD - VMD) on the permeate side [60, 87, 107, 124, 125] or by keeping a constant volume of air entrapped (Air-gap MD - AGMD) between

the membrane and a cold condensing plate on the permeate side [106, 126]. Figure 1-13 shows a schematic of the 4 different configurations.

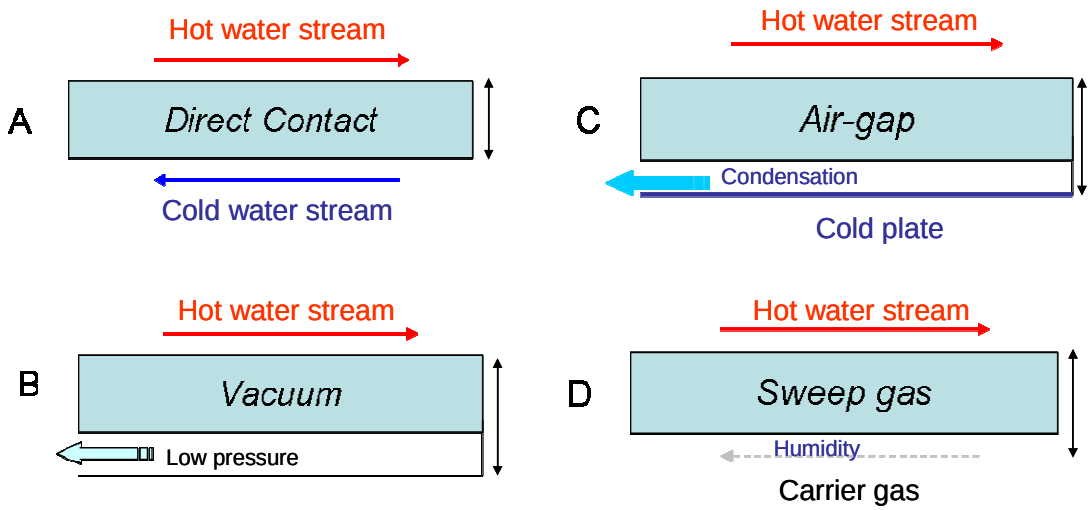

Figure 1-13 The four different MD configurations; A, B C and D respectively refer to DCMD, VMD, AGMD and SWMD

Each setup presents advantages and drawbacks accordingly with the application, energy requirements, product and separation efficiency sought as compared in Table 1-2. SGMD and VMD are generally preferred to separate two mixed liquids having different boiling points to avoid further treatments linked to the contamination of another carrier liquid on the permeate side [60, 67, 90, 127, 128]. On the other hand for water purification, water desalination, and product dewatering AGMD and DCMD are generally used since only the solvent is evaporated [63, 69, 129-134] from the bulk feed. Table 1-2 summarizes the applications in which the different setups have already been used. DCMD can be operated in either co or counter current, depending if both feed and permeate flow in the same or opposite direction.

Table 1-2 Fields of application in which MD technology has been used [82, 84]

Field of application	*DCMD*	*VMD*	*AGMD*	*SGMD*
Desalination and water treatment	✓	✓	✓	✓
Concentration of radioactive solutions in the nuclear industry	✓			
Removal of soluble and insoluble dyes (organic and inorganic compounds) in the textile industry	✓	✓		
Concentration of acids, removal of volatile organic compounds from water, separation of azeotrope aqueous mixtures such as alcohol/water mixtures and crystallization for the chemical industry	✓	✓	✓	✓
Removal of water from blood and protein solutions, wastewater treatment for health technologies	✓			
Concentration of juices and milk processing) in the food industry and in areas where high temperature applications lead to degradation of process fluids or organic compounds	✓	✓	✓	

Although the criteria developed in this section [61] apply to the 4 configurations, DCMD is generally preferred since it provides higher flux by reducing the size of the air-gap of the process. The air-gap in DCMD is composed by solely the membrane thickness/porosity whereas because of the additional feature required to condense the water vapor, it is larger in the other setups. Furthermore the membrane is DCMD provides the highest resistance to permeability [84] therefore will more accurately identify membrane performance and be a convenient comparison technique to identify the best membrane or material amongst a series of samples.

1.3.4 Membrane Distillation: theory of heat and mass transfer

Both heat and mass are transferred during a MD process. Controlling the temperatures of the feed, membrane surfaces and the bulk streams is fundamental to correctly master the process and calculate the permeance. Figure 1-14 shows the different parameters playing an important role in the process for a counter-flow configuration [100, 135-143].

T_i refers to the temperature, dT_i the temperature variation, m_i to the mass, dm_i the mass variation x_i to the concentration and dx_i the concentration variation, while the indice F and D respectively refer to the feed and permeate and the indices 1 and 2 refer to the membrane surface on the hot and cold side. Furthermore, the membrane thickness is noted t and the stream velocities are v_i. As seen in Figure 14, the temperature gradually decreases on the feed side from the bulk value down to the membrane surface temperature (yellow curve), while it gradually increases on the permeate side because of water vapor condensing from the bulk permeate up to the membrane surface. Thus mass is transferred from the feed to the permeate side, while heat is transferred in the same direction [58, 144, 145].

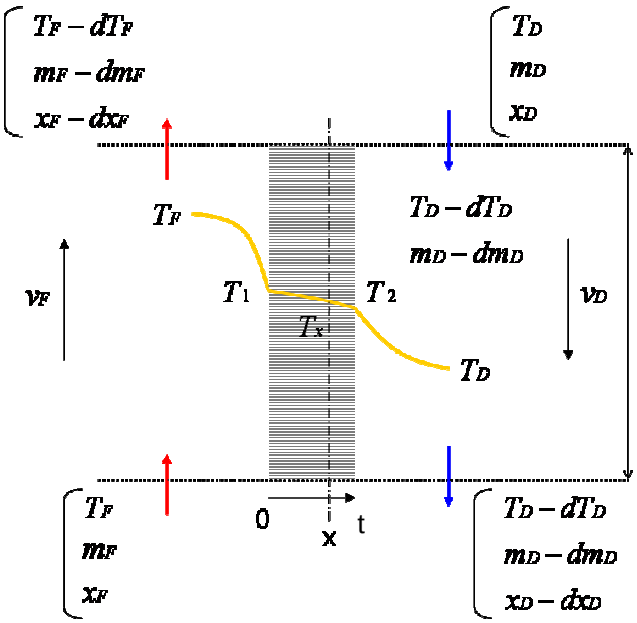

Figure 1-14 Heat and mass transfer in MD for a counter flow configuration

Theoretical derivations around MD mass and energy transport are well described [100, 106, 125, 136, 137, 142, 144, 146, 147]. However most of the models simplify the membrane structure and neglect thickness variations,

surface roughness and particularly simplify the complex pore structure of the membrane to cylindrical pores. Models have been written to take in consideration some of these parameters under specific conditions [86, 148-151].

Two properties, permeance, *f,* and permeability, *k*, are used to quantify mass transport across a membrane. The permeance is a true measurement of the amount of matter being transported across the membrane and for MD is a function of the processing parameters, while permeability enables comparison of membranes of different thicknesses. These two are respectively defined in Equations 4 and 5:

$$f = \frac{J}{A \times \Delta P} \qquad (1\text{-}4)$$

$$k = \frac{J \times t}{A \times \Delta P} \qquad (1\text{-}5)$$

where J (kg/s) is the flux through the membrane, t (m) the membrane thickness, A (m^2) the membrane area and, in the case of membrane distillation, ΔP (kPa) is the difference in vapor partial pressure across the membrane. The permeance can be determined by taking the gradient of a plot of flux against the vapor pressure difference, and dividing by the membrane area.

Furthermore, if the temperatures of the hot and cold streams are known, the vapor partial pressure can be calculated with Antoine's equation:

$$P = e^{\left(23.328 - \frac{3841}{T-45}\right)} \qquad (1\text{-}6)$$

where the partial vapor pressure P is in Pa and the temperature T in Kelvin (K).

It is generally accepted that mass transport through the membrane can operate in one of three regimes: (i) Knüdsen flow, (ii) molecular flow or (iii) a combination of both known as transition flow. The dominating regime is

indicated by the Knüdsen number (K_n), defined as the ratio of the mean free path (λ) to the pore diameter (d) [99, 109, 147].

For Knüdsen numbers, K_n > 1, the molecule - pore wall collisions dominate leading to Knüdsen type flow: For isoporous membranes with circular pores the permeance is given by [152, 153]:

$$f_K = \frac{2}{3} \times \sqrt{\frac{8M}{\pi R T_a}} \times \left(\frac{r.\varepsilon}{\tau.t} \right) \qquad (1\text{-}7)$$

where R represents the gas constant ($J \times K^{-1} \times mol^{-1}$), M the molar mass ($g \times mole^{-1}$), T_a the average temperature (K), r the average pore radius, t the membrane thickness (m), τ, the tortuosity and ε, the membrane porosity.

At the other extreme, for K_n<0.01, molecule-molecule collisions dominate leading to molecular flow through the stagnant air film trapped in the membrane. In this case the permeance is given by:

$$f_M = \frac{P_T D M}{R T_a} \frac{1}{P_{\ln}} \frac{\varepsilon}{t\delta} \qquad (1\text{-}8)$$

where D is the diffusivity of water vapor in air, P_T is the total pressure (air and water vapor) within the membrane and is assumed to be 101.325 kPa in this work, P_{ln} is the mean log average of the air pressure in the membrane defined as:

$$P_{\ln} = \frac{P_{air\,2} - P_{air\,1}}{\ln\left(\frac{P_{air\,1}}{P_{air\,2}} \right)} \qquad (1\text{-}9)$$

where P_{air1} and P_{air2} represent the air partial pressure on the hot and cold side of the membrane respectively.

At intermediate Knüdsen numbers 1>K_n>0.01, a combination of both transport mechanisms occurs. The total resistivity of the system is then equal to the sum of both Knüdsen and Molecular resistivity. This was modelled as

resistances in series in previous studies [99], leading to the following equation for permeance:

$$f_T = \frac{1}{1/f_K + 1/f_M} \qquad (1\text{-}10)$$

A few groups have shown that MD performance could be modelled by measuring the permeance of various gases in individual permeation tests [100, 103, 142, 147]. The limitations of the models generally lie in the approximations in the pore geometry and in the limited knowledge of heat transfer across the membrane. Furthermore, parameters such as tortuosity or true thermal diffusion remain difficult to investigate in situ.

1.3.5 Two limitations of membrane distillation: module design and temperature polarisation

Several parameters might affect the membrane performance in MD. Module design has been shown to be a critical aspect of the process. In fact a poorly designed module can lead to unwanted transfer of heat and thus flux losses while poor flow geometry may lead to temperature polarisation. The major issue limiting flux and performance in MD is temperature polarisation at the surface of the membrane. This phenomenon is intrinsic to the nature of the process and can not be fully avoided.

1.3.5.1 A critical step: the module design

Module design has been comprehensively studied in various publications. The fluid dynamics around the membrane has to be carefully considered to optimise performance, and to minimize heat losses and temperature and concentration polarisation [60, 131]. It is generally considered that the more turbulent the flow is in the module close to the membrane, the better the homogenise the temperature in the direction perpendicular to the membrane surface. High Reynold's numbers are

therefore preferred to enhance the turbulence and mixing, and thereby to reduce temperature polarisation. Module design is thus a critical aspect in MD and numerous studies have shown that the flow geometry, the material of the module or the shape of the exposed membrane will lead to difference in performance for the same membrane. It was shown that, in the case of flat sheet modules, wide and short modules offering high turbulent flows worked better than other configurations [60].

1.3.5.2 Temperature polarisation coefficient

There are two modes of heat transfer happening at the same time during MD: conduction of heat across the membrane material and module; and evaporation /condensation of the vapor across the membrane [135, 136, 146].

The material constituting the module and the membrane has to be carefully chosen to reduce heat transfers between the two streams [65, 66]. In DCMD conductive heat transfers across the module and membrane are not productive and should be minimized. In fact, if heat is being transferred, by conduction in the module for example, the global energy costs of the process will be increased and thus will the process efficiency decrease. As well, if there is significant heat conducted by the membrane, polarisation layers [90, 143, 154, 155] appear leading to a smaller temperature difference between the two streams and thus a reduction in both driving force and energy performance. As shown in Figure 1-14 the liquid is first being evaporated from the feed solution, leading to cooling this last. Evaporation is an endothermic process which means that the bulk liquid temperature will decrease between the input and the output on the hot side of the membrane module. The vapor is transferred across the membrane and condensed on the cold side, leading to an increase of the bulk permeate temperature between the inlet and the outlet. Condensation is an exothermic process leading to a local increase in temperature.

From this a temperature polarisation coefficient can be defined as:

$$\theta = \frac{T_1 - T_2}{T_F - T_D} \qquad (1\text{-}11)$$

Where the subscripts 1 and 2, and F and D refer to the same parameters as described in Figure 1-14.

It is however difficult to accurately monitor the temperature of the membrane surface and models have often been used to predict it from both inlet and outlet temperatures and the heat capacity of the material constituting the membrane. Homogenisation of the bulk liquid and the interface layer is the technique used to limit this effect.

1.3.6 Recent strategies and advances on membrane design for membrane distillation

While most of the investigated membrane body materials were up to date hydrophobic, a number of different strategies [156] have been reported on ways to integrate different degrees of hydrophobicity [75, 157, 158] on the surface of porous membranes. Although classically hydrophobic materials are sought to achieve high performance, it was demonstrated that hydrophilic [159] or hydrophilic/hydrophobic [88, 160] coatings were also potential ways to either improve the performance or the resistance of the membranes. These degrees of hydrophobicity were designed by combining different functional groups or by adding nanoparticles [161-163] at the surface of MD membranes. This was performed in order to change the surface properties such as the surface energy or the heat diffusivity and therefore maximize permeation, or reduce fouling, concentration polarization [118], material degradation [164, 165], or facilitate water evaporation. For instance, a fully hydrophilic material may, over time, be soaked with water and the air-gap thickness previously mentioned, will shrink to a point where bridging between the feed and permeate occurs and selectivity is lost. It was demonstrated that poly(ethylene glycol) / poly(vinyl alcool) coatings on top of PVDF membranes were more durable and exhibiting more stable performance than the pure PVDF supports [166]. In fact the addition of the hydrophilic layer was shown to reduce the impact of concentration polarization on the membrane surface.

Permeation was found to be more independent of the feed concentration and composition than in the case of a purely hydrophobic membrane. This was attributed to the higher surface energy of the membrane and to the improved surface wetting behavior by the processed liquids. Similar works investigated the addition of hydrophilic functional groups, such as carboxylic groups by UV/ozone treatment, or chemically grafting macro molecules on top of PVDF membranes [92, 97, 160]. It was also shown that cheap cellulose acetate membranes could be turned into efficient DCMD membranes by grafting the surface with hydrophobic poy(styrene) groups [159] while ceramic membranes were rendered hydrophobic by fluoroethylene grafting [163]. Therefore, surface energy is a key parameter to ensure high selectivity in DCMD [86] while also being critical to maintain high permeation over time. Furthermore a number of studies focused on the modification of the surface topology in order to reduce heat transfers and loss by conduction. These effects were primarily underlined in a number of studies focused on the characterization of modified membrane surfaces [89, 112, 167, 168]. Surface roughness was also found to highly affect dynamic wetting behavior, which is critical in MD to create and maintain a stable vapor/liquid interface [169].

1.3.7 Conclusion

MD is a promising technique to desalinate water. It can be competitive in the treatment of highly concentrated brines, as its performance is not affected by salt concentration. It can also be used to purify streams contaminated with organic foulants with less tendency for fouling than RO since it is non pressure driven.

However, improvements are still required in module design and membrane fabrication to achieve high permeance with high selectivity at low cost. Novel materials and approaches are therefore required before fully realising the benefits from large scale MD desalination plants.

1.4 Nano-materials and separation

In this section current research on Carbon Nanotube (CNT) structures engineered for separation will be discussed.

The number of publications on nanotubes has been growing exponentially over the past 20 years and CNTs are finding many potential applications in fields such as composite materials and separation as shown in Figure 1-15. In this section, a brief history of nanoparticles and nanotubes will be presented. Then CNT growth mechanisms and techniques will be explained. The most common properties of CNTs and possible treatment will be detailed followed by a review on the various CNT self-supporting and composite structures. Eventually the fields where CNT structures were used for separation will be presented in this review.

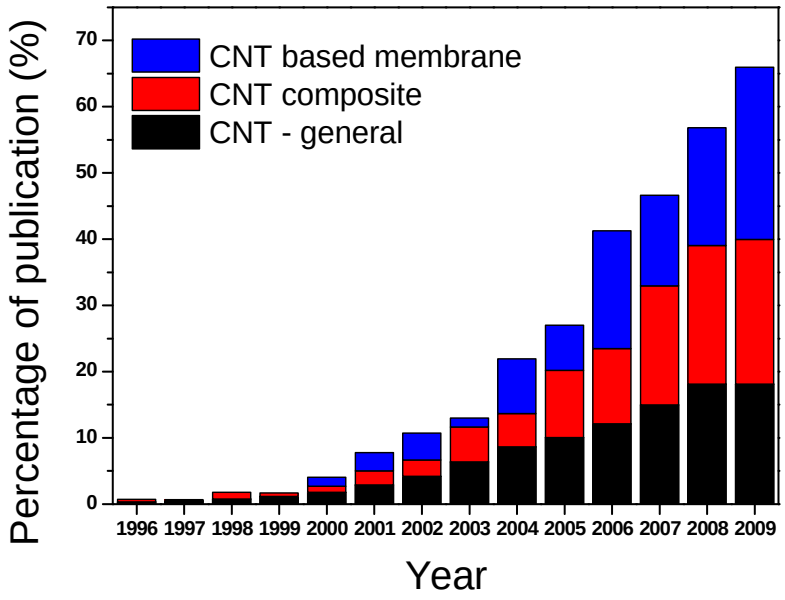

Figure 1-15 Statistics on CNTs - number of publication for (i) CNT in general; (ii) CNT composite; (iii) CNT based membranes

1.4.1 What is a nanoparticle?

There is no universally accepted scientific, industrial or international definition of a nanoparticle, but one given in the new PAS71 document developed in the UK is [170]:

"A particle having one or more dimensions of the order of 100nm or less".

This makes the size of particles or the scale of its features the most important attribute of nanoparticles. Nanoparticles exhibit higher specific surface areas than macro-particles enhancing the role of surface effects and adsorption on the laws ruling their physical, chemical and electrical properties.

1.4.2 From fullerene to nanoparticles … to nanotubes

Fullerenes are carbon based spherical clusters (Figure 1-16). Their discovery in 1970 led the way to the emerging field of nanotechnologies and nanomaterials. Before C_{60} and C_{70} were synthesised, it was generally accepted that large spherical molecules were unprocessable and unstable. However, Russian scientists calculated that C_{60} was stable and had a relatively large band gap. Fullerenes were discovered in 1985 by Kroto and Smalley [171]. Following these discoveries, groups worldwide started working on the growth of fullerenes and on the control of their properties. In 1991 Iijima and co-workers [172] showed that CNTs made of rolled up graphene sheets could be reproducibly synthetised. Their large aspect ratio, hollow interior and stability meant they were considered one-dimensional forms of fullerenes. Therefore, these new materials were expected to possess additional interesting electronic, mechanic and chemical properties [173] (Figure 1-16).

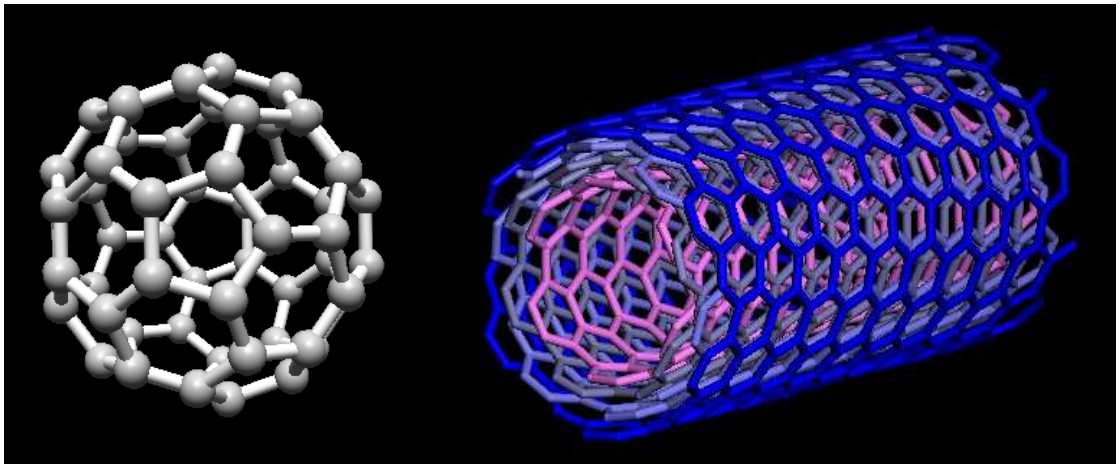

Figure 1-16: Left: fullerene C_{60} and; right: Multi walled carbon nanotube

Over the past 20 years nanotubes made of various materials have been synthesised. A nanotube can then be defined as a hollow fibre with diameter ranging between 1 and 100 nm. The number of walls varies depending on the nanotube type, history and growth conditions. Nanotubes can be fabricated as powder, or pristine, parallel arrays or a mesh of entangled fibres. Their length varies from a few dozen of nanometers up to a few millimetres. Figure 1-17 shows Transmission Electron Micrographs (TEM) of CNTs (CNT), Boron nitride nanotubes (BNNT) and Gold nanotubes (GNT) as examples of three very different nanotube materials. The CNTs and BNNTs present as a multi-layer structure, plans of pure graphene or boron nitride concentrically rolled up on each other, while gold nanotubes show a more bulk structure (Figure 1-17).

\

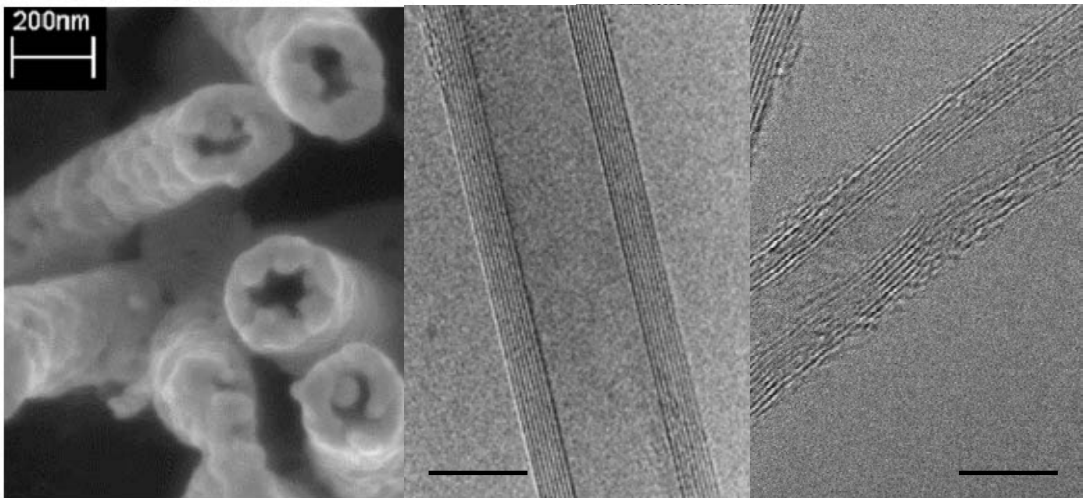

Figure 1-17 Examples of nanotube images. Left: SEM picture of Gold nanotubes; Middle: TEM image of boron nitride nanotube grown by ball milling; Right TEM image CNT grown by Chemical Vapor Deposition (CVD). The scale bars on the middle and right hand side images represent 5 nm

CNTs can be grown as single or multi-walled structures [172, 174, 175]. Nanobeads can be added onto the outer walls of the nanotubes to further enhance their specific surface area while chemical functionalisation of either the core of the CNTs or the shells [175-178] allowed an infinite range of property-tuneable nano-objects. Inorganic nanotubes have been successfully synthetised and are being used as block material for nanosensors, nanodevices or into hybrid organic materials. For example, boron nitride nanotubes were shown to exhibit very low thermal conductivity while being good electron conductors and could be used in the semiconducting industry as nanowires or transistors [179-181] or for gas storage applications [182]. Gold and copper nanotubes were synthetised by electroless plating the pores of alumina membranes with gold. These nanotubes show interesting conduction properties and opened the field to the growth of any kind of metal based nanotubes [183-185]. Tungsten IV sulphide nanotubes have shown promise in hydrogen and lithium storage, and ballistic protection because of their very high elastic moduli [186-188]. Bismuth nanotubes might find applications in semi-conducting materials [189, 190]. Molybdenum disulfide nanotubes were synthetised and could be used as catalysts in petrochemistry or as additives in lubricants [191, 192]. Titanium dioxide nanotubes could be

used as photocatalysts or in the electronic industry as semi conductors [193, 194]. It was also proposed to use them as hydrogen or oxygen sensors [195, 196] or into solar cells [197, 198]. Lastly even though silicon nanotubes [199] present a similar structure as CNTs they could offer superior properties in sensing [200] as lithium storage compounds [201, 202].

Each type of nanotube exhibits specific properties and behaviours. The scope of application is so large that many generations of researchers will keep working on their growth, characterisation and use in hybrid composite materials. We will focus on the growth techniques of CNTs in the next section.

1.4.3 Growth techniques of CNTs

In this section, the nanotube growth mechanism and the growth techniques will be presented. First the growth mechanism will be explained, since it is similar for every technique. The techniques will be compared and their differences discussed. There are more than 80 CNT providers that can be found easily on Internet with a Google search. The price of the nanotubes varies from a few USD to a few hundred of USD per gram depending on the growth technique used, the quality and the eventual post functionalisation.

CNTs are generally produced by three main techniques that are in 2010 all used for commercial production of CNTs: arc discharge, laser ablation and CVD.

In arc discharge, a vapor is created by an electric arc discharge between two carbon electrodes. Carbon vapor is produced which results in nanotubes self-assembly. In the laser ablation technique, a high-power laser beam is focused on a amorphous carbon material containing a feedstock gas such as methane or carbon monoxide. The yield with this technique is small but the CNT are of high quality, whereas arc discharge generally produces large quantities of contaminated material. The contaminants might be catalyst material or amorphous carbon. The CVD technique [203, 204] can be divided up into two main streams: Catalyst Continuous Injection (CCI) [203] or Catalyst Pre-Deposition (CPD) [205]. The type and quality of the CNT produced varies between these techniques and it is generally recognised that

CPD leads to higher quality CNT. Latest improvements in the technique allow some groups to grow SWNT and MWNTs with this method. However, the SWNTs produced with CVD have a larger diameter range than with laser ablation. On the other hand, CVD is easier to scale up, which currently favours commercial production.

Other techniques, such as water assisted CNT growth [206, 207], are being developed and lead to more efficient and less expensive ways to produce CNTs.

The average price of CNTs taken from several company websites is given in Table 1-3. Those CNTs were used in studies over the last 5 years as referred in publications [46, 47, 73, 208-213]. Over the past 10 years the average price of CNTs has decreased drastically although important price variations still exist between manufacturers. It is expected that the price will keep going down following higher demand for industrial and laboratory grade CNTs while quality improves to match the higher demand for reproducibility. World leading companies such as Arkema, Bayer and GE Plastics have setup production lines able to produce tons of CNT per year. Start-up companies have been in this market for more than 10 years and leading R&D companies are already able to provide reproducible and high quality CNTs in significant quantities. This will likely reinforce the price decrease and enable greater use of CNTs in commercialised macro-structures [214, 215].

Table 1-3 Prices of CNTs on 4 different website suppliers on the 30/06/2010. All prices in USD

	w% purity	*Diameter* nm	*Length* µm	*Arry* USD	*Nanoamor* USD	*NanoLab* USD	*Cheaptubes* USD
SWNT-1g	90	(1-2)	<20	118.8	350	2500	95
SWNT-1kg	90	(1-2)	<20	28776	99900	2500000	50000
MWNT-1g	95	(20-20)	(20-30)	58.8	17.2	25	10
MWNT-1kg	95	(20-20)	(20-30)	3477.6	3990	3500	2000
MWNT-1T	95	(20-20)	(20-30)				125000
MWNT+OH1g	95	(20-20)	(20-30)	21.36	75	140	25
MWNT+OH1kg	95	(20-20)	(20-30)	20340	7445	130000	3600
MWNT+OH1T	96	(20-20)	(20-30)				160000
Country				Germany	USA	USA	USA

1.4.4 CNTs: structure, properties and functionalisation

1.4.4.1 Structure and properties of nanotubes

CNTs are nanoscale cylinders of rolled-up graphene and can be capped at one or both ends with a half fullerene (Figure 1-17). They can be single walled (SWNT) or multi-walled (MWNT) depending on the number of concentric graphene cylinders. CNTs exhibit remarkable electrical [216] and thermal [210, 217, 218] conductivity, and are one of the strongest fibres known [176, 219]. These properties, combined with their nanoscale dimensions, have led to their intense study for a wide range of applications: from high strength composite materials [220, 221], to sensing [222] or separation [223]. However due to the limitations linked to CNT purity, growth parameters and affinity for bundling, fabricating macroscopic structures that have controlled geometries, porosity and pore shape, is still challenging.

1.4.4.2 Purification and dispersion of nanotubes

As prepared CNTs are often highly entangled and typically contaminated with impurities. These impurities include metal catalyst particles, such as Fe, Co and Ni, required for CNT growth as well as other carbonaceous by-products including amorphous carbon, fullerenes, and

graphitic nano-particles. The purification and dispersion of CNTs is therefore a critical step before further processing that can affect both the structure and properties of the final product [224-226]. The ultimate mechanical and electrical properties of CNTs self-assemblies, such as Bucky-papers (BPs) will be greatly affected by the dispersion state. A BP is a non-woven material made of entangled CNTs and will be more thoroughly presented in the following sections. This point is illustrated Figure 1-18 by which clearly shows the change in BP morphology due to differences in the initial CNT dispersion quality.

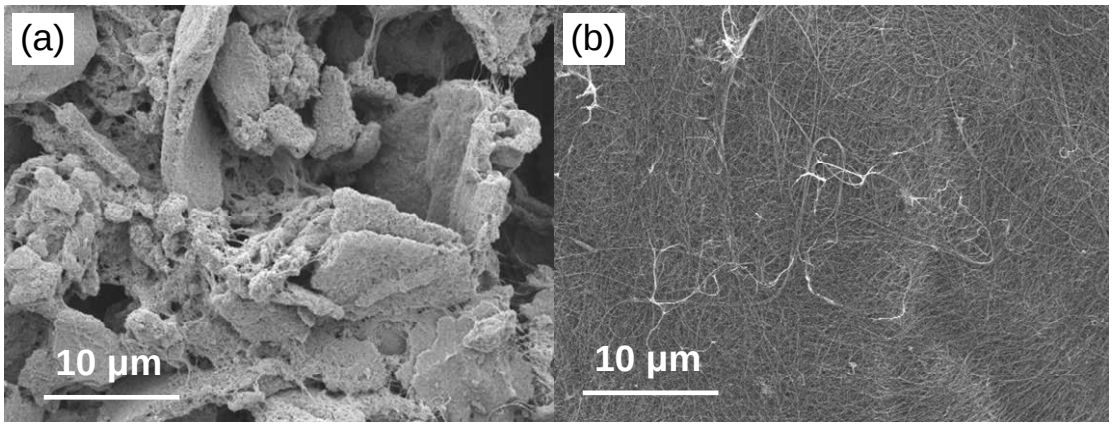

Figure 1-18 SEM image showing the surface of a BP formed from (a) poorly dispersed single walled CNTs and (b) well dispersed CNTs (2 keV, 9 mm working distance)

Purification inevitably employs some form of oxidative treatment in combination with physical processes such as filtration and centrifugation [227]. Nitric acid (HNO_3) or annealing is commonly used to remove carbonaceous impurities, which are oxidised at a faster rate than CNTs due to their less perfect graphitic structure. This treatment is often preceded and/or followed by another acid treatment, such as hydrochloric acid (HCl), to remove any metal impurities [228-230]. However these purification treatments can also damage and shorten the CNTs, as well as functionalize them with carboxyl and hydroxyl groups [231-233]. While this can be advantageous for dispersion into solvents such as water, it also alters the natural CNT properties, which may not be desirable.

CNT dispersion typically involves one or a combination of the following the following approaches [234, 235]: covalent functionalization of the CNT surface to improve their chemical compatibility with the dispersing medium [236, 237]; the use of a third component such as a surfactant [235, 238-240], polymer [241] or biomolecules (such as DNA [242]); mechanical treatments such as ultra-sonication and shear mixing.

Again, the dispersion steps need to be carefully chosen to suit the type of CNTs and the final application, so that the desired CNT properties are not adversely affected [24].

Unfortunately bundling is inherent to CNT dispersion as CNTs bundles and self-supporting assemblies are mostly held together by Van der Waals forces [75, 243-245]. CNTs dispersed in solutions tend to agglomerate and form macro sized bundles to minimize their interaction energy [235, 237, 238, 240, 246-248].

1.4.4.3 Functionalisation of the nanotubes

The surface of both inner core and shells of CNTs can be tuned by adding functional groups to enhance specific properties or reactivity [178, 213, 236, 249, 250]. Nanotubes have been functionalised with organic, inorganic or metal particles to match specific dispersability criteria, to enhance their affinity with other binding materials or to change their electrical or chemical properties [236]. The tips of CNTs have been functionalised with gate-keeper molecules at the CNT extremities to create pH responsive materials [251-253]. CNTs have also been functionalised with metal particles, such as nickel [254] to improve their affinity with hydrogen, gold [255-257] to improve their electrical conductivity or platinum to enhance their catalytic activity [258]. The CNT surface energy can be tuned, and the CNTs be rendered wettable by adding hydrophilic groups [259, 260] or super-hydrophobic by grafting specific groups on their outer shells [213, 261].

1.4.5 Assemblies of CNTs

1.4.5.1 Self-supporting structures: forests, webs, yarns, bucky-ribbons and bucky-papers

CNTs can be ordered into three distinct macro-structures. Several groups have reported the fabrication of self-supporting structures and their characterisation. One of the main advantages of creating CNT structure is to benefit from both the CNT mechanical and electrical properties and the versatility of their chemistry.

The first self supporting structures to be processed were CNT forests (Figure 1-19). CNT are aligned vertically on a substrate and can be peeled off by annealing or removal of their roots. This structure is generally the baseline for further processing leading to more complex structures. The morphology of the forest can vary depending on the growth process, the type of catalyst (geometry and surface chemistry) and the density of CNT on the substrate. Branching of CNTs leads for example to spinnable CNTs. It was also reported that webs of CNTs have been used to create sensors or highly conductive bridges for semi conductor applications. In this configuration a nearly 2 dimensional layer of CNT is used to benefit from the CNT intrinsic properties [261-263].

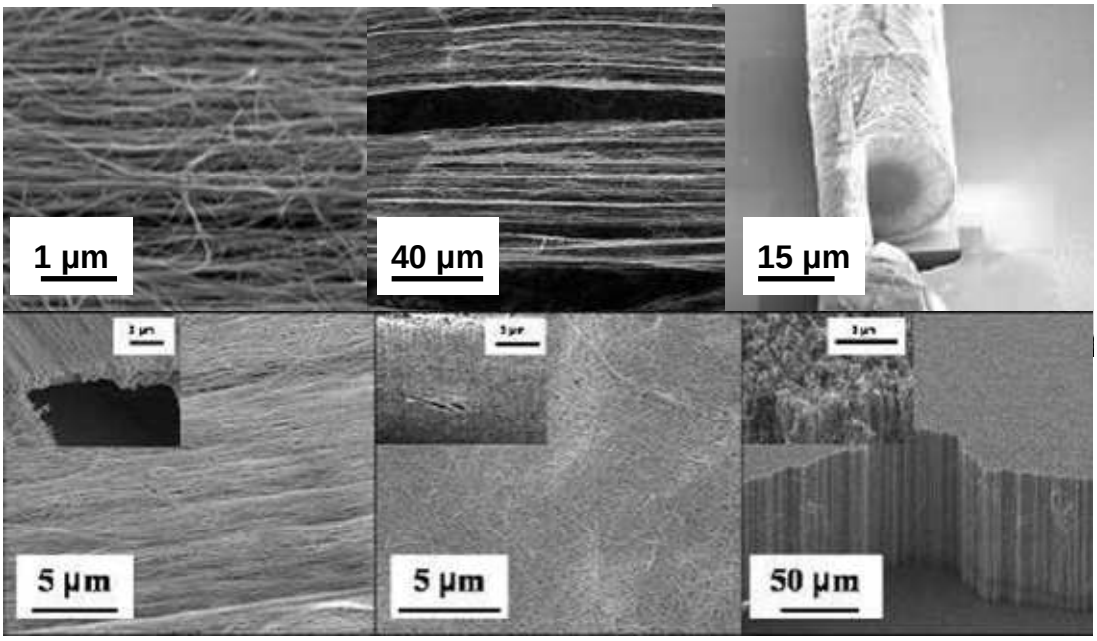

Figure 1-19 Various forms of CNT self-supporting structures; top left and middle: web; top right: yarn; bottom left: Bucky-Ribbon (BR); bottom middle: BP; bottom right forest

Groups have also reported the fabrication of pure CNT yarns from these spinnable CNT forests. In this case, the CNTs are pulled off the forest as a thin sheet, twisted and condensed to fabricate a high density CNT structure as shown in Figure 1-19. These yarns are being incorporated into knits or woven structure and might find applications in high-strength composite materials for ballistic protection or aerospace technologies (Figure 1-19) [219, 264].

Furthermore porous sheets of aligned CNTs called Bucky-ribbons (BR) have been processed. A BR is a thick dense web of CNT either made of several layers of webs condensed together or of spinnable CNTs or of the mechanical condensation of a forest by tangential compression. These structures exhibit high mechanical strength and stability while being extremely light weight. They however require either high quality CNTs or forests and good control over the fabrication steps (Figure 1-19) [208, 219].

The simplest structures that can be processed are BPs (BP). BPs are typically formed by first purifying the CNTs and then suspending them in a suitable solvent [265-268]. Dispersion of CNTs is a challenging task to achieve since it is highly dependent on the CNT length, diameter and surface

chemistry. To [269] achieve stable and resistant BP, the CNTs need to be both clear of impurities and disentangled in the suspension. Both pre-treatment of the raw CNTs and of the solution might be necessary depending of their history, to achieve suspensions of suitable quality. Once a well dispersed solution is achieved, it is filtered through a porous support such as a cellulose, poly(ether sulfone), poly(vinyl-difluorure) or poly(tetra-fluoroethylene) membrane which captures the CNTs to form an optically opaque CNT BP. The process of BP fabrication is shown in Figure 1-20.

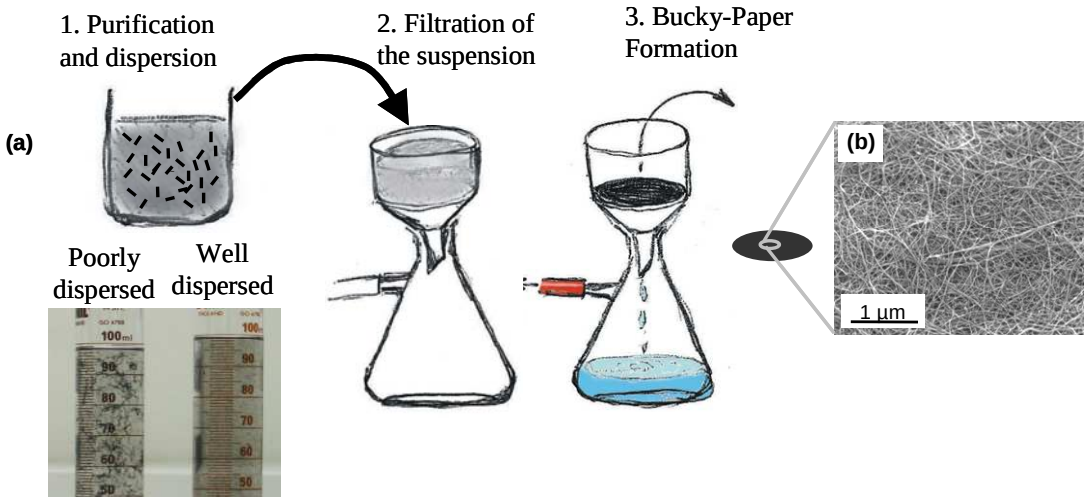

Figure 1-20 BP processing steps

CNT BPs are randomly distributed in a plane and show small off plane angles [270]. The degree of entanglement highly depends on their length and on the fabrication process but this lead to highly stable elastic structures with Young moduli exceeding 1 GPa [73, 176, 211, 247, 250]. The cake formed by filtration is then dried either with heat or vacuum before being either peeled off and used as a self-supporting structure or incorporated into a more complex composite structure (Figure 1-19) [73, 271-275]. CNTs are known to have a strong tendency to aggregate due to Van der Waals interactions, and it is these Van der Waals interactions which also hold the CNTs together into a cohesive BP [243-245]. Due to the simplicity of their preparation and to their suitability for composite material processing, BPs were one of the first macroscopic structures fabricated from CNTs and their mechanical, electrical and thermal properties have been extensively studied [75, 130, 230, 247, 272, 273, 275-285].

1.4.5.2 Incorporation into composite hybrid structures

There are numerous publications on CNT composite materials. Most of the applications look at improving either the mechanical or the electrical properties of nano-composite materials by loading polymeric or metallic matrices with nanotubes.

It was shown that even small weight ratios of nanoparticles can greatly affect the resilience, elasticity or resistance to ageing of plain composite materials [220, 221, 247, 279, 284, 286-288]. These composites find applications in high-tech sports equipment (tennis racket, water sport gears, etc…) and also in the automotive and aerospace industries. One of the advantages has been to decrease the weight and amount of material used in these applications and so have focused on increasing the strength and stiffness of the product by adding nanoparticles to achieve similar or improved performance [250, 289-291]. Networks of CNTs incorporated into polymers were also shown to improve electrical and thermal conduction which has led the way for the use of CNT/polymeric materials composite in semi-conducting and solar cell applications [292-294].

Coatings made of nanotube suspensions in polymers or inorganic matter have also been reported [295]. It was shown that ordered CNTs on surfaces could lead to the lotus leaf effect for fabrication of super hydrophobic structures [261, 296, 297]. Also, the antimicrobial properties of CNTs have already led to antimicrobial and anti-fouling coatings preventing deposition of organic matter or bacteria on sensitive surfaces [298-300].

1.4.5.3 CNT based membranes for separation application

Of the various structures that can be processed three main trends can be found in literature. The first one is related to the dispersion of CNT into an appropriate composite structure, where the load of CNT does not exceed generally 15-20 % in weight. The second kind of structures are membranes made of aligned CNTs where the pores consist of the inner cores of the CNTs. The third and last structure is called BP which is a non-woven like

structure where the CNTs are randomly entangled. We will review for these 3 structures the applications linked to membranes.

Dispersed nanotube in polymeric matrix

Dispersed CNT in polymeric matrixes have already found application in some separation technologies. It was previously shown that CNTs dispersed in poly(vinyl-alcohol) (PVA) could be used as pervaporation membranes [68, 301]. The performance of the membranes loaded with 1 to 5 %w/w of nanotubes showed improved mechanical performance compared to pure PVA membranes.

CNT Forest composite materials

CNTs are used as cylindrical pores across an otherwise impermeable thin film. This results in a membrane with well controlled nanoporosity with the only route for flow through the hollow CNT interior. These structures are promising for high permeability, high selectivity membranes and predictions of rapid flux through their hollow interior attracted the attention of material scientists in the early 2000's [302-307]. Molecular dynamic simulations have also shown that membranes made of sub nanometer CNTs, in theory, can be used for desalination via reverse osmosis [302, 308, 309].

The predicted rapid flux through CNTs is attributed to two factors [310]. First and foremost is the CNT's smooth, frictionless interior. This is predicted to result in specular, instead of diffusive, collisions between molecules and the CNT wall, leading to enhanced flow for (i) gases in the Knudsen regime and (ii) pressure driven liquid flow through a pipe (classically described by the Hagen- Poiseuille law). Secondly, for CNTs with diameters less than ~2 nm, molecular ordering and single file diffusion have been predicted to lead to the concerted movement of molecules. In particular, ballistic motion of water chains through the CNT interior was predicted [311-314] due to strong hydrogen bonding between water molecules and minimal interaction with the CNT wall.

While it is intuitively unfavourable for a polar molecule, such as water, to enter the non-polar interior of a CNT, experimental evidence seems to indicate otherwise. One of the first demonstrations of liquid flow through a

CNT was by Sun et al. who embedded an individual MWNT (inner diameter 150 nm) into an epofix epoxy resin followed by microtoming to form thin membrane slices. However it was the work of two separate groups from the University Laurence Livermore, USA, (Prof J. Holt) and the University of Kentucky, USA (Prof. B. Hinds) [251, 253, 310, 315-322] that caught the interest of the scientific community. Both groups independently fabricated membranes with a high density of aligned CNT pores and demonstrated fluid flow 2-3 orders of magnitude greater than that predicted by conventional fluid flow theory. The functionalisation of the CNT tips [251, 252] to gate fluid flow through the CNT pores or enhance their selectivity was also reported leading the way to gate-keeper CNT membranes and of the development of functional and active pores. Since these findings, a number of groups have reported on the construction and permeance of isoporous CNT membranes [323, 324]. For membrane construction, most groups used variations on the general approach outlined in Figure 1-21. Construction typically begins with a forest of aligned CNTs grown by Chemical Vapor Deposition (CVD) on either a silicon or quartz substrate. The growth parameters need to be carefully chosen so that the CNTs are free from structural blockages such as catalyst particles or bamboo type structures, which could prevent flow through the CNT interior. Once a CNT forest is grown, the spaces between CNTs are infiltrated with an impermeable material to form a continuous matrix. Finally, the excess matrix material and substrate are removed, opening up the CNT ends [223].

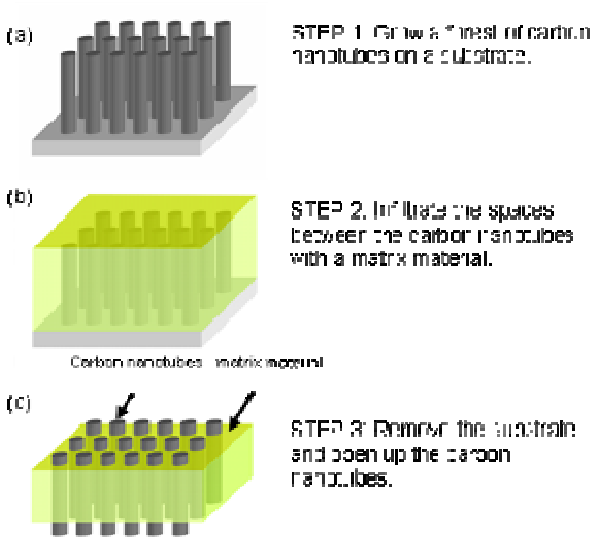

Figure 1-21 Aligned nanotube membrane [223]

CNT BP composite materials

As previously described, the term BP is used to describe a mat of randomly entangled CNTs prepared by filtration or alternative papermaking processes. Reinforcing the BP and the bonds between the CNTs was achieved in several ways including heavy ion irradiation [282] or filtration of low viscosity and low molecular weight polymer solution through the BPs [74]. BPs can be highly flexible and mechanically robust as demonstrated by the origami BP plane in Figure 1-22. Longer, narrower and more pure CNTs typically lead to stronger BPs with higher tensile strengths [73, 247, 272, 280-282].

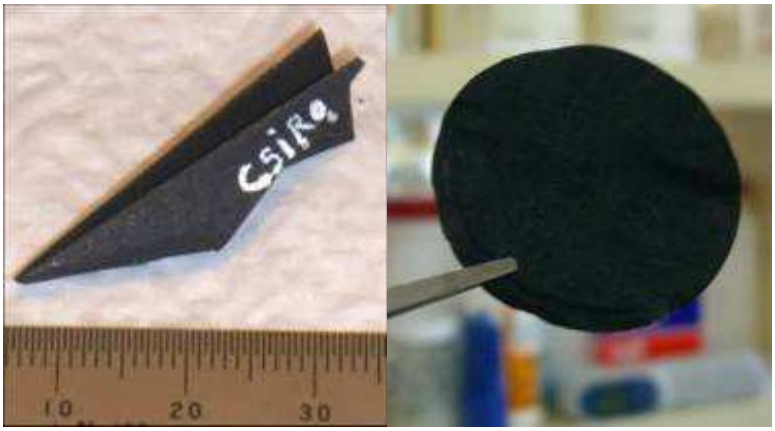

Figure 1-22 BP Left: Origami plane made from a BP demonstrating its flexibility and toughness; Right: image of a pure CNT BP

Several groups have demonstrated desalination of low salinity water using BP like structures in a capacitive de-ionization process [46, 47]. This application takes advantage of the electrical conductivity, large surface area and high porosity offered by BPs. The process comprised two electrodes arranged to form a parallel plate capacitor across which a voltage was applied to absorb salt ions of opposite polarity from a stream of salty water. The water between the electrodes was removed as fresh water, while the concentrate was produced when the applied potential was reversed. An electrosorption capacity of ~57 μmol/g was demonstrated, which was similar to a carbon aerogel electrode despite its lower surface area and is attributed to the more optimal pore size distribution of the BP [46].

Pure CNT BPs have also been used as fine filters. It was reported that a 2 μm thick CNT BP film supported on a cellulose acetate disc was capable of filtering fine particles of 100-500 nm diameter to a level that exceeded the standards set out for HEPA filters [295]. They also suggested that these BPs could be used to filter powdered organic dyes and condensed lead fumes in solution phase. Antimicrobial properties (in the absence of UV/visible irradiation) and the efficient removal of bacterial from contaminated waters have also been demonstrated. SWNT BP were effectively used to completely retaining E. coli cells (2 μm size) via size exclusion and also promoted their inactivation [298]. This inactivation was attributed to cell membrane damage on direct contact with SWNT aggregates. They also demonstrated exceptionally high removal of the model virus MS2 bacteriophage (27 nm diameter) due to depth filtration.

1.5 Conclusions and prospects

Several points showing routes of possible improvements clearly come out of this review.

First of all, membrane based technologies have shown very promising results in separation technologies to improve the actual performance or to reduce the energy consumption of the systems. Amongst the techniques that have attracted attention over the past 20 years, membrane distillation stands as an interesting alternative and complementary method to current state of the art desalination techniques. Since the separation and transport properties are directly related to the membrane properties used as an air-gap between the feed and permeate to create the water vapor gradient specific membranes offering engineered properties need to be designed. Energy costs are still an issue and even though work is being done to couple MD to solar panels, lost heat from industry or to work with recovered heat. Work on advanced membrane development is still required to enhance the process performance.

CNT structures have shown interesting and promising results in separation. The reported large flux through their interior reported has stimulated groups all around the world to benefit from their properties. Furthermore, due to the nature of graphene and to the semi uni-dimensional structure of CNTs, the numbers of functionalisations that can be undertaken to process novel material seem infinite. Practical applications for CNT BPs are still being sought. More than 10,000 papers have been published on CNTs just in the last decade, demonstrating that the faith in the future of CNT is very strong. The use of CNTs in separation has been demonstrated and several successful attempts have shown that CNT properties could be efficiently used for separation applications. The CNTs versatility, as well as past modelling studies, offered promising perspectives in various separation applications but demonstration in a practical way their potential and efficiency is still desperately needed. CNTs can be functionalised with a number of molecules (both organic and inorganic) to modify their surface properties or to increase their affinity with solvent or filling materials. Functional materials can thus be

fabricated by coating with specific chemical groups, or adsorbing an appropriate reactive particle on their surface. However, to develop useful materials, work is still required to better understand the properties of the macro-structures fabricated from modified CNTs and to control their processing conditions.

The membranes fabricated out of CNTs were typically difficult to process and offered small exposed surface area. In the case of the embedded forests of CNTs, it would be required to grow forests on very large wafers, which is limited by the reactor dimensions, or to master the condensation and alignment of CNTs in solution to process large and reproducible surfaces of CNTs ready to be embedded. For this reason, BPs, due to both the simplicity of their fabrication and to their processing reproducibility, appear as promising candidates. BP plain composites are already processed and applied in a range of applications: plain composites for aerospace and ballistics, the production of energy through fuel cells or solar cells, anti-microbial activities or separation of salts from aqueous solutions. Very few groups have used porous BP composites for separation applications and there is a clear need to increase the knowledge of their properties and separation performance in a range of applications.

This PhD thesis was aimed at fabricating advanced CNT BP / polymer for water purification and CNT BP / metal membranes, also for gas adsorption.

Chapter 2

2 Experimental details

This chapter will describe the main experimental techniques used over the period of this PhD. Rationale behind the use and benefits of the techniques, details of the experimental conditions and advantages for the characterisation of CNTs or BPs will be discussed. As this work required covering a wide range of material properties the characterisation techniques are presented in five sections and the corresponding sub-sections are listed below.

(i) Growth of the CNTs

The technology and growth conditions will be detailed.

(ii) Characterisation of the CNTs

Their structure, chemistry and stability needed to be monitored and assessed, and several techniques were required to fully understand their properties.

(iii) Characterisation of dispersed CNTs

As the critical step in bucky-paper formation was dispersion of CNTs into stable colloid suspensions, several techniques were performed on CNTs suspended in solution to determine their degree of dispersion as well as the stability of the suspensions.

(iv) Bucky-paper characterisation and composite materials processing

Several characterisation techniques were used to measure BP properties. A series of tests, having various purposes, were performed on the CNTs. The tests are separated into three sub-sections: (i) structural and surface properties, (ii) thermal properties and (iii) membrane related properties. The point of this separation is to emphasize and regroup techniques that have common purposes or that allowed us to focus on the same range of properties. The various techniques to process composite materials will also be presented.

(v) Membrane distillation rig and test conditions

Both the design of the rig and of the module are described and discussed. Furthermore, the operating conditions in which the BPs were tested are also presented.

A table indicating in which chapter of this work the techniques were used will be presented at the start of each sub-section.

2.1 Carbon nanotube growth

The carbon nanotubes (CNTs) used in this work were grown at CSIRO Materials Science and Engineering, in Dr. Stephen Hawkins' group. Researchers Jacinta Poole, Chi Huynh and Marta Redrado Notivoli grew the nanotubes and helped find the operating parameters to produce CNTs with appropriate properties. We acknowledge their work and thank them for providing us with high grade CNTs.

All the CNTs were multi-walled and CNT will be used as an abbreviation for Multi-walled Carbon Nanotubes. This sub-section will describe briefly the Chemical Vapor Deposition (CVD) and Catalyst Continuous Injection (CCI) growth techniques as well as presenting the major parameters involved in the CNT growth. As some of this work is still confidential and conducted by others, only general growth working conditions and growth parameters are described here.

2.1.1 Growth technique

Chemical Vapor Deposition (CVD) of CNTs was first reported in 1993, 2 years following their discovery. CVD is a common method for the commercial production of carbon nanotubes and brings the advantage over other methods by offering both high yields and good quality (high purity) CNTs.

To grow CNT by CVD, a mixture of two gases, a carbon source gas and a carrier gas are heated to the carbon source gas decomposition temperature while being injected into the reactor. The high temperature initiates the carbon-source gas decomposition while the carrier gas helps keep a constant flow all across the reactor, thus guaranteeing homogeneous deposition of carbon. Carbon nanotubes then grow at the sites of metal catalyst following a two step process: (i) the carbon-source gas is decomposed at the surface of the catalyst particle, and (ii) the carbon is

transported to the edges of the particle, where it agglomerates to form the walls of the nanotube.

2.1.2 Processing conditions

Silicon wafer substrates were prepared and coated with metal catalyst particles. The substrates were silicon wafers and 5 nm thick iron nano-particles, deposited by thermal evaporation from a resistively-heated alumina-lined tungsten boat, were used as growth catalysts. The silicon wafers were placed into a quartz tube and positioned in a furnace. Prior to growth, an acetone-free acetylene supply was vented for at least 20 min into the reactor in order to stabilise the flow and flush any gas contaminating the wafers. Then an acetylene/helium mixture at a 5/95 v/v ratio was flushed into the quartz tube at flow rates between 600 and 800 sccm, and the heating was turned on to maintain temperatures typically between 670 ºC and 710 ºC. The heating time varied between 10 and 30 min depending upon the length desired. Upon growth completion, helium was vented through the reactor for 5 min in order to eliminate possible reactants and waste residual acetylene. These conditions were detailed in a previous paper by Huynh and Hawkins [175]. A schematic diagram of the process is given in Figure **2-1**.

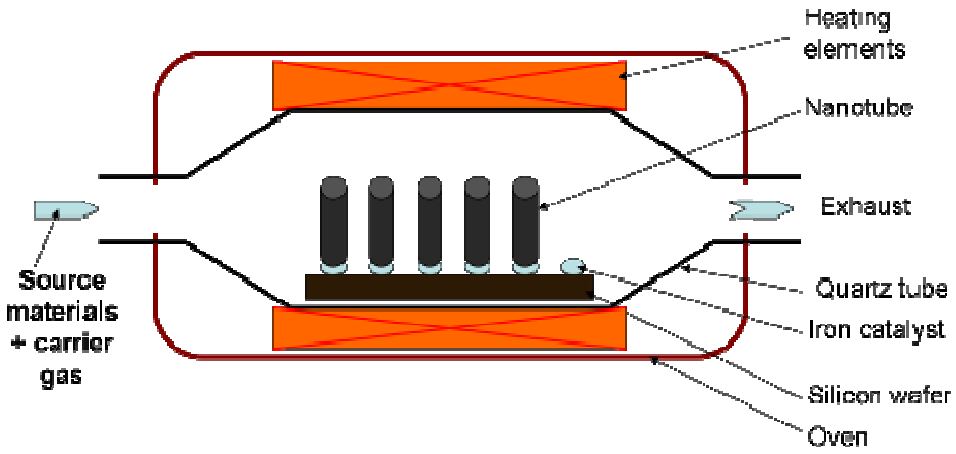

Figure 2-1 Carbon nanotube growth schematic in a Chemical Vapor Deposition (CVD) process

A second method of producing nanotubes, Catalyst Continuous Injection (CCI), was used at the start of this project. These CNTs will be referred as CCI CNTs in the following chapters. The main advantage of CCI over CVD growth is the higher production yield. However, CNTs grown by CCI generally also contain more impurities from inclusion of catalyst particles, and may also contain amorphous carbon on their outer walls. In CCI the catalyst is continuously injected during heating. This leads to a highly entangled network of nanotubes as opposed to the aligned and separated nanotubes forests produced by CVD [203]. Their length was also always between 300 and 400 μm. Their dispersion required very strong mechanical shearing, which tended to break the CNTs and shorten them. For these reasons the CCI CNTs were not heavily used.

Typically, CVD and CCI CNTs presented 10 and 40 walls respectively, and exhibited outer diameters of about 15 and 50 nm. Examples of Transmission Electron Micrographs (TEM) showing the morphology and basic properties of the two kinds of CNTs are given in Figure 2-2.

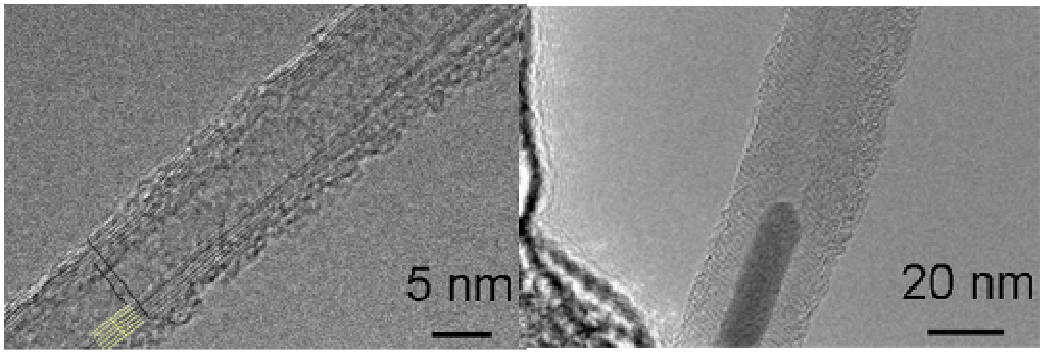

Figure 2-2 TEM pictures of the two kinds of CNTs used in the study. The average length of the CNTs was 300 μm while the outer diameter of the CVD (left) and CCI (right) CNTs were 15 and 50 nm respectively

2.2 Nanotube characterisation

The characterisation of the CNTs was undertaken with several techniques and apparatus which are listed in Table **2-1**. A comprehensive description of the rationale behind the use of each technique is given in the following section. Several properties such as the thermal stability as well as surface crystallinity or functionalisation were critical before further treatments, dispersion or use in composite structures. Furthermore, each characterisation technique is referenced in Table **2-1** to the corresponding experimental chapter where the results are reported.

Table 2-1 Techniques and CNT properties related

Technique	*Property*	*Chapter*
Transmission Electron Microscopy (TEM)	Imaging surface and crystallinity	3; 5
Thermal Gravimetric Analysis (TGA)	Thermal degradation and purity	4; 5
Fourier Transform Infra-Red (FTIR) & Energy Dispersive X-Ray Spectroscopy (EDS)	Functionalisation, presence of elements on the surface	5
X-Ray Photo-electron spectroscopy in Air (PESA)	Stability of the surface energy	5
Raman spectroscopy	Presence of defects and isotropy of the CNT assembly	4; 5

2.2.1 Transmission Electron Microscopy

Transmission Electron Microscopy (TEM) is a microscopy technique whereby an electron beam generated by an emission source is transmitted through a sample. To obtain good contrast, the thickness of the sample has to be smaller than one hundred nanometers. As the beam goes through the sample, it interacts with the specimen and an image is formed and focused onto a screen such as a fluorescent screen or a CCD camera.

In the case of CNTs, TEM is appropriate since it shows the number and integrity of the walls emphasizing, for example, clear differences between amorphous (sp3) and crystalline (sp2) carbon. All the work in this study was undertaken on a FEI Tecnai F30 Transmission electron microscope (at Bio 21, Victoria - Australia). In this case, the images were typically taken under vacuum and at 100 keV. The emission source was a tungsten filament. To prepare the TEM samples, nanotubes were either drawn from a CNT web and condensed with acetone, or dispersed in propan-2-ol and filtered on a glassy carbon - copper grid. Some nanotubes were entrapped on the grid.

Examples of low magnification images of the glassy carbon layer where CNTs were deposited are given in Figure 2-3.

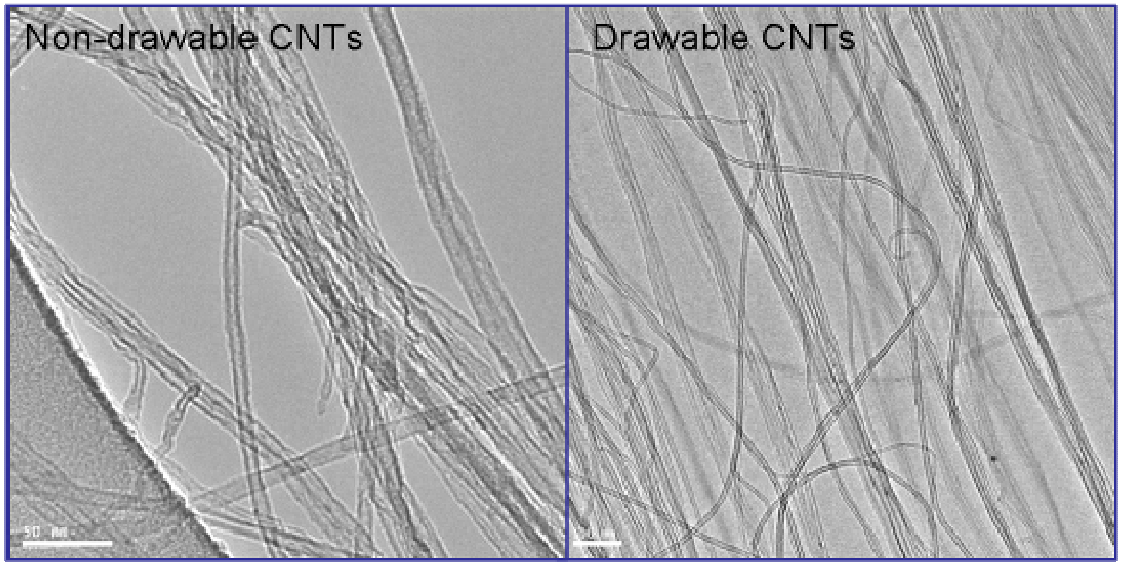

Figure 2-3 TEM images taken at 100 keV of CNTs. Left: non-drawable CNTs with glassy carbon on the bottom left. Right: drawable CNT aligned in web

2.2.2 Thermal Gravimetric Analysis

Thermal Gravimetric Analysis (TGA) was used to determine the thermal stability of a sample over a gradient of temperature. The weight was recorded as a function of temperature and properties such as solvent content, thermal stability, glass transition, melting point or degradation can be derived. TGA is commonly used on organic matter as their chemical stability is generally highly dependant on their thermal behaviour. This method is also

used to reveal the composition of hybrid organic/inorganic compounds, as the inorganic materials are not degraded at temperatures less than 1000ºC, where most carbon based structures (expect diamond) are carbonised.

In the case of CNTs, TGA is used to assess the purity of the nanotubes. As described previously, iron catalyst nano-particles are used to start the growth of the CNTs and their presence can be quantitatively measured by TGA by monitoring the residual weight after carbonization. As the temperature increases, the mass of the sample decreases over time. This is linked to three phenomena: (i) desorption of adsorbed gas on the CNT surface, (ii) sp3 carbon carbonization and evaporation and (iii) sp2 carbon carbonization [325, 326]. As functionalised CNTs commonly present a higher level of sp3 carbon, their degradation temperature was recorded to be lower than that of pure CNTs. The presence of functional groups, such as hydroxyl or carboxylic groups will induce amorphous carbons (sp3) into the pure graphene structure and replace some of the Pi-bonds [327]. Furthermore, these groups are also oxidised faster than pure graphene, thus greatly affecting the behaviour of the CNTs under thermal stress.

A Perkin Elmer Exstar S11 TGA/DTA 6300 was used. The heating rate was kept constant at 10ºC/min while the temperature was varied between 25ºC and 1000ºC. CNTs have been shown to thermally degrade from 480-600ºC. Comparing TGA curves following different treatments was a useful tool to determine whether the CNTs were degraded or modified and this technique was used to assess chemical modifications and purity of the CNTs.

2.2.3 Fourier Transform Infra-Red & Energy Dispersive X-Ray Spectroscopy

Fourier transform infrared spectroscopy (FTIR) is a technique used to obtain the infrared spectrum in absorption, emission, photo conductivity or Raman scattering of either a solid, liquid or gas sample. FTIR spectrometers typically collect spectral data in a wide spectral range, from 400 cm^{-1} to 7,000 cm^{-1}. CNTs are difficult to characterize with FTIR in both transmission and adsorption, as they do absorb a large amount of the laser light across all frequencies and since a high quantity of adsorbed water can

be found due to their naturally high specific surface area. The obtained raw data need to be carefully treated to obtain the characteristic peaks [328-331]. The sample preparation needs to be precise and the CNTs were, in this study, dispersed by milling and embedded in Potassium Bromide (KBr) pallets. It was important to properly backwash and dry the CNTs, as reagents adsorbed on their surface could lead to misinterpretation of the graphs by adding virtual peaks to their response. Therefore the CNTs were backwashed with deionised water and acetone before being dried at 60 ºC in a vacuum oven. The signal of CNTs treated under different conditions were measured and compared, which gave qualitative and valuable information on the nature of the bonds being formed at their surface. A Nicolet Nexus from Thermo Electron Corporation was typically used. The resolution was 1 cm^{-1} and 9 scans were performed and averaged for each sample. The detector was a DTGS KBr with a working range between 400 and 4,000 cm^{-1}.

This technique was also used in coordination with Energy-Dispersive X-ray Spectroscopy (EDS) to detect the presence of inorganic materials on the CNTs. EDS is an analytical technique used for the elemental analysis or chemical characterization of a sample and is based on X-ray fluorescence spectroscopy which relies on the interactions between electromagnetic radiation and matter. The analysis of the X-ray emission spectra by the matter will change according to the elements present in the sample. EDS analysers that were part of Scanning Electron Microscopes (SEM) or TEMs were used while imaging. EDS gives an elemental composition of the surface composition and revealed to be a useful technique to quantify adsorption of inorganic materials onto the CNTs and to check their purity after specific treatments or use in the Membrane Distillation rig.

2.2.4 X-Ray Photo-electron spectroscopy in Air

Photo-Electron Spectroscopy in Air (PESA) was used determine the Work Function (WF) of the CNTs to attest to their stability following treatments performed on their surface. In solid state physics, the WF is the minimum energy needed to remove an electron from a solid surface to a point

an infinite distance away from the solid surface. All surfaces/materials have a WF, and changes in the chemistry of the surface affect its value. In the case of CNTs we used PESA to determine the change of WF after UV/ozone exposure and the stability of the treatment over time. This was a powerful technique to determine both the quantitative amount of functional groups present on the CNT external walls and to assess their stability before undertaking further treatments. This was crucial in measuring the efficiency of some functionalisation experiments.

The work function was determined using a Riken Keiki AC-2 Photo Electron Spectroscopy in Air (PESA) Spectrometer. A power setting of 10nW was used for all samples.

2.2.5 Raman spectroscopy

Raman spectroscopy relies on inelastic scattering through a sample from a monochromatic light source. Photons interact and excite the molecules of the sample resulting in a shift in the matter energy. When matter relaxes, photons are emitted as molecules return to a lower rotational or vibrational state. The energy shift gives information about the phonon modes in the system. In practice, a sample is illuminated with a laser beam at a given wavelength and the resulting photons are focused with a lens and filtered through a monochromator.

Several parameters can be deduced from the Raman spectra of CNTs (see Figure 4). First, the Radial Breathing Mode (RMB) can be used in the case of single walled CNT (SWCNT) to study the diameter and to probe the chirality of the CNT. Secondly, the G-band in the case of graphene appears when two carbon atoms close to each other show differences in crystallinity. This can be used to determine if there are changes in the carbon atom distribution and crystalline structure of CNTs. The G-band frequency can be used to distinguish between semi-metallic and metallic SWCNTs and to also show charge transfers in the case of doped CNTs. Both RBM and G-band are first order peaks. In the second order peaks, D and G', information regarding the electronic and vibrational properties of the CNTs can be found. These

parameters provide information on the structure of the side walls in MWCNTs. In practice defects and functional groups can be deduced by comparing baselines from non-treated and treated CNTs. A semi-quantitative analysis can be done to show the impact of a series of treatments on CNT characteristics (Figure 2-4).

In this study, Raman spectroscopy was carried out on a Renishaw Raman spectroscope with a 514 nm laser. The tests were performed with a power of 10% of the nominal laser intensity (50 W) to avoid damaging the CNTs surface.

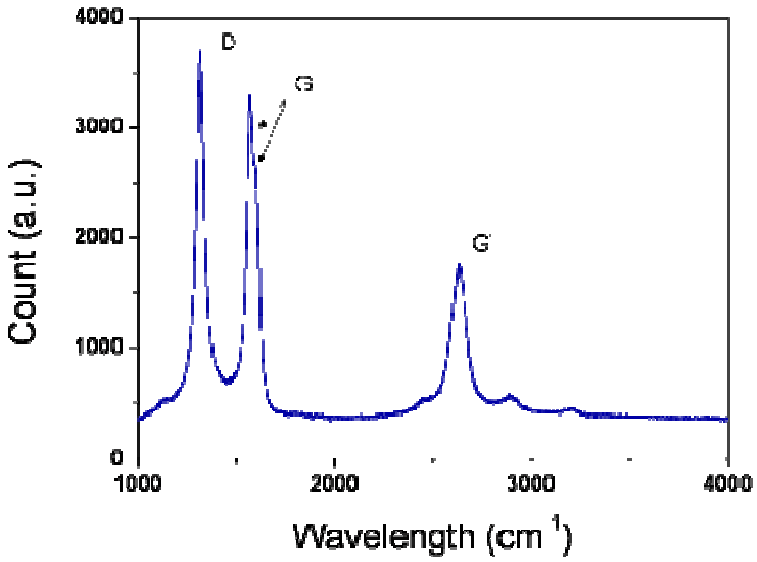

Figure 2-4 Raman spectra of as grown CNTs. The D, G1 & G2 double peaks as well as G' peak are clearly visible. The RBM is not visible on this graph and is not relevant for MWCNTs

2.3 CNT dispersion characterisation

To process homogeneous and reproducible BP, CNT need to be individually dispersed and suspended in solution. Due to Van der Waals interactions between the CNTs and the strong affinity of the CNT for each other, bundling is inherent for CNT dispersions and stabilizing suspensions revealed to be challenging.

One of the main issues with CNT detection is their very high aspect ratio. As the ratio of their length over their diameter is very high, few experimental setups can qualitatively detect them. The aspect ratio is defined as:

$$\nu = \frac{Length(m)}{Diameter(m)} \qquad (2\text{-}1)$$

For example, a CNT exhibiting a length and a diameter of respectively 200 µm and 20 nm will have an aspect ratio of 10^3. In the case of the CNTs used in this work, the aspect ratio was estimated to be comprised between 10^3 and 10^4.

Various methods can be found in the literature, as developed previously in Chapter 1, to suspend and disperse CNTs. This includes for example, surface functionalisation, long and powerful sonication, or the use of surfactants. However, all these techniques presented drawbacks for the final utilisation of the CNTs. The addition of hydrophilic groups on the CNTs would decrease the hydrophobicity, enhancing the risks of wetting of the membrane. Also, harsh sonication conditions would have shortened and damaged the CNTs, thus likely decreasing their mechanical properties and increasing the reactivity of the CNTs. Surfactants might have been difficult to remove from the CNT surface and would, in this case, have affected the contact angle and surface wetting of the membrane.

Furthermore, as the natural hydrophobicity and the quality of our nanotubes were some of the major incentives to use these CNTs, pre-functionalisation of the surface was not considered at the start of the project. For all these reasons, the work was primarily focused on developing a low impact dispersion method that would offer the advantage of being non-damaging and non-impacting on the final membrane properties. This protocol will be described in detail in Chapter 3, dedicated to dispersion.

2.3.1 UV/visible spectroscopy

Both UV/visible spectroscopy and electrophoretic light scattering were used to quantify the macro-bundle formations and to observe the kinetics of bundle formation after dispersion of the CNTs [332, 333].

UV/visible spectroscopy relies on the absorption of ultra-violet / visible light by matter. It was used to determine the bundle size distribution across a small volume of liquid. Since CNTs are black and the solvent (propan-2-ol classically) is transparent at wave numbers above 200 cm^{-1}, UV/visible spectroscopy could be used to determine both the bundle size distribution (peak position) and their concentration. However, Brownian motion of the CNTs in the solution revealed to greatly affect the spectra and made reliable concentration measurement difficult. A Cary 300 Bio UV/visible/NIR spectrophotometer was used for these measurements. This technique could, however, also be used to show the bundling kinetics of the CNTs.

The linearity of the Beer-Lambert law is, however, considered to be limited by a number of factors. Non-linearity of Beer-Lambert law can appear for several reasons, including deviations in absorptivity coefficients at high concentrations (>0.01M) due to electrostatic interactions between molecules in close proximity or scattering of the light beam due to particles in the sample solution. Furthermore, Brownian motion of the CNTs in solution might also alter the spectra and possibly offset and shift peaks. Therefore, the bundles could clearly have an impact on the spectra depending on how well the CNTs are dispersed. This technique was pursued to get a qualitative distribution of CNT bundles.

2.3.2 Nano-sizer

Electrophoretic light scattering was performed on CNT suspensions after various cycles of dispersion to evaluate the bundle kinetics and to estimate the bundle size distribution. Once again, Brownian motion in solution revealed to be an issue and even though trends of the bundling kinetics were found, no direct correlation between the signal and the bundle size were easily obtained. A Zeta Sizer Nano ZS was used to perform the tests.

Dynamic Light Scattering (DLS) measures Brownian motion and relates this to the size of the particles. Particles in solution are illuminated with a laser and fluctuations of the intensity are analysed in the scattered light. Thus, if a small particle is illuminated by a light source such as a laser, it will scatter the light in all directions. In the case of multiple particles, the scattering pattern will consist of areas of bright light and dark areas where no light is detected. Furthermore, particles suspended in a liquid are never stationary and are constantly moving due to Brownian motion, which is the relative movement of particles due to random collisions with molecules of the liquid that surrounds the body. An important feature of Brownian motion for DLS is that the speed of the particles is inversely proportional to their size, as defined by the Stokes-Einstein equation:

$$D = \frac{k_B T}{6\pi \times \eta \times r} \qquad (2\text{-}2)$$

Where k_B is the Boltzmann constant, T the absolute temperature of the bulk liquid surrounding the particle, η the viscosity of the liquid (considered to be low in the case of Stokes –Einstein) and r the average particle radius.

The particle size distribution is calculated from the correlation function of scattering signals taken at different times. Differences across a sample over time (as for example particles entering or leaving the measurement zone) will unfortunately lead to a progressive decrease of the correlation function proportionality to the particle movement or agglomeration. As

Brownian motion is related to size average particle radius, larger particles will move slower than smaller particles. Thus, the fluctuation in intensity of the scattering pattern will change more slowly in the case of large particles . Similarly if small particles are being measured, the intensity of the pattern will fluctuate faster. The Zeta sizer will then use an adequate algorithm to extrapolate the size distribution from the correlation function extinction. In the case of high aspect ratio nano-particles, such as CNTs, the Zeta Sizer will not be able to detect individual CNTs but only spherical agglomerates of the nanoparticles. This is due to the fact that the hydration diameter of the CNT is large compared to their true diameter and to the large variations between the CNTs length and diameter leading to different scattering patterns [334, 335].

This method of analysis assumes spherical particles were being measured. In the case of CNTs, because of the very high specific ratio and of the unpredictable “cloudy” shape of the bundles, the results had to be carefully used and analysed. For these reasons DLS could not be used directly for bundle size distribution determination, but could be a useful tool to characterize the bundling kinetics over time after various treatments. A ZS90 Nanosizer from Malvern was used for these tests with similar solutions to those described for the UV/visible studies. Further details on the solution preparation and rationale behind their preparation will be given in Chapter 3.

2.3.3 Optical imaging

As the two previous methods did not bring any quantitative results to the kinetics of agglomeration, it was preferred to analyse the agglomeration process by visual observations and optical microscopy. Optical images of suspensions were taken with cameras to show the change in bundling with time, solvent and temperature. The images were qualitatively compared to assess the dispersion criteria. As shown in Chapter 3, the difference between the various solutions was clearly obvious and macro bundles could be seen by eye or optical microscopy. Optical images and videos were recorded during and after sonication and compared to show the impact of the treatment. The concentrations were always similar and pure solvent and clean

glassware was used to avoid any contamination. The glassware was cleaned with soapy water and thoroughly rinsed with deionised water. A camera Exilim (10.1 mega pixels from Casio) was used in macro mode to take the pictures shown in chapter 3. The analysis or alterations were done on the free software GIMP2.

2.4 Bucky-paper characterisation

A Bucky-Paper (BP) is defined in this work as an entangled mesh of individual CNTs. In the following chapters we will distinguish between self-supporting BP, made only of nanotubes and composite BP, made of CNT and a given reinforcement material. The nature of the reinforcements will be described and further discussed in the next chapters.

A description of the characterisation techniques used to quantify and measure the BP properties will be given in this section. In the scope of this work, several domains have been investigated. First, material characterisation was carried out. The mechanical and surface properties of the BP were tested to obtain a general understanding of the material properties. As heat exchange is critical in membrane distillation, the thermal properties of BPs were also studied. Eventually, membrane related properties were investigated which included porosity, surface pore size and thickness of the BPs.

These three sub-sections and the affiliated characterisation techniques are given in Table 2-2 and Table 2-3. For each technique the reader can find the corresponding experimental chapter in which it was mostly used.

Table 2-2 Materials properties

Technique	*Property*	*Chapter*
BET	Specific surface area	4; 5
Instron testing	Mechanical properties (tensile tests)	4; 5
Goniometer	Contact angle	4; 5
Small Angle X-Ray Scattering	Thermal expansion, CNT distribution	4; 5
Differential Scanning	Specific heat	4

Calorimetry		
Laser Flash technique	Thermal diffusivity	4
Thermal conductivity meter	Thermal conductivity	4
Environmental Scanning Electron Microscopy fitted with hot stage	Thermal expansion	4
Modulated temperature – thermo mechanometry	Thermal expansion	4

Table 2-3 Membrane properties

Technique	*Property*	*Chapter*
Scanning Electron Microscopy with ion beam column	Surface pore size, degree of entanglement of the CNTs in BP	3; 4; 5
Porometer & Amicon cell	Pore size distribution & Limit entry pressure	4; 5
Pycnometer	Porosity	4; 5
Altisurf & micrometer	Thickness	4; 5

2.4.1 Structural and surface properties

2.4.1.1 BET

The specific surface area of a material is a critical property in separation as it provides an indication of the available surface area for adsorption. Specific surface area can be estimated by adsorption of Nitrogen (N_2) after completely degassing a sample. Adsorption is the process whereby atoms or molecules from an adjacent gas or liquid get attracted to an exposed solid surface. Such attraction forces, adhesion or cohesion, lead to self-assembly of molecules on the surface in mono or multi layers. The amount of gas that will adsorb is directly proportional to the surface area available and is reported in terms relative to the mass of the sample to be expressed as a specific surface area. Several models (BET, Langmuir, Freundlich, Kisluik, and Henderson-Kisluik) have been developed depending on the regime of adsorption that the material is undertaking.

In the case of CNTs, the specific surface area depends on their inner and outer diameters. If the CNT tips are open, gas can adsorb on both inner

core and outer shells. In our case, as the CNT tips were not etched, we considered that the obtained BET specific surface area was directly correlated to the outer shell surface area of the CNTs and that no gas adsorbed inside the CNTs. Any modification to the wall structure might have some implications on the gas adsorption properties and on the exposed surface area.

In this work, an average BET (from Brunauer-Emmer-Teller) surface area was determined by N_2 adsorption on a Micromeretics Tristar 3000. The samples were first degassed in a preparation cell at temperatures between 100 and 300 ºC for 10 to 70 hours and then analysed at 77 K. Typical adsorption graph are given in Figure 2-5.

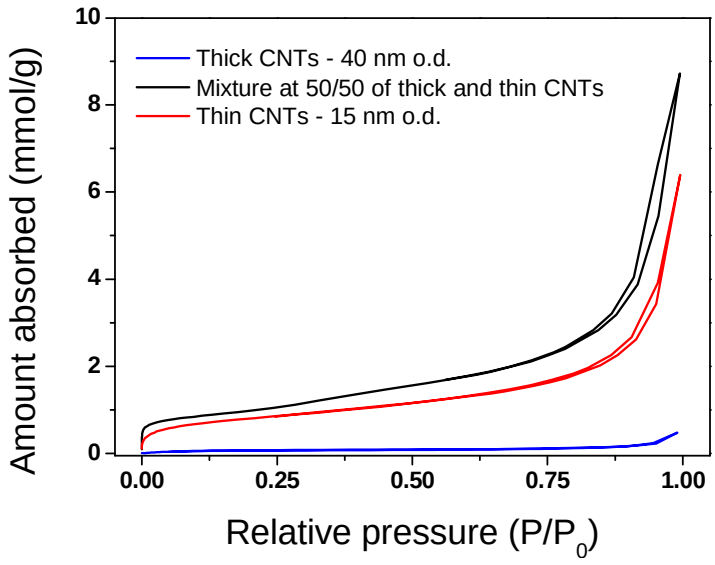

Figure 2-5 BET isotherms on three different batches of nanotubes. Thick (40 nm o.d.) CNT and thin (15-20 nm o.d.) CNTs were used and mixed together

2.4.1.2 Instron testing

The mechanical properties of the BP were investigated by measuring their tensile modulus. Tensile mechanical tests of the self-standing BPs were performed on an Instron with a 10 N load cell and a 2.5 mm/min rate of extension. The sample strips were 10 mm in length and 2 - 2.5 mm in width.

2.4.2 Goniometer

As the surface energy of the membrane is crucial and needs, in case of DCMD of water, to be as low as possible. Measuring the contact angle of the membrane with water was found to be an easy and quick way to check the impact of treatment on the membrane wetting properties. Contact angles were measured with a Pocket Goniometer PG7 from Fibro system. The average deionised water droplet size was typically 4 µL. A drop of water was deposited onto the flat sheet membranes and images were recorded every 30 s by the goniometer webcam. The software extrapolated the contact angle from the curvature of the drop reported to the baseline position. Images of static and dynamic wetting were recorded. Tests with propan-2-ol, acetone, and aqueous solutions were also performed.

An example of contact angle measurement on a BP membrane is given in Figure 2-6.

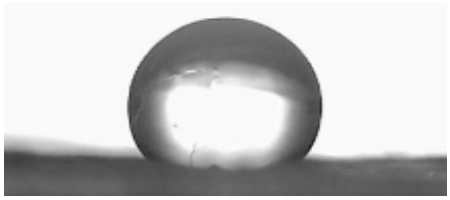

Figure 2-6 Contact angle with a 4 µL droplet of deionised water over a BP.; the Contact angle is ~ 125º

2.4.3 Small Angle X-Ray Scattering

Small Angle X-Ray Scattering (SAXS) is used for the determination of the microscale or nanoscale structure of particles. It is a powerful technique to reveal the average particle sizes, shapes, distribution, and surface-to-volume ratio. The samples can be solid or liquid, dense or porous and may contain solids, liquids or gaseous phases of similar or mixed material. The structure of ordered systems like lamellae, and fractal-like materials can be studied. SAXS is accurate, non-destructive and usually requires only minimal sample preparation. In practice, a monochromatic beam of X-rays is sent towards the surface of a sample from which part of it is scattered, while most x-rays go through the material without interacting with it. An X-Ray scattering pattern

can be monitored on a detector typically situated behind the sample and perpendicular to the direction of the primary beam that initially hits the sample. These scattering patterns contain data on the structure of the sample.

In our set of experiments, the X-Ray source was the Australian Synchrotron. As electrons preferentially travel in straight lines in materials, a change in their pathways will induce an X-Ray emission that can be focused for the purpose of various experimental works on the different platforms at the Australian Synchrotron. Here the X-Ray source was generated by changes in the electron's trajectory caused by a series of magnetrons.

Two different series of tests were carried out on the SAXS. First, CNTs organised in various macrostructures were examined under various X-Ray exposures. Bucky-papers, webs, bucky-ribbons, aligned forests and yarns were tested and their diffraction patterns compared to assess the impact of the CNT distribution on the diffraction patterns. Furthermore, thermal expansion tests were carried out on the SAXS. A Linkam stage was fitted into the SAXS chamber to do thermal expansion tests and scattering patterns were collected at various temperatures steps. The heating rate was 50 ºC/min and the samples were kept for 5 min at each temperature step (25, 50, 100, 150, 200, 300 and 400 ºC) for stabilisation.

The camera length, or distance between the focal point and the sample was 1.4 m while the reciprocal Q range was comprised between 12.5 and 560 Å.

2.4.4 Thermal properties of the BPs

As thermal exchanges are crucial in Direct Contact Membrane Distillation the thermal behaviour of the BPs had to be studied and understood to better analyse the water vapor permeation results. Several experiments including thermal conductivity, diffusivity and expansion were carried out to determine the thermal properties of the CNT BPs.

2.4.4.1 Differential Scanning Calorimetry

The specific heat of the CNT structures was determined by differential scanning calorimetry (DSC) on a DSC 7 from Perkin Elmer. Specific heat is an intrinsic property of a material and corresponds to the energy required to increase a unit mass or molar quantity of material by 1 ºC. If there is no phase transition or chemical reaction, the specific heat should be a positive number changing gradually with temperature. To determine the specific heat we used the ASTM standard E-1269-05 called: *Standard test method for determining specific heat capacity by differential scanning calorimetry* (ASTM E-1269 05). Aluminium pans were used and the sapphire mass was 29.3 mg. Several runs of standards were also necessary. The DSC was calibrated prior to any test with Zinc iridium and zinc before acquisition of the baseline and of the sapphire heat flow (iridium of mass 14.78 mg and zinc of mass 8.86 mg). In our case, the three samples tested were respectively the aluminium pan (average mass of 28 mg), the same as the one used to hold the sample, a sapphire of given purity and mass and the sample itself in the aluminium pan. The CNTs were tested at temperatures between 20 and 240 ºC with a 10 ºC/min gradient between each temperature, while each plateau lasted for 30 min. The temperature cycle is given in Figure 2-7. The purge gas was nitrogen at a flow rate of 50 mL/min. The mass of the BP samples was always higher than 20 mg.

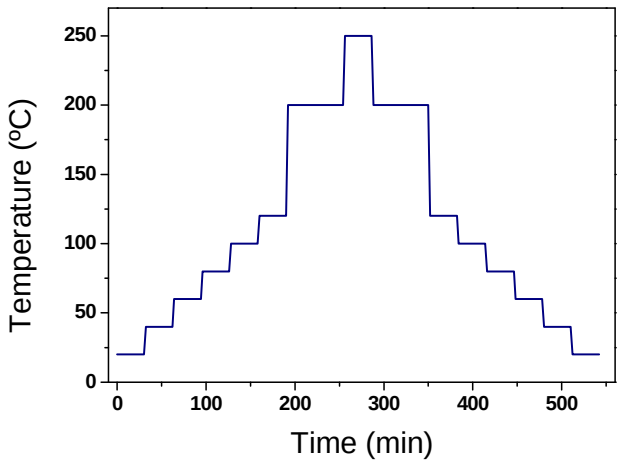

Figure 2-7 Temperature cycle for the determination of the CNT specific heat by DSC

2.4.4.2 Laser Flash technique

Thermal diffusivity tests were performed at CSIRO Minerals on a Laser Flash Anter F15000. In this method, a short pulse of heat was applied to one side of a sample using a uniform laser, and the temperature change on the back face was recorded with an infrared detector. A schematic diagram of the setup is given in Figure 2-8. The laser-flash thermal diffusivity (LFTD) system was used to acquire data over a large range of temperatures (from 20 to 160ºC) and measurements were done every 20ºC. The thermal diffusivity α was defined following Clark and Taylor:

$$\alpha = \frac{1.38 \times t^2}{\pi^2 \times t_{1/2}} \qquad (2\text{-}3)$$

Where t is the thickness of the sample and $t_{1/2}$ the half time to reach the maximum intensity after the thermo-shot (laser pulse).

The thickness of the sample was measured at the different steps. A non-woven material made of Carbon Nano-Fibres (CNF) bought from NanoAmor Corp. was used as a standard. These CNFs had an average outer diameter of ~250 nm and a length of ~500 µm. Furthermore, prior to testing, each sample was gold coated on both faces to improve the thermal diffusion at the surface. The gold coating also improved the thermal diffusion of the top layer. The top surface was then carbon coated to prevent reflection of the laser light from the surface to assure total heat absorption at the top of the sample. The coating thickness was minimized to reduce its impact on the sample properties. It was estimated to be of ~ 10 µm on average by SEM analysis by comparing two areas on a sample partially coated on half of its surface. Either carbon paste or carbon sputtering were used for the carbon coating.

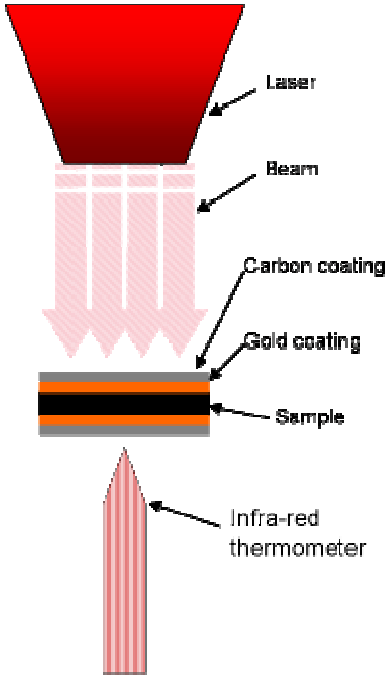

Figure 2-8 Concept of the laser flash technique

2.4.4.3 Thermal conductivity meter

Thermal conductivity was directly measured on 300 µm thick BP using an Armfield Limited Thermal conductivity meter HT1-A. The samples were placed between two copper cylinders. A correlation between the power provided to the circuit and the thermal conductivity can be calculated according to:

$$\lambda_{th} = \frac{\Pi \times t}{A_{contact}} \quad (2\text{-}4)$$

Where $A_{contact}$ is the surface area of exchange (m^2), Π the power input of the conductivity meter (W) and t the sample thickness.

The power used was 10 W and the cooling water temperature was 12ºC. Stable measurements were achieved within 10 -15 minutes for each sample.

2.4.4.4 Environmental Scanning Electron Microscopy (E-SEM) fitted with hot stage

An Environmental Scanning Electron Microscope (E-SEM) fitted with a heating stage was used (at CSIRO Minerals) to determine the thermal expansion of BPs structures. The samples were cut in 3 mm strips and placed within a specially designed copper holder. The exposed cross section was observed in the E-SEM chamber in a controlled atmosphere and the expansion over temperature recorded. Tests from 10ºC to 500ºC were performed in vacuum, Argon (Ar) and water vapor based low pressure atmospheres. A K-type thermocouple was embedded within the holder and at a distance of ~ 1mm from the sample to ensure an accurate reading of the temperature. The thermal expansion was calculated in % of the initial sample thickness. A schematic diagram of the setup is given in Figure 2-9.

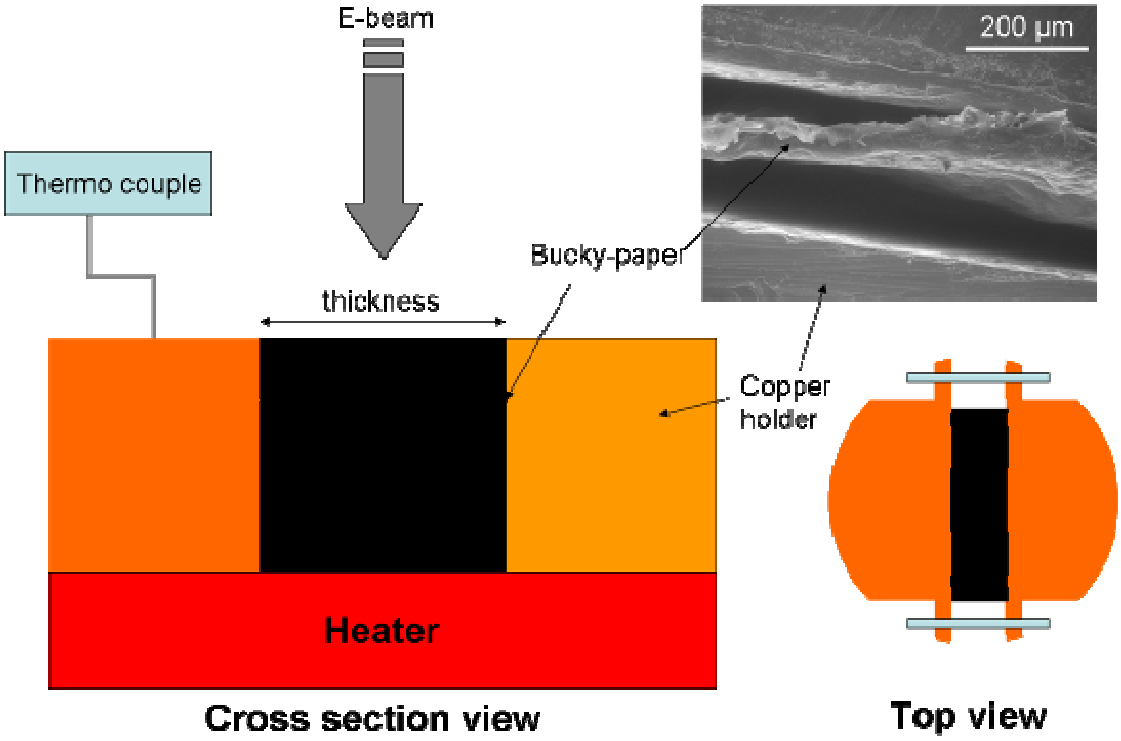

Figure 2-9 E-SEM thermal expansion setup

2.4.4.5 Modulated temperature – thermo mechanometry

Modulated Temperature – Thermo-Mechanometry (mt-TM) is a novel technique that involves the application of an oscillating temperature to a linear/isothermal underlying heating rate. The modulated temperature program induces a sinusoidal response in specimen dimension changes that can be resolved into reversing (in-phase with ΔT) and non-reversing (out-of-phase with ΔT) components. This allowed observation and determination of thermal expansion, thermal and structural relaxation, and morphological changes. A TA Instruments Q400EM Thermo-mechanical Analyser was used to measure the thermal behaviour of the BPs. Dimension changes are called reversible if in-phase and irreversible if out-of-phase with the modulated temperature program. The phases were separated and analysed, giving an overview of the permanent and non-permanent deformation of the sample with heat. The temperature range varied from 20ºC up to 150 ℃ at a rate of 0.5 ℃·min^{-1}. A sinusoidal modulation with amplitude of 2 ℃ and a period of 3 min was superimposed on the temperature ramp. Prior to testing, all samples were first degassed overnight, and then kept in a desecrator for 8h. Furthermore, to eliminate part of any prior thermal history, the samples were maintained at 150 ℃ for 5 min. The samples were cooled at 10 ℃·min^{-1} to 80 ℃ for testing. Strips of BP were cut into strips of 10 mm by 5 mm and placed onto the stage for testing. Their thickness for these tests was between 150 and 250 μm.

2.4.5 Membrane properties

2.4.5.1 Pore size determination and surface analysis

Three complementary techniques were used to characterise pore size. Firstly a surface apparent pore size was determined from SEM images taken with a Philips FEG SEM at 2 kV. Each image was taken under the same conditions to reduce errors when comparing pore sizes between membranes. At least 3 images per sample were taken and the scans were performed at low frequencies (120 mS) to increase the pixel content. The CNTs were sufficiently conductive to not require metal coating which also avoided any

additional error in the pore size estimation. The images were analysed using the software, ISIS, and the edge-pores were not taken in consideration for the calculations. The minimum, mean and maximum average pore size distributions were calculated using Feret's approach. In this method, 3 diameters are calculated for each pore, corresponding to the minimum, mean and maximum pore sizes, which gives information on the pore shape. However, this method only presents a surface apparent pore size and other tests were required to confirm the pore size distribution.

The second method relied on particle size exclusion tests to determine the particle size cut off. These tests were performed by filtrating Bovine Serum Albumin (BSA) and nano-particles (purchased from Sigma Aldrich) through the Bucky-paper membranes. BSA has an average diameter of 5 nm while the nano particle diameters were 50nm (polystyrene-amine modified), 100 nm (polystyrene-sulphate modified) and 500 nm (polystyrene-sulphate modified). The particle diameter distribution was measured using a ZetaSizer and agreed well with the manufacturer's specifications. The solute concentration was analysed either by UV-visible spectro-photometry or Fluorescence spectro-photometry depending on the reactivity of the components.

Thirdly, a porometer was used to determine the pore size distribution as well as the bubble point of the membranes. Samples were tested in a capillary flow porometer from Porous Materials Inc. The tests were performed in wet up / dry up mode with Galwick as the wetting media and either air or nitrogen as the pressurizing gas. The flat sheet samples were discs of 1 cm diameter and were supported with a stainless steel grid. The pressure varied from 1 to 500 psi and was controlled with steps of 0.02 psi/s.

Gallium Focus Ion Beam (FIB) milling was used to produce thin and reproducible cross sections over a few microns. Pore size and inner pore analysis was performed on the images processed on the FIB-SEM (Bio 21, Melbourne Victoria). A FIB-SEM works with two columns (electron beam + ion beam) which allowed simultaneous cross-sectioning and imaging of samples. The gallium ion beam hits perpendicularly the sample surface and sputters a small amount of material. As the primary beam scans the sample surface, the

signal from the sputtered ions and secondary electrons is collected to form an image. Very high resolution is possible with this technique at low primary beam currents while at higher primary currents, fast sputtering rates can be achieved, allowing both precision milling and large cross-sectioning.

A FEI Nova dual beam, focussed ion beam - combined SEM system and gallium ion beam instrument equipped with an EDAX (EDS), a Pt-deposition system and a micromanipulator at Bio 21 Institute, Melbourne Australia was used to characterise the BPs. Cross sections of the BPs were made by milling the surface with a beam of Gallium (Ga) ions at beam current between 0.3 and 7 nA. Imaging was realized at a tilt angle of 52º (as shown in Figure 2-10) while the working distance was typically 5 mm for an E-beam current of 2 – 5 keV. An example of cross sectioning is shown in Figure 2-11.

Furthermore, use of the Gallium ions for etching the BP surface allowed patterning of straight pores across a BP. This allowed the fabrication of 400-500 nm pore size membranes.

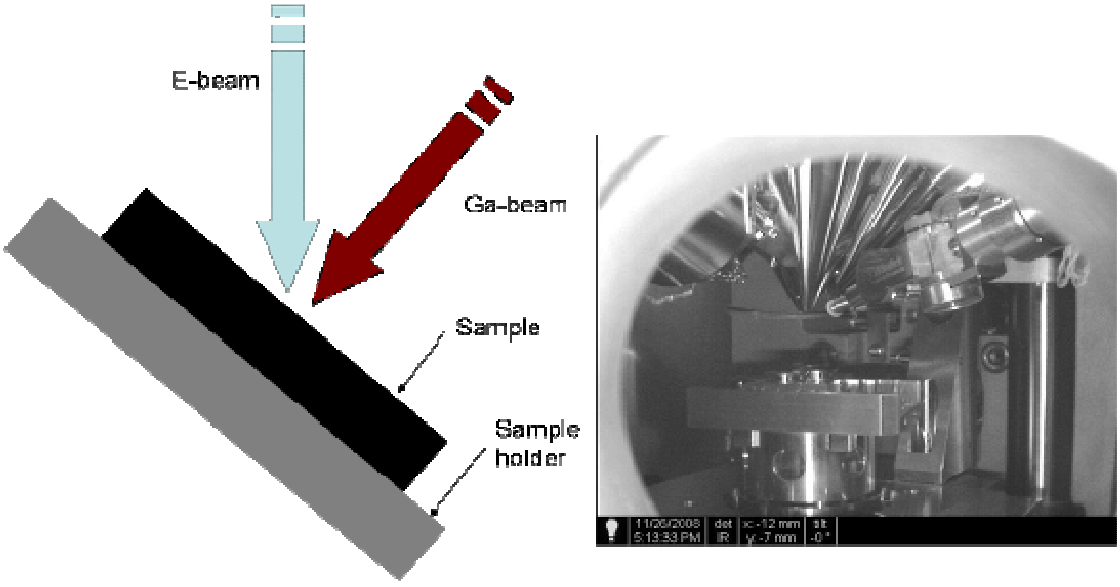

Figure 2-10 Left: Principle of a dual beam FIB-SEM. Right: optical image of the chamber

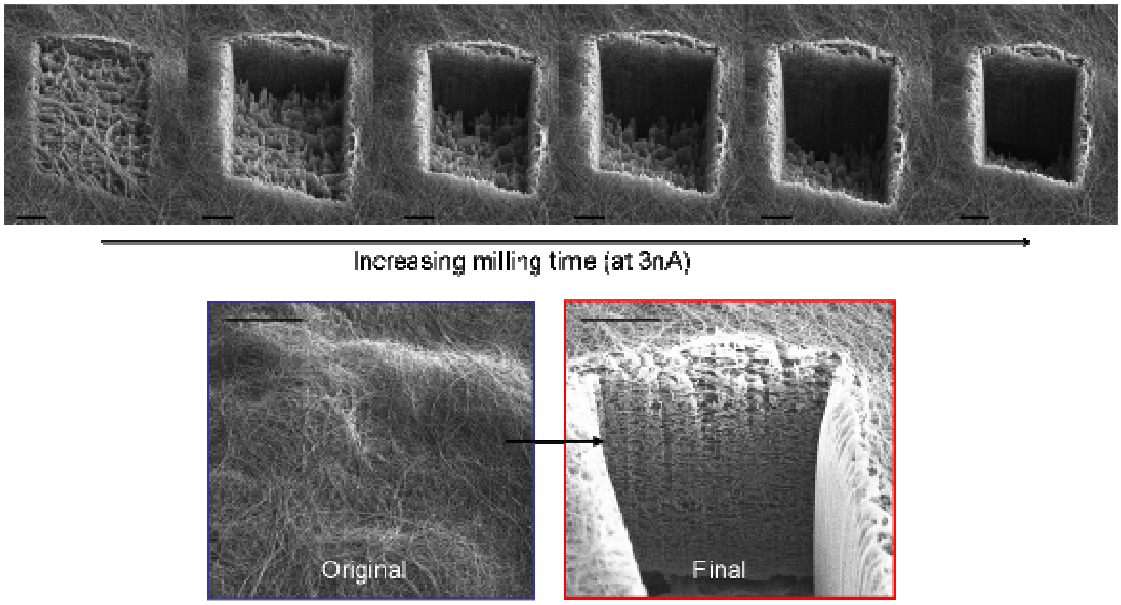

Figure 2-11 Impact of the ion beam on the BP surface. Progressive milling revealed the internal structure of the BPs. The scale bars on the top images correspond to ~1.5 μm, while the scale bars on the two bottom images correspond to ~2 μm

2.4.5.2 Porometer & Liquid Entry Pressure (LEP)

Pore size distribution measurements were made on a Capillary Flow Porometer from Porous Material Inc, NY USA. In addition to pore size distribution, this also provides a bubble point measurement for membranes. In liquid porometry, a non-reacting liquid, typically alcohol based, is used to wet the membrane pores. Once the pores have been wetted, the membrane is pressurized by an inert gas (N_2) to remove the liquid from the pores and allow direct gas flow. The differential pressure required to empty a pore is related to its diameter, d as shown in Equation 5:

$$d = 4\gamma \frac{\cos\theta}{\Delta P} \quad (2\text{-}5)$$

Where γ is the surface tension of the liquid, θ the contact angle and ΔP is the differential pressure across the pore.

As the contact angle of low surface energy liquids can be assumed to be close to zero, d can be assumed to be inversely proportional to the differential pressure across the membrane pores. The gas flow rate across

the dry membrane is used as a reference to calculate the pore size distribution as a function of the differential pressure.

Liquid Entry Pressure (LEP) works on a similar approach and tests were performed in an Amicon cell with deionised water. The pressure was increased in 5 psi increments and the samples maintained at each pressure for 10 mins until equilibrium was reached. The 15 mL cell was sealed with o-rings and pressurized with laboratory grade N_2. A clear flexible tube located under the cell on the permeate side was used to collect the water permeating across the membrane. The LEP was considered as the pressure when the first drop of liquid water was seen on the permeate side.

The bubble point measurements were done on a porometer with Galwick, as described in ASTM F316.

2.4.5.3 Porosity measurement

The membrane porosity was measured using a 2 mL pycnometer following the procedure outlined by Smolders et al. [61]. A minimum of 3 samples was used to calculate the average porosity. The experiment involved measuring the mass of sample in two different liquids. The first liquid (propan-2-ol) wets the membrane and enters the pores, while the second liquid (deionised water) does not wet or fill the pores. Once immersed, the sample was left for 20 mins and then sonicated for 2 mins at low power (150 W and 20ºC) to remove any trapped air bubbles. Prior to changing liquids the sample was dried in a vacuum oven for 20 mins. The porosity was then calculated according to:

$$\varepsilon = 1 - \frac{\rho_b}{\rho_a} * \frac{(M_1 + M_2^a - M_3^a)}{(M_1 + M_2^b - M_3^b)} \quad \text{(2-6)}$$

where ε is the porosity, the superscripts a and b correspond respectively to propanol-2-ol and water, ρ is the liquid density, M_1 is the mass of the dry sample, M_2 is the mass of the bottle filled with liquid ,and M_3 is the mass of the bottle plus sample filled with liquid.

Porosity measurements were also carried out on an AccuPyc II 1340 1-cm^3 Gas Displacement Pycnometer from Micromeretics at 19 psi. Ten equilibrium measurements were averaged to provide a mass of helium adsorbed per surface area. The calculation method was similar as that of the liquid pycnometer but the gas pycnometer led to more reproducible measurements. The access to this device was, however, restricted and only a limited number of samples were tested this way. This method was less time consuming, more accurate and reproducible than the liquid pycnometer. The accuracy of the Helium pycnometer tests was ~1% while the liquid pycnometer always showed large variations over the same samples depending on the wetting of the material and the possible presence of air bubbles in the structure. The He technique was preferred and the results presented here come from this method unless otherwise stated.

2.4.5.4 Thickness measurement

Thickness profiles of the samples were measured on a white-light profilometer (Altisurf 500). Variations in the thickness measurements were found and periodic checks were necessary to ensure that the correct thickness was used for the calculations. The changes in thickness were mostly due to the presence of bundles in the structure. Bumps of a few hundreds of nm up to a few microns were found. They, however, did not represent more than 1-2% of the total thickness of the samples.

A Kincrome electronic digital micrometer gauge with a precision of 1 µm was also used to check the thickness of the BPs. As the BPs were quite compressible, several measurements were taken on different spots of the samples and averaged. The values reported were taken at low compression force before deforming the samples.

2.4.6 Composite materials processing techniques

2.4.6.1 PTFE coating

BPs were coated with PTFE with an in-house fabricated radio frequency (RF) sputterer from RMIT (Melbourne, Victoria). The 60 mm wide 99 % pure PTFE target was set at a 70 mm distance from the flat sheet BPs which were sequentially exposed on both sides for 8 min at room temperature and 80 W (argon process pressure of $1.2x10^{-2}$ torr). Then both uncoated and coated BPs were hot pressed at 80 ºC with a layer of poly(ethylene) grid [278], used as a mechanical support.

2.4.6.2 Polymer infiltration

Self-supporting BPs were infiltrated with 5 w% polymer/solvent solutions by vacuum filtration. The samples were thoroughly backwashed with DMF and propan-2-ol before being dried at 60 ºC overnight in a vacuum oven.

2.4.6.3 Alkoxysilane functionalisation

Three batches of CNTs were exposed to ozone, generated by a Novascan PDS-UVT, UV/ozone cleaner, in a confined chamber for respectively 10, 30 and 60 min. The samples were positioned at a 30 mm distance from the UV lamp which had an intensity greater than 36 mW/cm^2 and ozone output greater than 50 ppm. This oxidation treatment was necessary to form hydroxyl and carboxylic active sites on the surface of the nanotubes. The hydroxyl functionalised CNTs were then exposed to lithium aluminium hydride ($LiAlH_4$) to reduce the carboxylic groups present on their surface. Typically, CNTs were suspended in toluene and horn-sonicated for 30 min in a cooled water bath. $LiAlH_4$ was added and the solution stirred at 30℃ for 60 min. Then 2.0 ml of a 2M HCl solution w as added to remove the reducing agent. The CNTs were washed sequentially with toluene, ethanol and acetone prior to being vacuum dried overnight at 100 ℃ [213].

The second step of the process involved the chemical reaction of the hydroxyl groups with the alkoxysilane moieties. Typically, CNTs were suspended in toluene and sonicated for 15 min. Then a 1.0 wt% GPTMS/toluene solution was added (30 mL for 100 mg of CNTs) and stirred at 65℃ for 6 h to achieve silanization. Eventually unreacted GPTMS was washed out with methanol until a clear permeate was obtained and the CNTs backwashed sequentially with deionised water and acetone. The silanised CNTs were dried overnight at 100℃ [213, 336].

2.4.6.4 Latex bead templating

Propan-2-ol / CNT 20 mg/L suspensions were produced by sonicating chemical vapor deposition grown CNTs at 150W and for sequences of 15 min [175]. The samples were processed by uniformly mixing 1 μm polystyrene (PS) latex beads (purchased by Sigma Aldrich, latex beads L2157) with the solvent dispersed CNTs at a ratio of 0.05 mg bead /L. The mixed suspensions were filtered through a Millipore filtration unit to obtain a self-supporting polystyrene/CNT BP. Permanent low speed stirring was applied to the solutions to avoid decantation and phase separation. A first series of samples was backwashed and dipped for 24 hours in technical grade dimethyl-formamide (DMF) to dissolve the polystyrene based-latex beads, while a second series of samples was heated in a 99.9% pure N_2 atmosphere at 350 ºC to carbonize the polystyrene beads.

2.4.6.5 Gold electroless plating

Electroless (ES) deposition was performed to fabricate gold reinforced BPs. In the first step referred to as sensitization, the membrane was immersed in a solution of 0.026 M $SnCl_2$ and 0.07 M trifluoroacetic acid in a solvent of 50:50 methanol:water for 45 min followed by rinsing in methanol for 5 min. This was followed by the second step, referred to as activation, where the membrane was immersed in a solution of 0.029 M ammoniacal $AgNO_3$ for 30 min. The membrane was then rinsed in methanol for 5 min and immersed in water before placing the membranes in the plating bath. In the third step,

referred to as displacement deposition, the silver coated membrane was immersed in the gold plating solution consisting of 0.079 M $Na_3Au(SO_3)_2$, 0.127 M Na_2SO_3, 0.625 M formaldehyde and 0.025 M $NaHCO_3$. The temperature of this bath was ~1–4 ℃ at pH = 8. The plating time varied from 1 h up to 30 h which significantly reduced the pore size of the membrane without closing the pores. Finally, the membranes were thoroughly rinsed in deionised water and ethanol and air-dried at room temperature.

2.5 Direct contact membrane distillation rig design

A Direct Contact Membrane Distillation (DCMD) rig was built to test to the performance of the membranes in direct contact membrane distillation. Membrane Distillation can be operated in four modes [59], but DCMD exhibit high flux as the air-gap is limited to the membrane thickness thus making materials comparison more accurate and precise. Furthermore as both sides get contacted with water, it is also the best method to compare materials properties such as limit entry pressures, wetting or impact of surface pore size. It is the most restrictive setup as the membranes need to be hydrophobic on both sides and present a very low thermal conductivity, which is less critical in the case of air-gap or vacuum MD. This section will first briefly describe the design of the module and of the setup before detailing the working conditions in which the membranes were tested.

In DCMD of saline waters, the membrane is used as a separation barrier between a hot brine feed and a cold permeate of fresh water (Figure 2-12). This schematic figure describes water vapour transport across a porous membrane during DCMD. Thus, the two liquid streams are only connected by the air-gap present in the membrane.

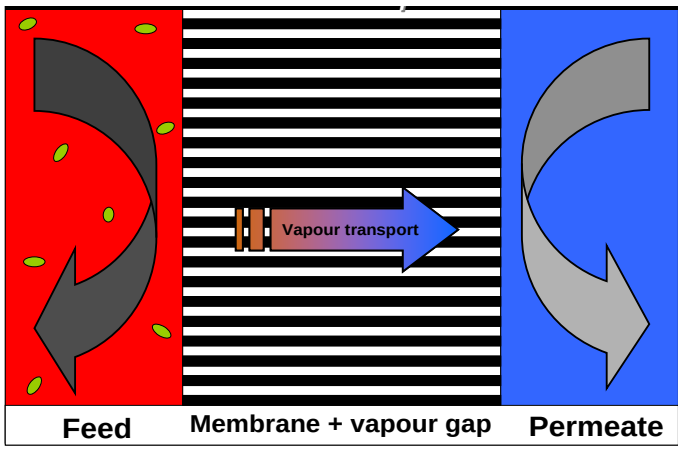

Figure 2-12 Principle of DCMD

Tests were performed in a module in counter current flow mode, with deionised water, on the cold side, and synthetic seawater on the hot feed side

(35 g/L NaCl solutions). The cell was designed to offer turbulent flow, thus preventing the formation of stagnant layers at the membrane surface. An angle of 45º was formed between the inlet and outlets with the membrane cavity, thus forcing the water to come in contact with the membrane. The module was made in poly(tetra fluoro ethylene) (PTFE) to benefit from the good insulation properties of the material, limiting the thermal losses and heat exchanges which were not related to the process during the test. Vuiton ® o-rings were used to seal the membrane and the module, and Tygon ® tubing were used to transfer water from the reservoirs to the DCMD module. The chamber where the membrane was sealed was a flat cylinder, which diameter and height were respectively 25 mm and 2 mm. The membrane test area was a disc of 5 cm^2. A small module was used to reduce the effect of module size related to temperature drops. Therefore, flux or permeance is less affected by temperature profiles as temperature was almost constant on each side of the membrane. A schematic diagram of the membrane module is given in Figure 2-16. Periodic cleaning with deionised water and propan-2-ol of the module, pump heads, glassware and tubing between tests was conducted to remove possible salts deposited in the equipment.

The experimental design involved the use of a double head peristaltic pump (Pump: Cole Palmer Masterflex, model 7521-25; Head: Easyload II, Model 77200-60), to pump the hot and cold streams through 50 cm long heat exchangers. The hot and cold heat exchangers were respectively connected to a CS Lauda C6 heater and to a Thermo Scientific Neslab RTE-7 cooler. The heater (CS Lauda C6) and cooler (Thermo Scientific Neslab RTE-7) enabled a wide range of operating temperatures tuneable between 2ºC and 100ºC.

Solution conductivity, temperature at both inlets and outlets of the module and water volume on the cold side were recorded over time to assess performance of the membrane and to ensure that salt rejection remained high. Typically, the flow rate for each stream, setup on the pump, was maintained between 200 and 300 mL/min corresponding to velocities in the module between 0.006 and 0.01 m/s, while the inlet temperatures of the water streams were kept constant. The cold side temperature was generally kept

constant over each series of tests while the hot side was varied to achieve differences in the partial vapor pressure of water across the membrane.

The volume change on the cold side was monitored with a graduated column directly connected to the cold water reservoir. Pictures were recorded with a webcam every 10s. The precision of the reading linked to the water level fluctuation and to the reading was of ~ 0.5 mL. This allowed in situ, real time measurement of water transport across the membrane. Temperature and conductivity on the cold side were data logged. A schematic diagram of the DCMD test rig is shown in Figure 2-13 and pictures of the rig are shown in Figure 2-14.

The driving force in MD is the difference in water vapor pressure between the two sides of the membrane air-gap. The absolute variations of pressure (ΔP) were derived from Antoine's law and calculated as a function of the temperature measured at the inlets of the module on both side of the membrane (Figure 2-16). Antoine's law is given in Equation 7. Depending upon the feed and permeate temperature variations from one up to a few degrees were found between the inlets and outlets. The module outlet temperatures were found to vary by 1 - 3 % compared with the inlet temperatures.

$$\log(P^{\circ}) = A - \frac{B}{T + C} \qquad (2\text{-}7)$$

Where P is the vapor pressure, T the absolute temperature in K and A, B, C are constants that need to be determined through experiments. Tables are available in the Handbook of Chemistry and Physics (63rd edition, pages D-196 to D-198) for water vapor and were used to fit the curve given in Figure 2-15.

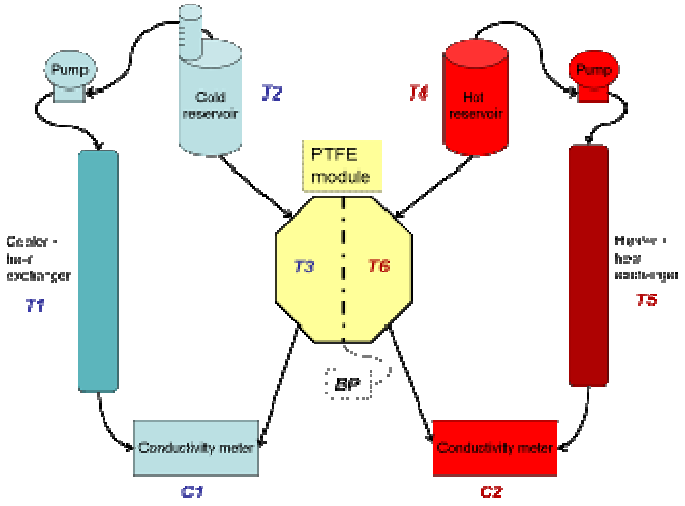

Figure 2-13 Schematic diagram of the test rig

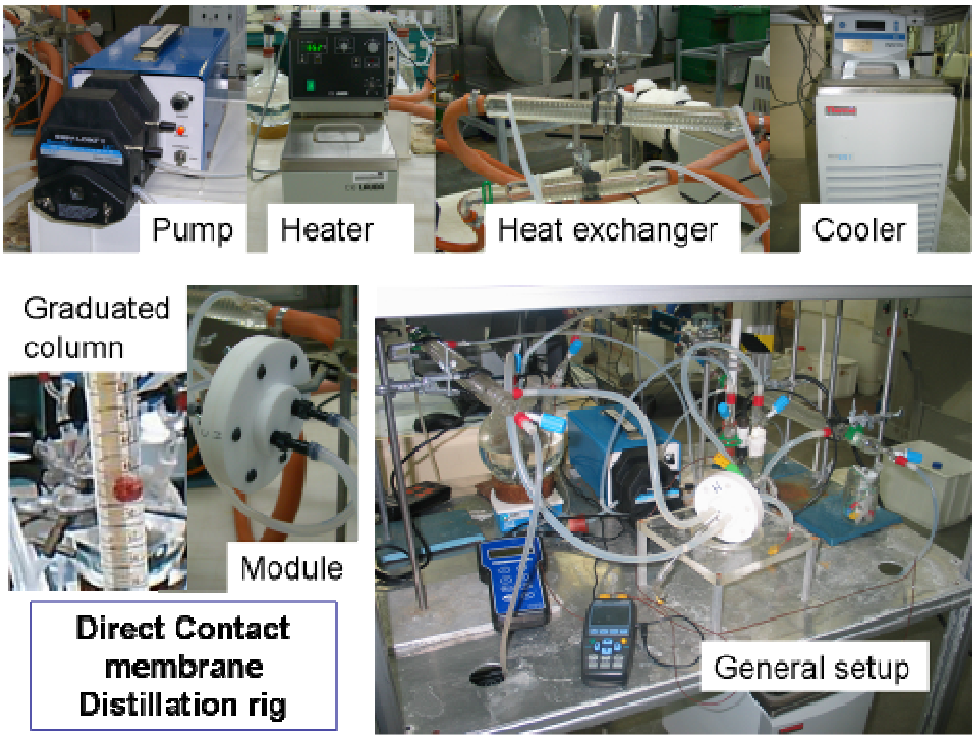

Figure 2-14 Optical images of the rig with the main parts highlighted

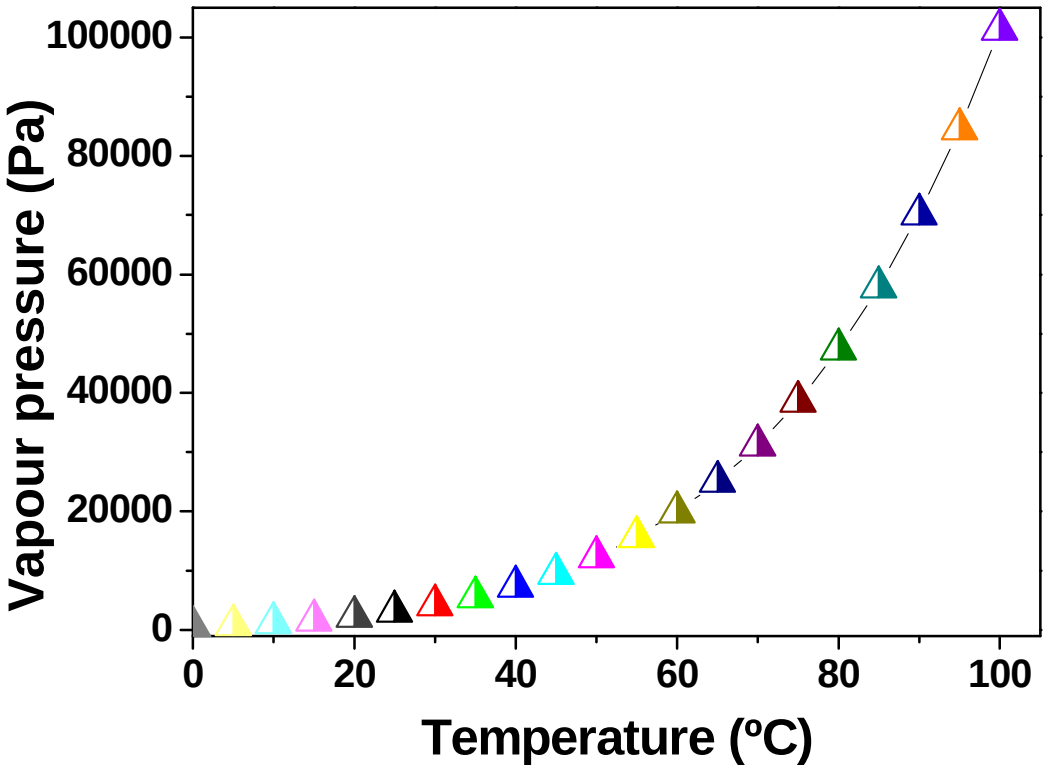

Figure 2-15 Graph of vapor pressure as a function of temperature (Antoine's law)

The results of the tests were considered if no leak had occurred during the test and if the membrane integrity was intact after at least 2 h of continuous testing. The level of water, as well as the temperatures, flow rates and conductivity were also carefully recorded so that the results were as reproducible as possible. The results will be reported as flux and permeabilities, which was found to be the most suitable way to compare membranes of different thickness and geometrical properties.

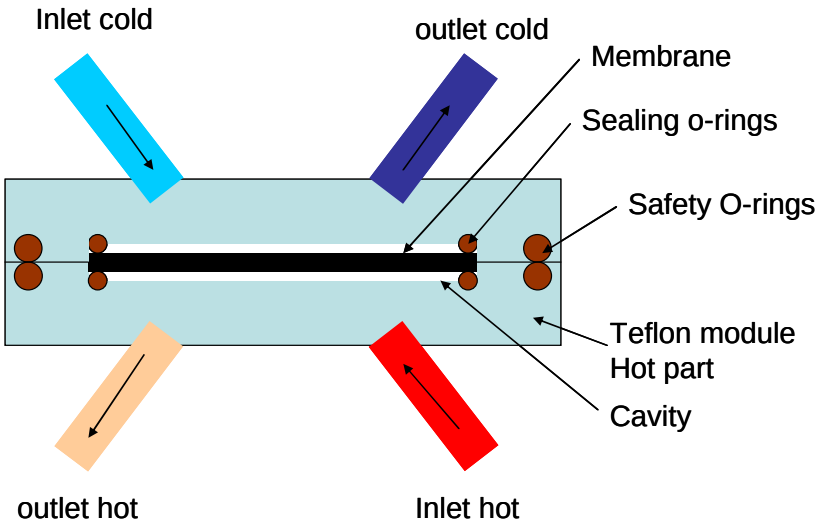

Figure 2-16 PTFE module geometry

Chapter 3

3 Dispersion of CNTs in solution and self-supporting BP processing

This chapter explores the unique properties of CNTs in their dispersed state. CNTs have been investigated in a very large range of applications over the past 20 years. Recent work and commercialised products showed that CNTs could be used for example as potential additives in adhesives, coatings and thin film or as reinforcements for high strength composite materials. The benefits of the use of CNTs are typically an increased resistance to thermal stress, harsh chemically reactive and corrosive environments, extreme pressures and abrasion. However once grown, CNTs are typically available as dry pristine material and can be conveniently and stably dispersed prior to further uses and/or treatment. Their dispersion revealed to be challenging due to the CNT tendency to form bundles at a very fast pace.

3.1 Introduction

Numerous methods have been demonstrated to efficiently disperse CNTs, but the quality and long term stability of these suspensions are still issues that need to be addressed (cf. Chapter 1 on Literature review – section dispersion).

In this work, BP processing, both the length and the surface chemistry of the CNTs were critical as shortened CNTs would lead to poorer mechanical strength of the final BPs and defects on the CNTs outer wall surfaces would lead to possible functionalisation and a loss of hydrophobicity. Furthermore, as the BPs were fabricated by vacuum filtration from CNTs suspended in a suitable solvent, the stability of the suspension over time was also crucial. Since well dispersed CNT suspensions are difficult to produce due to their strong tendency to bundle and agglomerate, efforts were focused on developing a dispersion method that would (i) not damage the CNTs while (ii) leading to suspensions where the CNTs would be individually dispersed and their (iii) stability over time would exceed the duration of the CNT filtration. This tendency to bundle becomes particularly apparent over time, where well dispersed CNTs slowly aggregate into larger structures.

Furthermore, the two kinds of CNTs used - CCI and CVD - presented various initial degrees of entanglement and different dispersion processes had to be undertaken. Thus various solvents, surfactants and dispersion processes were first tested and will be reported. A method involving the use of propan-2-ol and cycles of freezing and sonication at low intensity was preferred and will be described. As CNTs aggregate and bundle they typically cover a very large range of size and shape distributions and finding a method that would be both qualitative and quantitative in describing these changes revealed to be challenging.

This chapter will first introduce what a CNT bundle is and then review the work done on the dispersion of the two kinds of CNTs used: CCI and CVD. Eventually the main characterisation techniques used to assess dispersion parameters will be presented and the rationale behind the dispersion method chosen will be explained.

3.2 Bundling in CNTs: origin and shape of bundles

CNTs bundles stick together solely by Van der Waals forces solely [75, 243-245]. As nano-materials typically expose a very high surface area per gram of material, they tend to agglomerate to minimize their surface energy and reduce their exogenous interactions [237, 238, 240, 246-248]. As this is their nature one must adapt and find ways to process them into macro-structures before they have the time to agglomerate and characterisation methods that can allow the determination of a very broad range of sizes simultaneously are required to monitor the aggregation process. In the following section, examples of agglomerations are revealed by SEM imaging the surface of BPs.

Several techniques can be used to characterize colloidal dispersions as presented in Figure **3**-**1**. However, due to the very large range of CNT bundle size no technique is able to fully characterize, both qualitatively and quantitatively CNT suspensions.

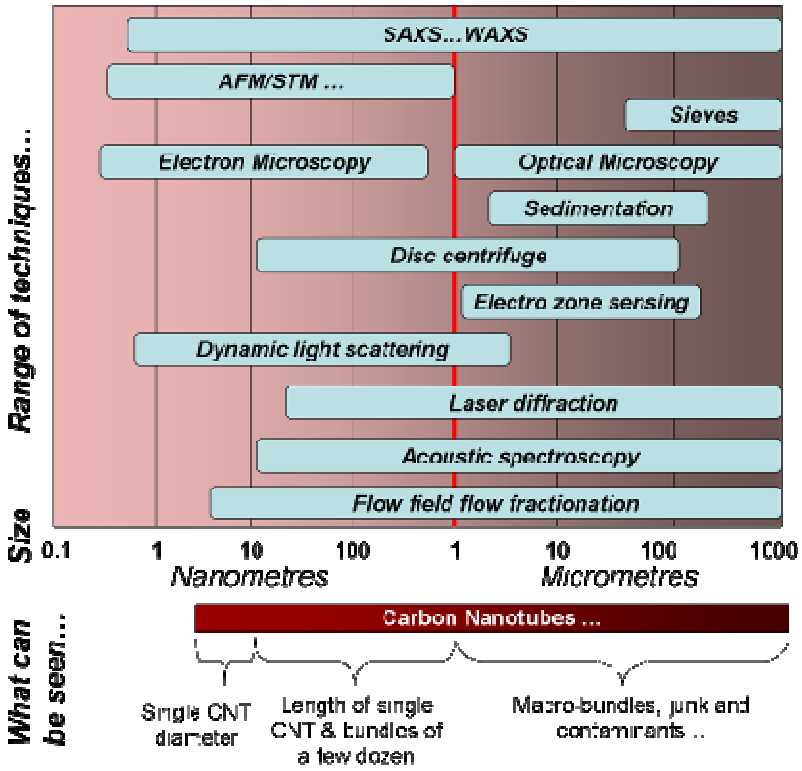

Figure 3-1 Range of colloidal characterisation techniques associated with typical CNT and CNT bundles dimensions

Dense CNTs bundles typically form either (i) during the CNTs growth, (ii) the recovery of the CNTs from their growth substrate by mechanical entanglement or (iii) the initial dispersion steps because of solvatation effects. Regarding the CVD grown CNTs, the tubes were naturally parallel to each other and presented a low degree of entanglement on their growth substrate (Figure 3-2). However, CCI grown CNTs presented a much higher degree of entanglement (Figure 3-2) and required more pre-treatments. BPs made of poorly dispersed CNTs will lead to structures composed by macro-bundles and thus offer poor mechanical strength.

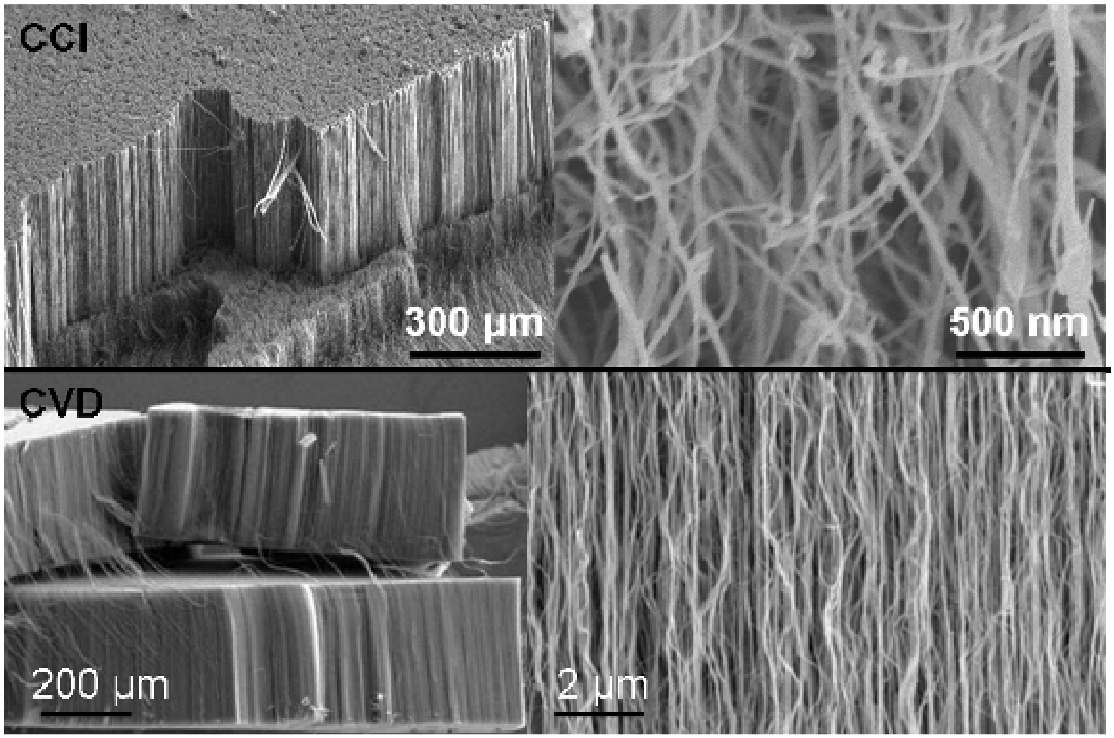

Figure 3-2 Top: As grown CCI CNTs. Left: low magnification of a forest where macro bundles are visible; Right: high magnification of the CNTs alignment. Bottom: As grown CVD CNTs. Left: magnification of a forest. Right: magnification on the CNT to show the high degree of alignment. Most of our CVD CNTs came from these batches

As an example, commercial non-treated CNTs were used to fabricate BP and the morphology of the different structures compared. It is clear from Figure 3-3 that the quality and purity of the CNTs affected the final BP. As seen on the SEM images, large contaminants were found to pollute the CNTs. Bundles agglomerated forming macro-sized aggregates that needed to be dislocated and broken to fully benefit from the CNTs properties.

Prior to their dispersion, the CNTs recovery consisted of scraping off the CNTs from their growth support with a scalpel. As shown in Figure 3-4, BPs made of poorly dispersed CCI and CVD CNTs are presented in Figure 3-4, upon ineffective dispersion, the bundles become highly stable and were difficult to break apart thus justifying the development of techniques to effectively disperse the CNTs. The CNTs produced at the CSIRO were more easily dispersed and purer than the commercial CNTs, which is one of the reasons why this supply was preferred. However as shown on the images,

macro bundles were also present thus requiring further treatment to fully individualise the CNTs.

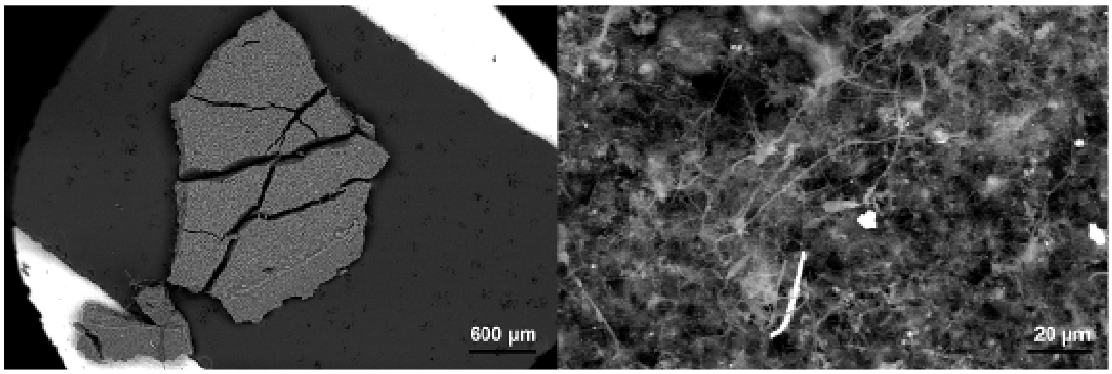

Figure 3-3 Example of highly entangled commercial CNTs. Source CNTs (left) and made into BP (right). The CNTs are embedded into amorphous material and show a very large degree of entanglement

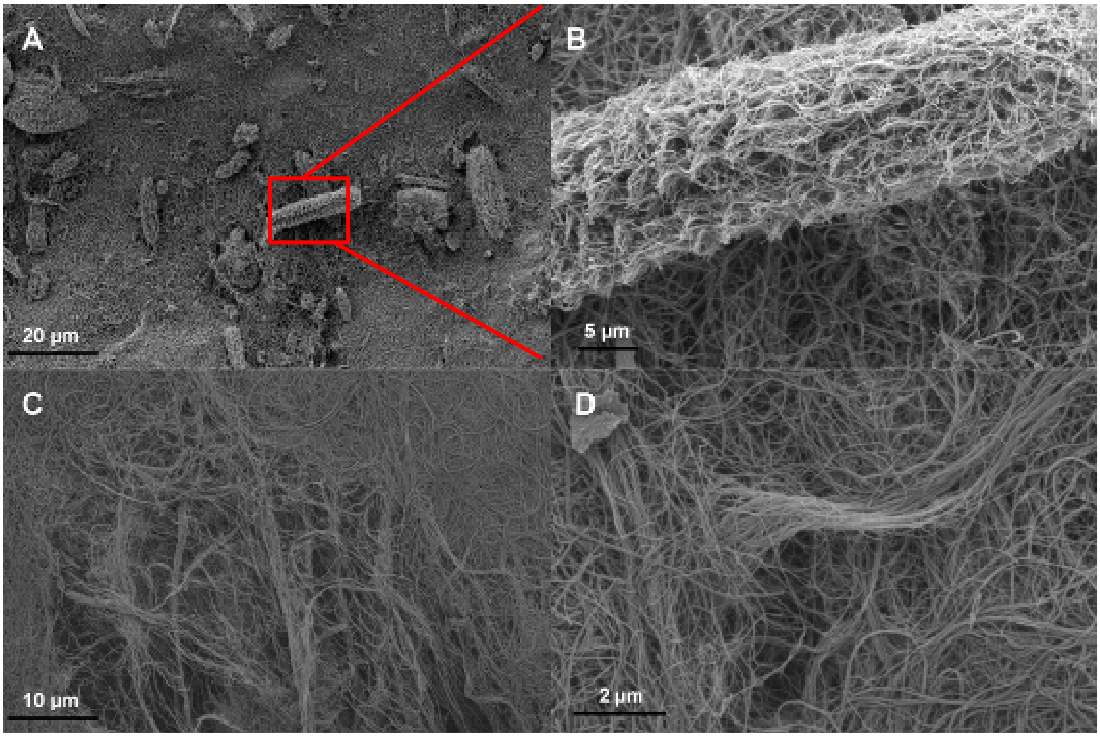

Figure 3-4 SEM images showing CNT bundles (A) CCI bundles scattered on the surface and partially embedded in the BP thickness; (B) spot zoom of (A) on dense CCI bundle where the CNTs are clearly highly entangled; (C) large defect due to a CVD bundle with a low density structure and (D) spot zoom of (C) on CNT rope-style bundle with highly intricated structure.

3.3 Rationale for the dispersion method

CNTs were naturally entangled and efforts were required to debundle and stabilize them into homogeneous suspensions prior to further treatments. As both the chemical functionalisation of the CNTs and very harsh sonication were initially excluded to avoid damaging the CNTs, only pure solvents or surfactant/solvent solutions were investigated as dispersion media.

Previous studies [234, 235, 238, 248, 337] showed that, although efficient in dispersing CNTs [338, 339], surfactant molecules used to disperse CNTs tended to stick very well onto CNT surface thus making their removal and cleaning complicated. Tests were performed on CNTs dispersed in propan-2-ol with 0.1 and 0.5 % of Trimeric Nonylphenol Polyoxyethylene-ether (TNP) and it was shown that even after 3 back-washings the contact angle with deionised water was still lower by 10-15 degrees (i.e. more hydrophilic) than that of the CNTs dispersed into pure propan-2-ol. Since the surface energy of the membrane was critical and needed to be absolutely reproducible, the use of surfactant was also avoided.

For these reasons a method involving low CNT concentrations, sonication and temperature was initially adopted.

3.3.1 Dispersion of the CCI CNTs

A study undertaken by Dr. Dong Wook Chae, former post-doctoral fellow at the CSIRO MSE was focused on a new dispersion mechanism to produce long term stability CCI suspension. This work has not published yet but should be submitted very soon. To facilitate the current work, CCI CNTs pre-dispersed by this method were used as a starting material.

The process involved the dispersion of the CCI CNTs under high shearing stress in a viscous media. The CNTs were blended with a poly(saccharide) based solution and mixed to be mechanically dispersed. After mixing, the solution was first diluted with hot deionised water and stirred. The CNTs were filtered and collected through a cellulose filter media and rinsed with 60 ºC deionised water to remove the remaining sugar. Several of

these rinsing steps were necessary until all the poly(saccharide) was removed and clear permeate obtained by filtration across the CNT cake. Once cleaned the CNTs were easily redispersed into alcohol based solutions.

This dispersion method yielded highly dispersed and stable solutions that could last for several months. However, the high shear forces involved heavily damaged and shortened the CNTs. Unfortunately no other dispersion method was found to provide sufficient energy to break apart the CCI CNTs bundles without damaging the CNT walls and thus creating defects in their structures as shown in Figure 3-5. Amongst the defects formed during this process, collapsed walls, presence of amorphous carbon and CNT cleavage were commonly found. For this reason CCI CNTs were not used extensively for BP production, but only used for comparisons and in mixtures with the CVD CNTs (Chapter 4).

Figure 3-5 TEM of CCI CNTs after high shearing dispersion

3.3.2 Dispersion of CVD CNTs

3.3.2.1 Effect of different solvents

As shown in Appendix 1, CNTs do behave very differently depending on the polarity, volatility and surface tension of the solvent. Exposed to the right kind of solvent CNT forests can for example form fractal patterns of very precise geometries. The choice of a suitable solvent for the CNT dispersion will rely on its affinity with the CNTs and on the stability of the CNT/solvent interactions.

Several solvents were first tested and mixed with small amounts of CNTs. Figure 3-6 shows CNT-solvent solutions composed of ~ 10 ml of

solvent and a ~0.05 mg of CVD CNTs. The solvents used are listed in Figure 3-6. The CNTs were dispersed by first shaking by hand the flasks and followed by two sonication sessions at 30ºC for 5 min. As shown in Figure 3-6 the degree of dispersability varied greatly depending on the solvent used. The size and shape of bundles are clearly different and vary from a low density 'cloud' of CNT for propan-2-ol to small and dense bundles in deionised water.

The stability of the CNT bundles was also tested in the different solvents after mild sonication (150 W for 10 min at 20 ºC). No major change in the visual classification was found even after several cycles. Other parameters such as the solvent price, toxicity or volatility were considered. Propan-2-ol was found to be a cheap, flammable but reasonably safe and non toxic solvent. It was also available in reasonable quantities in the laboratory which was critical to disperse large quantities of CNTs.

For these reasons pure propan-2-ol was preferred and will be the only solvent used in the following work.

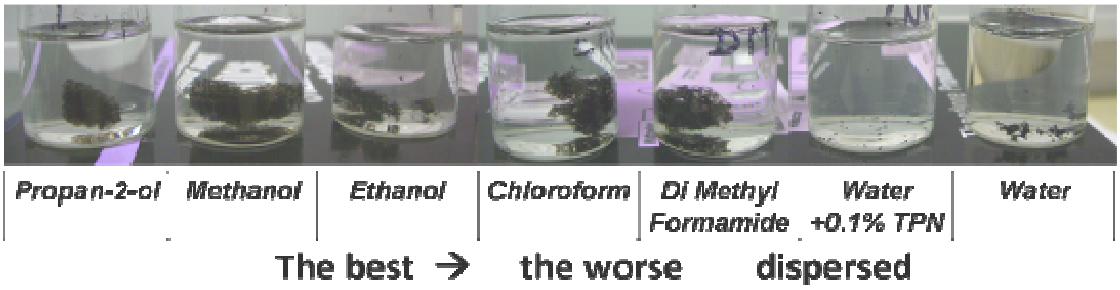

Figure 3-6 Dispersion of CVD CNTs into different solvents in a stable state

3.3.2.2 Dispersion protocol

Amongst the most efficient and convenient techniques, sonication in solution has been shown to produce reproducible suspensions. However, the sonication method and intensity have to be carefully chosen to avoid damaging the CNT walls and shortening them [340]. During sonication of CNTs in solution, the liquid jet streams resulting from ultrasonic cavitation, overcome the bonding forces between the nanotubes, and separate the tubes [248, 341, 342].

The work in the next section was undertaken in order to find an appropriate method to qualitatively assess the CNTs dispersion state. A study to characterize the CNT bundle size distribution would have been interesting but was not pursued as it did not directly fall within the scope of this PhD. Figure 3-7 shows an example of CVD CNT dispersed by horn sonication.

The intensity used (given in the figure) is critical and the debundling effectiveness clearly improves with increasing energy. Acceptable dispersion states were obtained for the CVD CNTs by horn sonication after only 15 to 30 s of treatment. The bundles were clearly broken and solutions were this way stable for a few minutes at room temperature.

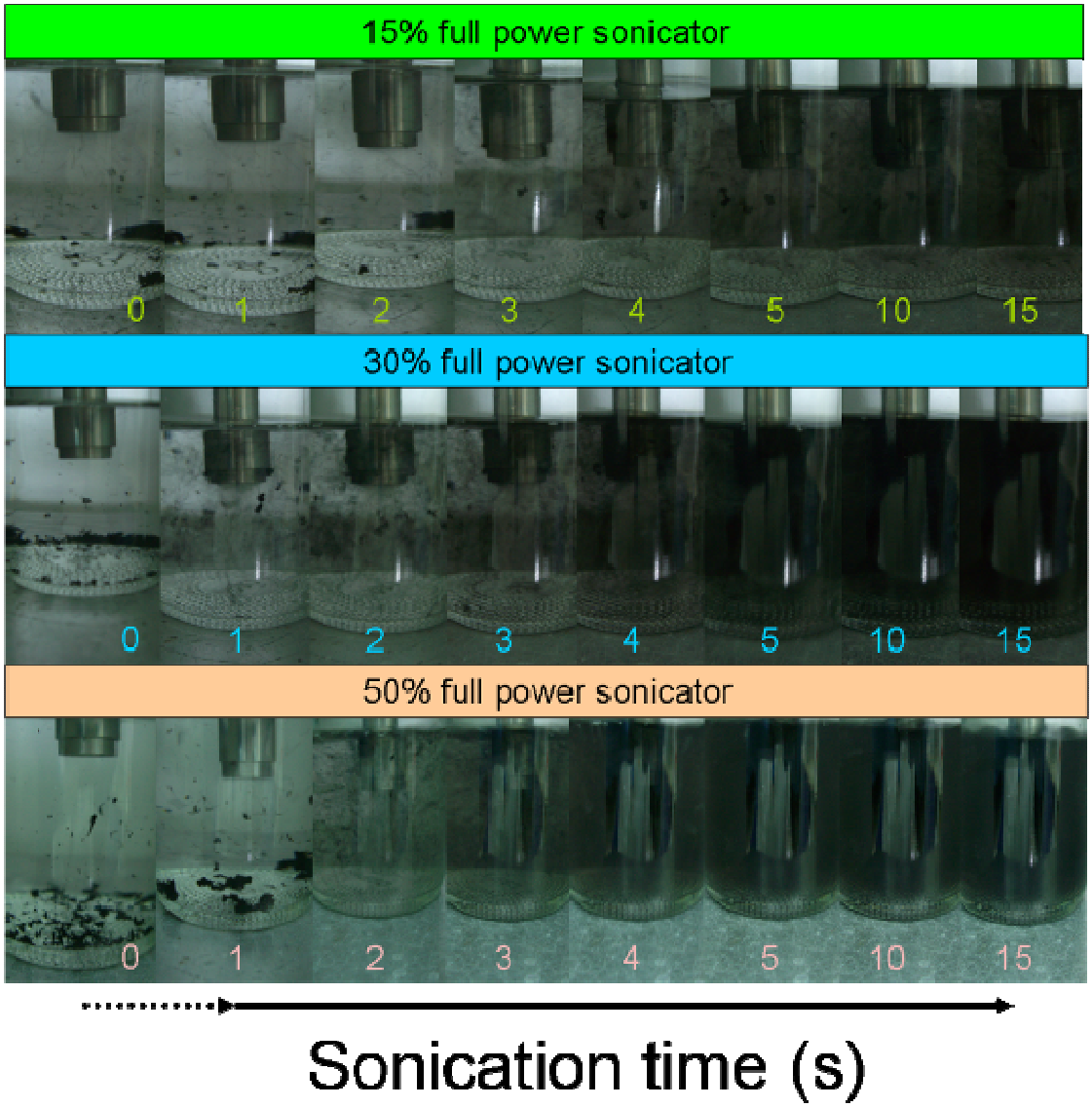

Figure 3-7 Example of the horn sonication efficiency at various powers. Nominal power was 150 W = 100%. The time is given in seconds of sonication. The solutions were initially at room temperature.

However as shown in Figure 3-8, horn sonication did lead to damaged CNTs. The TEM micrographs show how CNTs walls were broken and defects induced into the CNT structure. This was not desired as any defects in the CNT structure, as shown in the next chapter was a possible weak point in the structure. It could induce both mechanical defects in the BPs and wetting of the surface and pores. For this reason a bath sonicator was preferred (Figure 3-9) as it induced lower degree of damage to the CNTs. However, as the horn sonicator efficiency was higher, it was used to pre-disperse some highly entangled batches which will be specified when used in this work.

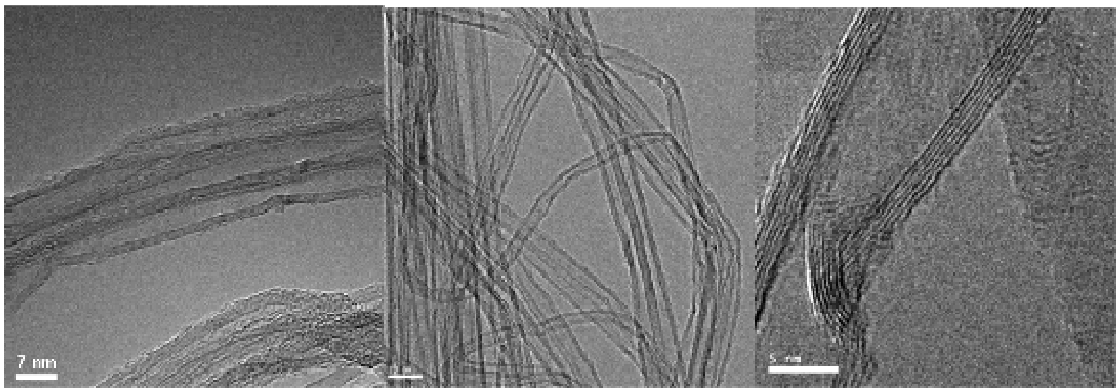

Figure 3-8 TEM of CVD CNTs after horn sonication

Figure 3-9 Example of solution sonicated in the bath sonicator. The bath is composed of deionised water

3.4 Dispersion characterisation results

The CNT suspensions were characterized to better understand their agglomeration behaviour as well as quantify the bundle size distribution. The relatively easy dispersion stability of these nanotubes was an asset for spectro UV-visible testing.

First, UV-visible absorption spectra of these solutions were measured for several days day after ½ hour of sonication at 150 W at 20℃. These tests were carried out to assess if the Beer-Lambert law could be applied to these structures. Then, a similar study was undertaken using of a Malvern Zeta Sizer, and optical images of the suspensions were taken to confirm and interpret the results.

Eventually a study on the investigation of the effect of the sonication temperature on the dispersion stability and the sonication efficiency will be presented.

3.4.1 Suspensions preparation for the pre-study

Suspensions of 26 mg/L CNTs in propan-2-ol were prepared. Both CCI and CVD based suspensions were first sonicated 3 times for 20 min at 150 W and at 20ºC. The solutions were stirred for 5 min between each sonication and were kept at 20ºC. The test solutions were diluted 10, 100 and 1000 fold in propan-2-ol. The solutions names are given in Table **3-1**.

Table 3-1 Concentrations of the solutions

CCI:	CVD:
CCI-A = 0.026mg/L	CVD-A = 0.026mg/L
CCI-B = 0.26mg/L	CVD-B = 0.26mg/L
CCI-C = 2.6mg/L	CVD-C = 2.6mg/L

This section will be divided into three sub-sections. First the results of UV/visible spectroscopy will be presented. Zeta Sizer results will be shown

and eventually optical images showing the dispersion state will be presented and analysed.

3.4.2 UV/Visible results

3.4.2.1 CCI

The results in Figure 3-10 show that absorbance relates to the dispersion state of the CNTs. The noise and peaks between 190 and 199 are related to the non transparency of propan-2-ol.

The solution CCI-C was especially interesting since changes over time were clearly visible. Each curve corresponds to a measurement performed on a different day. The wave numbers of main peaks are listed in Table 3-2. As shown in Figure 3-10, 3 peaks are clearly defined. The intensity of the peaks diminished over time which showed that the additional sonication steps helped improve the dispersion. In fact after day 3 no major changes were found and all the curves were considered similar. The diminution of the background intensity was attributed to the fact that the main CNT bundles were dispersed within the first 2 cycles of sonication.

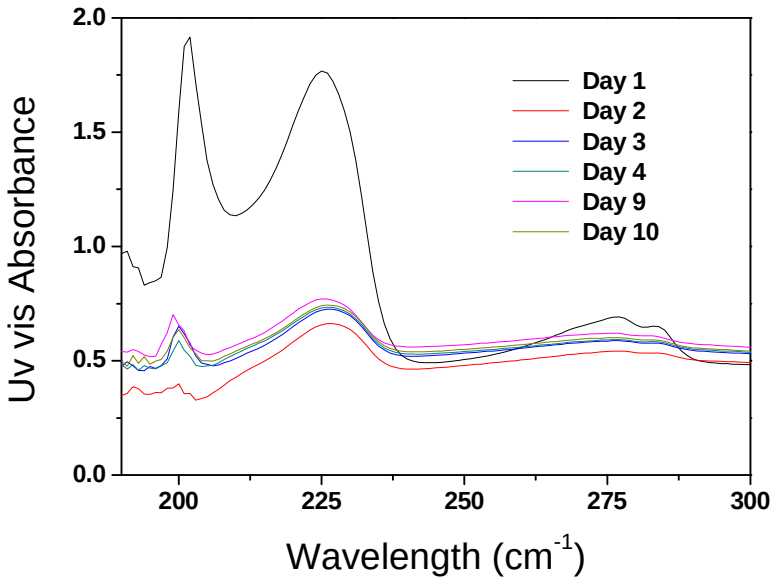

Figure 3-10 UV-visible absorption spectra for CCI CNT at 2.6 mg/L. The solution was sonicated for 30 min at 150 W (20ºC) every day for 10 days

Table 3-2 Main absorption peaks found for the CCI CNTs (2.6mg/L)

Peak number (see Figure 10)	Peak wave length
1 (propan-2-ol)	199
2 – Peak 1	225
3 – Peak 2	277
4 – Peak 3	284

At lower concentrations the peaks are still present but their amplitudes were highly diminished in proportion to the concentration drop. No shifts in the previous peak positions were found. Figure 3-11 shows that the 0.26 mg/L series follow the same trend as the 2.6 mg/L series. Absorbance at a given wavelength was found to follow a linear behaviour against concentration. A linear regression coefficient higher than 0.98 was calculated at the main peak intensity, confirming that a CNTs suspension may be considered for low concentrations as homogenous (threshold value is $\sqrt{3}/2=0.886$) and that the Beer Lambert law was considered to be valid for the CCI CNTs at low concentration (Figure 3-12).

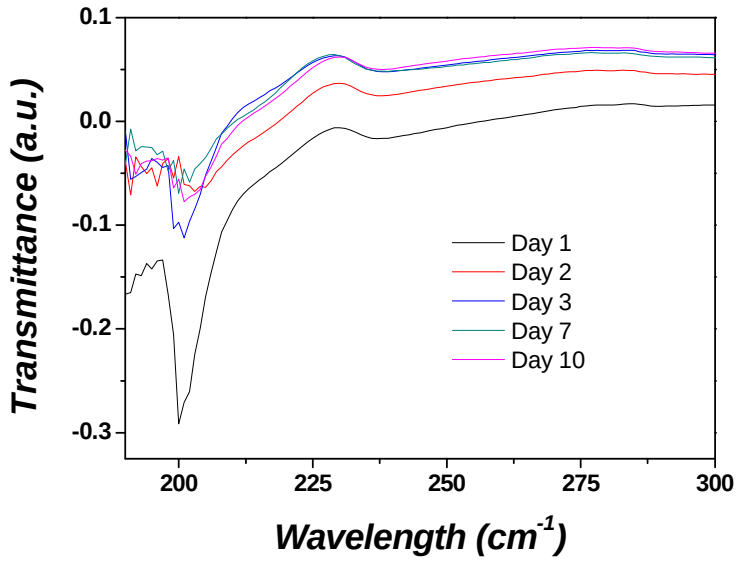

Figure 3-11 Transmittance for CCI 0.26mg/L for CCI-C

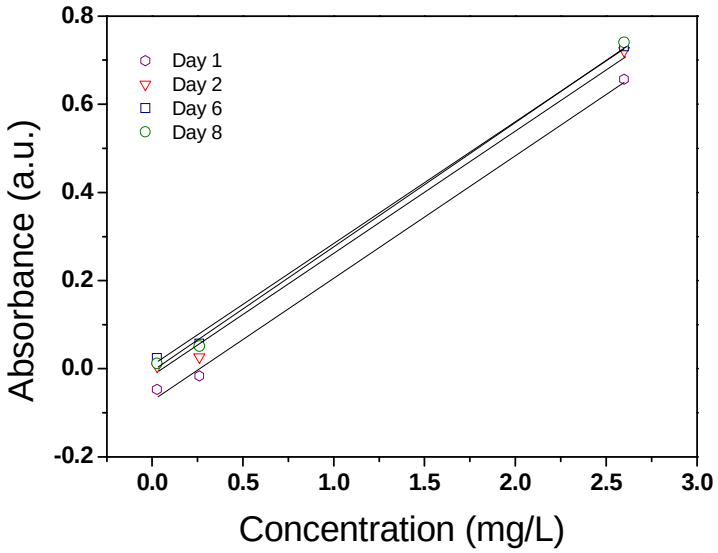

Figure 3-12 Absorption as a function of concentration for the CCI CNT solution at 20ºC at 225 cm^{-1}

It was then considered from these results that sonicating the suspension 3 times would be sufficient to obtain reproducible, well dispersed suspensions.

Unfortunately further analysis of the results to determine the bundle size from the spectra was challenging and no coherent calculation of the bundle size distribution could be obtained from these results as available theory and models [343, 344] are designed for spherical particles and not for very complex aggregates geometries such as CNTs bundles.

3.4.2.2 CVD CNT dispersion

A similar study was performed on the CVD CNT to understand better the kinetics of dispersion of the nanotubes and to improve the dispersion process to obtain a homogenous stable solution. However, here again, the reproducibility of the UV/visible spectra obtained in the same conditions as 4.2.1 could not be conclusively used for bundle size determination. This was again attributed to the large distribution in bundle sizes and the study did not continue.

Significant differences were visible between the three samples. Figure 3-13 corresponds to suspension CVD-C and was less tortuous with fewer peaks than its counterparts CVD-A and CVD-B (Appendix 1). However, because of the very high poly-dispersity of the signal and the very broad background of the spectra it was impossible to correlate the peaks to any bundle size.

This method, even if it could show qualitative difference over time was not conclusive and other characterisation methods need to be investigated.

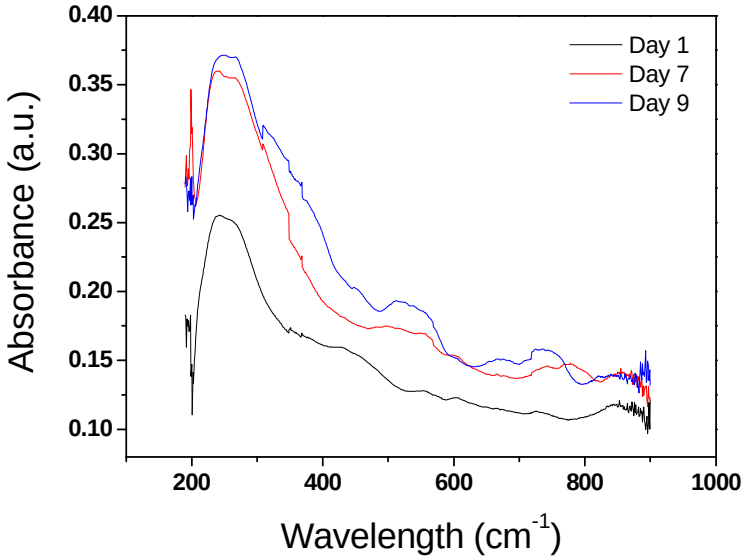

Figure 3-13 Absorbance CVD – C after 1, 7 and 9 days of sonication

3.4.3 Zeta sizer

A nanoparticle sizer was used to determine CNT bundle distribution size. Similar solutions as the one used for the UV/Visible tests were prepared and tested in a quartz cuvette. An example of the correlation function obtained for CCI CNTs is given in Figure 3-14.

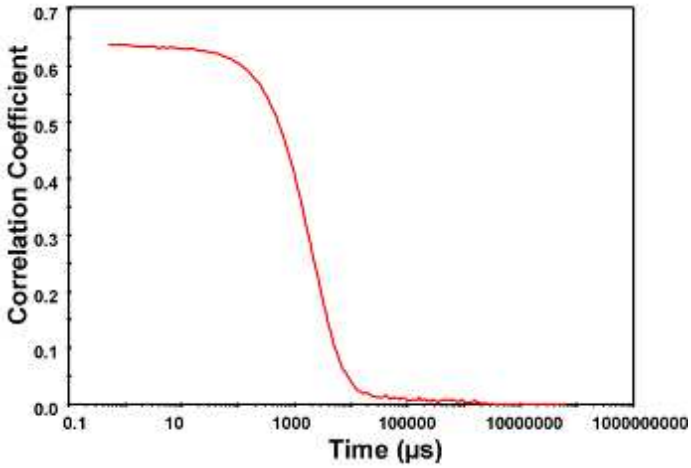

Figure 3-14 Example of correlation function for CCI CNTs at 0.26 mg/L and tested after freezing.

The bundle distribution as a function of intensity was estimated for the CCI CNTs. In fact, a quit narrow distribution was always obtained even if "visually" the suspensions looked inhomogeneous. This can be attributed to the resolution of the Zeta Sizer that cannot see particles bigger than 10 µm in diameter whereas visual observation can better recognize larger aggregates.

The same tests were performed with CVD CNTs but because of the large polydispersity of the suspension no acceptable measurements were obtained. An example of curves obtained for the CVD sample is given in Figure 3-15. The series the average bundle size tended to decrease and new peaks around 80 nm appeared which corresponded to smaller bundles of a few nanotubes similar to that reported in Figure 3-4.

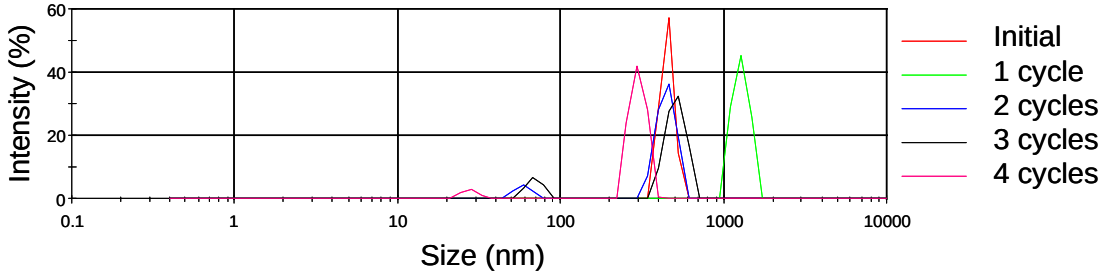

Figure 3-15 Bundle size distribution curve for the CVD-A solution

3.4.4 Visual inspection of the dispersions

As shown across this chapter optical images were good indications of the CNTs dispersion. Avoiding macro bundles in concentrated solutions was unlikely but could be minimized by processing quickly the solutions after sonication.

This was emphasized by decantation tests which were done on several batches of CNTs to show the agglomeration and bundling process. As shown in Figure 3-16, CVD CNTs tend to agglomerate very quickly even at low concentrations. Thin and long CNT bundles can be seen being formed in the solution following the slow movement of the macro bundles. These movements could be linked to Brownian motion or to thermal currents in the liquids. Slight temperature differences might lead to a gradient of temperature across the liquid causing liquid movement.

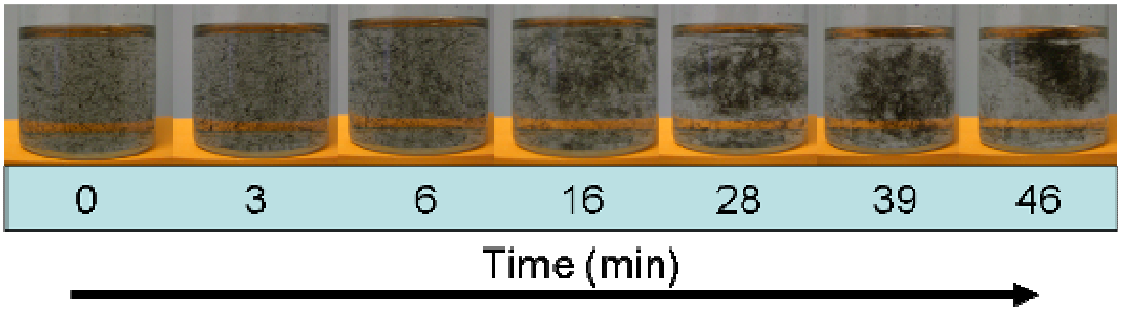

Figure 3-16 Decantation test: bundling of CVD CNTs in propan-2-ol over time, after 2 min of sonication and shaking by hand at room temperature

Furthermore, the improvement of dispersion after several sonication steps was observed more clearly by visual techniques. The size of the macro bundles visually decreased after several sonication tests leading to more homogeneous suspensions (Figure 3-17). Bundles were however still present in suspension but their number and size were drastically reduced.

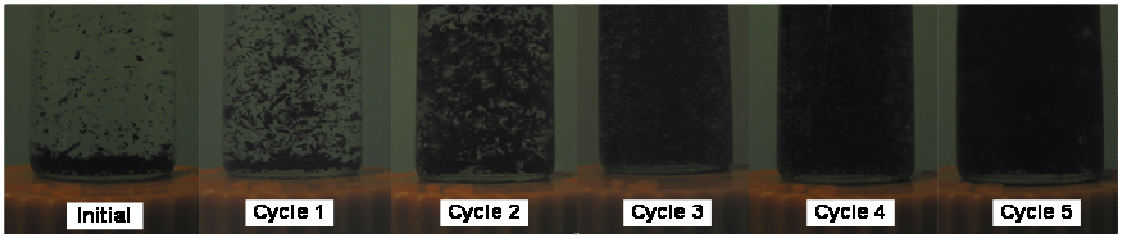

Figure 3-17 Impact of several sonication steps on the dispersion of CNTs in propan-2-ol. The images were taken within the first 2 minutes after sonication was completed; a cycle corresponds to the sonication of the solution at 150 W, 20 ºC and for 5 min

The optical analysis, a simple qualitative method, was used to assess the dispersion state of the suspension and I always performed it to guarantee optimal reproducibility.

3.4.5 Effect of temperature during sonication on the dispersion: solution freezing

Interestingly, the shape of the UV-visible curves for CCI-A and CCI-B if sonicated at higher temperature than 20 ºC were found to be much complex. Many new peaks were found on the spectra showing a larger dispersion in bundle size. This polydispersity was attributed to the increased sonication temperature. As discussed further in the next section the temperature of sonication seemed to greatly impact on the dispersion state of the CNTs. The graphs for the CCI-A and CCI-B at 40 ºC solutions are shown in Appendix 1.

The impact of the temperature of sonication was optically estimated on the CVD solutions as shown in Figure 3-18. Three different temperatures were investigated (20, 40 and 60ºC). The solutions were sonicated 30 min at 150 W every day at a consistent temperature and then tested in the UV/visible spectrophotometer. Then the suspensions were left for 23 hours at room temperature before undertaking the next day test. Upon visual inspection, it is clear from Figure 3-18 that the best dispersed and suspended CNT solution was C. The spectrum of the absorbance of CVD-C is shown in Figure 3-13. Larger bundles were visible in solution for higher sonication temperatures.

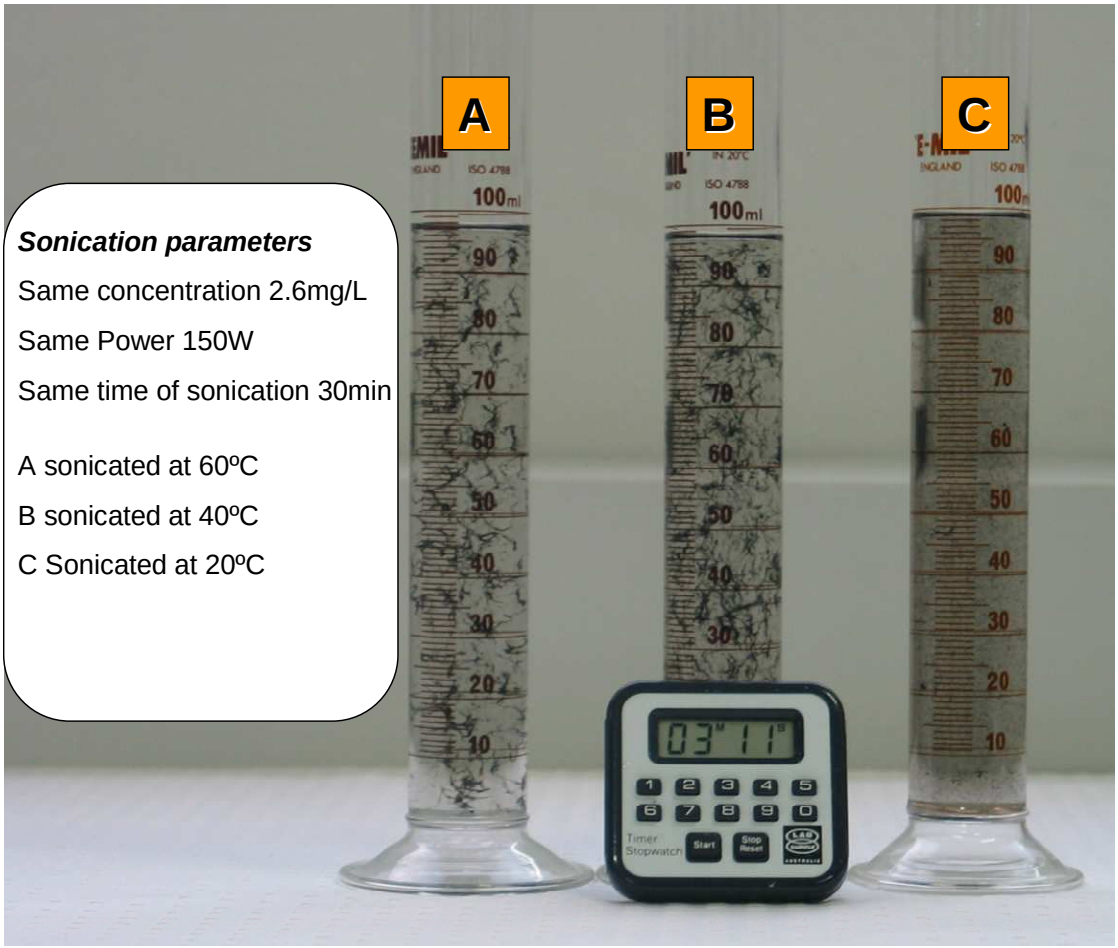

Figure 3-18 Example of CVD CNTS solutions - decantation test

This result suggested that temperature was a critical parameter in the CNT dispersion. Furthermore the shape of the macro bundles formed during the decantation of the previous solution over time was also found to be different (Figure 3-19). These looked loosely bundled and more filamentous compared to the tightly packed bundles originally seen. A video showing snapshots of a 6 h decantation test is also provided in the supplementary materials.

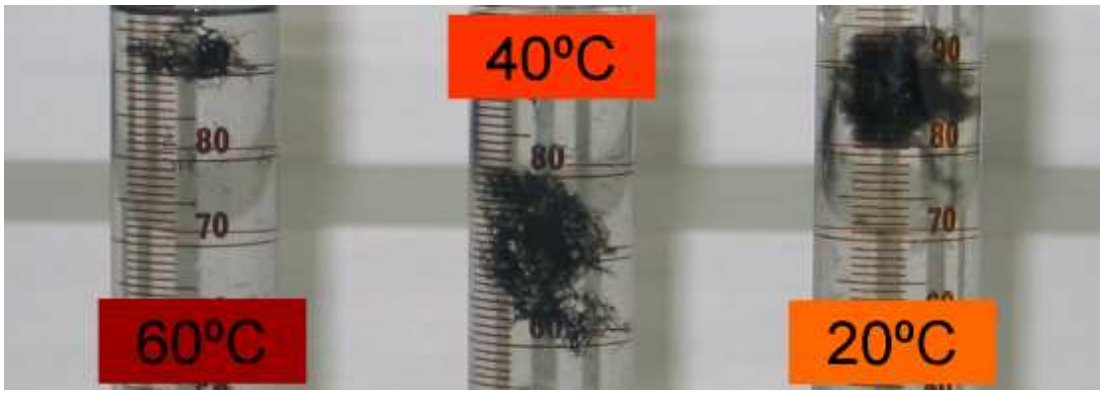

Figure 3-19 Dispersion state after sonication at 20, 40 or 60 ºC for 30 min; this picture was taken after 180 min of rest and the CNTs were fully settled into bundle structures

Following this trend, tests were performed at an initial sonication temperature of -17 ºC and under the same conditions as previously described. The temperature of the bath sonicator could not be maintained at -17 ºC for long period of time as the suspension warmed up because of the heat generated by sonication. A typical temperature time curve recorded for a sample sonicated at -17ºC is given in Figure 3-20. The temperature increased rapidly within the 5 first minutes of sonication up to 25 ºC. This likely diminished the efficiency of the low temperature sonication. For these reasons it was preferred to first “freeze” at -17 ºC the suspensions prior to sonicating them for 5 min time periods. This method appeared to be more appropriate rather than long period of sonications.

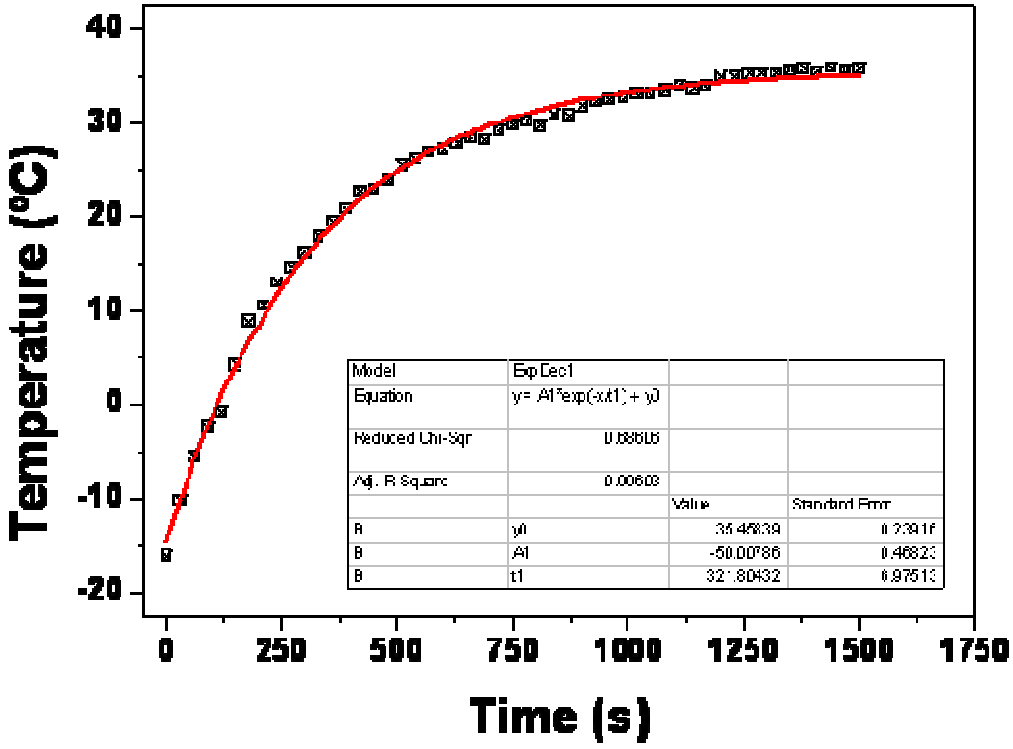

Figure 3-20 Change in sonication temperature recorded for an initial -17ºC sample at 150 W

As illustrated in Figure 3-21 the bundle distribution seemed to broaden at lower temperatures and sonication intensity with sonication time. Optical images of the suspensions after freezing are shown in Figure 3-22 correlate well this trend. The CNT bundles clearly look smaller after a few cycles. Furthermore the dispersion state at -17ºC for solutions highly concentrated (~100 mg/L) was also visually better than that of solutions sonicated at higher temperatures but macro bundles remained visible and agglomeration happened faster than at low concentration.

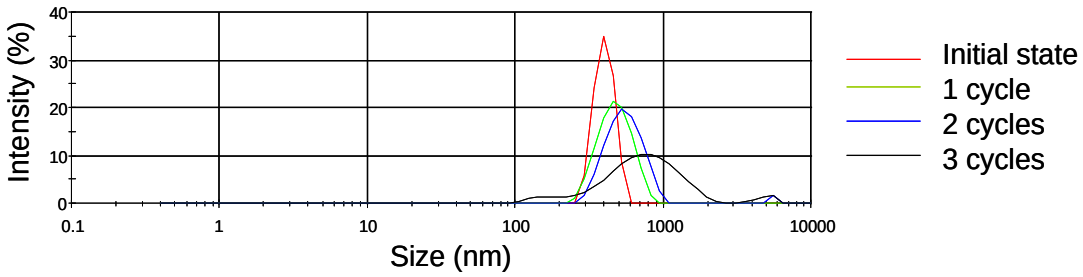

Figure 3-21 Zeta sizer CCI bundle size distribution; a cycle corresponds to the freezing of the solution followed with sonicated 150 W for 5 min; the same sample undertook 3 cycles

Figure 3-22 Improvement of the CNT dispersion after 3 freezing cycles

The origin of this behaviour was attributed to the change of the CNT/CNT and CNT/solvent interactions. A similar behaviour was reported in [345, 346] where temperature responsive polymers were used to disperse SWNTs and MWNTs. The improvement of the dispersion a lower temperature was then related to the polymer Lower Critical Solution Temperature of the polymer (LCST). Below this temperature the polymer becomes miscible in the solvent which potentially maximizes the interactions polymer/CNTs.

However, in the case of the present study the improvements were attributed to the change in the CNT/CNT interactions. Several combined and concurrent actions happening might explain this phenomenon and is developed in the following section. The first theory relies on the change in the CNT/CNT interactions as a function of temperature. The second theory is based on the temperature dependence of Brownian motion of CNT in solution and their impact on entanglement. The third theory relates to the solvent

properties and to the changes in physio-chemical properties in regard to its interactions with the CNTs and the final theory considers the role of air bubbles in the agglomeration process.

The main interactions, which are considered to rule the adhesion of CNTs, are based on the van der Walls (VdW) forces between close CNT walls [243-245, 347]. VdW forces typically include interactions between atoms, molecules and surfaces. They are composed of 4 terms, the importance of which varies greatly according to the materials polarity and electrostatic properties. The terms are namely, (i) repulsive component derived from the Pauli exclusion principle which prevents the collapse of molecules, (ii) attractive or repulsive electrostatic interactions between permanent charges or dipoles (known as the Keesom force), (iii) induction or polarization which is known as the Debye force and (iv) dispersion forces known as London forces which arise from the interactions between non-polar multi-poles [244]. These interactions are typically derivated from the Lennard Jones Potential (LJP) which is used to approximate the isotropic part of the VdW forces [348, 349], corresponding in the previous list to both attractive and repulsive terms as a function of the distance between the bodies. As CNTs are commonly considered to be non-polar [350, 351] and slightly negatively charged [176, 259] due to the curvature of their graphene walls, approximating the CNT/CNT interactions by only London and Keesom's forces has been considered as a simple and still accurate way to describe their interactions [347, 352-354]. Recent work on the polymerisation of low molecular weight alkenes was carried out to include a temperature dependence parameter in the LJP [348] in order to explain the deviation of some thermo-physical and thermo-chemical properties when compared with predicted values. Their model showed better agreement with experimental values of potentials. It is possible that the CNTs bundling kinetics and the interactions between the CNTs in solution are also temperature related since CNTs have a graphene based structure.

Furthermore, the movements of CNTs at low concentrations in solutions have been shown to be related to Brownian motion [242, 355-357], corresponding to the apparent random movement of particles in a fluid. The diffusion coefficient of particles D as defined by equation 1 is directly

proportional to temperature which shows that a decrease in temperature will reduce their diffusion and tend to stabilize the suspension. This might reduce the possibility for entanglement. The increased contacts and movements of and between the CNTs at higher temperatures may explain the fact that bundles were harder to break up and separate.

$$D = \frac{k_B T}{b} \qquad (3\text{-}1)$$

Where k_B is the Boltzmann constant, T the absolute temperature in K and b the linear drag coefficient on the particle from Stokes/low Reynolds regime.

A temperature drop will also affect the solvent properties. Viscosity especially will increase inversely as a function of temperature which could help, as in the case of the viscous media used to disperse the CCI CNT, break up bundles. A decrease of temperature from 20 ºC to -17 ºC will increase the propan-2-ol viscosity by 7.5 times (Figure 3-23). The propan-2-ol needs to be removed from between the CNTs in order for them to bundle. At low temperature, if this removal is slowed because of higher viscosity, there may be sufficient time for the sonication to be efficient and to separate the CNTs before they have the time to further bundle. The dielectric constant and the solubility parameter of the solvent would also be changed which would likely affect the CNT/solvent and CNT/CNT interactions.

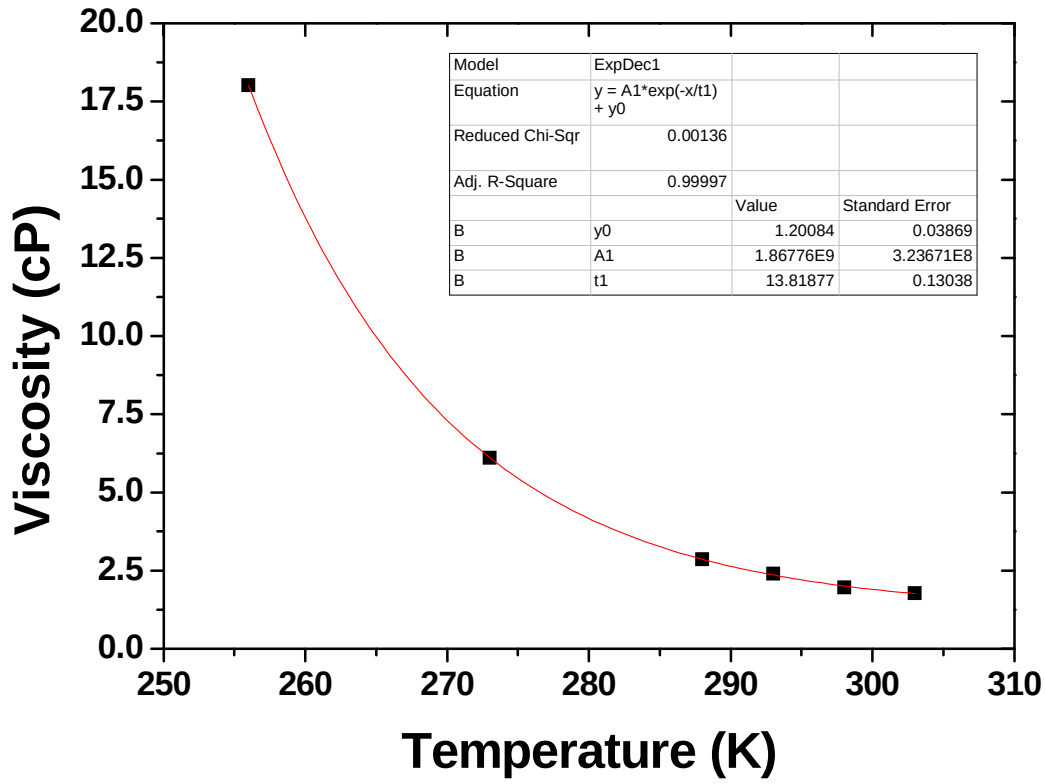

Figure 3-23 Propan-2-ol viscosity as a function of temperature, data from Handbook of Chemistry and Physics 63rd Edition CRC press

Finally the presence of air bubbles between the CNTs was shown in literature [358] as well as in Appendix 1 and degassing of the solution was found to help the initial dispersion step. It is possible that remaining air bubbles and that air dissolving in the solvent help the formation of the bundles. Air bubbles have been shown to stick to hydrophobic surfaces and to help the adhesion of hydrophobic bodies [359-362] and to lower heat transfer by insulating the hydrophobic surfaces from the bulk fluid in contact [363]. E-SEM pictures (Appendix 1) show the formation of arches between water bubbles and the CNT BP surface on large scales (20 to 50 µm). This confirmed that air was present and possibly entrapped between the BP and the water. Furthermore, the diameters of CNTs trapped in water nano-bubbles and visible by transparency were measured in an E-SEM saturated with water vapor. An increase of 12 to 16 % of the diameter was found, which corresponded to a 3.5 nm air thickness on the CNT surface. This value correlated well with reported values of thin air layers on hydrophobic surfaces of 5 to 15 nm [364].

3.5 Dispersion protocol chosen for this study

The following protocol was established that related sonication to the damage of the CNTs when made into BP:

1) Dispersion of ~50 mg into 1L of 99.99% pure propan-2-ol
2) Freezing at -17.5ºC in the freezer
3) Sonication in a bath sonicator at 150 W and for 5 min
4) Steps 2 and 3 repeated up to 5 times
5) Storage of the solution in the freezer until next use

If stored for more than a week the suspensions were re-sonicated once and shaken by hand until reasonable visual dispersion was obtained.

3.6 Self-supporting Bucky-paper processing

The CNT BP membranes were processed by vacuum filtration of the CNTs dispersed in 99.8% analytical grade propan-2-ol [280] following the previous dispersion protocol. Once homogeneous dispersions were achieved, the solutions were filtered under vacuum (dP= -95 kPa) on a 47 mm diameter Millipore filtration unit. The solution was stirred at low speed to reduce bundling formation and to homogenize the CNT distribution. The CNTs were typically filtered onto a poly(ether sulphone) (PES) 0.2 μm-pore size Millipore membrane which was found to be an adequate substrate to peal off the BP to form a self-supporting membrane. The thickness of the BP was controlled by the concentration of the solution and BPs were generally between 30 and 50 μm. Processing BPs thicker than 200-300 μm revealed to be challenging as the compaction of the CNT cake became non-homogenous. The filtration time increased exponentially with desired BP thickness (Figure 3-24). The samples were eventually vacuum-dried in an oven at temperatures between 40 and 60ºC for 2 to 8 hours.

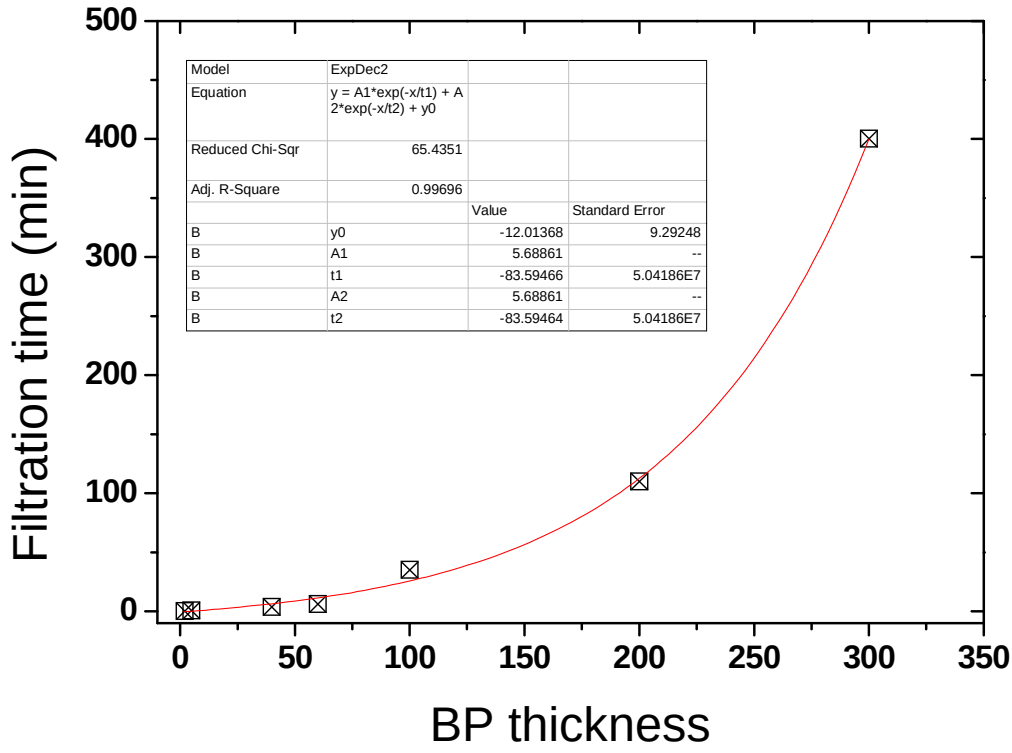

Figure 3-24 BP thickness filtration time dependence

The filtration procedure is described in Figure 3-25 and pictures of the Millipore filtration and of the stirring device are shown in Figure 3-26.

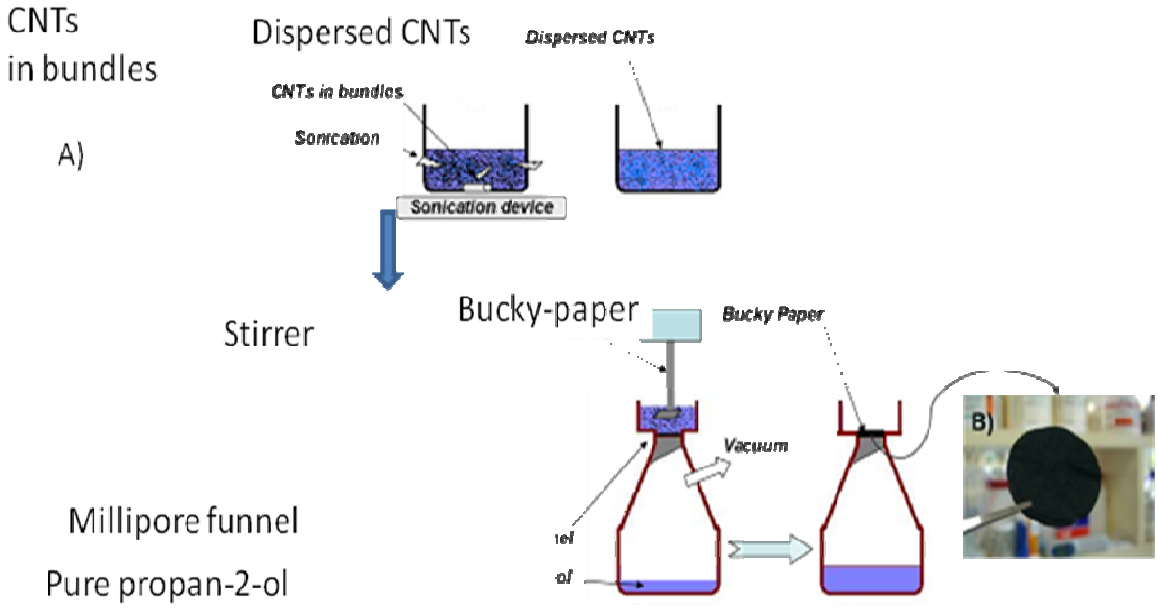

Figure 3-25 A) BP fabrication process; B) Optical image of a self-supporting BP

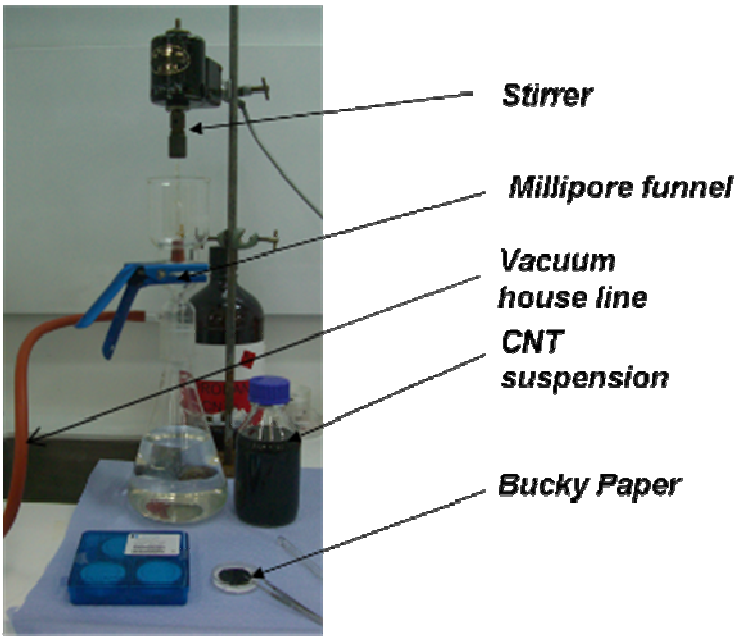

Figure 3-26 Filtration setup

3.7 Conclusions

CNTs have strong affinity for each other, in most solvents. This affinity is associated with the CNTs acting to minimise their interfacial contact to the solvent and reduce their surface energy. Retaining the original CNTs properties while processing well dispersed suspensions of CNTs that were stable over time revealed to be challenging. The suspensions were found to be stable for short period of times (a few minutes) which was found satisfactory since in the time frame of the BP processing. A homogeneous CNT dispersion method that offered stability over the filtration time and that did not induce too much damage on the CNTs was established. This protocol was followed for the preparation of the self-supporting BPs and of the substrate for the BP used in various composite material structures. This step was critical to obtain reproducible and systematic processing of self-supporting BPs.

The temperature dependence of CNT dispersion is a new feature of CNT colloidal behaviour and was not previously reported in the literature. The role of air bubble formation on and between the CNTs during sonication would need to be investigated as it might explain some of the difficulties encountered to efficiently suspend them in solution. Furthermore this temperature dependence behaviour was attributed to several factors and it is likely that a combination of those happen simultaneously to improve dispersion. First, the Van der Waals energy between CNTs is reduced at lower temperatures. This was proposed to explain part of the natural adhesion properties of the CNTs. However, as shown through this chapter, entanglement is a dynamic process and individual CNT movement, due to Brownian motion in solution might also be part of the bundling kinetics. As Brownian motion is temperature dependant, a decrease of the temperature would explain the change in solubility thus possibly reducing collisions and contacts between CNTs. This could possibly explain the least entanglement and better suspension stability at lower temperatures. Finally, as the viscosity of the propan-2-ol, the main solvent used in this study, does sharply increase between room temperature and -17ºC it is possible that shearing forces were

increased, as it is the case on the CCI poly(saccharide) pre treatments, thus helping the dispersion of the CNTs.

More work to better understand these phenomena would be required to explain the dispersion phenomena but this did not unfortunately fit into the scope of this work. Studying the role of the air trapped on the cavitation forces during sonication, as well as the VdW interactions of CNT in solution might be ways to better understand this behaviour.

Chapter 4

4 PVDF, PTFE and self-supporting Bucky-paper membranes for Direct Contact Membrane Distillation: preliminary tests and benchmarks

Hydrophobicity, porosity and thermal conductivity are the three main properties that an appropriate membrane must possess to be efficiently used in DCMD. Several materials, including organic and inorganic materials, were shown to be suitable for DCMD.

This chapter presents the work done on pure carbon nanotube membranes. The self-supporting membranes were characterised and used as a starting point for the study of the composite membranes presented in the next chapters.

The work was partially presented at the Australian Water Association summit on Advanced Membrane Materials in February 2009 (oral presentation in plenary session), at the International Congress on Membranes 2008 (ICOM08 in Honolulu - Hawaii, USA) (poster presentation) at the 1st Student symposium of Victoria University and partially published into the Journal of Membrane Science under [75].

4.1 Introduction

As described in Chapter 1 the flux across a membrane is dependant on geometrical and surface energy parameters and can be summarized as follows:

- the membrane must be porous and hydrophobic (wetting criteria)
- the pores must be tight enough so that the Liquid Entry Pressure (LEP) of the membrane is higher than the stream pressure (or the total pressure applied to the membrane) to avoid wetting
- the pores must large enough to offer minimal resistance to the vapor flux (Knüdsen diffusion)
- the thickness of the membrane must be small to minimize the vapor diffusion total path length (Knüdsen)

Amongst the materials available, two polymers, PVDF and PTFE, were shown in literature to be appropriate materials for MD membranes. To set up a benchmark the rig was tested with several commercial membranes at a series of feed and permeate temperatures and flow rates. The structure and properties of macro-structures made only of CNTs were challenging to characterize due to the large range of features composing their morphology: complementary techniques had to be adapted from a nano up to a macro field of view. CNTs in a BPs are held together solely by Van der Waals forces and by their entanglement creating a non-woven like structure. Little work has been published on the practical use of CNT macro-structures made of purely nanotubes (c.f. Chapter 1) and there is a real need to demonstrate their potential and limits to fully comprehend where this technology can lead us.

This Chapter will demonstrate, as a proof of concept, that BP can be efficiently used as membranes. Material characterisation results, required to analyse the behaviour and performance of self-supporting BPs are be presented along with direct contact membrane distillation tests carried out on the self-supporting membranes to underline the BP potential and show where research should be heading.

4.2 Membranes characterisation

4.2.1 Bucky-paper morphology

BP membranes are essentially mats of randomly entangled CNTs. Long and thin CNTs were preferred to bring more strength to the final non-woven membrane while being flexible enough to entangled and form a 3D network. The morphology was clearly discerned from SEM images of the surface, such as in Figure 4-1A and 1B, and of cross-sections milled by Focused Ion Beam (FIB), as presented in Figure 4-1C. Furthermore the cross-sectional images showed that the CNTs tend to form a layered structure with very few CNTs aligned perpendicular to the surface offering an off-plane angle of a few degrees only. The surface was relatively smooth with roughness ranging from a few hundred nanometres to a few micrometers, as visible in Figure 4-1A and presented in Appendix 3. Thanks to the well dispersed CNT suspensions, the membrane surface and cross section were uniform and free from large CNT-bundles [365]. Small bundles made of a few CNTs were however sometimes visible on the surface.

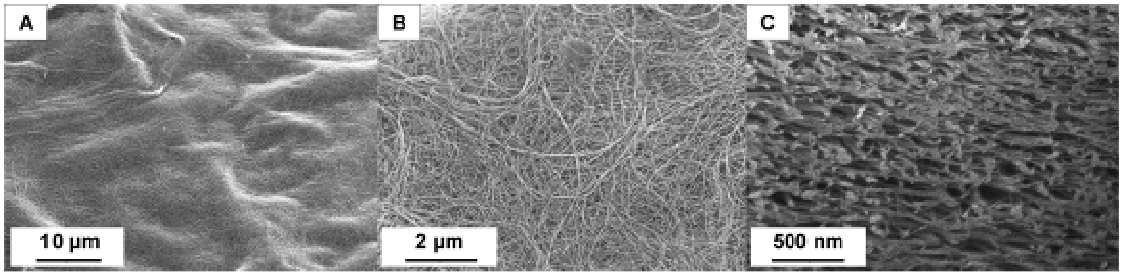

Figure 4-1 SEM images of (A), (B) the BP membrane surface (tilt 52º and 0º respectively), (C) a cross section milled using the focused ion beam (tilt 52º)

As shown in Figure 4-2 large pore morphology differences were visible between PTFE and PVDF membranes. The pore shapes are quite different and are revealed by FIB SEM (top inserts). Membranes made of PVDF and PTFE presented different aspects and features but were both in essence highly porous and hydrophobic thus perfectly fitting MD requirements and

therefore were used as a benchmark in this work to compare with the BPs. The main features and properties of the PVDF and PTFE membranes, such as hydrophobicity, pore size or porosity, were investigated and are presented in Appendix 3.

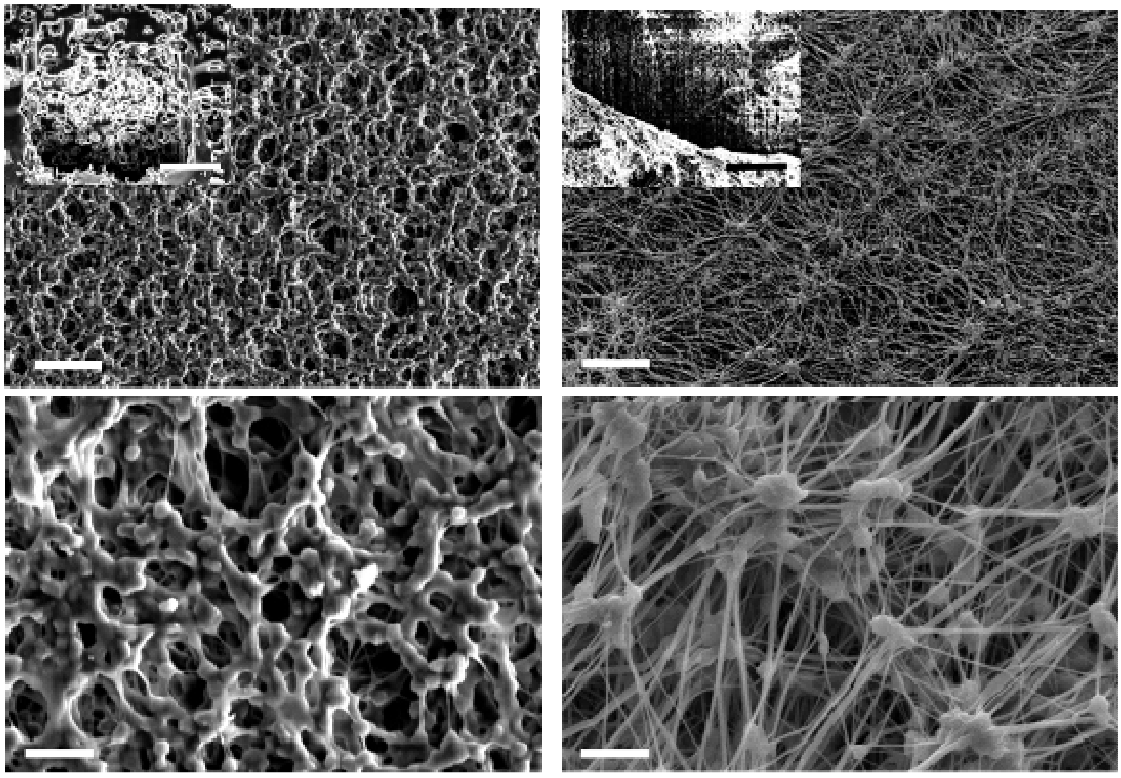

Figure 4-2 Morphology of left: PVDF, right: PTFE. The scale bars of the top images represent 600 nm while the one of the bottom images represent 200 nm

4.2.2 Pore size distribution

4.2.2.1 SEM analysis

Mixtures of CNTs, CCI and CVD, at 10 different mass ratios were prepared (Table 4-1 and Appendix 2). As the CCI CNTs were thicker than the CVD this mass ratio obviously does not represent well the number distribution between each kind of CNTs. The CVD CNTs were obviously more numerous in the case of the CCI50 for example. Mixing the two kinds of CNTs was challenging as both had different bundling kinetics but long stirring times at

low room temperatures and freezing lead to homogeneous dispersions. The analysis of the surface pores showed that the average pore size could be tuned by mixing CNTs of different diameters together. Figure 4-3 shows the macroscopic differences visible under SEM for three samples, CVD100, CCI50 and CCI100. The increase of pore size over the series is clearly visible. It seems however that the CNT dispersion was not completely homogeneous as small bundles of CNTs can be found. In the case of the very low mass ratio of CCI CNTs, the first three samples (CVD100, CCI10 and CCI20) were very similar (Table 4-1). The whole trend was, however, interesting and demonstrated an easy way to tune finely the membrane surface pore size. The average pore size for each series is given in Table 4-1 and examples of the image analysis are shown in Appendix 2. The average pore size was found to increase with the content of CCI CNTs, which was attributed to their larger diameters. As diameter increases packing becomes less efficient and larger interstitial gaps were found.

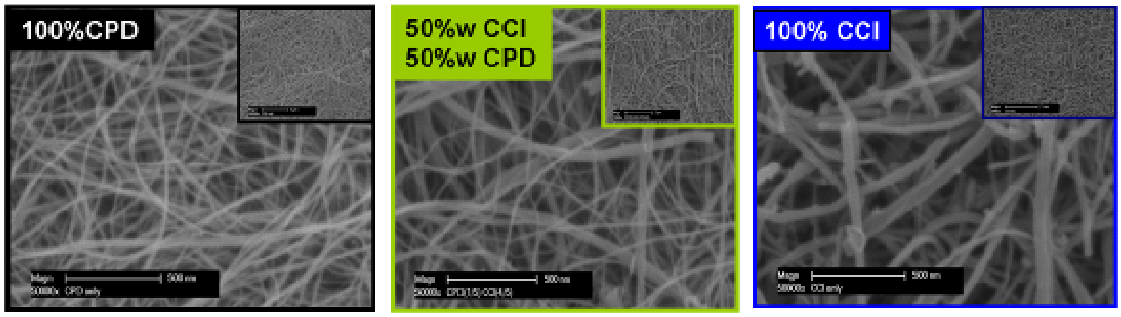

Figure 4-3 SEM images of BPs composed of different CNTs types and mix ratios. Left 100% CVD. Middle 50%CCI / 50% CVD. Right 100% CCI

SEM images were used to determine the surface apparent pore size distribution. However as this technique is not representative of the inner membrane structure, particle size exclusion tests were carried out to measure a size cut off while pore size distributions were evaluated by porometry. Series of BP made of solely CVD or CCI CNTs, or of mixtures of the two, were processed and analysed. Minimum, mean and maximum average pore size distributions as well as pore sphericity and pore surface area were determined by SEM analysis (Table 4-1, Figure 4-4 and Appendix 3). For each pore, three different dimensions were calculated corresponding to the

average minimum, mean and maximum dimensions. Several parameters such as sphericity or aspect ratio were calculated using these dimensions.

In the case of the CVD CNT BPs an average pore size of ~22 nm was found with ~95% of the pores falling below 73 nm. As shown in Figure 4-4 the pore size distribution for a CVD membrane was very narrow and more than 75% of the pores were between 15 and 55 nm. Very little differences were sometimes found between the three pore sizes calculated (average, maximum @95% and maximum at 75%), which will be confirmed by the sphericity calculation showing that the pores had homogeneous dimensions. This is critical, as for a given pore area the pore geometry can vary greatly. For example long thin pores will have a different behaviour to wetting than smaller round pores of the same pore area. The CVD CNT BP offered a more homogeneous and less broad pore size distribution over the CCI CNTs as shown in Figure 4-5.

Table 4-1 BP mean pore size and sample names. The three main samples studied are in bold

Sample name	CCI content	Average pore size	Max pore size @ 95%	Max pore size @ 75%
	%	nm	nm	nm
CVD100	**0**	**22**	**73**	**46**
CCI10	10	21	69	38
CCI20	20	29	73	42
CCI40	40	52	155	81
CCI50	**50**	**55**	**146**	**83**
CCI60	60	62	155	99
CCI80	80	63	176	105
CCI100	**100**	**68**	**190**	**110**

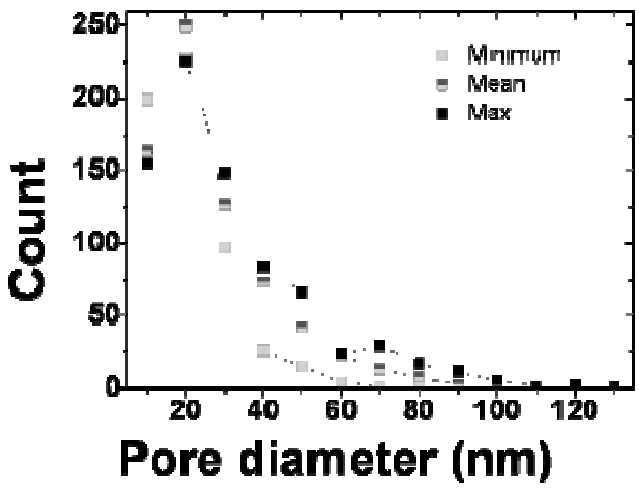

Figure 4-4 Pore size distribution of a CVD CNT BP membrane as determined by SEM imaging of the surface

As shown in Figure 4-5 the Feret's maximum pore size of the CVD100, CCI50 and CCI100 were respectively of 75, 170 and 270 nm. As the performance of the membrane, such as the permeance and the Liquid Entry Pressure (LEP) are directly related to the maximum pore size, controlling the pore size distribution was critical.

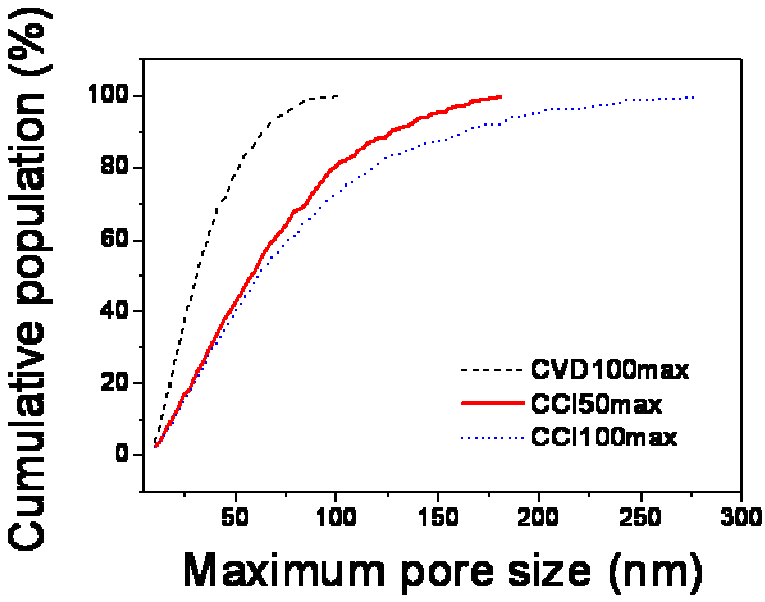

Figure 4-5 Maximum pore size determined by Feret analysis on a pure CVD CNT BP, a 50/50 CVD/CCI CNTs and a pure CCI CNT

The aspect ratio of the pores, defined as the ratio of the maximum Feret's and the minimum Feret's pore size were calculated and found to be

close to 1.8 on average for all the samples regardless of the CCI content. As, an ideal circular pore would have an aspect ratio of 1, these values indicate that the pores are not spherical but may be elliptical where the ratio of the two main diameters was about 2 (Figure 4-6). This correlates with Figure 4-3 where the pores of the different membranes presented the same geometry. The sphericity of the pores, which corresponds to the relative ratio of the maximum and minimum Feret pore size, was always found to be around 0.3 thus emphasizing the polygonal nature of the pores as opposite to a perfect pore that should exhibit sphericity of 1. It was however assumed in order to simplify calculations in the following sections that pores were cylindrical and the average mean pore size determined by this method was used. These values gave the best fit if compared with values calculated from the other diameters (minimum and maximum).

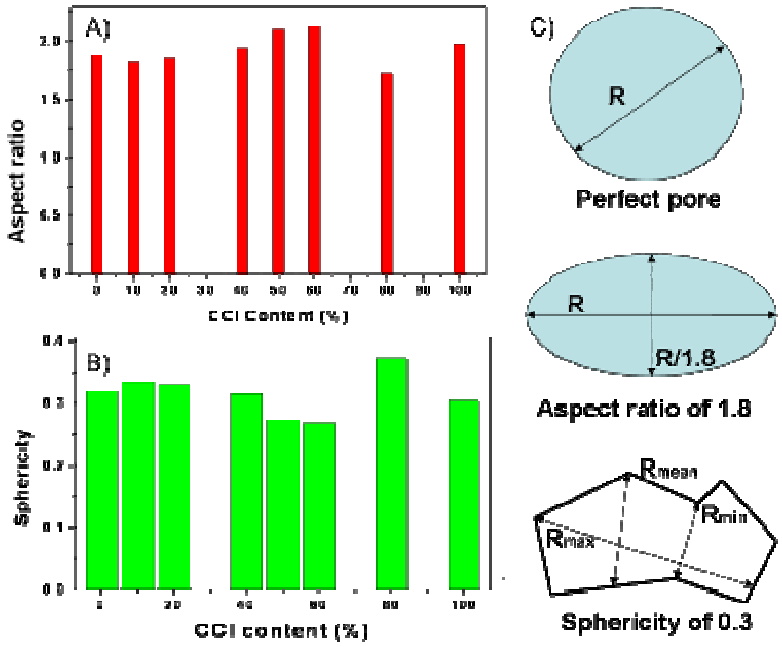

Figure 4-6 (A) Aspect ratio, (B) sphericity of the pores for the different ratios of CCI CNTs and (C) pore geometry related to the aspect ratio and sphericity for the same surface area

4.2.2.2 Latex beads filtration

Latex beads were filtered through CVD CNT BP. A cut off value comprised between 50 and 500 nm was found as shown in Figure 4-7. This

correlated well with the 20 to 50 nm average mean pore size determined by SEM analysis for the same sample where 75% of the pores felt. Bovine Serum Albumin (BSA) completely passed through the membrane while latex beads (50, 100 and 500) were all partially or fully rejected.

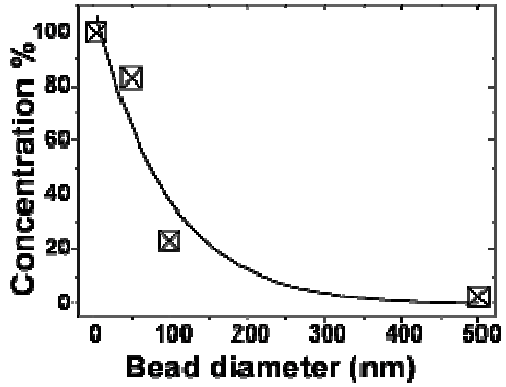

Figure 4-7 Pore size selectivity determined from particle exclusion tests

Gold colloids (5 nm) were also used and filtered through the BPs. Curiously their rejection was higher than that of the 20 nm and 50 nm latex particles. This was attributed to the high adhesion forces between metals and CNTs. Furthermore, SEM images of the BPs after testing showed that gold aggregates had formed at the surface of the BP.

The fact that these pores were polygonal and that they can be modelled as ellipse has an important impact on this series of test. This means that the particle selectivity will tend to show the minimum dimension of the ellipse only and therefore other characterisation methods were sourced. This preliminary study was very useful to get an insight of the BP pore size and shape but was not satisfactory since it only showed either the pore surface (SEM) or gave us only a very broad idea of the pore size distribution (beads). As reported later in the following sections perm-porometry was used and allowed us to test a larger number of samples in a shorter time while also being a more accurate technique to obtain the pore size distribution.

4.2.2.3 Perm-porometry

Eventually perm-porometry was also carried out on the CNT BPs. An average pore size of 33 nm was found in a wet-up / dry-up setup. Galwick was used as the wetting media while dried air was used to obtain the dry curve. The Galwick wicked very well into the pores and was well suited for these tests. The wet sample was exposed to a gradient of pressure whereby the pores were gradually discharged of Galwick in accordance to their diameter. Then pure nitrogen was passed through the membrane under the same gradient and the dry curve obtained. Both bubble point and pore size distribution were determined and are shown in Figure 4-8. The pressure varied between 500 and 3500 kPa and the membrane surface area was 2.46 cm^2. An example of wet-up/dry-up curves are shown in Appendix 2. The average pore size of the CVD BP was found to be 31.8 nm for a bubble point pressure at 779 kPa. The data were average over 3 samples.

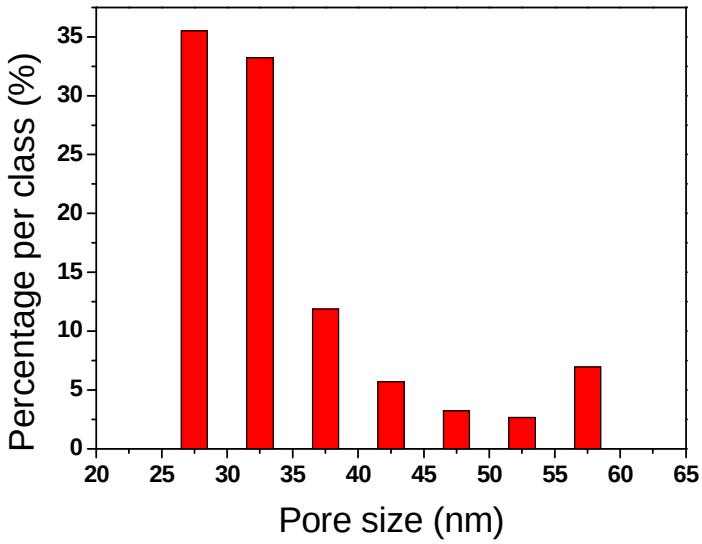

Figure 4-8 Pore size distribution for self-supporting BP obtained by porometry in wet-up/dry-up mode. Galwick was used as wetting liquid

Examples of pore size distribution obtained for the PTFE-P002, PTFE-02, PTFE-P045 and PTFE-M1 measured with a porometer are given in Figure 4-9. Large variations with the manufacturer data were found for both PTFE-P002 and PTFE-M-1, while the other membranes showed pore size closer to the manufacturer data.

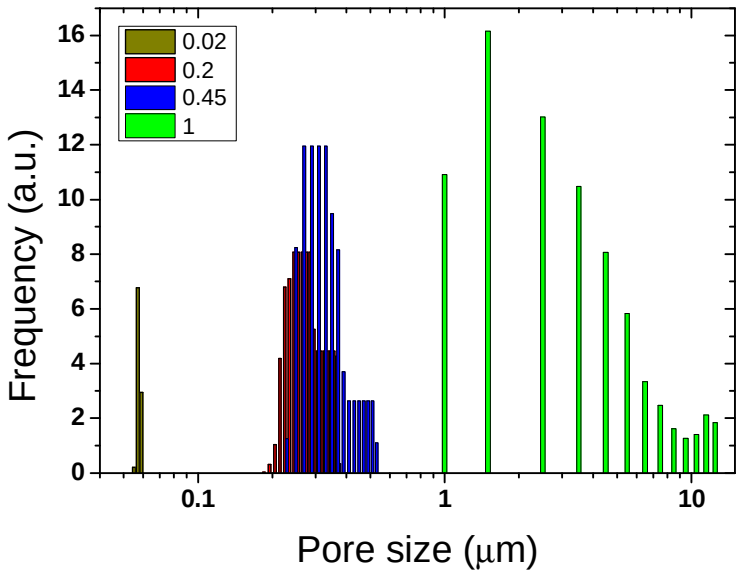

Figure 4-9 Porometer pore size distribution for 4 PTFE membranes; the nominal pore size are respectively 0.02, 0.2, 0.45 and 1 μm

4.2.3 Porosity

Both liquid and helium pycnometer tests indicated porosity comprised between 88 and 92%. Furthermore to reveal the porosity of the BPs a thin 100 nm thick membrane was filtered onto a TEM copper grid and images were taken at different tilts (from 35º to 155º) to show the spaces between the CNTs. The sample was prepared with CVD CNTs in a similar manner as that was generally used to make BPs. The concentration of the suspensions was however lower to be able forming a very thin layer of CNTs at the surface of the porous grid. A video made with these pictures can be found in the supplementary materials and reveals the spaces between the CNTs. This very large porosity was undoubtedly an advantage for DCMD as it offered a larger surface of exchange between the air-gap and the water meniscus.

4.2.4 Thickness

The surface of a CVD CNT BP was mapped with an Altisurf to reveal the homogeneity of the thickness. Strips of samples were cut and stuck on a double side carbon sticky tape, which was stuck on a glass slide for level reference. As shown in Figure 4-10 the profile of the section was clearly

visible and macro-bundles of CNTs, were issues for the CCI CNTs as shown on the top graph. The CVD CNTS offered a much smoother surface that was more compatible with membrane processing (bottom graph). Variations of a few microns were found on average over the tests but the surfaces were generally found to be very even. The main issue with this method was the sample preparation as the BP must not be squeezed or damage and must be correctly place on the tape to avoid misreading. Tests performed on poorly dispersed CNTs could show the presence of large bundles as shown in the top graph in Figure 4-10.

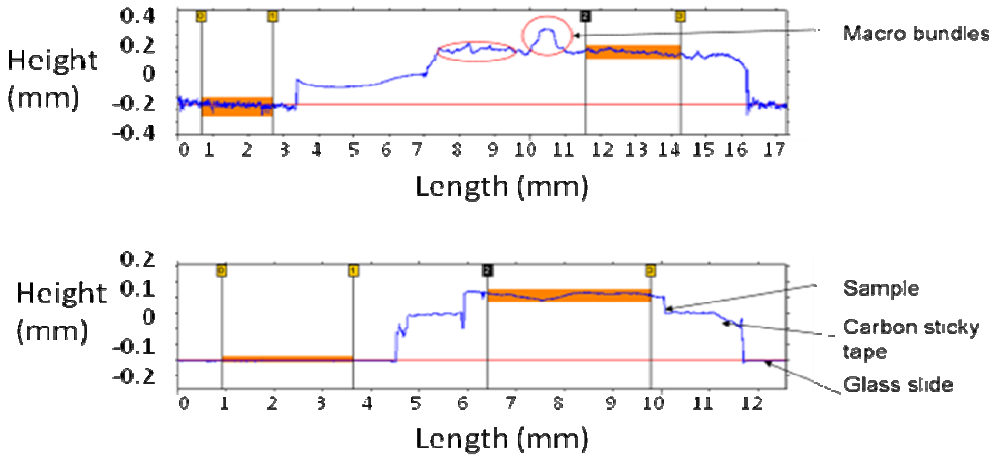

Figure 4-10 Altisurf thickness measurements. Top: CCI CNT BP; Bottom CVD CNT BP

As shown in Figure 4-11 a sample laid across a piece of carbon tape (blue and dark blue) had a very even thickness across all its entire surface. A small bump is visible on the top right of the image and this was an artefact due to one side of the sample not being stuck on the carbon sticky tape support.

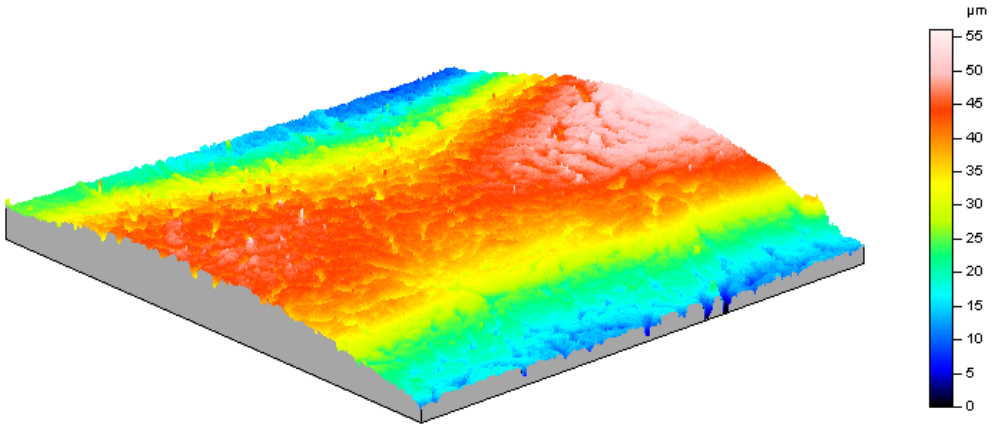

Figure 4-11 Altisurf thickness mapping – blue and dark are the lowest profiles, while red and white show the highest profiles

4.2.5 Specific surface area

Nitrogen adsorption was used to calculate the specific surface area by the BET method and tests were performed on both CNT types. The dispersity in values measured varied considerably depending on the samples tested but an average specific surface area of 197 m^2/g and 36 m^2/g were respectively found for both CVD and CCI BP. The measurement of the BET specific surface area also requires a very precise measure of the mass of the sample as well as making sure that the sample is properly degassed before saturating its surface with N_2. For these reasons the scattering of the BET reported values in Table 4-2 is not abnormal and could be related to the CNTs dimensions.

Table 4-2 BET values from literature and our group

Group	Growth method	*Walls*	*Inner diameter*	*Outer diameter*	*Specific surface area*
			nm	nm	m2/g
Muramatsu et al. [366]	HiPCO	1	-	1.01-1.26	642.0
Cinke et al. [229]	HiPco raw (Fe22%w)	1	-	0.93-1.35	577.0
Cinke et al. [229]	HiPco step1 (Fe0.4%w)	1	-	-	968.0
Cinke et al. [229]	HiPco step2	1	-	-	1,587.0
Muramatsu et al. [281]	CCVD	2	0.74-0.87	1.41-1.56	569.0
Inoue et al. [367]	-	-	4.00	10 (+/-2)	268.0
Smajda et al. [102]	CCVD	-	3 - 6	15-25	197.7
CSIRO - CVD	CCVD	6	5	9 (+/-1)	197.1
CSIRO - CCI	CCI	40	4-6	40	36
Onyestyak et al. [368]	Acetylene decomposition	7--8	4.2	9.4 (+/-3)	130-250
Cooper et al. [369]	laser ablation		1--10	10--100	350-450

As shown in Figure 4-12, the average BET specific surface area of the membrane decreases as an inverse exponential with the number of walls (data taken from references in Table 4-2 and our own measurements). This directly relates to the outer diameter of the CNTs as less surface area per gram of CNTs is available for thicker nanotubes. Impurities present on the CNTs [229] will also affect the BET surface area, and might decrease by more than 50 %. Our CNTs were naturally fairly pure as demonstrated by BET and did not require any acid treatment to remove amorphous carbons or iron catalysts.

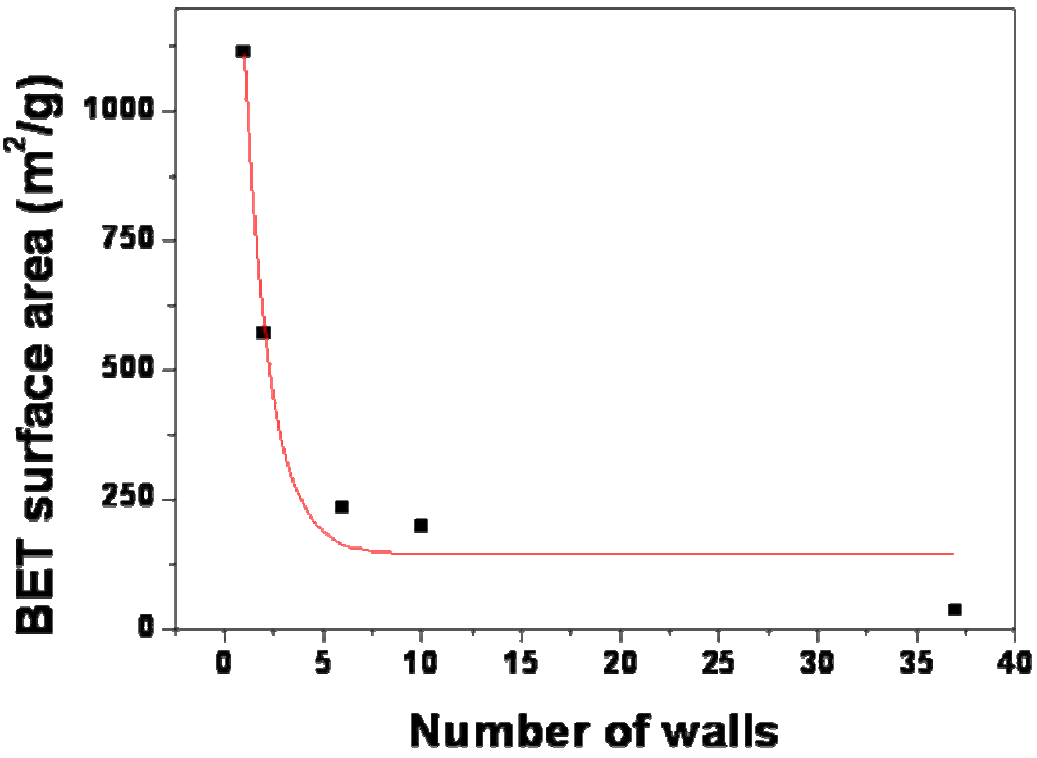

Figure 4-12 BET surface area as a function of the wall number for the different CNTs in Table 4-2

4.2.6 Contact angle

Contact angle tests were carried out with deionised water on BP membranes made of CVD CNTs exhibited a high contact angle of ~120 º (+/- 7 º) while the CCI CNT BPs exhibited a lower contact angle of 110 º +/- 5 º. The increase was slight but is noticeable in Figure 4-13. Dynamic wetting tests showed that water wicked faster in the case of the CCI CNT BP. A change of ~30% of the volume droplet was found to occur over 30 min of tests.

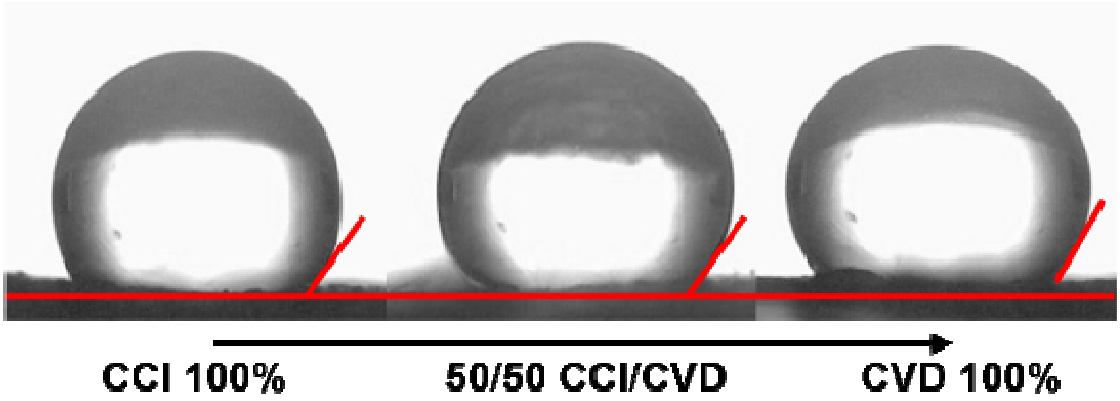

Figure 4-13 Deionised water contact angle on BPs. Left: 100% CCI; middle 50/50 CCI/CVD and right 100% CVD.

Furthermore, micrographs were taken in an E-SEM with water vapor saturated atmosphere to ratify of the hydrophobic nature of the BPs (Figure 4-14). Vapor at too high vapor pressure (above 0.3 kPa) was shown to progressively condense on the CNT BPs despite their clearly hydrophobic nature (droplet insert in top right Figure 4-14). Arches formed, as shown in Figure 4-15, to minimize the surface of contact between the water and the CNTs. These results confirmed the hydrophobic nature of the CNTs at the nanoscale.

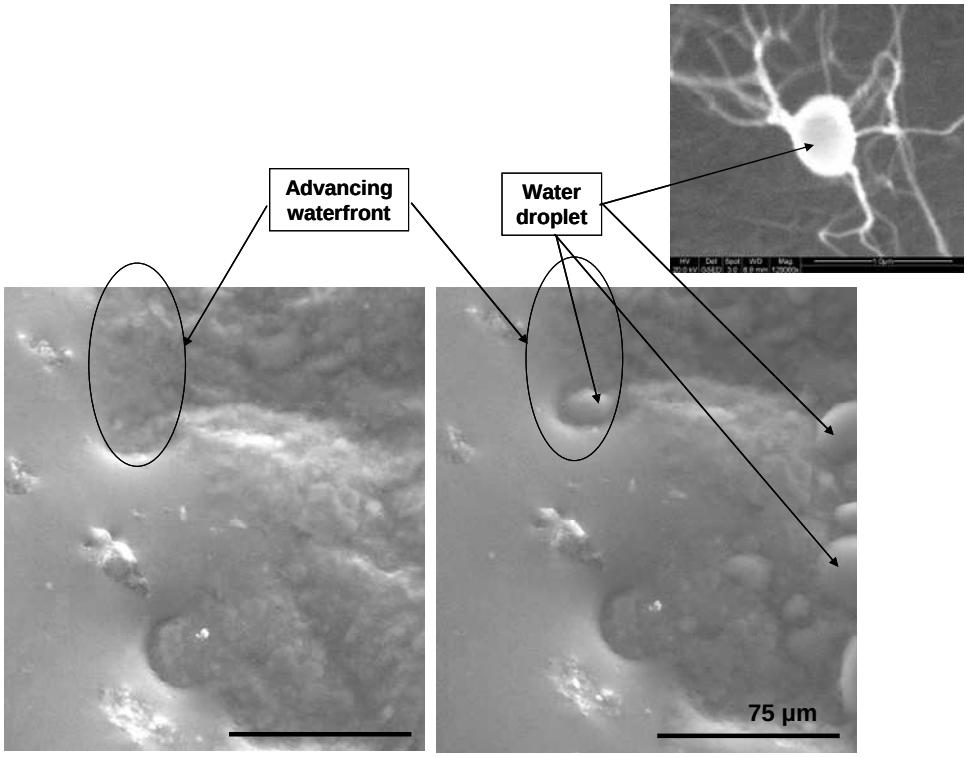

Figure 4-14 E-SEM micrograph showing water wetting at the surface of a CNT BP; the water pressure was increased from 0.1 to 0.3 kPa; the scale bar is given on the right image and the scale bar of the insert is 1 µm

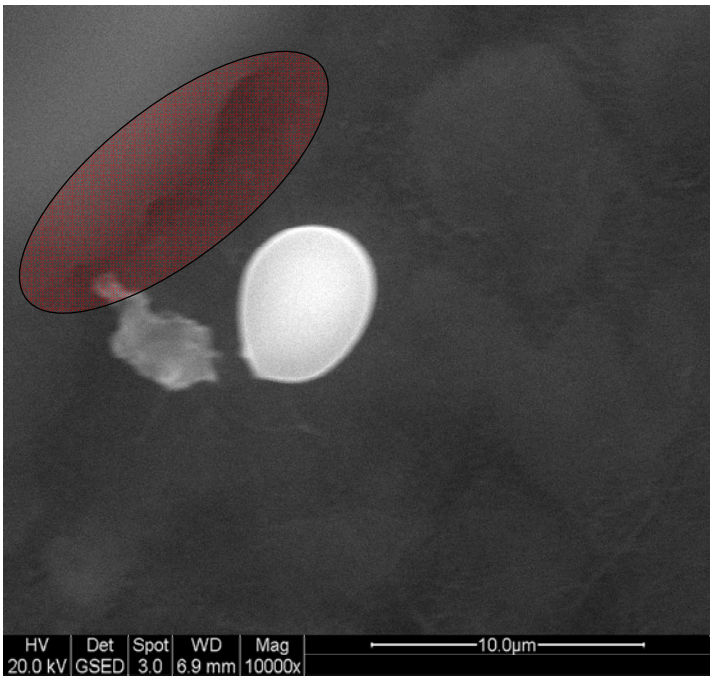

Figure 4-15 E-SEM micrograph showing the hydrophobic nature of the BP (water vapor adsorbing)

4.2.7 Mechanical tensile behaviour

Tensile tests were performed and showed that BP made of CVD CNTs offered an average modulus of ~1 GPa (+/- 0.15 GPa). Tests carried out on CCI CNTs were not successful as the mechanical stiffness of pure CCI BP was not high enough to be measured. Test realized on 50/50 CCI/CVD BPs gave moduli ~0.7 GPa (+/- 0.2 GPa) but tended to break at the grips, thus making the measurements uncertain. The high dispersity in the value was very often linked to the difficulty to cut thin strips of BPs with constant width without damaging the edges. The lower mechanical stiffness of the CCI CNT BPs was attributed to the fact that the CCI CNTs were much thicker than the CVD CNTs, which offered fewer connections and inter CNTs contacts. These CCI BPs as previously demonstrated exhibited the larger pore size as well as the lower specific surface area thus reinforcing the idea that the CNT diameter had great impact on the membrane properties. A typical tensile test for a CVD BP is shown in Figure 4-16.

As a comparison ~60 % porous commercial PVDF and PTFE membranes, tested under the same conditions, respectively gave moduli between 0.2 to 0.3 GPa and 0.4 to 0.5 GPa thus showing that the BP exhibit higher mechanical stiffness than polymeric materials. Furthermore, the viscous and plastic zones were predominating in the case of the polymeric membranes at higher loads, while the BP exhibited a mostly elastic behaviour. Part of the decline between 0.2 and 0.5 % was attributed to the large porosity and to CNT reorganisation within the structure.

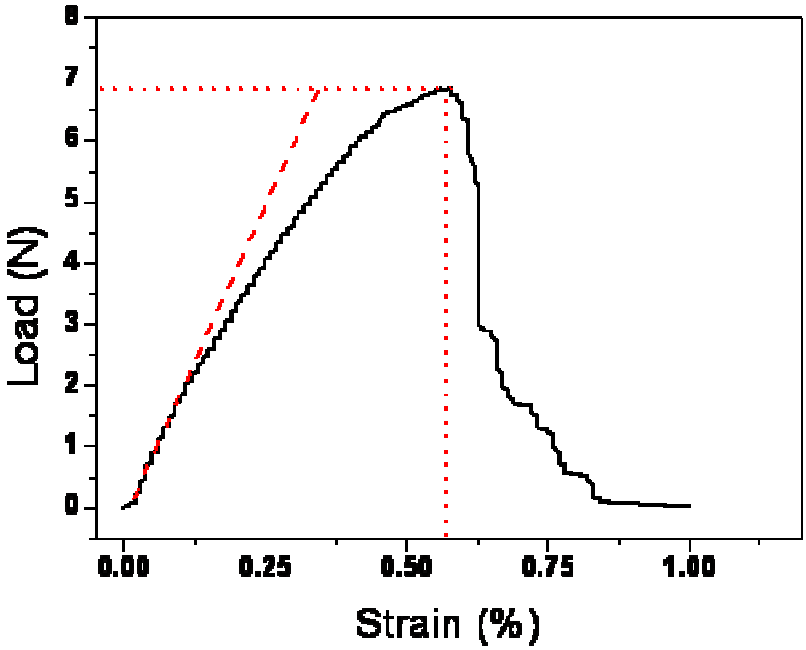

Figure 4-16 Example of tensile test; the modulus is calculated from the tangent to the curve at "0" strain while the maximum load (here ~6.85 N) is given at the maximum strain before failure (0.545 mm)

4.2.8 Thermal behaviour

One of the most important membrane parameters is its thermal conductivity which directly impacts the process efficiency. Most of the heat transferred across the membrane should be carried with the vapor and heat losses due to conduction through the membrane material should be minimised. A thermal behaviour study was carried out on the CNT BP to better understand their impact on the heat flux exchange during the MD [136, 370]. Several parameters were measured including the specific heat of the BP, the thermal conductivity and diffusivity and the relationship between thermal expansion and temperature.

4.2.8.1 Specific heat

The specific heat of the CNT was estimated by DSC calorimetry. A value of 0.62 $J.g^{-1}.K^{-1}$ was determined close to the values reported from graphene (0.71 $J.g^{-1}.K^{-1}$) and to that of commercial carbon fibres (0.68 $J.g^{-1}.K^{-1}$). In the literature a large range of values, from 0.5 up to 0.8 $J.g^{-1}.K^{-1}$ can be

found for CNTs [371-375]. No differences were expected and it confirmed that the CNTs were quite pure and that their thermal behaviour was similar to that of graphene.

As a comparison the theoretical specific heat of PVDF and PTFE are respectively 1.08 and 1.04 $J.kg^{-1}.K^{-1}$ thus requiring more energy per gram to be heated up. This means in essence that PVDF and PTFE membranes should in theory conduct heat less than CNT structures.

4.2.8.2 Thermal conductivity

Using the thermal conductivity meter, the thermal conductivity of the BPs were measured to be between 2 and 4 $W.m^{-2}.K^{-1}$ with an average value of 2.7 $W.m^{-2}.K^{-1}$. This is very low in comparison to the high thermal conductivities (~700 $W.m^{-2}.K^{-1}$) [208, 210, 218, 279, 376-378] that have been predicted and reported for individual multi-walled CNTs [102, 279, 379]. For MD, this smaller conductivity is preferred from a performance point of view. The difference is likely due to the high porosity of the membrane structure combined with the BP's layer structure and the relatively poor heat conductivity at interconnects between CNTs [216, 380, 381]. It was shown that phonons do not travel easily within a CNT between its walls and between CNTs in contact [371, 372, 380, 382]. As a comparison, tested PTFE membranes show conductivities ~0.25 $W \times m^{-2} \times K^{-1}$, 10 times lower than the BP membranes which reinforces the fact that less thermal conduction should occur compared with BP membranes.

4.2.8.3 Thermal diffusivity

Figure 4-17 shows that the thermal diffusivity of a BP was estimated to vary between 9 and 12 $cm^2.s^{-1}$ between 295 and 375 K. This was found to be about an order of magnitude higher than a non woven material made of 200 nm thick carbon nanofibres.

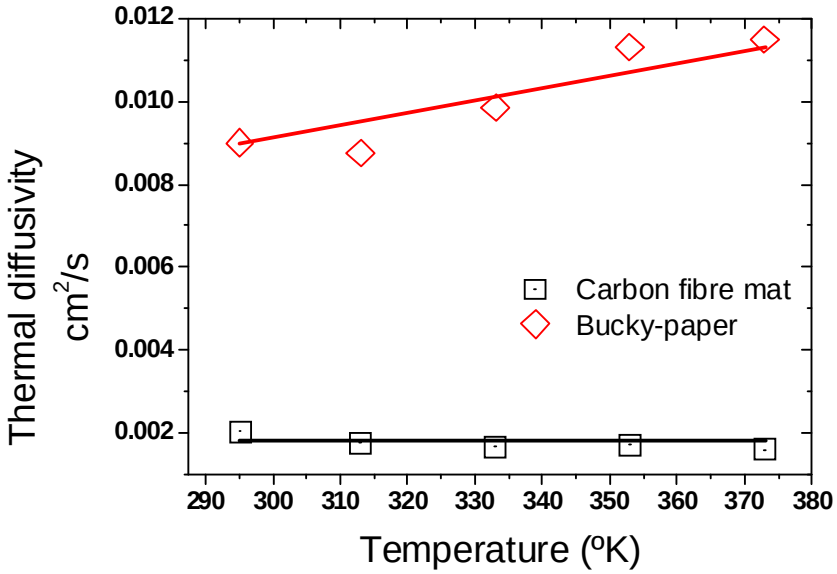

Figure 4-17 Thermal diffusivity of a BP compared with a non-woven of carbon fibres fabricated from fibres purchased from Nanoshell

These values were found to be much lower by 2 to 3 orders of magnitude than that reported for plain polymeric materials [383-385]. The differences may be related to the very high porosity of the BP material compared to that of dense thin films of polymer. Furthermore these values were found to be similar to that of other CNT based porous materials [210, 217, 381, 386].

Typical heat responses as well as the thermal diffusivity of other CNT based materials (forests and bucky-ribbons) are given in Appendix 4 for comparison.

4.2.8.4 Thermal expansion

Thermal expansion was considered as one of the important properties of the membranes due to the large temperature variations occurring during DCMD tests. As the membranes in DCMD are used as heat exchangers and heavily stressed (temperature differences from 20 up to 90 ºC between both sides of the membrane) it seemed important to investigate the thermal expansion of the BPs in order to better understand the membrane behaviour in the rig. Three methods were used to characterize the thermal expansion.

The first method involved heating a BP in an E-SEM and recording the dimension change over time, temperature and atmospheric composition. This method was time consuming and considered problematic at the beginning of the tests due to the possible errors in pixel readings to calculate the thermal expansion. For this reason another method was developed.

The second method called Modulated Temperature – Thermo-Mechanometry was used to determine the deformation of a BP under thermal stress. This method gave on average similar results as one-SEM, but these were subject to error due to the deformation imposed by the mechanical probe on the BP. Since BPs are flexible structures, the mechanical stress imposed by the probe could lead to greater deformations. For this reason a non-contact method was sourced.

The third method involved heating a BP on a hot-stage in a SAXS (at the Australian Synchrotron facilities) and analysing the X-rays diffraction patterns. This is an indirect method, as no contact is required to measure the deformation, and was thus considered more effective to confirm the thermal expansion data. The results of the three methods will be presented in the next section.

4.2.8.4.1 E-SEM analysis

Three different atmospheres were used, with water vapor at either 0.3 or 1 kPa or argon at 0.3 kPa. As shown in Figure 4-18 negative thermal expansion, corresponding to a contraction of the sample was always found to occur. The thermal expansion values are reported in Table 4-3.

The values of thermal expansion was found to be negative which was attributed to the BP large porosity (>90 %) allowing thickness to reduce as CNTs slipped and condensed in denser bundles. The presence of water reduced the likelihood for contraction by a factor 3 to 5 which was attributed to the screening of the water vapor absorbing part of the heat while condensing on the CNTs. The results indicated that CNT BP should be stable in hot and wet environment. Furthermore the stability of the data made of them very promising materials for exposure to large temperature variations exposed materials as the contraction coefficients were found to be very low.

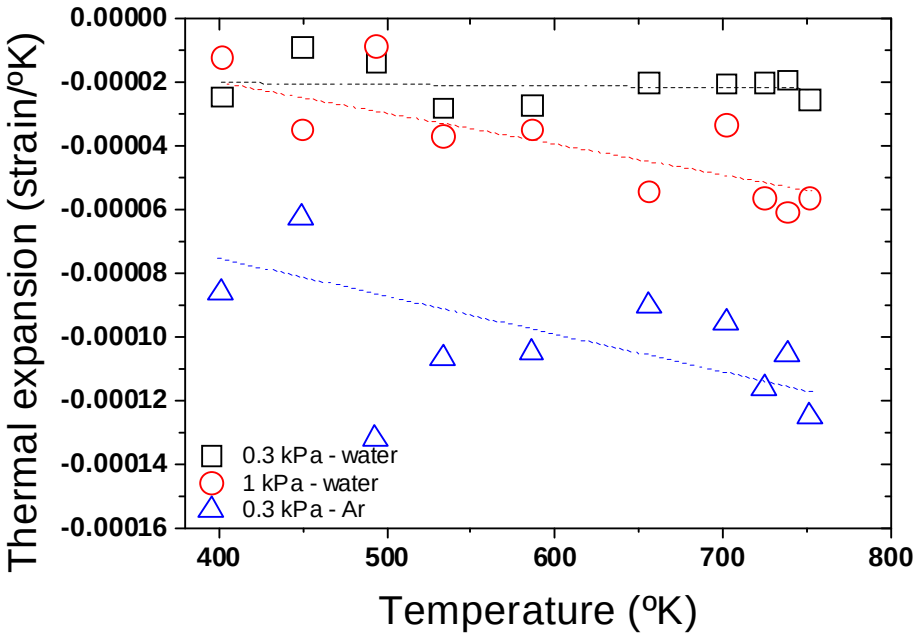

Figure 4-18 Thermal contraction of the BPs under different atmospheres

Table 4-3 Thermal expansion coefficients from E-SEM analysis

Atmosphere	*Slope of the curve ($m.m^{-1}.K^{-1}$)*
0.3 kPa water	$-2.05*10^{-6}$
1 kPa water	$-1.65*10^{-3}$
0.3 kPa Argon	$-6.8*10^{-3}$

4.2.8.4.2 Thermomechanical analysis

The mt-Tm allowed the determination of both reversible and irreversible deformation. As shown in Figure 4-19 the BP sample dimensional changes were dominated with irreversible deformation. The calculation of the global thermal expansion coefficient gave once again negative gradients. A thermal expansion coefficient of $-1.31*10^{-4}$ $m.m^{-1}.K^{-1}$ was calculated from Figure 4-20 which was comparable with the E-SEM measurements. A 350 µm thick BP was used for this study.

The origin of this contraction was attributed to the CNT bundling caused by the energy provided in the form of heat. Concerns related to the contact between the probe and the sample were raised as the variations between the runs were found to be quite high. For this reason, and since the homogeneity of the CNT distribution within the BPs still had to be

demonstrated, a third method was sourced to both confirm this trend and better understand the CNT distribution.

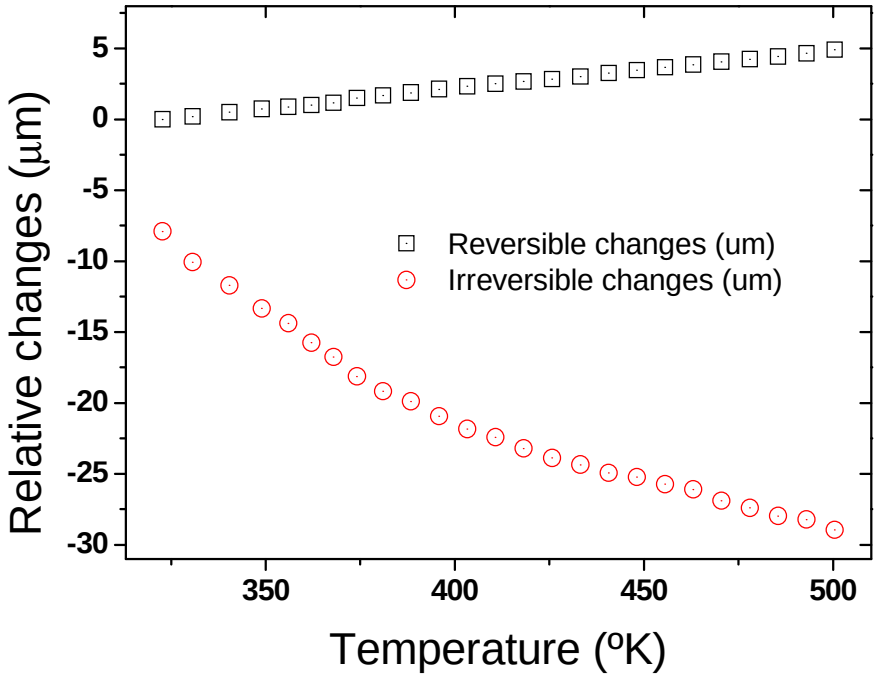

Figure 4-19 mt-Tm dimensional changes as a function of temperature

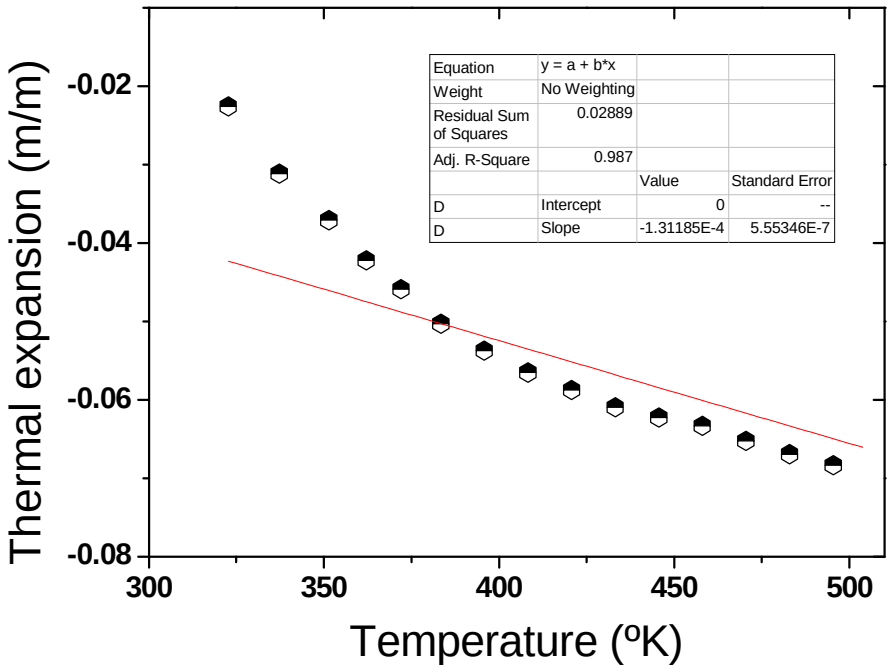

Figure 4-20 Thermal expansion with the mt-Tm method

4.2.8.4.3 SAXS analysis

SAXS experiments were carried out at the Australian Synchrotron to determine possible differences of morphologies, such as nanotube orientation or distance between the CNTs, as a function of the structure (forest, yarn, bucky-ribbon, self-supporting BP or composite BP) or of temperature. As shown in Figure 4-21, very different patterns were visible depending on the CNT distribution and orientation within the structure.

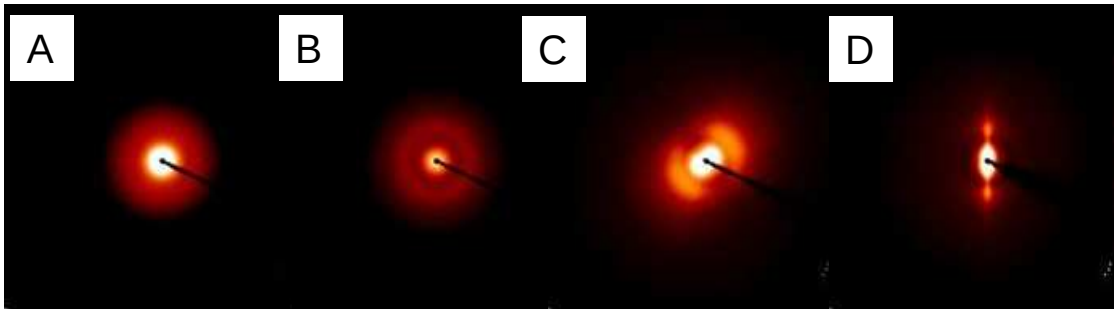

Figure 4-21 SAXS diffraction patterns for various macrostructures made purely of CNTs; A: CVD CNT BP; B: CNT forest (on its silicon wafer); C: CNT yarn (pattern across its diameter); and D: CNT bucky-ribbon (10 webs condensed)

As reported in the literature, several specific features could be detected, including the CNT/CNT distance, the space between the CNT walls [387], the type of CNT distribution (anisotropic [388], aligned in a plan normal to the beam, twisted around an axis or parallel tubes in line with the beam [389, 390]). This first experiment confirmed that clear differences were visible in intensity and type of features detected. Further details are given in Appendix 5 on the comparison between the structures.

The BP signals were found, as expected, to be fairly anisotropic and only one peak around 80 Å was revealed which was attributed to the CNT inner tube. The distance between the CNT walls was hardly visible due to the imaging window used which was focused on larger features. The global scattering intensity was found to decrease for the self-supporting BP with increasing temperatures as shown in Figure 4-22. This intensity relates to the

amount of X-rays that can go through the sample. A high intensity typically relates to a low density material and the intensity decrease was attributed to the sample deformation as a function of increasing temperature.

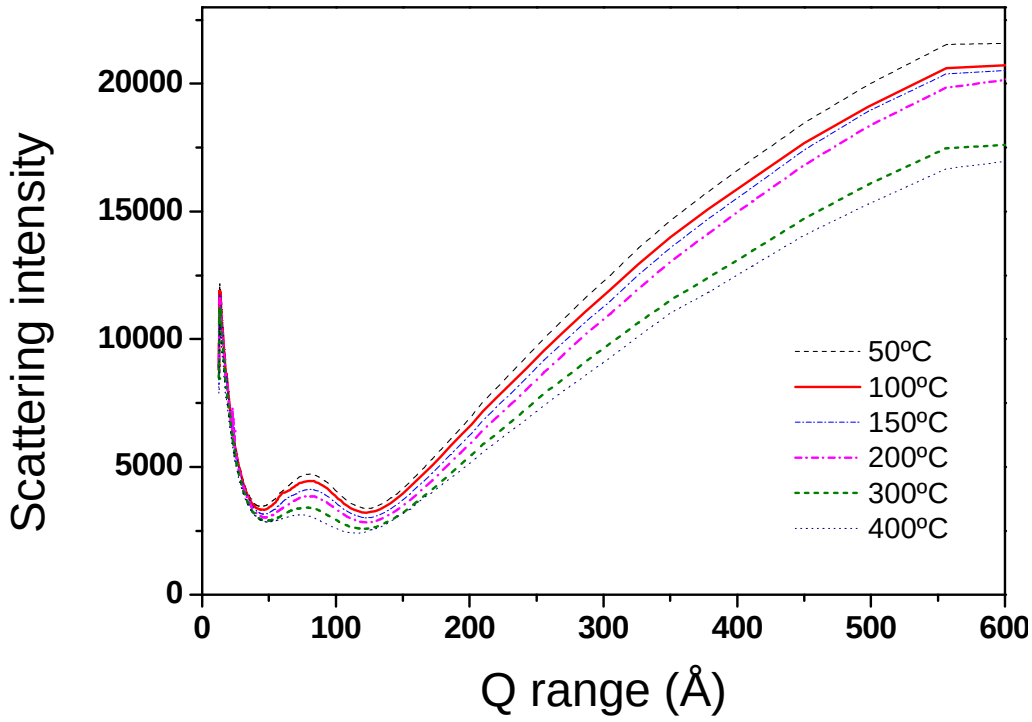

Figure 4-22 Scattering intensity of the signals at different temperatures

According to the definitions of the Guinier radius R_G (Appendix 5 [387, 391]), it seems that as temperature increases, the scatter from the small scale features reduce in number while their size decreases. It is likely that in this case, due to the increased temperature and to the natural large porosity of the BPs, CNTs tend to aggregate within the BP thus densifying the structure.

The q-range window used in this work might have been too narrow to fully comprehend all the dimensional changes over the different CNT characteristic lengths. The chosen window covered a range from 4 up to 50 nm which was initially thought to be sufficient to cover the range where CNT would agglomerate and form denser or looser bundles. However work by Zhao et al. [387] on the bundling kinetics and bundle formation showed bundles may spread over a larger range. The samples were exposed to different acid treatments to provide information on their dispersion state. At values lower than 100-300 nm, all their samples behaved identically.

However, after 24 h of treatment their SAXS patterns undertook a flip at q-ranges values corresponding to ~300 nm features. This was attributed to a change in the bundle morphology that they described as precipitation, or aggregation, of the tubes. Their dispersion method seemed to start having a clear effect for longer treatment times clearly shifting up intensity, which was attributed to looser bundle formation.

In our case, positive thermal expansion, corresponding to a true expansion, may be happening on both individual CNTs and small bundles at low q-range values, corresponding to sub 100 nm bundles. These smaller features (usually called “knees” on the SAXS patterns) could be attributed to already dense CNT interconnects (such as dense “knots” or agglomerates). Their thermal expansion might then be proportional to the natural positive thermal expansion of individual CNTs graphene walls. On the other hand, at higher Q, the features may correspond to looser bundles such as the ones optically visible and presented in Chapter 3. As the density of those features is much lower, the spaces present between the CNTs may be filled up with air, instead of solvent which may affect the thermal expansion of the structure. The Van der Waals forces may help attracting the CNTs together thus overcoming the individual CNT thermal expansion to form denser structures up to a maximum bundling density. This might justify the negative thermal expansion, corresponding physically to a thermal contraction.

The Q-range chosen for these tests was found a posteriori to be slightly too low (shift towards small features) to be conclusive. Features of a diameter between 10 and 50 nm were visible, which corresponded mostly to the contribution of single CNT or small agglomerates of CNTs. Therefore the global behaviour on a macro-scale was found difficult to interpret and more SAXS tests at higher Q would be required to fully comprehend the BP behaviour.

The Luh graph (Figure 4-23) amplifies the structural feature over time. We can see that the structural features decrease in steps until frame 50 where the temperature comes back down to 50 ºC before starting the 2nd heating cycle. A permanent contraction noted h is visible as the Q^2 values greatly differ between the start of the 1st cycle and the end of the cooling. This is an important feature as it shows that the BP are thermally stable but can

endure permanent deformation due to thermal stress at high temperatures (above 200 – 250 ºC). This permanent deformation correlates well with the mt-Tm tests which demonstrated that an important part of the deformation was permanent and non reversible at high temperatures (above 300 ºC) [387].

Despite the fact that no thermal expansion coefficients were calculated from this experiment, the SAXS measurements clearly showed that CNT BP were physically affected by large temperature variations and that thermal ageing such as permanent deformation were to be expected above 200 ºC.

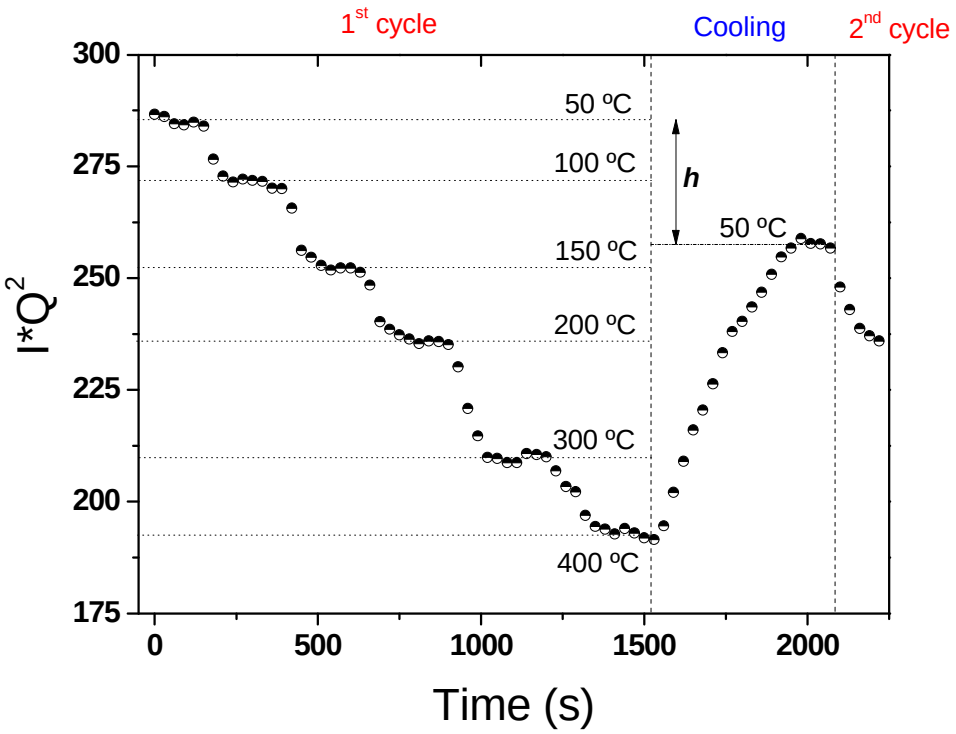

Figure 4-23 Luh graph plotted as a function of time; the time/frame dependence was defined by a 30 s interval between each shot

The thermal properties of the self-supporting BPs have been studied. It was shown that the thermal conductivity and diffusivity of the structure was lower than that predicted for individual nanotubes. This was attributed to the anisotropic structure of the BP and to the large porosity of the structure, as phonons do not diffuse easily between walls and CNT/CNT connections. Furthermore the thermal expansion of the BP structure was investigated over a large range of temperatures. It seems clear that BP are stable up to 100 ºC, which is the maximum operating temperature in DCMD while thermal

contraction, including permanent deformation, seem to occur at higher temperatures.

The thermal properties of the CNT BP membranes were found to closely match that of polymeric membranes such as PVDF and PTFE. The conclusion from this study it is likely that BP would naturally conduct heat better than PTFE, thus indicating likelihood for more heat transfers. BPs however showed very good thermal stability at high temperature differences and in wet environments which would be valuable on long term tests in DCMD or other applications where polymeric materials degrade too fast.

4.3 Direct contact membrane distillation test

Polymeric membranes were used to calibrate the rig and to compare with BPs. As PTFE membranes were shown to exhibit the highest flux in the literature (see Chapter 1). it was used as a benchmark and efforts were focused to progressively improve BP performance. The CCI CNTs were unfortunately not tested in DCMD. They presented several drawbacks over the CVD CNTs, such as lower contact angle and specific surface area. Furthermore, BPs fabricated from the CCI CNTs were also more fragile than the CVD BPs. The very large surface pores created with the CCI CNTs revealed to be a challenge as wetting of the membrane occurred faster leading to irreversible loss in integrity and to possible direct bridges during the MD tests. Only the CVD CNTs were then available and the rest of the study will only show results related to those CNTs. It was, however, interesting that the average pore size could be nearly doubled by only mixing CNTs of different diameters together. This might open for further discussions and opportunities for optimisation of CNT BPs for particular applications.

This section will first present DCMD results for the polymeric membranes presented in the previous sections and then compare them with self-supporting BP membranes.

4.3.1 DCMD tests on reference membranes: benchmark

4.3.1.1 Impact of hot feed and cold permeate temperatures

These tests were performed with PTFE-M045 membranes. The flux was shown to increase with increasing hot temperature as seen in Figure 4-24.

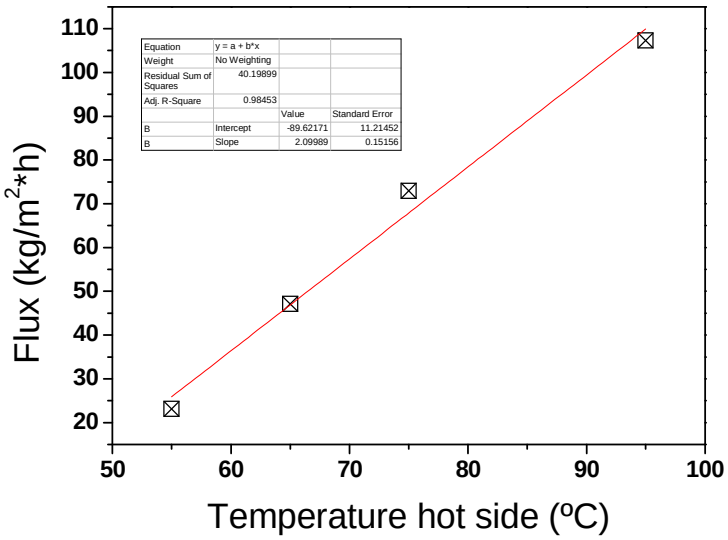

Figure 4-24 Impact of hot feed temperature change at constant cold temperature (5 ºC) with a PTFE 0.45 µm pore size membrane

4.3.1.2 Impact of membrane pore size

PTFE-P002, PTFE-P02 and PTFE-045 were used to assess the impact of the average pore size on the membrane permeability. As expected from the theory larger pore size membranes lead to larger flux (Figure 4-25) and permeabilities (Table 4-4). An average thickness of 50 µm was used for the permeabilities calculations.

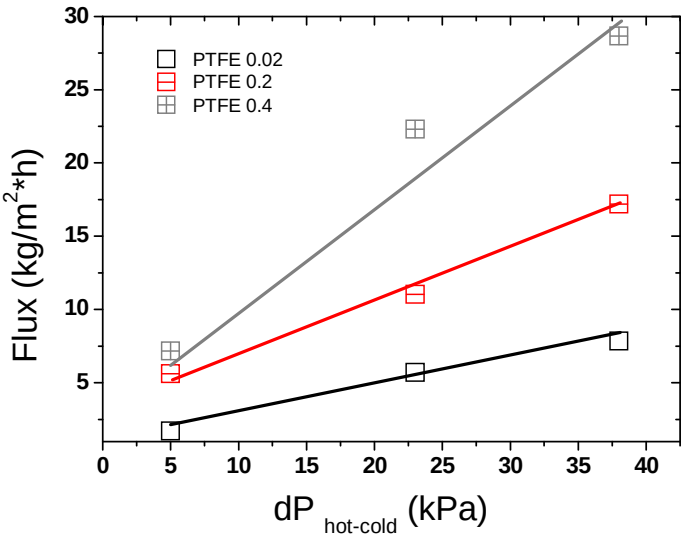

Figure 4-25 Impact of average pore size on the water vapor flux

Table 4-4 Permeabilities and permeances calculated from Figure 4-25

Pore size	Slope	Permeance	Permeability
nm	$kg.(m^{-2}.h^{-1}.kPa^{-1})$	10^{-8} * $kg.(m^{-2}.s^{-1}*Pa^{-1})$	10^{-12} * $kg.(m^{-1}.s^{-1}.Pa^{-1})$
20	0.22	6.08	3.04
200	0.47	13	6.5
450	0.82	22.76	11.4

As seen in Appendix 3 the membrane permeability is directly proportional to the average pore size. However other parameters in the membrane such as tortuosity and porosity might have changed since the slope of the linear fit is not proportional to the change in pore size. Other effects such as temperature polarisation or membrane compaction due to the support might also explain this difference from the theory.

The results for the 0.22 µm pore size PVDF membranes are given in Appendix 3. Those membranes exhibited lower flux than the PTFE membranes at similar pore size and porosity. This was attributed to the difference in hydrophobicity. The membranes thickneness were found to be similar and are reported in Appendix 3.

4.3.2 BP membranes: flux and permeability

The DCMD tests were carried out on different CVD BP membranes having similar thickness. Tests were performed at 3 different hot stream temperatures, leading to different water vapor pressures across the membrane. The flux typically increased over the first 15 min before stabilising. This first step was related to the equilibria of the water temperature stream across the module and reservoirs and data were acquired after stabilisation for accurate flux calculation. However, this stabilisation was often followed by a slow decline until the membranes broke (Figure 4-26). The origin of this declining flux is still uncertain. It should not be related to direct bridges across the membranes as the conductivity on the cold side was stable for the first 300 min but started increasing over the end of the test Figure 4-26. It may be related to temperature polarisation, linked to the BP thermal conductivity. However we strongly suspect that physical ageing of the BP membranes is responsible for this behaviour. The declining flux of the BP membranes may also be linked to a progressive compaction of the membrane due to pressure from the hot and cold water streams [392, 393]. A previous study has shown that the permeate pressure has an impact on the flux and membrane behaviour [59]. The sample data are given in Table 4-5.

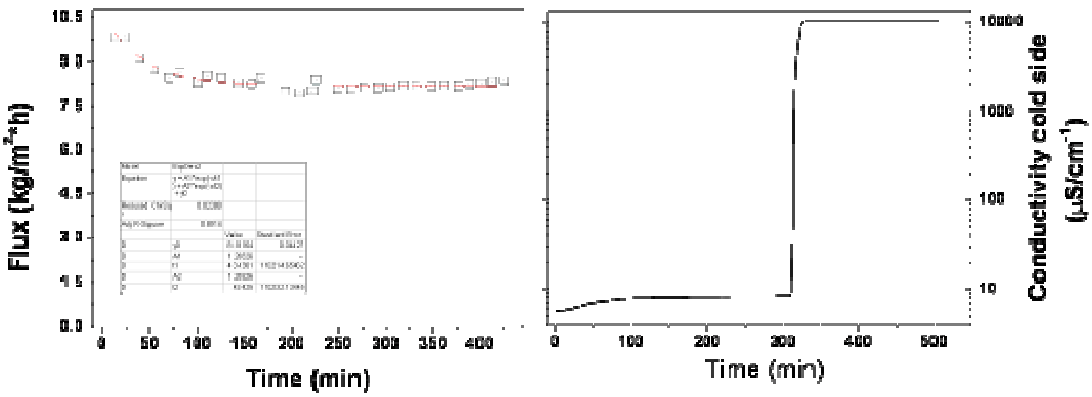

Figure 4-26 Left: Flux across a 40 µm thick BP membrane at T_{hot} and T_{cold} respectively of 65 and 5 ºC. Right: cold side conductivity. Temperatures were stable and varied only by 1 to 2 ºC

Table 4-5 Membrane performance and properties

Membrane	Mass (mg)	Thickness (µm)	T_{ave} (℃)	ΔT (℃)	ΔP (kPa)	Rejection (%)
PTFE	20.9 (8.61)	205 (30)*	41	29.1	12.7	100
			32	46.8	15.02	100
			39	59.5	28.81	100
			45	65.9	42.29	100
CVD BP	4.75	45	27	41.2	10.89	99.99
	6.65	55	45	63.8	40.43	88.46
	7.98	42	36	53.2	22.73	94.08

* the thickness of the complete structure is ~205 µm while the active layer is ~30 µm thick.

The flux for the BP membranes is plotted in Figure 4-27 as a function of the partial pressure difference across the membrane after 2 hours of operation. More than 30 membranes were tested but only a few worked long enough to reach stable flux. The flux was calculated from an average of 2 samples or less. Large variations between the samples tested occurred. The largest fluxes were obtained at 40 kPa of pressure difference and were up to 12 kg/m^2*h achieved over 60 min of tests. No major permeate conductivity increased occurred for this sample over this period of time therefore showing the intact integrity of the membrane for short period of times. This value was used as a benchmark for the next chapters.

The partial pressure differences were calculated using the temperatures measured for the hot and cold reservoirs and applying Antoine's law equation (Chapter 1). These pressures were obtained by taking the temperature in the bulk solution in the module very close to the membrane surface. Experimental errors and especially the impact of the vaporisation of the water and thermal conductivity of the BP structure are likely to affect this reading and corrections needed to be made to control the pressure. Those readings were questionable as only the membrane surface temperature should be used to calculate the vapor pressure. However as measuring is challenging, it was decided to use these temperatures as reference in this work.

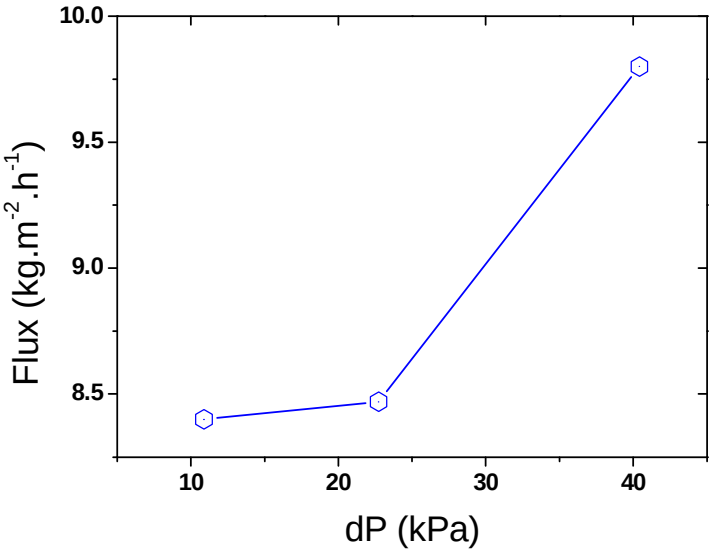

Figure 4-27 Flux across BP membranes as a function of the water vapor pressure difference between the two streams

To calculate the permeability, the slope of a linear fit to the flux vs. the water vapor pressure difference (Figure 4-27) was calculated and multiplied by the average membrane thickness. As a steady and stable flux was difficult to observe with the self-supporting BP membranes, it was difficult to accurately determine the dependence on partial pressure difference. A linear fit to the data in Figure 4-27 gave a permeability on the order of 0.8×10^{-12} $kg.m^{-1}.s^{-1}.Pa^{-1}$. This value was low compared to reported and experimentally obtained values for PVDF or PTFE membranes.

A number of factors may explain the lower permeability measured for the BP membranes and will be discussed in Chapter 6. Table 4-6 compares the experimental permeability values with theoretical values calculated using equations (1-4) in Chapter 1.

Table 4-6 Permeance and permeability of the BP and PTFE membranes

	Membrane	
	BP	PTFE
Permeance*	10^{-8} kg.($m^{-2}.s^{-1}.Pa^{-1}$)	
Experimental	1.38	70.38
Theoretical		
- Knüdsen	50 ± 13	386 ± 3
- Molecular	201 ± 53	288 ± 18
- Transition	40 ± 10.5	164 ± 5.5
Permeability*	10^{-12} kg.($m^{-1}.s^{-1}.Pa^{-1}$)	
Experimental	0.83	21.1
Theoretical		
- Knüdsen	26 ± 1	116 ± 0.6
- Molecular	104.5 ± 8	86.3 ± 5.5
- Transition	20.8 ± 1	49.4 ± 1.6

* The uncertainties are associated with differences in temperatures used for the different tests and membrane thicknesses in the case of permeance. Both these effects only had a minor affect. A tortuosity of 2 was used for all calculations

The temperature polarisation in the module at different feed temperatures was investigated on series of membranes [143, 147, 394]. The membrane temperature was recorded over time and the bulk temperature was calculated by averaging the temperature of the flows going in and out of the module and small temperature differences were recorded. Two thermo-couples were placed at both entrance and exit on each side of the module. The temperature polarisation was then calculated with equation 1.

$$\theta = \frac{T_1^m - T_2^m}{T_1^b - T_2^b} \qquad (4\text{-}1)$$

Where the subscripts 1 and 2 are respectively for the hot and the cold side, T^m stands for the temperature of the membrane surface as measured in the previous section and T^b is the temperature in the bulk solution.

The temperature polarisation coefficients were close to 1, as shown in Figure 4-28. The temperature polarisation was compared with that of a 0.45 µm pore size PTFE membrane. These values show that temperature polarisation is not affecting too greatly the permeance behaviour. As BPs present thermal conductivities 10 times higher than PTFE membranes, more conductive heat exchanges may be happening between the feed and permeate streams, therefore justifying the temperature polarisation difference between the two membranes.

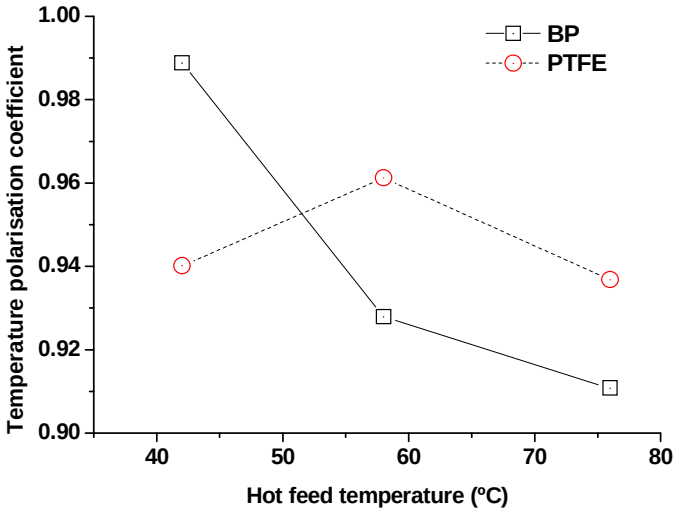

Figure 4-28 Temperature polarisation as a function of feed temperature. The test conditions were kept similar as a classical DCMD test

4.3.3 Membrane integrity and lifespan during DCMD

The integrity of the BP membranes was investigated in two ways. First, the conductivity of the cold reservoir was monitored with time. If only water vapor crossed the membrane, then the electrical conductivity of the cold solution should progressively decrease in proportion to the amount of water transferred. Most BP membranes showed a very slight but progressive increase in conductivity corresponding to desalination efficiencies between 88 and 99% as shown in Table 4-5 and Figure 4-29. Furthermore, after 4 to 7 hours of testing a rapid increase in conductivity was typically observed for the BP membranes indicating that liquid water was breaching the membrane allowing salt passage from the hot to the cold stream.

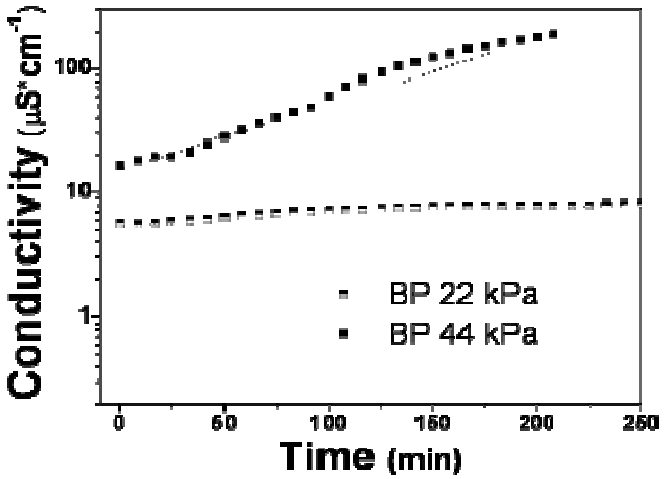

Figure 4-29 Example of conductivity over time on the cold side

The membranes were characterised after membrane distillation testing using Focused Ion Beam milling and SEM imaging. As shown in Figure 4-30, micro-cracks were present and seem to represent regions of delamination between the CNT layers. EDX analysis also confirmed the presence of sodium and chloride within the micro-cracks, while none was detected in regions away from the cracks. It was suspected that the ageing of these membranes was accelerated due to the operation of MD apparatus which incorporated two pulsating peristaltic pumps. This causes an oscillation of the membranes, and potentially delamination of sheets nanotubes as they are held together solely through Van der Waals forces [244, 395]. It was likely that the gradual formation of micro-cracks as well as compaction of the membrane contributes to the loss of flux observed during operation for the BP membranes. Various approaches, such as composite structures and the addition of polymers were being investigated to avoid the formation of cracks (see Chapter 5).

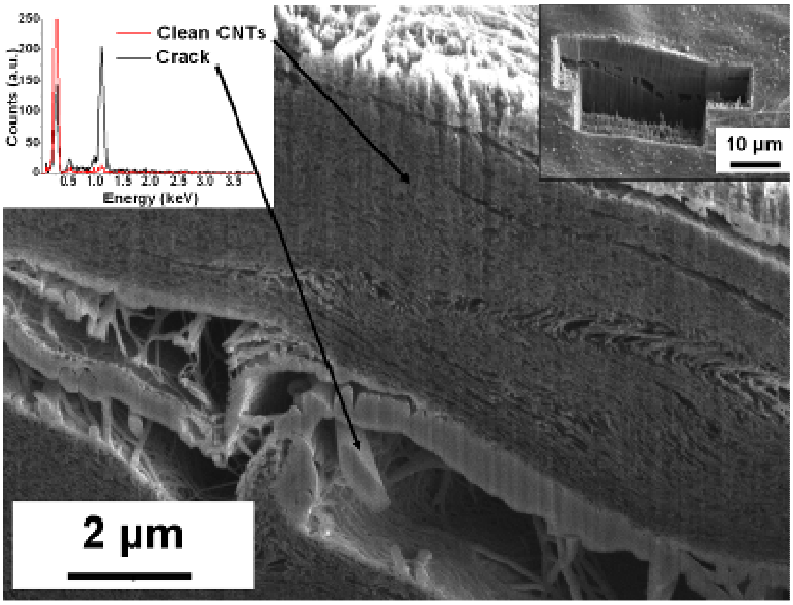

Figure 4-30 SEM images at 5 keV and 7.5 mm w.d. showing a cross-section through a BP membrane after testing. The section was milled with a focused ion beam and the image was taken at a 52° tilt. The left inset shows EDX curves taken inside and well away from the crack. The right inset shows a low magnification view of the cross section

4.3.4 Surface fouling

Fouling is generally not a major issue in MD but backwashing can be sometimes necessary to remove the adsorbed particles, salt crystals or organics. In the case of separation of heavy organic compounds, such as dairy products (Figure 4-31-A2), a dense film, composed of both bacteria nad/or organic foulants, can form at the surface progressively reducing the flux and likely the separation efficiency if the film grows towards the permeate. However in the case of synthetic seawater the fouling was very minor and only a few salt crystals were found even after long period of time (4h on Figure 4-31-A3, B2 and B3). The presence of NaCl was found on both PTFE and BP membranes but at very low concentration. As the samples were not washed prior to imaging, it is likely that some salt crystals just adsorbed upon drying. The top right insert in Figure 4-30 also shows the presence of aggregates which were identified as being salt crystals.

Fouling was not found to be a major issue in these experiments and none of the membranes tested in the following chapters showed tendency for

fouling. This was an interesting point and did reflect the smooth and frictionless properties attributed to graphene when in contact with low fouling potential pure salt solutions [396].

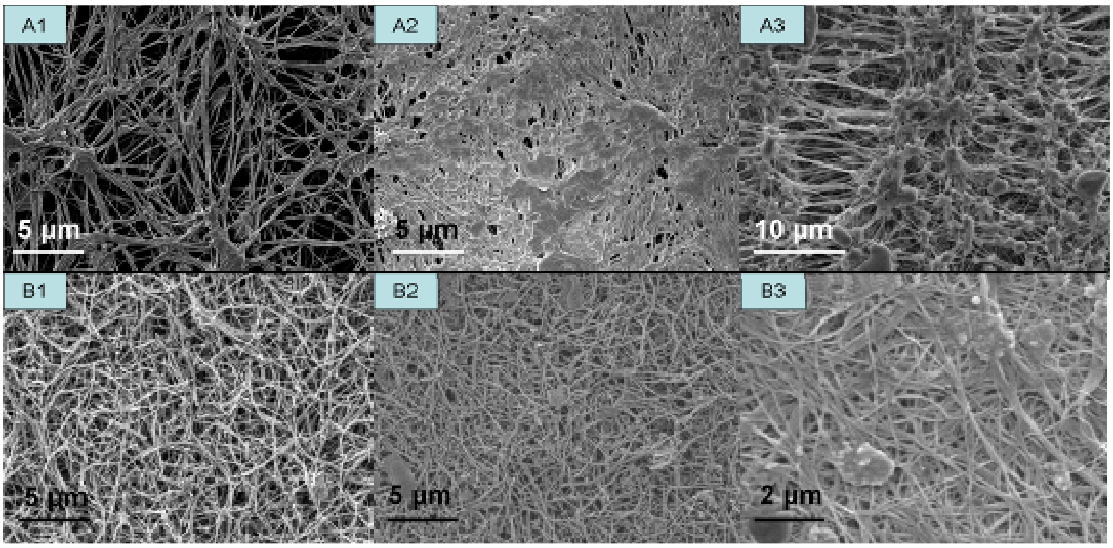

Figure 4-31 SEM images of surfaces after DCMD of a low concentration whey / water solution; The A series corresponds to 0.45 um pore size PTFE membranes while the B series to BPs

4.4 Conclusions and recommendations

CNT BP membranes were fabricated by vacuum filtration and characterised to determine their suitability for MD. They were found to have many properties favourable for MD. For example they exhibit a high contact angle (~120 degrees), high porosity (~90%), and relatively low thermal conductivity of 2.7 kW/m^2*h. These properties are better than most of polymeric membranes conventionally used in MD and compare well with PTFE membranes which are the highest benchmark for comparison. Most importantly desalination was successfully demonstrated using CNT BP membranes in a DCMD setup. The best results gave 99% salt rejection and a flux rate of 12 kg/m^2*h at a water vapor partial pressure difference of 22.7 kPa. The PTFE membrane series performed in accordance with Knüdsen diffusion after corrections of their intrinsic properties. The PTFE 20, which exhibited a similar average pore size as the nanotube membrane, performed better than the self-supporting BPs. This was attributed to a pore shape and possibly to lower tortuosities more favourable to Knüdsen diffusion. The difference with the other PTFE membranes was attributed to both the much larger pore size (of more than 1 order of magnitude). Some issues were also encountered during DCMD testing such as a decline in flux with time and delamination of BP membranes due to the formation of micro cracks. However it is important to stress that these BP membranes were not supported and were composed solely by CNTs. The use of self-supporting BP membranes in membrane distillation seems limited as their performance did not exceed that of similar PTFE membranes, the best benchmark available on the market at the moment.

Self-supporting CNT BPs have unique structural and surface properties and have great potential in many day-to-day and high-tech applications. Their processing is cheap, straightforward and reproducible leading to very homogeneous and versatile structures. The BP low friction properties, and anti fouling properties may also lead to their use in other separation technologies where materials offering reduced fouling and anti-biofouling properties are being investigated. The robustness of the BPs could then be

integrated into composites as a protection layer for more active surfaces. The democratisation of nanotechnologies and the decreasing prices of nano-materials will certainly push the development of further simple nano-materials based macro-structures in the next decade. Companies in the United States of America [397, 398] already offer large CNT BP sheets for sale and it is likely that the applications of CNT in future technologies will be partly via BP.

In summary, self-supporting CNT membranes have physical and surface properties beneficial for MD but do not exceed the performance of actual membranes. The work in this chapter was a proof of concept that self-supporting CNT structures can be used for water desalination and aimed at improving our understanding of the BP properties. This was a critical step in the engineering of improved membranes and for other applications of BPs. In fact, other approaches relying on the fabrication of composite BP membranes might however resolve some of the issues and lead to enhanced performance membranes. The next chapters will present the work done on the optimisation of the BP membranes with an emphasis on supported and composite structures for improved lifetime and permeability.

Chapter 5

5 Composite BP membranes: improving the properties of self-supporting BPs for higher separation and adsorption efficiency

This chapter will present various ways to processed improved performance membranes for water vapor permeation and gas permeation. Routes to chemically functionalize individual carbon nanotubes and to modify CNT BPs will be presented. A novel approach using CNT BPs as templates for composite membranes will be demonstrated. Parts of this work have been published in *Material*s, *Membranes*, *Journal of Membrane Science* and *Desalination*

5.1 Introduction

In this chapter several types of composite structures were processed from self-supporting CNT structures to improve the BP performance presented in Chapter 4. Several structures were investigated to cover a large range of opportunities and applications. These composite structures were aimed at exploiting the desirable CNT BP properties, while also benefiting from additives to achieve enhanced mechanical stiffness and performance. The membranes were characterized with various techniques and their performance in gas permeation, gas adsorption and membrane distillation tested. The rationale behind these experiments was motivated by equations 5-1 and 5-2 ruling flux and performance in MD.

As described in Chapter 1, the flux across a porous MD membrane will rely on both the water vapor pressure difference across the membrane and on 4 main geometrical parameters intrinsic to the membrane, namely its average pore size, porosity, tortuosity and thickness. To maximize the flux and the permeability, it is therefore recommended to process thin membranes with large porosity and pores as straight and wide as possible. Unfortunately wetting of the membrane may occur at low trans-membrane pressures for membranes exhibiting low LEPs. This can be controlled by tailoring the membrane surface energy or hydrophobicity and by balancing the pore size to obtain high flux membranes with anti-wetting properties.

$$f = K(T,M) \times \frac{\varepsilon . r}{\tau . t} \qquad (5\text{-}1)$$

$$LEP > \frac{-2B.\gamma_L.\cos\theta}{r_{\max}} \qquad (5\text{-}2)$$

Work in this chapter has primarily focused on increasing the BPs hydrophobicity by adding highly hydrophobic materials on the CNTs to both increase membrane ageing stability and its wetting behaviour. Furthermore

investigations to increase the porosity and average pore size were also carried out to optimize the performance in MD.

Firstly, experiments were performed to enhance the mechanical stability and reduce the impact of ageing over time. BPs were sandwiched between two layers of poly(propylene) grid to enhance the mechanical stiffness and avoid mechanical ageing during membrane testing. In a similar approach, BPs were infiltrated with polymer solutions and polymer aggregates were added within the structures in order to enhance the bonds between CNTs and reduce possible crack formation during performance tests.

Secondly, as the surface hydrophobicity was shown to be a critical parameter to achieve high flux and separation, several routes to modify the surface energy of the CNTs were undertaken. In every approach, care was taken not to heavily modify the CNT BP internal structure, and to keep pore size and porosity comparable with self-supporting BPs. First BPs were coated with a thin layer of PTFE. In another approach, CNTs were side functionalised with either alkoxy-silane (GPTMS) or fluoro-silane (FAS-17) molecules. These treatments involved pre-treatments of the CNTs and several chemical reactions in sol-gel routes to strongly graft the chains on to the CNTs outer walls.

Thirdly, efforts were put into modifying the porosity and pore size of the BPs to maximize the membrane permeance. First, results on the impact of the addition of sacrificial latex beads in the BP structures on the gas permeation properties and membrane specific surface area will be presented. Secondly, a novel approach to grow gold nano-particles within a BP structure will be shown. These two sets of experiments were aimed at demonstrating that CNT BPs could be successfully used as a template material rather than just a unique membrane to engineer advanced property membranes.

5.2 Composite processing and characterisation

5.2.1 Mechanical reinforcement of the structure

5.2.1.1 Sandwich BP

Composite sandwich CNT BP membranes were produced by two methods. The first method involved direct hot pressing a self-supporting BPs between two layers of porous poly(propylene) (PP) supports. The three layers were placed between two stainless steel plates and hot-pressed at 36.9 kN for 15 min at 80ºC. The resulting structure is referred to throughout the following text as the “sandwiched BP” composite.

The second structure was a slight variation of the first and is referred to as the “filtered sandwiched BP” composite. Suspensions of dispersed CNTs were filtered through a PP support (with a PES membrane underneath). In this case, the CNTs were collected on and within the pores of the PP support. The PP-CNT cake was sandwiched with another layer of PP support and hot-pressed under the same conditions given above. The properties of these membranes were very similar to that of the sandwiched BPs. Only the thickness of the active BP layer was increased due to the presence of CNTs within the grid support pores.

The “sandwiched BP” composite structures were expected to exhibit similar properties to the self-supporting BPs. The primary effect of the PP support layers was to reduce the BP surface area exposed to both permeate and feed streams. The porosity of the support was measured to be ~55% via SEM imaging (Figure 5-1). The support macro pores were ovals with major and minor axes of 750 μm and 300 μm, respectively. The process of hot pressing may have also slightly compacted the BP structure. The specific surface area of “sandwiched BP” should be similar to that of a self-supporting BP membrane, as the PP support does not penetrate far into the BP active layer. The surface hydrophobicity of the composite was also reduced to ~90-100º compared to 120º for the pure BP because of the PP higher surface

energy that increases the composite affinity for water and the likelihood for wetting.

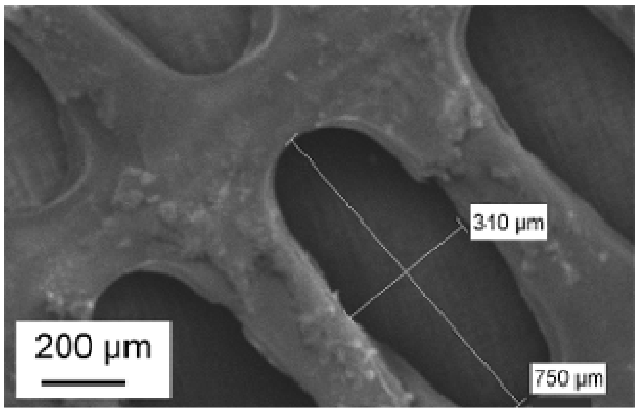

Figure 5-1 Representative SEM image of the structure of the PP support

5.2.1.2 Polymer infiltrated BPs

A number of “polymer infiltrated BP” membranes were formed by vacuum filtration of a 5% polymer/solvent solution through the self-supporting BP. Solutions of either PS or PVDF in dimethyl-formamide (DMF) were used. After polymer infiltration, analytical grade DMF was filtered through the membrane, to backwash the membrane and removes any non-bonded polymer.

The polymer infiltrated BP membranes exhibited a lower specific surface area of ~50 m2/g, as well as a reduced hydrophobicity (~100° contact angle), compared to pure self-supporting membranes. As shown in Figure 5-2, aggregates of polymer were visible on the BP surface after infiltration of the 5% PS solution. The PS appears to partially coat the nanotubes reducing the membrane specific surface area and BP porosity. The reduced hydrophobicity was attributed to the higher surface energy of the infiltrated polymer [399]. The characterization results are summarized in Table 5-1.

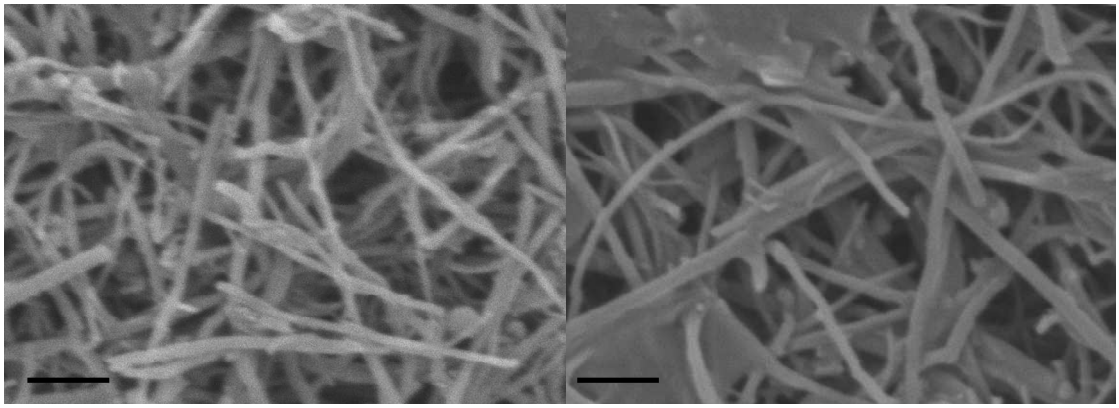

Figure 5-2 Representative SEM image of at the surface of a PS infiltrated composite BP membrane; the scale bar corresponds to 500 nm

Table 5-1 Properties of the sandwiched and polymer infiltrated BPs

	Thickness µm	Contact angle º	Porosity	Pore size range (SEM) Nm	BET m2.g-1
PTFE-02	200	115-125	70	200-400	21
Sandwiched BP	40-60	90-100	62	25-100	197
PS infiltrated BP	40-60	95-100	55	25-100	50
PVDF infiltrated BP	40-60	95-100	-	25-100	-
PP support	100	95-100	55	310-750 µm	-

5.2.2 Enhancing the hydrophobicity of the BPs

5.2.2.1 PTFE coating

BPs were coated with PTFE with an in-house fabricated radio frequency (RF) sputterer from RMIT. SEM imaging revealed that the PTFE coating formed a thin continuous and porous film at the surface of the BP (Figure 5-3-C). The membrane surface did not seem to be drastically changed and neither blockages nor polymer agglomerates were visible in the images. The measurement of the CNT diameters before and after coating confirmed the measurement of the PTFE thickness on a glass slide reference inserted during the coating which was estimated to be less than 10 nm. The coated membranes had a similar pore size distribution compared to that of the non coated BPs (Figure 5-4), although a slight shift towards smaller pore size was detectable and the average pore size determined by porosimetry fell from

31.8 nm down to 20.4 nm and was attributed to the PTFE presence (Table 5-2). The porosity of the membrane (88 % +/- 2%) was found to be mostly unchanged before and after coating which confirms that the PTFE is depositing only on the outer surface of the BP and not depositing within the pores. When compared to the PTFE membranes, the average pore size of the non-coated and coated BPs were found to be smaller by 40 and 55% respectively while their porosities were found to be higher by 25%.

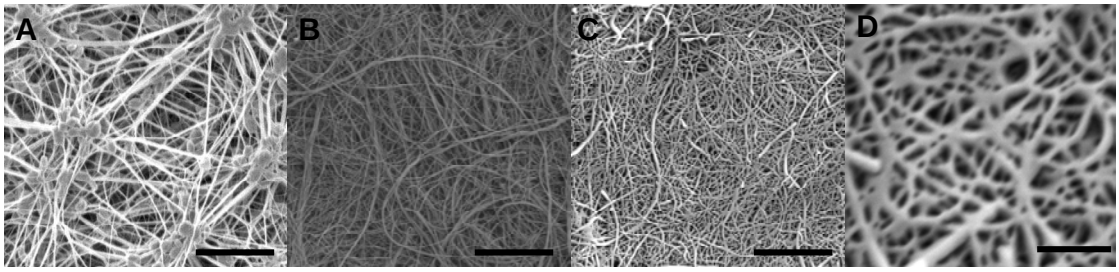

Figure 5-3 SEM micrographs of A: PTFE membrane; B: Bucky-paper and C&D: PTFE coated BP. The images were taken at 5 keV and 5 mm working distance after iridium sputtering. The scale bars of A, B and C correspond to 2 µm while D corresponds to 300 nm

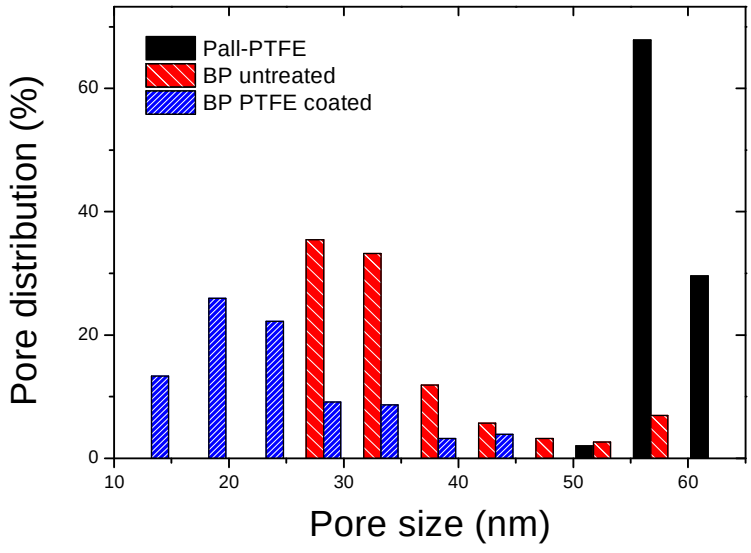

Figure 5-4 Membrane pore size distribution. The porometer pressure varied between 300 and 3500 kPa and the tested surface area was a disk of 10 mm of diameter supported on a metallic porous grid

The bubble point and contact angle of the BP membranes increased from 783.9 kPa and 118˚ without the PTFE coating to 1005.9 kPa and 155˚ with the PTFE coating (Table 5-2 and Figure 5-5). The increase in bubble point was attributed to the tighter pores and higher contact angle following PTFE coating, and the contact angle of the PTFE-coated BP was superior to that of the Pall-PTFE membranes (Table 5-2). Even though the manufacturer specifications indicated that the PTFE membranes should have a nominal pore size of 22 nm, our measurements (both SEM estimation and porosimetry) gave an average pore size of 57-58 nm. Additionally, the porosity of the reference material was found to be 30 % lower than that of the BP membranes, but the bubble point was similar to that of the BP untreated membrane.

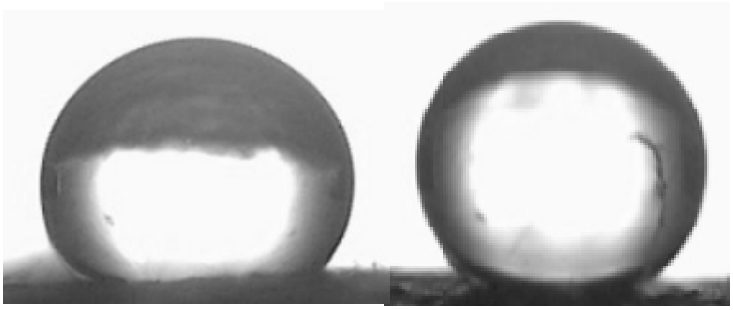

Figure 5-5 Contact angle pictures. On left: uncoated BP; and right: PTFE coated BP

Table 5-2 PTFE coated membrane properties

Sample	Average pore size	Contact angle	Porosity	Bubble point
	nm	º	%	kPa
Pall-PTFE	57.4	145	66	772.9
BP untreated	31.8	118	90	783.9
BP PTFE coated	20.4	155	88	1005.9

5.2.2.2 Alkoxysilane modification

Another route to enhance the hydrophobicity of the BPs was to functionalise the outer walls of the CNTs with 3 - glycido - propyl-tri(methoxysilane) (GPTMS) chains. The CNTs were first UV/ozone treated to create active hydroxyl groups and eventually silanised to enhance their

hydrophobicity. Thorough characterisation at different steps of the treatment i.e. (i) after growth, (ii) after ozone treatment and (iii) after silanisation was carried out and the impact of the treatments on the modified membranes analysed. This work was performed at the European Membrane Institute in Montpellier, France.

TEM images in Figure 5-6 show that the as grown CNTs were of high purity and presented homogenous and regular crystalline walls (Figure 5-6-a). After 10 and 30 min of ozone treatment (respectively Figure 5-6-b and -c) the outer walls were degraded and defects, in the form of hydroxyl and carboxylic groups as well as vacancies, were formed in the structure. Aggregates were visible after silanisation which was attributed to the alkyl chains of the alkoxysilane molecules (Figure 5-6-d). Amorphous carbon was visible on the outer shells of the CNTs after ozone treatment and seemed to be reduced after silanisation. The presence of the alkyl chains led to less sharp imaging by screening the electro beam from the crystalline walls as seen in Figure 5-6. Presence of silicon was assessed by EDS on the surface of a CNT using the TEM (insert 2 in Figure 5-6). The amount of silicon was small but greater than that of the raw nanotubes (insert 1 in Figure 5-6) The presence of copper is attributed to the copper TEM grid on which the CNTs were deposited.

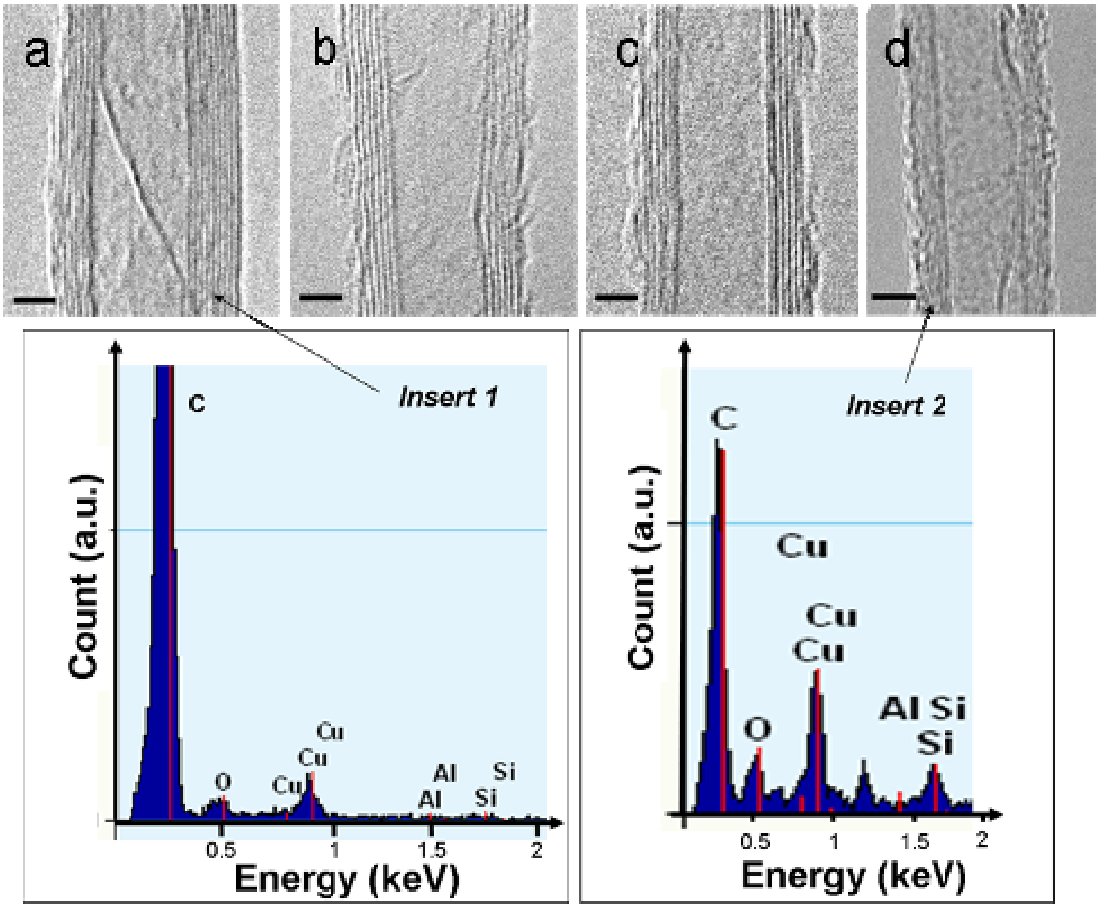

Figure 5-6 Transmission electron micrographs taken at 100 keV. The scale bar represents 5 nm. a: non treated CNTs; b: 10 min ozone treated CNT; c: 30 min ozone treated CNT and d: 30 min ozone treated CNT after silanisation. Insert 1: EDS of as grown CNTs; Insert 2: EDS of silanised CNTs

Raman spectroscopy showed a decrease of the G band at 2750 cm^{-1} with increasing treatment. The G-band was shown in previous work to correlate directly to the amount of defects being created on the CNTs [17-20] (Figure 5-7). In this case it confirms the fact that functional groups are being grafted on the CNTs outer walls.

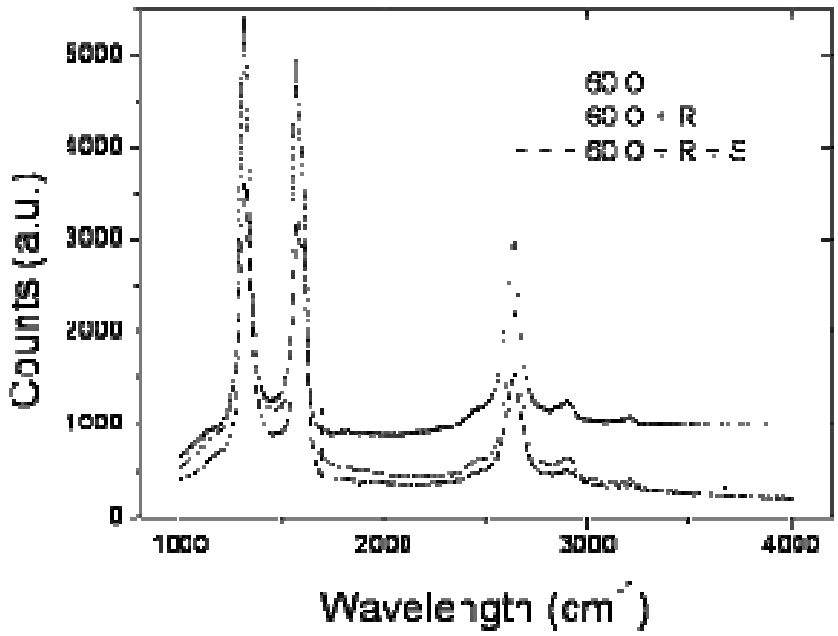

Figure 5-7 Raman spectra of CNTs before and after silanisation; O = ozone treated only, O+R = ozone treated + reduced, O+R+S = ozone treated + reduced + silanised; The D and G band lie respectively at 1350 and 2750 cm^{-1}

Furthermore, the presence of silane groups after treatment was confirmed by FTIR (Figure 5-8). Bands at 2848 and 2921 cm^{-1} appeared after silanisation and were attributed to the stretching of Si-O groups present on the GPTMS [213]. Even though the signal was weak due to high signal noise, these groups were still present on the samples even after rinsing away excess GPTMS and washing the bucky-papers, thus indicating the GPTMS was grafted to the CNTs.

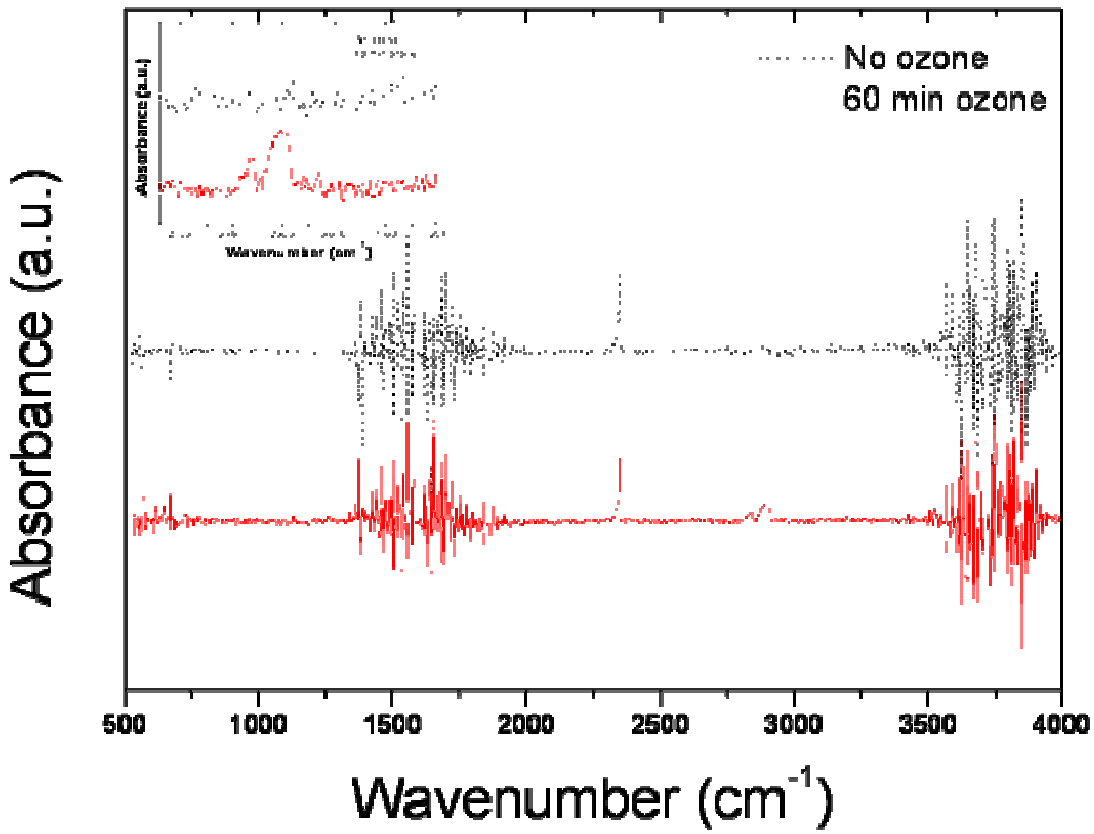

Figure 5-8 FTIR spectra for as grown (top curves) and alkoxysilane modified CNTs (bottom curves – UV treated, reduced and silanised) after 60 min of UV/ozone exposure; the insert corresponds to a zoom from 2700 cm^{-1} up to 3100 cm^{-1}

XPS was performed on the surface of the CNTs at different stages of their treatment. As shown in Figure 5-9, before silanisation the content of oxygen increased as a function of UV/ozone exposure time. The amount of oxygen present, attributed to both hydroxyl and carboxylic acid group formation on the CNTs, went up to ≈4.2% after 30 min of UV/ozone exposure while the silicon content remained low and constant. Oxygen atoms were attributed to both hydroxyl and carboxylic groups thus justifying the reduction step before silanisation to reduce the acid groups. The oxygen/carbon ratio decreased after silanisation which was attributed to the alkyl chains present from the GPTMS (Figure 5-9). Furthermore, the Si/C ratio of the silanised CNTs was a factor of 3 greater than the raw nanotubes. This directly correlates with hydroxyl groups being attacked to form the alkoxysilane groups on the surface of the CNTs [213, 336].

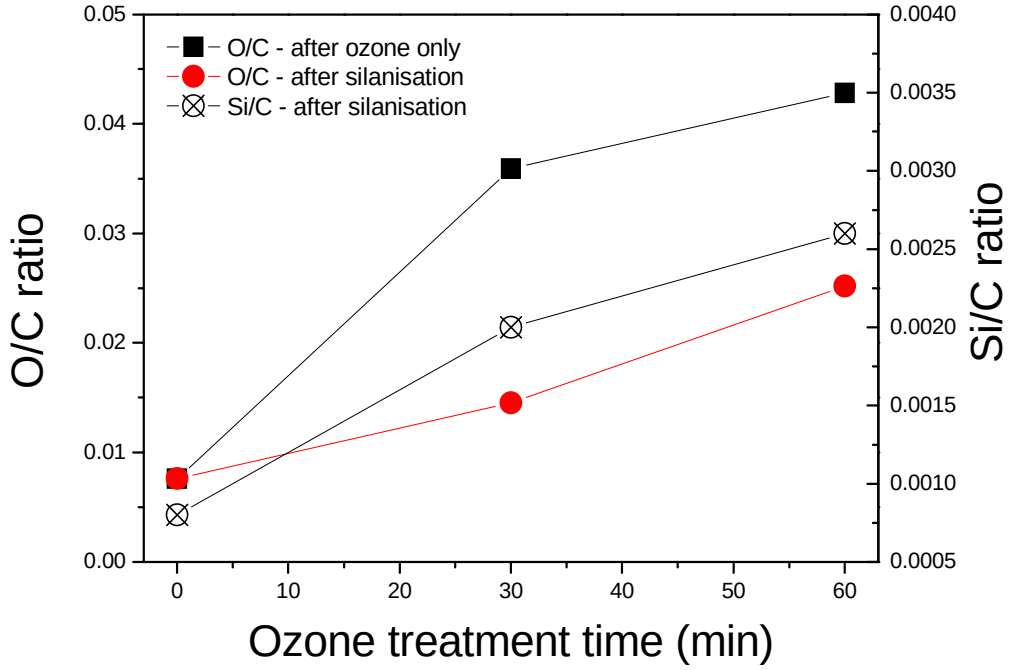

Figure 5-9 XPS analysis showing the oxygen/carbon and silicon/carbon ratios on the hydroxyl-functionalised CNTs before and after silanisation

Furthermore, TGA performed on both hydroxyl and silanised functionalised CNTs, between 20˚C and 900˚C showed (i) presence of residuals (2-3%) after carbonization above 600˚C, which was attributed to the presence of silicon and (ii) increased oxidation resistance as the CNT decomposition temperature shifted from 515˚C to 555˚C. The improved thermal behaviour was related to the lower number of reactive sites (hydroxyl groups and amorphous carbon) after silanisation as well as the higher thermal stability of silicon compared to carbon. TGA curves of non functionalised CNTs, as displayed in Chapter 4, show residuals of less than 1 % thus confirming that the presence of extra materials on the CNTs.

Contact angle measurements were obtained for bucky-papers fabricated at various stages of the CNTs life: after growth, after ozone treatment and after silanisation. The as-grown CNTs offered an average contact angle of 120˚ clearly indicating their natural hydrophobicity. After UV/ozone exposure the contact angle dropped gradually as a function of ozone exposure time down to 30˚ after 60 min of ozone treatment. This trend was expected due to the hydroxyl and carboxylic groups present. After silanisation the CNTs hydrophobicity was found to be enhanced relative to the

as-grown CNTs and contact angles between 135˚ and 140˚ were measured (Figure 5-10). The practical impact of these surface energy changes were evidenced by conducting direct contact membrane distillation experiments.

Furthermore the LEP drastically increased after silanisation. As grown CNT BPs exhibited LEP of ≈193 kPa while silanised CNT BPs LEP increased to 441 kPa (Table 5-9). The silanisation, therefore, helped improve the stability of the membrane over pressures larger than that applied during DCMD. The higher LEP is correlated to the improvement of the hydrophobicity as more pressure is required to permeate water through the membrane.

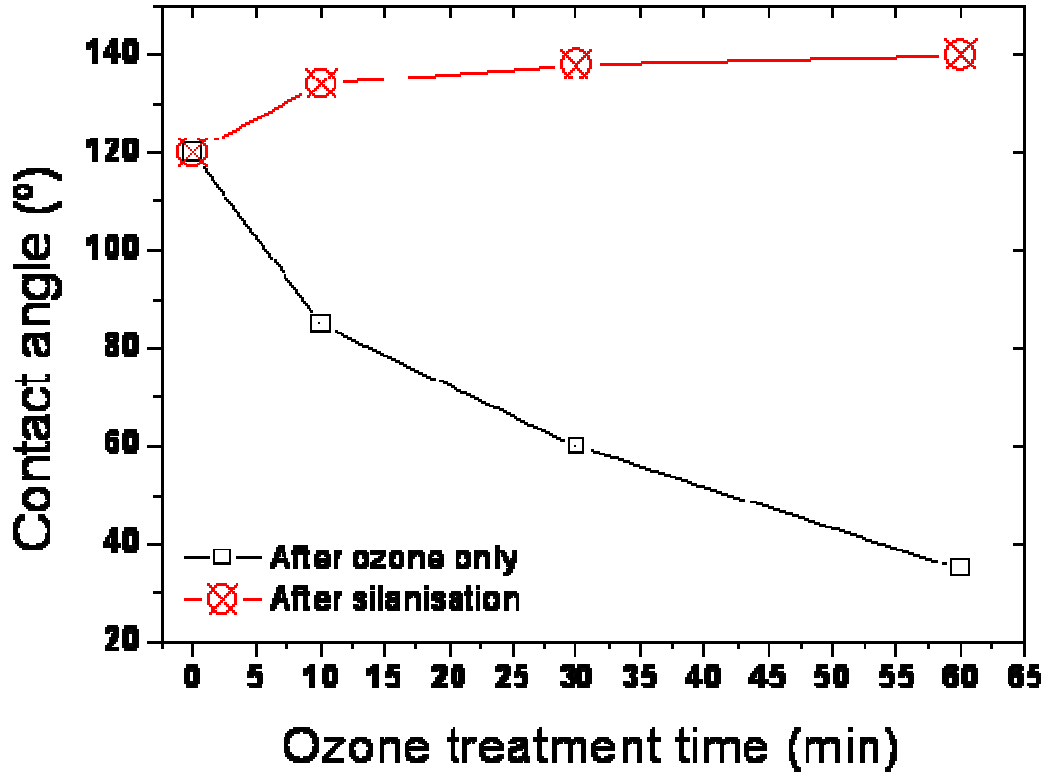

Figure 5-10 Contact angle with deionised water. Samples (i) after hydroxyl grafting and (ii) after silanisation

Comprehensive characterisation of the alkoxysilane functionalised CNTs and of BP membranes at different stage of their treatments was performed. A simple two step alkoxysilane treatment permitted recovery of the hydrophobicity of the UV/ozone modified CNTs. Furthermore, the alkoxysilane modified carbon nanotube membranes presented increased hydrophobicity compared to their untreated counter parts which is likely to result in increased lifespan and permeability. Up to 4 w% of alkoxysilane chains were grafted on

the CNT surface but a higher surface coverage might be beneficial to further increase the hydrophobicity and performance.

In fact deeper penetrating pre-treatments on the CNTs such as high energy X-Rays, plasma or gamma irradiation could lead to a treatment over the whole thickness of the BP. This could possibly lead to a higher number of hydroxyl groups on the CNT surfaces. Also coating with more hydrophobic additive materials such as fluoro-silane is a suggested route to engineer super-hydrophobic surfaces, and this is discussed next.

5.2.2.3 Fluorosilane modification

Fluorosilanes, FAS 17, were grafted through a sol-gel approach, similar to that of the alkoxysilane, onto the CNT outer walls. However to create more active sites onto the CNTs, the BPs were exposed to high energy X-Rays at the Italian Synchrotron. The X-ray treatment and the sol-gel process treatment were performed in Italy at the Italian Synchrotron by Benedetta Heinz, Dario Buso and Paolo Falcaro. A schematic of the process is shown in Figure 5-11.

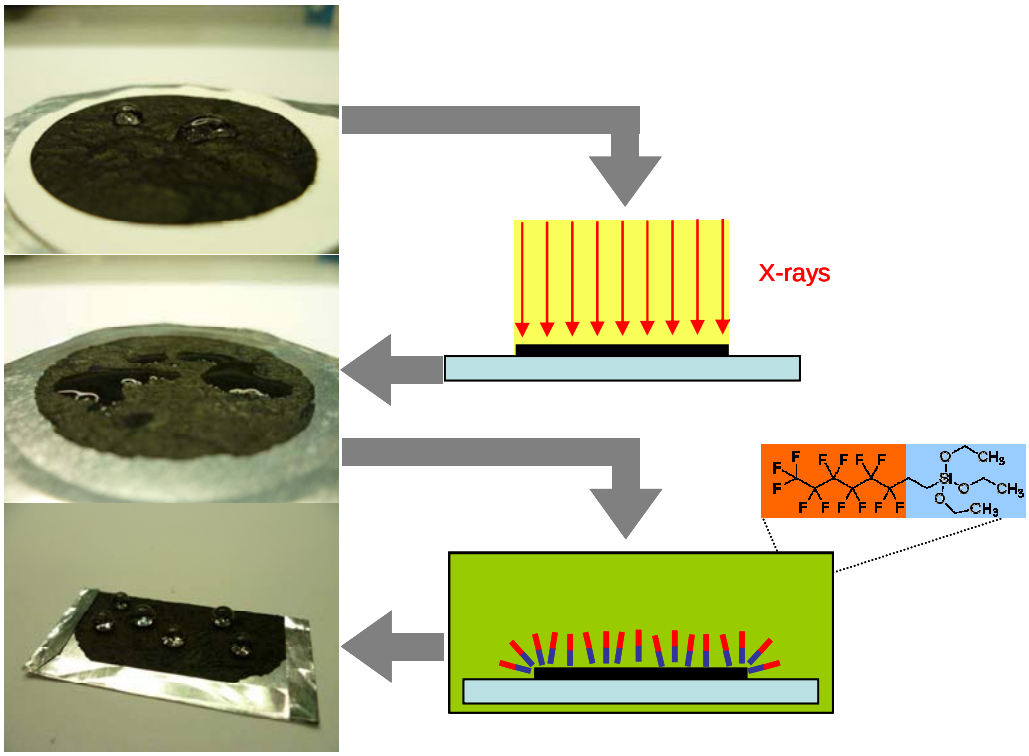

Figure 5-11 Schematic diagram of the BP functionalisation and the impact of X-rays on the hydrophobicity

Hydroxyl groups were created on the CNTs surface via X-Ray exposure thus making the surface highly hydrophilic. Then the sample was dipped into the fluorosilane solution and reacted overnight to graft the chains to the CNT surface.

The contact angle was estimated from droplet images in static and dynamic mode. The change in contact angle is clearly visible between the images in Figure 5-12. The contact angle for the non treated surface was found to stand between 115 and 120 º. After X-Ray exposure the contact angle sharply dropped due to the enhanced hydropillicity and was measured at less than 50 º in static and rapidly decreased down to 22 º after 30s of test in dynamic mode (Figure 5-13). The contact angle after fluorination increased to more than 140º thus clearly showing the impact of super-hydrophobic chains on the BP surface energy.

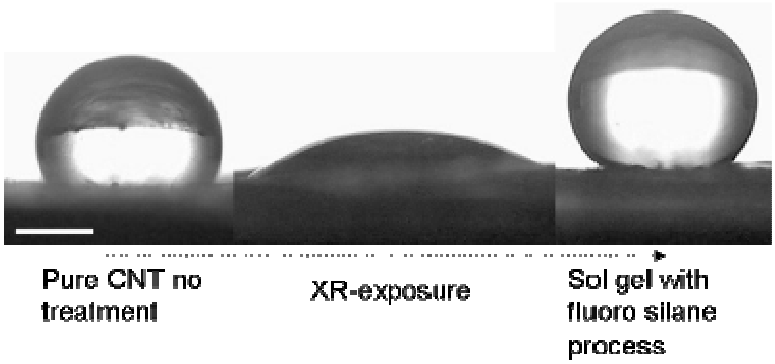

Figure 5-12 Contact angle on non treated, X-Ray exposed and fluorosilanised BPs. The scale bar represents ~500 µm

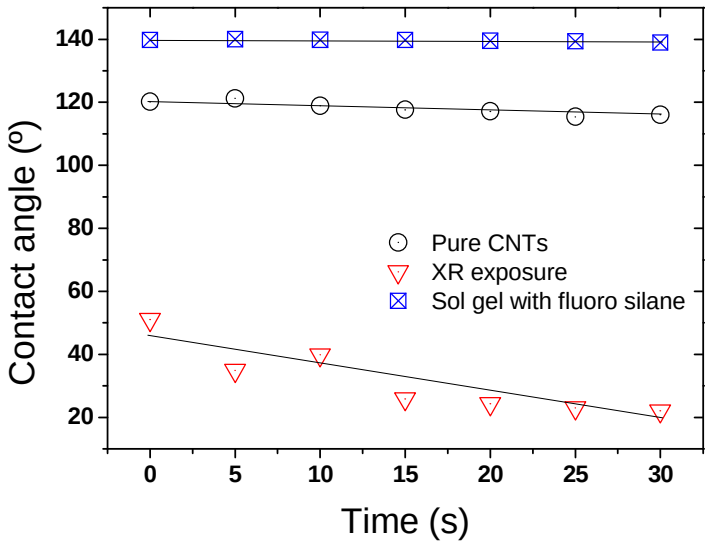

Figure 5-13 Contact angle results for the 3 tested membranes

The samples were characterised by XPS to analyze the presence of hydrophilic groups. This showed that hydroxyl and carboxylic groups are present over the surface after X-ray exposure while fluorine was confirmed after fluorination. The sample was tested on both sides and no major difference was found verifying the X-rays penetrated the whole structure and chemically modify the CNTs.

These CNTs were unfortunately not processed in sufficient amount to fabricate enough BPs for testing. It does demonstrate that many routes are available to modify the hydrophobicity of the CNTs and potentially improve the BP performance in DCMD.

5.2.3 Changing the pore size and porosity of BP

Controlling pore size and porosity is of prime importance to engineering structures for improved separation performance with specific surface properties. In this section composite material structures made of CNTs with reproducibly engineered macro-pores inside their structure were processed. Several approaches were undertaken to change the specific surface area of the material, increase both average pore size and porosity. This section will present 3 distinct studies. The impact of the addition of latex nano-particles in the BP structure and their removal from the membrane was investigated.

Then the opportunity to mill pores by a lithographic approach is presented. Finally, the impact of gold nanoparticles, grown inside a BP, on the porosity, pore size and surface energy will be presented. Even though most of the work was focused on fabricating better BP membranes for water desalination several studies were also focused on changing the gas adsorption properties by growing gold nanoparticles within the pore of the BPs. These samples were tested for gas permeation and gas adsorption as their surface energy was found to be not suitable for desalination.

5.2.3.1 Sacrificial beads addition

Highly porous BPs were fabricated from pure CNTs by dispersing and stabilizing polystyrene beads within a CNT suspension. The polystyrene beads were then either dissolved or carbonized to generate macro pores of different shape and properties. Comprehensive sample characterisation was performed and the impact of tuning porosity is demonstrated.

As shown in Figure 5-14 1 and 2, Focus Ion Beam milled cross sections of the reference, non templated BPs, the CNT distribution is very even and neither cracks nor macro-bundles were present in the structures (Figure 5-14). After addition of the beads, the composites were shown to be composed of successive layers of beads, evenly distributed in small clusters with denser layers of nanotubes (Figure 5-15 - A1 and A2). Furthermore, the presence of the beads greatly changed the global morphology of the BPs, clearly creating macro voids and pockets within the structure as shown after carbonization (Figure 5-15 - C1 and C2). In this case, macro voids were formed in the sites of the beads thus forming cavities of size equal to the diameter of the beads. Additionally, the dissolution of the beads led to the collapse of the cavities, which was attributed to the strong solvent/CNT interactions and to the PS wicking in such a confined spaces (Figure 5-15 - B1 and B2).

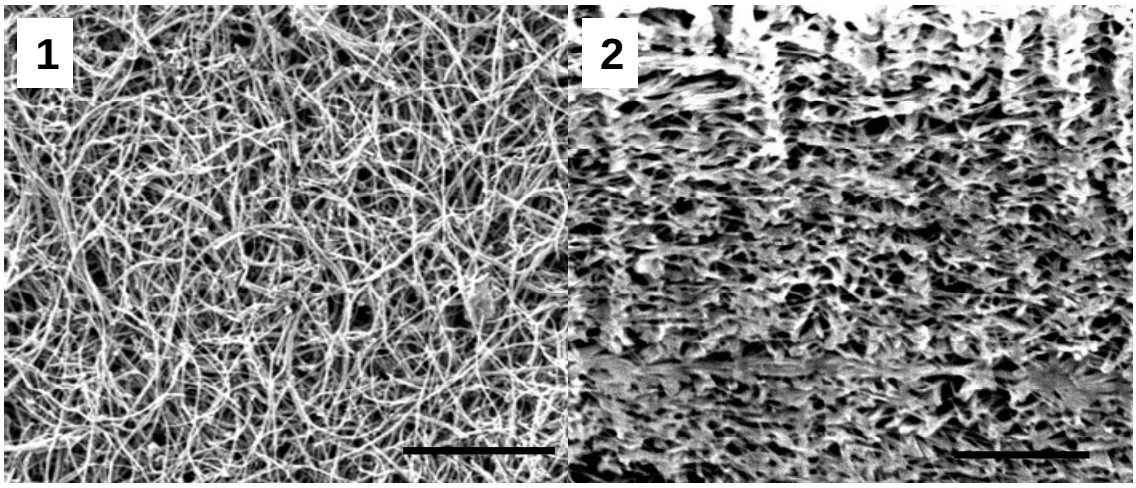

Figure 5-14 SEM micrographs of non bead reinforced BP. 1: surface; 2: cross section. The scale bar corresponds to 1 μm

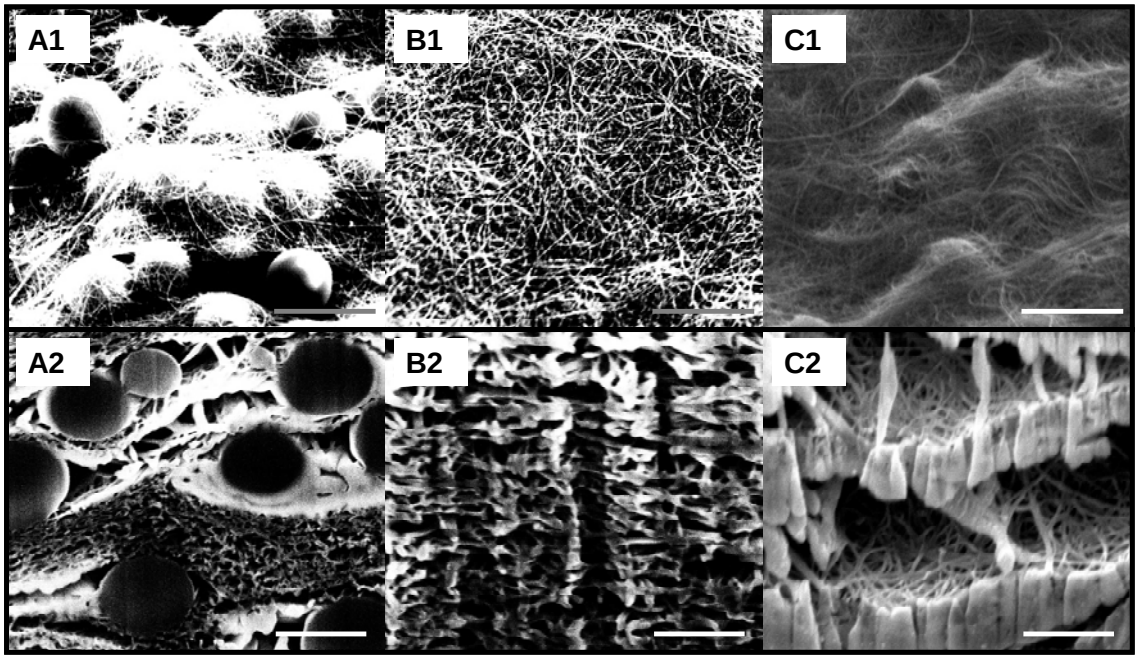

Figure 5-15 SEM images of BPs surface and cross sections for 1 μm poly-styrene bead reinforced BPs. Images A1 and A2 correspond to the composite after filtration of the bead/CNT suspension, while B1 and B2 were taken on samples after bead dissolution, and C1 and C2 on the bead/CNT composite after carbonization. The micrographs were taken at a tilt of 52º. The scale bars on the micrographs correspond to correspond to 1 μm

The pore size distributions of the membranes are given in Figure 5-16. As previously demonstrated the pore size distribution of BP structures can be precisely determined by perm-porometry. The distributions tended to narrow after either dissolution or carbonization of the beads compared to the non-treated bead/CNT composite. The average pore size decreased from 37 nm down to 32 and 33 respectively (Table 5-3). This trend was attributed to the fact that the beads form a non-continuous network across the BPs. Pore size was not increased since the beads did not for a fully interconnected 1 µm large network.

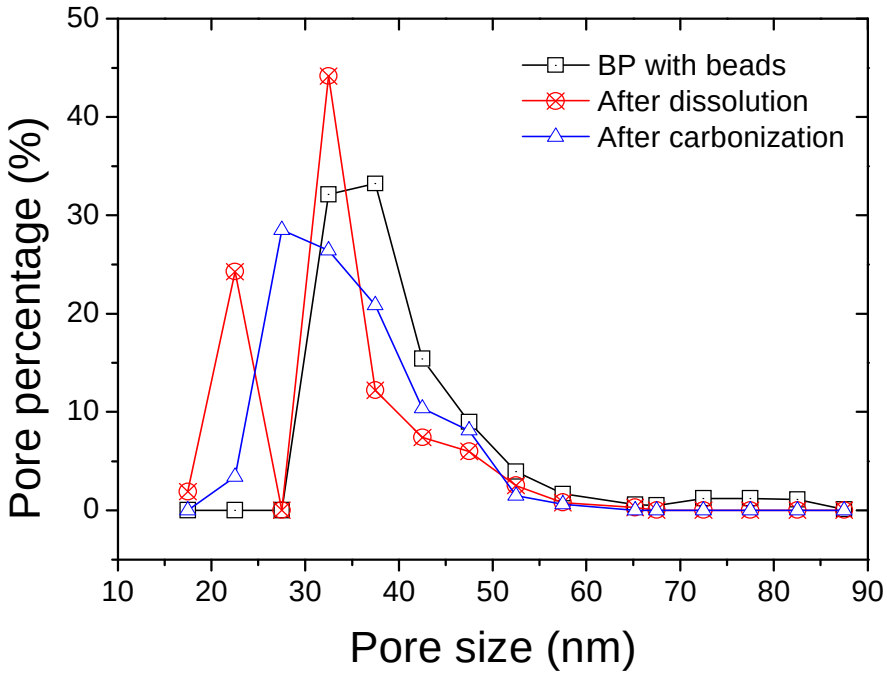

Figure 5-16 Pore size distribution of the bead reinforced BPs

Furthermore, the bubble point of the structures sharply increased after dissolution or carbonization. This was attributed to the tighter pores. Decreased specific surface area was obtained after both dissolution and carbonization, confirming the impact of the beads on the materials porosity and available surface area (Table 5-3). This trend was previously reported for infiltrated BPs [278] where PS/CNT composites were found to have specific surface areas up to 70 % lower than self-supporting BPs.

The pore size shift and as the specific surface area reduction were attributed to the fact that all the beads were not fully removed and that part of

the PS stayed within the pores. This added mass reduced the available surface area, thus diminishing the specific surface area of the samples.

Contact angle measurements performed on the composite membranes showed that the addition of beads lead to an increase in surface energy. The carbonized samples were the most affected with a contact angle about 30º less after carbonization. This was attributed, respectively to the polystyrene presence for the dissolved composites and to the amorphous carbon formation for the carbonized samples.

Table 5-3 Bead reinforced composites properties

	Thickness	Modulus	Average pore size	Bubble point	Contact angle	BET
	µm	GPa	nm	kPa	º	m2/g
BP reference	10 (+/- 2)	0.95	32	783	120	197
BP + beads	8 (+/- 3)	0.35	37	532	118	90.7
BP + beads dissolved	7 (+/- 2)	0.21	32	735	105	135.6
BP + beads carbonized	6 (+/- 3)	0.99	33	760	92	97.5

Typical tensile extension graphs showing the tensile behaviour of composite BPs are displayed in Figure 5-17. The modulus of the structures was found to decrease after simple addition of beads or bead dissolution while it increased after carbonization as reported in Table 5-3. As shown in Figure 5-15, shells of carbons were formed at the sites of the beads after carbonization. The increased modulus was attributed to these carbon shell formations, bridging and linking CNT on a micrometer scale. The semi-dense shells likely gave more cohesion and stiffened the composite as compared with the non treated BP reference in Table 5-3.

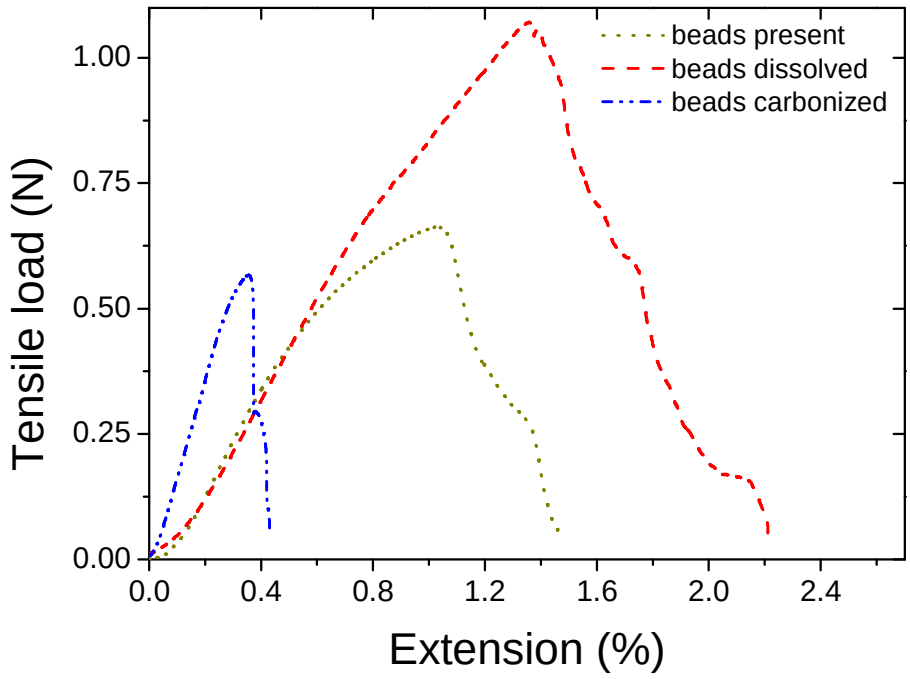

Figure 5-17 Tensile/extension typical curves for the series of reinforced BPs

5.2.3.2 Focus Ion Beam milling

Focus ion beam milling was also performed to form straight pores across a BP sample. The pores were milled with a 0.7 nA power Ga beam and were 500 nm wide for a length of ~5 µm as shown in Figure 5-18. The BP was purposely processed thin to limit the impact of aspect ratio on the milling. It demonstrated that BPs were stable enough to allow direct lithography on their surface. Unfortunately neither permeation nor DCMD tests were performed on this membrane since it was torn because of mishandling before being tested.

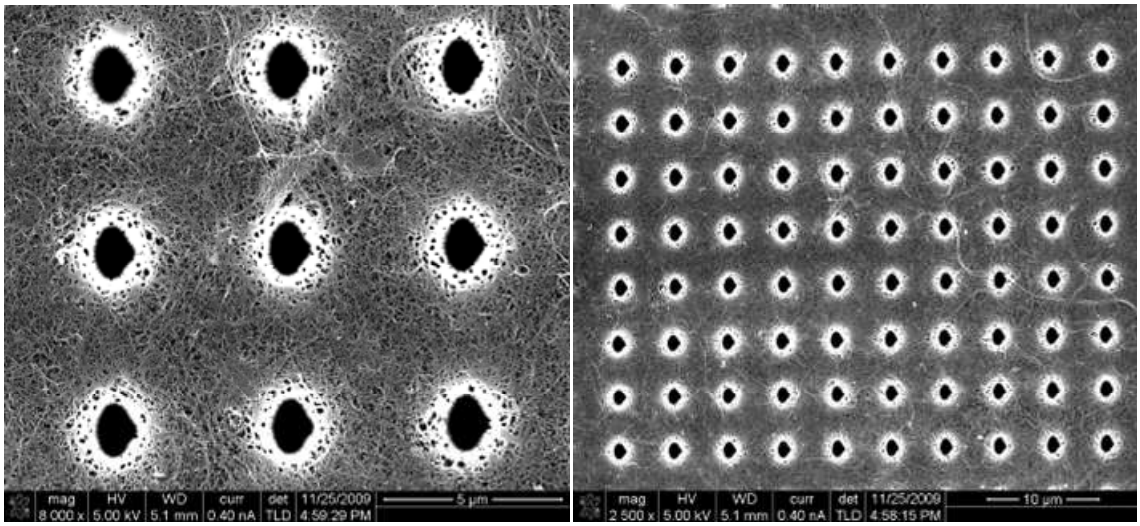

Figure 5-18 FIB milling across a BP

5.2.3.3 Gold/CNT BP composites

The formation of a large number of close but individualised gold nanoparticles in a confined space will lead to a material offering a high efficiency for adsorption [400, 401], sensing [269] or catalysis applications [255, 402]. As previously demonstrated, CNT BPs can exhibit very large porosities up to 90% [73] as well as benefitting from the large aspect ratios of the CNTs to produce high specific surface areas available for nanoparticle growth and lightweight materials [403]. Growing gold nanoparticles on the CNTs side walls within the pores of a BP is a way to maximize the gold deposition within a 3D structure while fabricating a highly light-weight, tough structure. The control of their growth and distribution across the sample as well as their size and site growth distribution is critical, since it will rule both homogeneity of the size distribution and aggregation of the metallic particles.

This approach is a novel technique to potentially engineer gas separation materials offering high surface area of activated material capacity [185, 404, 405]. CNTs large surface area and light-weight structures are combined with gold surface properties [400, 406] to fabricate and control the porosity, pore size and adsorption kinetics of the material by changing the amount and size of gold nanoparticles formed by electroless plating [407] within highly porous CNT BPs. Self-supporting BPs were processed and UV/ozone treated to form hydroxyl groups on the outer CNT walls [259, 260]. The procedure of electroless gold deposition within porous materials has been

described by Martin et al. [408] and was previously used to fabricate pure gold nanotubes [185]. The plating time varied from 1 h up to 30 h, to control the amount of gold deposited, nanoparticle shape and material porosity.

The outer walls of the CNTs showed either partial vacancies or breakages over the length of the samples examined by TEM. Some of these defects were hosts to hydroxyl or carboxylic groups while others were recombined carbons. Amorphous carbon was also visible on the outer walls. The addition of these functional groups was found not to alter neither the geometrical pore size and porosity nor the permeation properties of the membrane.

During ES coating of BPs the coverage of gold is dependent on the number of sites available for the chelation of tin originating from the initial ozone treatment while the deposition rate is dependent on the gold plating bath conditions such as the temperature, concentration and pH. These factors all impact the resulting metal-BP structure. The ES process proved to be a suitable method to produce homogeneous structures, as shown schematically in Figure 5-19.

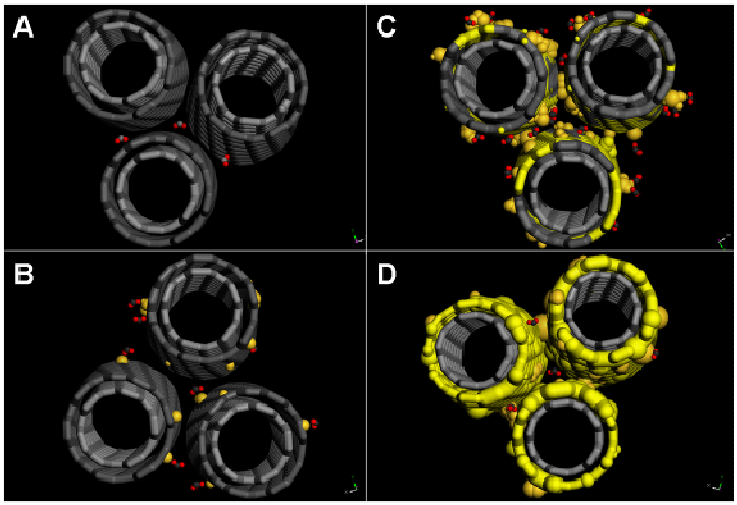

Figure 5-19 Scheme of the gold plating process; A: initial material; B: 1 h; C: 5 h and D: 10 h of plating. Gold nano-clusters form and grow on the CNT outer walls forming a homogeneous and continuous layer at long plating times

The gold content rose from ~10% for 1h of plating up to 90% after 26 h. The slope of the coating rate decreases after 20h and seems to reach a

plateau (Table 5-4) which indicated a progressive decrease in gold deposition in the BP pores. It has been shown that the deposition of electroless gold is preferentially deposited on the surface of the membrane rather than within the confinement of a pore, therefore, once the pore size becomes restricted gold deposition will not be favoured within the BP and hence the deposition rate of gold within the membrane decreases [280]. Furthermore, plating was performed in static mode, meaning that the BPs were immersed and kept in the solution but no flow was forced through their pores once the process started. To sustain a high rate of gold deposition, one would need to inject fresh solution in situ during the test or ensure better flow and homogeneity of the solution across the BP, as lower concentrations of gold near the CNT surface that arises from the deposition process leads to reduced rates of deposition (Table 5-4).

The increase in gold content with time fits well with the decrease in linear resistivity of the BP samples. Table 5-4 presents the impact of the plating time on the electrical resistance of strips of BP. The sample resistance sharply decreased even after the addition of small amounts of gold.

Furthermore, from the TGA results (Figure 5-20), the CNTs were shown to be stable up to 300 ºC and to start decomposing around 500–550 ºC. Residuals, such as possible iron catalysts or other inorganic particles after carbonisation were found to be negligible compared to the carbon mass of the reference samples. In the case of the gold plated samples, the CNTs started decomposing at lower temperatures in the range of 420 ºC to 590 ºC. This was attributed to the presence of the hydroxyl groups and defects created during the ozone treatment which left free sites for attack by oxygen [409].

Table 5-4 Properties of the gold electroless plated samples

Plating time	*hours*	*0*	*1*	*5*	*20*	*30*
Gold content	w%	0	10	28	89	90
Porosity	v%	90	85	78	62	41
Surface pore size	nm	25	25.1	23.5	15.8	7
Resistance	Ohm/cm	924	3.2	1.46	0.1	0.02
Specific surface area	m^2/g	197	305	229	88	37
Gold coating rate	g/hour	0	0.1	0.26	0.09	0.06

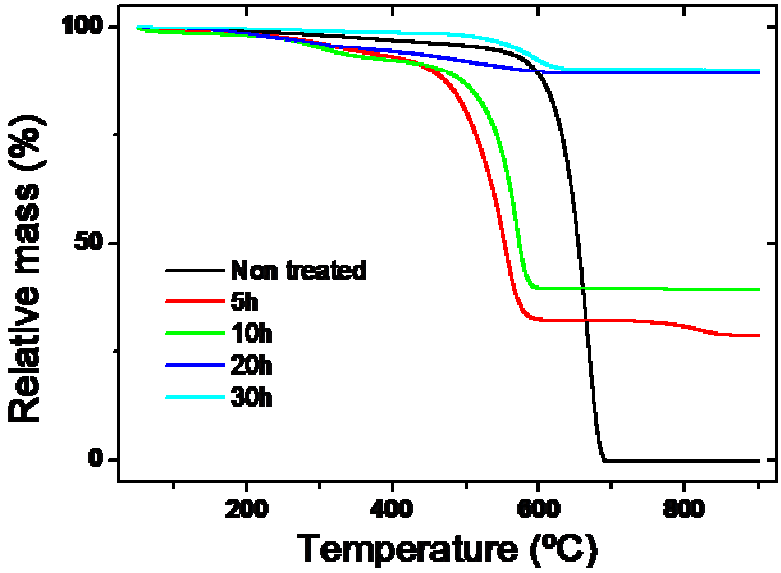

Figure 5-20 TGA analysis results

The internal pores were still available for Helium and N_2 as both pycnometer and BET tests indicated that gas could still penetrate the membranes. The BET surface area increased during the first hours of treatment, which is linked to the presence of a low amount of well dispersed and growing gold nanoparticles across the sample (Table 5-4 and Figure 5-21). The gold nanoparticles have a very high specific surface area which adds to the already large CNT specific surface area. In fact, as the plating continues the nanoparticles grow and coalesce which results in a reduction of the specific surface area of the sample after 5 h of treatment. At longer plating times (above 10 h) the gold begins to fill up the pores, thus reducing the BET surface area to less than the original BP sample. This trend can also be correlated to the electrical resistance of the samples. Even with 1h of plating the electrical resistance is decreased by nearly 3 decades showing that even small amounts of gold can have major impacts on the CNT BP properties and on their potential application. The porosity measurements correlated very well with the trend obtained from the SEM images. Pycnometer tests showed that (Table 5-4 and Figure 5-21) the porosity decreased from 90% for a pure CNT BP down to 40% within the first 30 hours of plating.

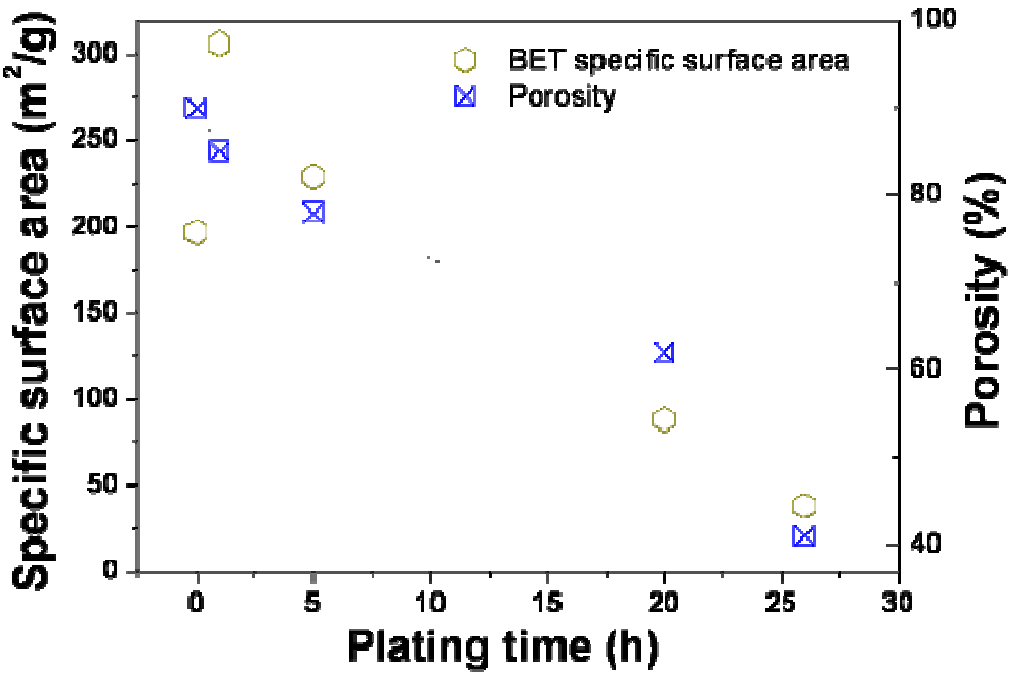

Figure 5-21 The porosity of the BPs was shown to continuously decrease with plating time whereas their specific surface area initially increased by up to 50 % of the reference value before dropping to 25 % of the reference value

Pore size distribution, determined by perm-porometry, was broadened and the average pore size reduced from 28 nm for a non platted reference BP down to respectively 23 and 17 nm after 10 h and 30 h of plating (Figure 5-22). This change was well correlated well with the FIB SEM cross sections taken and presented in Figure 5-23. The homogeneous decrease of pore size, combined with the gold surface energy, leads to interesting structures at longer plating times that could be used for nanofiltration applications.

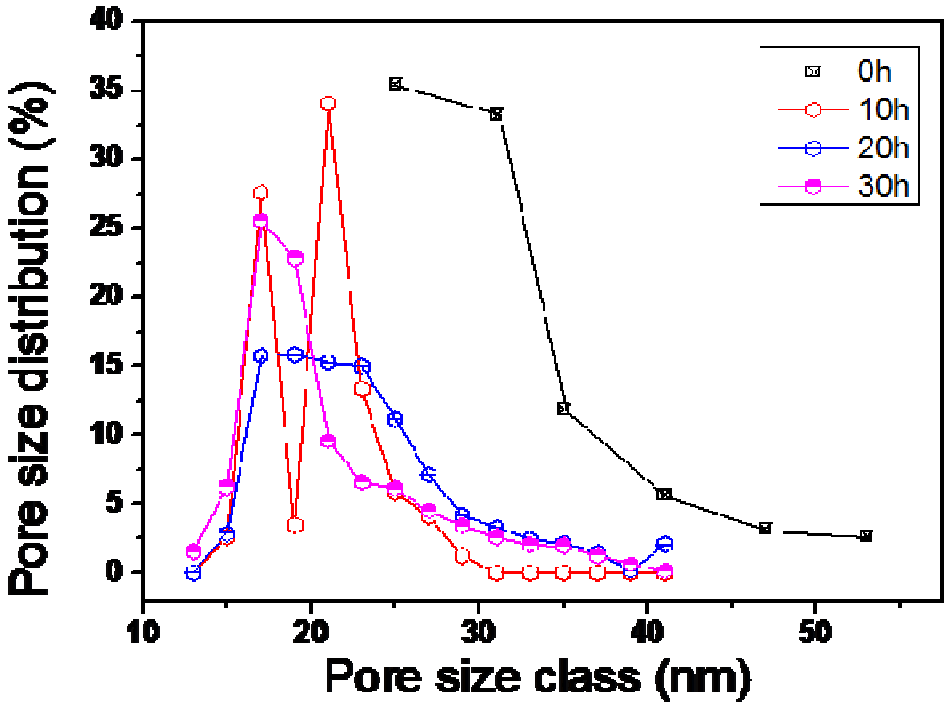

Figure 5-22 Pore size distribution determined by porometry

The inner structure of the BP membranes was revealed by FIB milling the surface of the membranes. As shown in Figure 5-23, the reference was homogeneous and the distribution of CNTs even across the sample thickness. The BPs were infiltrated with the plating solution and gold nano-clusters started forming on the surface and in the bulk of the porous membrane. From these nano-clusters, as shown between 1h and 5h of coating, a homogeneous coating spread on both the surface and in the porous matrix progressively covering the nanotubes and thus forming a continuous layer of gold. The CNTs appeared uniformly coated after 20 h of coating time when nano-clusters start growing onto the exposed gold surface progressively reducing the porosity and closing up the inner pores (26 h).

Gold was first deposited on defects created on the CNTs. From these sites gold nanoparticles grew and covered the CNTs progressively but without filling up the structure or blocking the pores. Figure 5-23 suggests that the structure may remain porous even after lengthy plating times. Particles of gold first deposited on the nanotubes were tin and silver had adsorbed. Their size was found to be close to the CNT diameter for small plating times. After 1 h of plating, gold nano-particles of ~10–30 nm were found on the CNTs. After

approximately 10 h of plating a continuous network was formed inside the BP on the CNTs leading to a new homogenous surface made of pure gold in which the CNTs were entrapped.

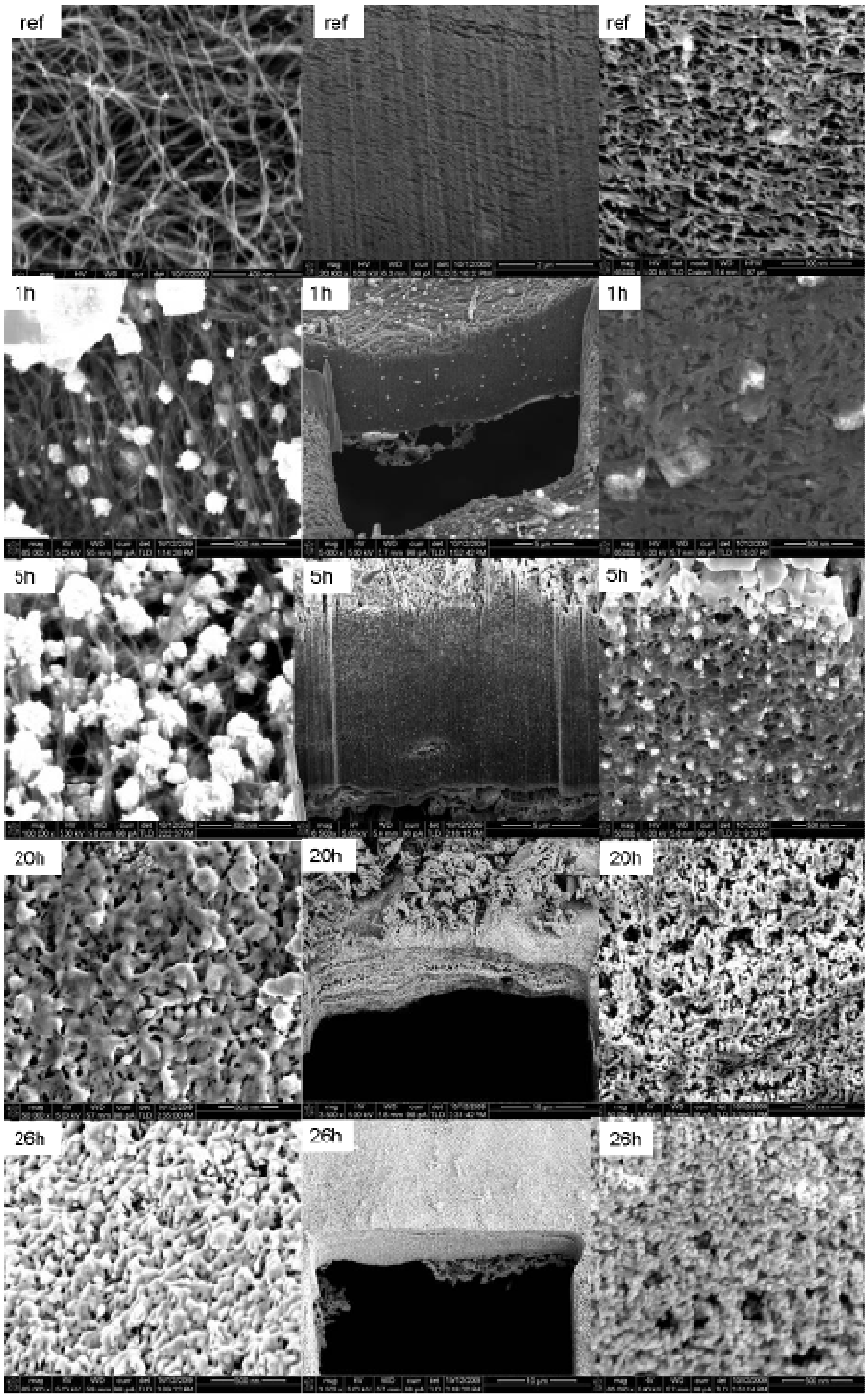

Figure 5-23 Scanning Electron Micrographs taken on a Focus Ion Beam (FIB) SEM. Cross sections were performed at an intensity of 7 nA and images

taken at a tilt angle of 53º. The working distance was 7.5 mm and the surface was not coated with any conducting metal

5.3 Adsorption and permeation results

This section will be divided into 2 main areas to cover all the adsorption and permeation tests performed.

Firstly, the DCMD tested membranes will be presented and the different composite structures compared. The composite membranes will be compared with the PTFE membranes and self-supporting BPs presented in Chapter 4. Then the gas permeation and adsorption results mainly performed on the bead reinforced and gold reinforced BPs will be presented. The gold/CNT composites exhibited interesting gas adsorption properties and their behaviour will be discussed.

5.3.1 Membrane distillation

As presented in the previous section, several structures were specifically engineered for improved DCMD performance. The sandwiched, polymer infiltrated, PTFE coated and alkoxysilane functionalized CNTs are compared in this section. Each composite CNT membrane was tested in the DCMD setup for a range of experimental conditions. Except otherwise stated the water vapor partial pressures, calculated from Antoine's equation and the stream temperatures, were comprised between 5 and 45 kPa.

$$P = e^{\left(23.328 - \frac{3841}{T-45}\right)} \qquad (5\text{-}3)$$

where the vapor partial pressure P is in Pa and the temperature T in Kelvin (K).

5.3.1.1 Flux and permeation

5.3.1.1.1 Sandwiched and infiltrated BPs

While self-supporting BP membranes presented fluxes of 6 to 10 $kg.m^{-2}.h^{-1}$, the composite membranes showed fluxes of up to 15 $kg.m^{-2}.h^{-1}$. As expected from theory [84] , the flux increased linearly with water vapor partial pressure for each membrane. Permeances were calculated by taking the gradient of the best linear fit to the curves in Figure 5-24. Then, permeabilities were calculated by multiplying the permeance value by the average active layer thickness. Permeability is the most suitable way to compare membranes of different thickness and geometries.

Permeabilities between 1.6 and 3.3 x 10^{-12} $kg.m^{-1}.s^{-1}.Pa^{-1}$ were determined for the composite CNT membranes [410]. These values were up to four times that measured for the pure, self-supporting BP membranes, clearly demonstrating the benefit and potential of composite CNT membranes.

“Sandwiched BP” membranes gave the best permeabilities of all the composite BP membranes, with a value of 3.3 x 10^{-12} $kg.m^{-1}.s^{-1}.Pa^{-1}$. Although the “filtered sandwiched BP” membrane is very similar in structure, its permeability is half that of the “sandwiched BP” membrane (Table 5-5). This resulted from a thicker CNT active layer as those membranes were processed by filtering the CNTs through the PP support so that CNTs likely occupy the pores in the PP support in addition to forming a layer on top of it. The lower permeabilities measured for the “polymer infiltrated BP” membranes are consistent with the characterisation results, which indicated reduced porosity and specific surface area due to the polymer presence.

Furthermore both improved salt rejection and longer lifespan compared with the self-supporting BPs were achieved (Table 5-6). This was attributed to the mechanical reinforcement brought by the PP support and the infiltrated polymers.

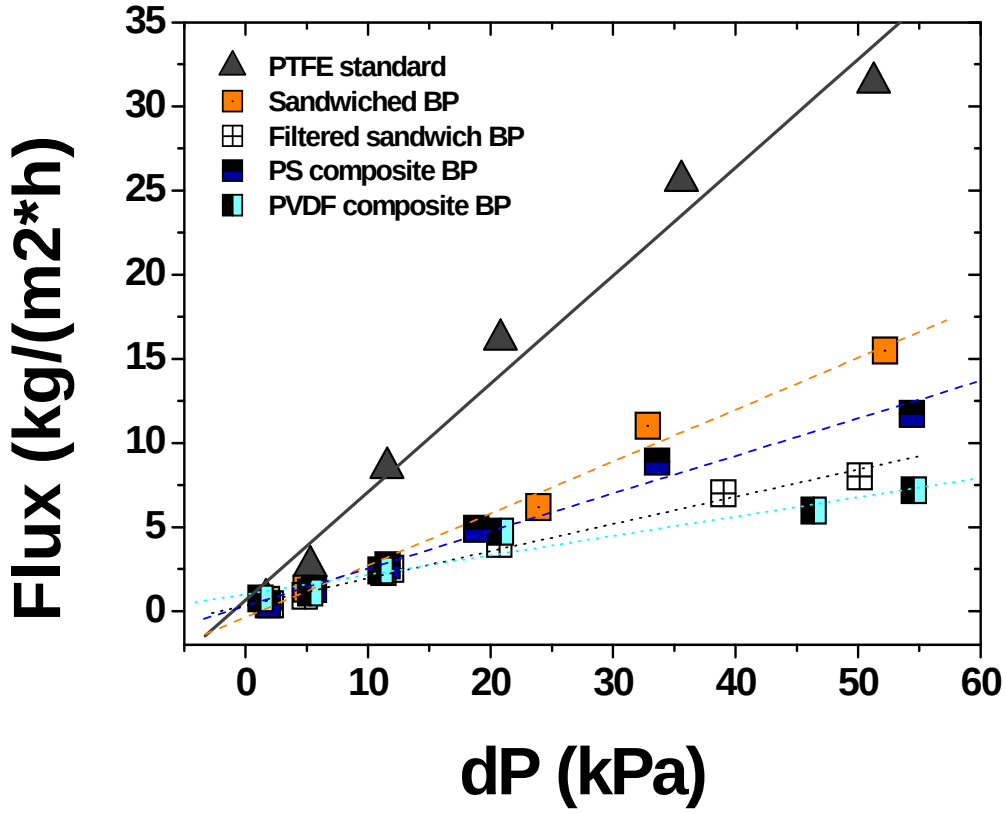

Figure 5-24 Flux as a function of vapor pressure difference (dP) across the membrane. The vapor pressure difference was controlled by varying the hot side temperature (20ºC; 35ºC; 50ºC; 65ºC; 85ºC 95ºC) while maintaining a constant cold side temperature of 5ºC

Table 5-5 Properties of BPs membranes and DCMD results. The thickness was estimated by SEM imaging

	Thickness	Porosity	Permeability
	µm	%	10^-12 *kg.m-1.s-1.Pa-1
PTFE220	~200	70-75	5.51
Self-supporting BP	from 20	85-90	0.83
Sandwiched BP	~120-140	~62+	3.31
Filtrated sandwiched BP	~120-140	-	1.55
Polymer infiltrated PS	~40-80	~55+	2.57
Polymer infiltrated PVDF	~40-80	-	1.89
Poly-propylene support	~100	-	-

Table 5-6 Salt rejection and lifespan of sandwiched and infiltrated BPs

Sample	Salt rejection %	Lifespan hours
PTFE 0.2µm pores	99.9	>40
Self-supporting BP	~ 90	3
Sandwiched BP	95.5	39
Filtrated sandwiched BP	94.7	34
Polymer infiltrated PS	98.5	19
Polymer infiltrated PVDF	96.5	16

5.3.1.1.2 PTFE coated BPs

The flux across the PTFE coated membranes was found to increase linearly with the water vapor pressure gradient. The square regression coefficients for best linear fit were reasonably close to 1 and respectively found to be 0.98, 0.97 and 0.99 for the Pall-PTFE, self-supporting BP and BP PTFE membranes (Figure 5-25). As shown in Table 5-7, even though the average pore size distribution of the BP PTFE coated was smaller than the Pall-PTFE membranes, their permeability was higher and the membrane exhibited similar lifespan over the timeframe of these experiments and salt rejection.

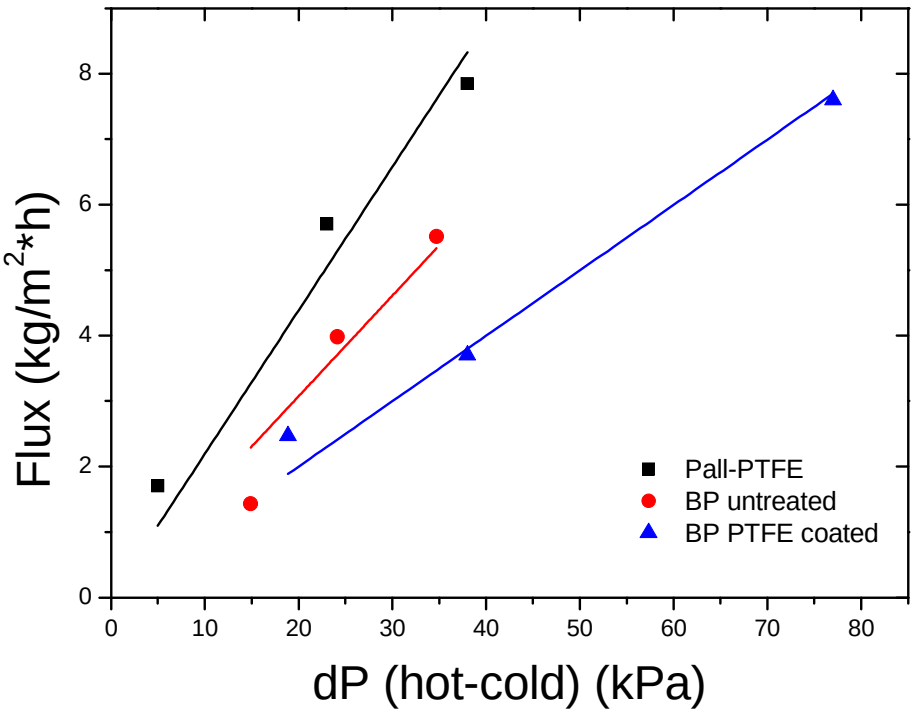

Figure 5-25 Flow across the membranes as a function of the vapor pressure difference (dP) across the membrane. Stream flow rates = 300 mL/min or 0.7 m/s. The hot stream temperature was varied between 55 and 95 ˚C while the cold stream was kept constant at 5˚C

Table 5-7 Permeability and thickness of the membranes

Sample	Thickness μm	Permeability (*10^{-12}) $kg.m^{-1}.s^{-1}.Pa^{-1}$
PTFE20	35 (+/-5)	2.13
BP untreated	45 (+/-5)	1.92
BP PTFE coated	105 (+/-5)	3.05

PTFE coated BPs exhibited improved properties compared to both their untreated counter parts and to commercial membranes (Table 5-8). The difference was attributed to the higher hydrophobicity of the surface and to an increased porosity compared to the PTFE membranes, making these membranes very promising structures for use as separation membranes in membrane distillation. Coating thin layers of polymer on top of carbon nanotube bucky-paper has been showed to be an effective method to improve the mechanical stability and durability of the membranes.

The increase in flux might also be attributed to the formation of a thin air layer between the water and the membrane surface at the interface pore/stream. This behaviour was previously reported for super-hydrophobic surfaces. The increased hydrophobicity would then improve the membrane performance by preventing the water from wicking in the pores and reducing heat transfers and therefore the impact of a temperature polarisation layer on the membrane surface and within the surface pores [411-413].

Table 5-8 Salt rejection and lifespan of the PTFE coated BPs

Sample	Salt rejection %	Lifespan hours
PTFE20	99.9	> 40
BP untreated	97.5 (+/-1.5)	10
BP PTFE coated	99.9	> 40

5.3.1.1.3 Alkoxysilane modified CNTs

A series of silane-functionalised CNT BP membranes were tested and showed improved lifespan, salt rejection and mechanical resistance compared to their non-treated counterparts. As shown in Figure 5-26, the flux across similar thickness membranes nearly doubled in the case of the silanised nanotubes (Table 5-9). The salt rejection of the silanised CNTs membranes was always higher than 97% while the pure CNT BP offered a salt rejection between 95 and 97% (Table 5-10). Furthermore, lifespan of the membranes also increased by more than 50% (Table 5-10), which was attributed to the increased hydrophobicity. As the water had more difficulty entering the membrane, its ability to propagate cracks was inhibited. The presence of the short aliphatic chains helped repel liquid water and thus limited the wetting of the surface pores offering less surface area for water condensation and wicking.

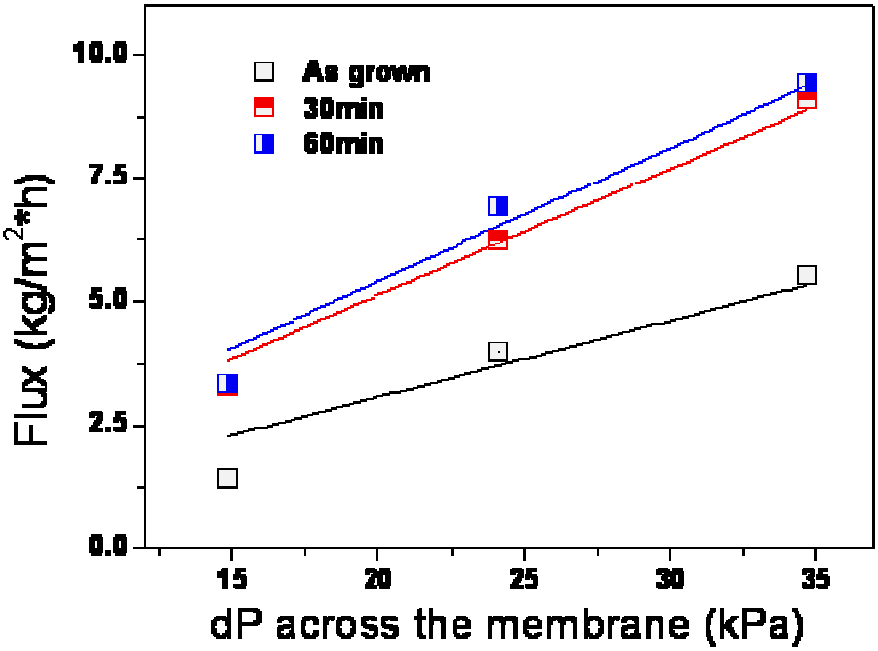

Figure 5-26 Water vapor flux across the alkoxysilane modified CNT membranes in DCMD. The feed and permeate stream flowrates were 300 mL/min. Vapor pressure drops were estimated from temperature measurements at the inlets and outlets of the membrane module. The hot solution was a synthetic seawater solution (3.5 wt% NaCl) while the cold stream was deionised water. The time of ozone treatment is given as an indication of the relative given amount of alkoxysilane grafting (30 or 60 min)

Table 5-9 Properties of the membrane in DCMD. The standard deviation is given when data available.

Ozone treatment time	min	0	30	60
Thickness of active layer (BP)	µm	75 +/- 5	62 +/- 5	60 +/- 5
Permeability (.10^{-12})	$kg.m^{-1}.s^{-1}.Pa^{-1}$	3.19 +/- 0.1	4.39 +/- 0.1	4.5 +/- 0.1
Limit entry Pressure (LEP)	kPa	193 +/- 20	413 +/- 14	441 +/- 14

It is noteworthy that the flux across the membranes is likely to be limited by the membrane support that partially screens the BP surface and considerably increases the membrane thickness. This configuration is, however, a good compromise to test all the CNT BP under the same conditions and to prevent the BP from degrading too quickly as previously shown [278]. The increase in flux was attributed to the higher hydrophobicity

of the material [86, 414] since the water meniscus surface will be increased thus offering more exchange surface available for water evaporation. This also seems to reduce the membrane sensitivity to temperature polarisation as the boundary layer gets expelled from within the pores and more exposed to delaminating from the bulk water flow on the membrane surface. Furthermore, the flux for both 30 and 60 min silanised membranes were very similar. This could be attributed to either the short lifespan of UV/ozone treatments over time, or to the saturation of the surface with hydroxyl groups before 30 min of ozone treatment. The fact that the contact angle tests were similar also confirms this hypothesis.

Table 5-10 Properties of alkoxysilane modified BP

Ozone treatment time	*min*	*0*	*30*	*60*
Average salt rejection	%	96.5 +/- 8	98.3 +/- 2	97.9 +/- 2
Lifespan	hours	10	>15	>15

5.3.1.2 Lifespan and salt rejection

The composite BP membranes exhibited improved salt rejection and lifespan compared with self-supported structures. The lifespan was defined as the time taken for the salt rejection to drop below 90%. Slow rises in permeate conductivity were detected over DCMD tests of less than 40 h and hence a reduced salt rejection, was observed over time for most of the tested BP membranes. This is related to membrane ageing as discussed in greater detail below. The best lifetime of 40 hours was recorded for the sandwiched and PTFE coated composite membranes which was more than 13 times higher than that for self-supporting BP membranes. Most of the composite BP membranes lasted for over 25 hours, whereas all of the self-supporting membranes cracked within 3 hours of continuous testing. This improvement was likely due to the extra reinforcement provided by the PP supports and infiltrated polymers. A typical conductivity rise is shown in Appendix 4.

The average salt rejection was increased from 90% for self-supporting BPs to 95% on average for the composite BP membranes (Table 5-6, Table 5-8, Table 5-10). This salt rejection was averaged over a series of DCMD

tests at different temperatures (i.e. series average from average test salt rejection data). Salt rejection of ~98.5% were usually reached for the first tests in a series at the first set of temperatures but continuous testing progressively led to a decrease of salt rejection as the membrane aged.

While testing self-supporting BPs, it was assumed that the high crack rate propagation was due to mechanical ageing due to the pulsation of the membrane in the module from pressure variations caused by the peristaltic pump, thus reducing efficiency and lifespan of the membranes. The addition of the PP support layers or of infiltrated polymers led to increased stiffness and improved lifespan and more stable membranes. The surface of the sandwiched membranes was also more protected from flux variation because of the protective PP layer, since it was directly exposed to less shearing force. It did, however, reduce their apparent porosity and direct surface of contact, thus diminishing the active transfer surface area of the BPs. Furthermore the addition of hydrophobic chains, in the case of the alkoxysilane modified CNTs and of a highly hydrophobic thin surface for the PTFE coated samples was shown to greatly improve the resistance of the BP to crack formation and ageing. This was attributed to the fact that liquid water was less likely to permeate and wick into the pores. The cohesion forces of a BP have been shown to be entirely related to van der Waals forces. Thus do BPs are held together by both moderate range interactions between the CNTs and degree of CNT entanglement. If a third media, such as water vapor, is introduced, it is likely that the interactions will be diminished possibly leading to CNT displacement s and reorganisations.

Cross sections through the BP structures made by Focus Ion Beam milling clearly show the formation of cracks in some regions (Figure 5-27). EDS analysis indicated the presence of sodium in these cracks, confirming that they form pathways for salty water to cross the membrane from the feed to permeate. Chlorine was not reported since the 5 k eV accelerating voltage used was not sufficiently strong to detect a signal from this element. However, crack formation in the composite CNT membranes was diminished compared to the pure self-supporting structures, with longer lifespan and a slower rate of conductivity increase in the permeate.

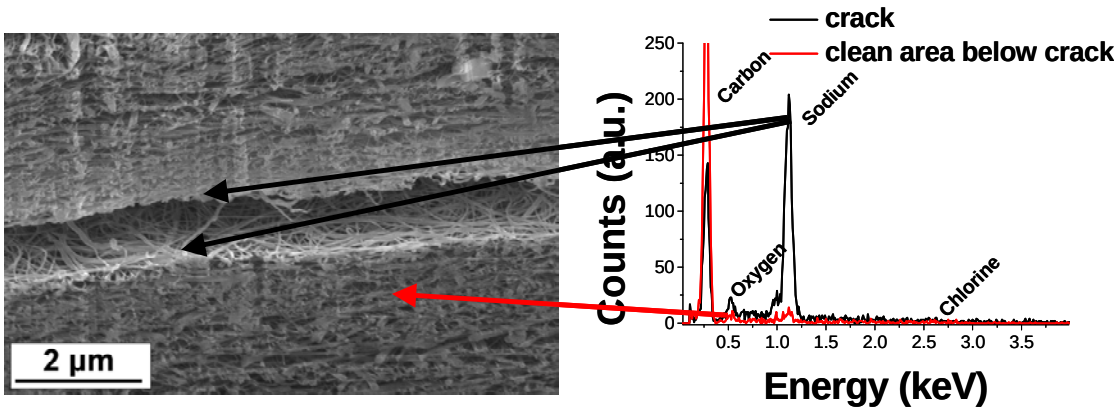

Figure 5-27 Left: SEM image of a section milled with a Focus Ion Beam through a BP membrane after testing in the DCMD setup. Right: corresponding EDS analysis showing the presence of salts in the crack

5.3.2 Gas adsorption and permeation

5.3.2.1 Sacrificial beads addition and removal

Air permeation across the porous structures did not seem to be affected by the presence of beads (Figure 5-28). A very slight decrease in permeance was found after both dissolution (14.5 %) and carbonization (26.8 %) compared with the reference sample which was attributed to the presence of excess organic matter clogging some pores (Table 5-11). In the case of the dissolved beads it is likely that the PS was not completely removed from the static dissolution step and led to bridging and aggregation between CNTs within the BP structure. The polymer presence was confirmed by the FIB SEM cross sections where denser areas were found (Figure 5-15). Furthermore, after carbonization the change in flux was not considered as significant but was attributed to the presence of amorphous carbon being redeposited from the carbonization of the beads as dense shells.

The BET specific surface area was, however, found to be higher after dissolution which is likely due to closed dead end pores at the sites of the beads. Those half closed pores do increase the surface for adsorption but decrease the permeability as no gas can travel across the carbonised beads.

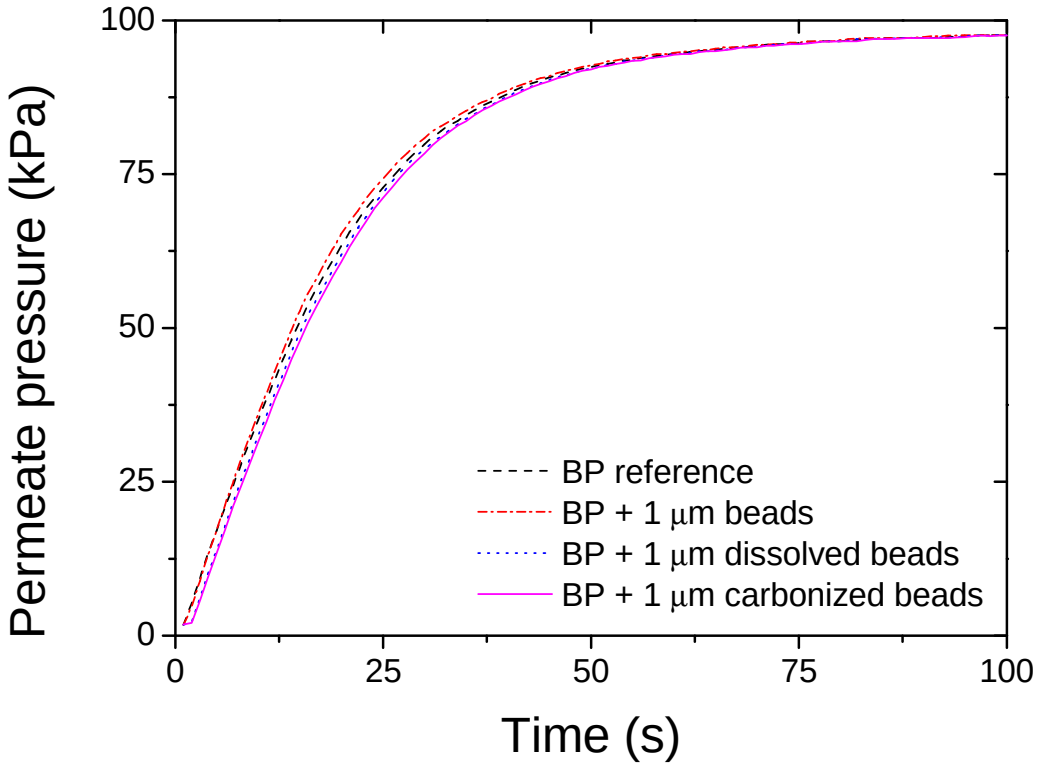

Figure 5-28 Air permeation across the bead reinforced BPs

Table 5-11 Air permeability of the bead reinforced composites

	Permeability .10 -11 $kg.m^{-1}.h^{-1}.Pa^{-1}$
BP reference	2.61
BP + beads	2.55
BP + beads dissolved	2.23
BP + beads carbonized	1.91

The use of sacrificial beads and their removal by carbonization offers several advantages over solvent dissolution since it did not affect the inner structure and did not collapse the macro voids generated at the sites of the beads as this was the case for the solvent dissolution process. Furthermore the structures were also shown to become stiffer after carbonization while retaining most of the other characteristics of non bead reinforced BPs. This was attributed to the amorphous carbons forming bridges between CNTs as shown in Figure 5-15. The permeability of the membranes was shown to slightly decrease after both dissolution and carbonization, which was

attributed to the presence of extra organic matter decreasing the accessible volume for the permeating gas. The increase in tensile modulus presented in Table 5-3 showed that the material was strengthened after bead carbonization thus making them interesting for applications where strong materials are required. A method to remove the amorphous carbon, without altering the modulus, would lead to enhanced permeation membranes and would be required to fully benefit from the created cavities.

These membranes were also tested in DCMD but did not perform well. The beads dissolved BP membranes seemed to be too dense for the water vapor to permeate as no significant flux was achieved even after 5 h of tests. It seemed that either the porosity of the membranes was decreased or the tortuosity of the composite increased so that water vapor did not permeate. Furthermore the carbonized samples leaked straight after immersion, leading to an immediate rise in conductivity on the cold side. The reason for this leakage was attributed to the high surface tension forces due to the cavities present and to the increase of capillary forces. Contact angle measurements performed on all the bead modified structures also showed a decrease in contact angle compared to the self-supporting BPs (Table 5-3). Those structures were, therefore, not considered as useful membranes for DCMD.

The change in inner porosity and the creation of the macro-voids was found to be interesting and potentially to inspire other work. The BP membranes in general exhibit excessively large air permeation to be useful tools for improved gas separation or gas sequestration membranes. However, the presence of macro-cavities could be used for the growth of other nano-particles, or be filled up with a more selective material, such as metal organic framework crystals or an inorganic matrix, for improved separation efficiency.

5.3.2.2 Metal reinforced BPs

Air permeation tests with dried air were performed on a series of metal reinforced membranes. The tests were carried out in a closed system where the feed was filtered, dried air and the permeate chamber evacuated to low pressure. Measurements were conducted by passing dried air through the

membrane from the feed to the permeate side until reaching equilibrium. No significant changes in permeation were observed at the different plating times and an average rate of permeation of 0.06 mol·s–1 (+/– 5 %) was calculated from the curves thus indicating that the change in pore size had no major significance on the permeation (Figure 5-29).

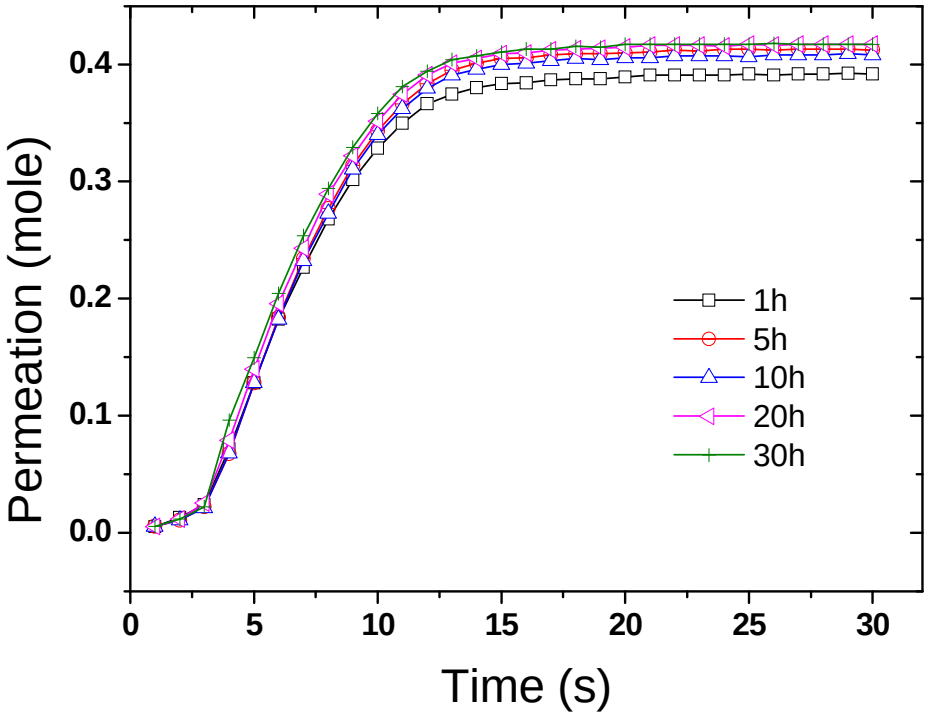

Figure 5-29 Dried air permeation across gold plated CNT BP. The corresponding plating times are given in hours in the legend

The adsorption of several gases (CH_4, CO_2, CH_4, N_2) were tested over the series of samples with different degrees of metal reinforcement.

The 1 h and 5 h plated samples exhibited much higher absorption of CO_2 compared to longer plating times. The highest adsorption at STP was observed for the 5 h plated sample which showed a high affinity for CO_2 as shown in Figure 5-31-A. This in fact did not correlate with specific surface area since the 1 h platted sample exhibited a higher one. The relative ideal selectivities of the other gas over CO_2 were found to vary between 3 and 10 (Figure 5-31-B). This was attributed to the CO_2 catalytic conversion by gold catalysis [415]. CO_2 adsorbed on the gold nano-particles and was converted into hydrocarbon by hydrogenation of the CO_2 from the gold proton donors.

The role of metal particles in this process was previously studied [416-418]. Furthermore it is likely that CO_2 showed much higher selectivity than the other gas because of the high number and good dispersion of the nanoparticles as shown in Figure 5-23. This confirms that the specific surface area of the sample is important and that the particle size and distribution across the sample will determine the gas adsorption. In fact the gold exposed surface, more than the nanotubes seem to control the gas adsorption.

H_2 adsorption was also performed at 77 and 87 K on both 1 h and 5 h plated samples and the enthalpies of adsorption were calculated to be higher than 6 and 10 kJ/mol respectively (Figure 5-32-A). The volume of H_2 adsorbed was found to be maximum for the 5 h plated membranes (Figure 5-32-B) although the specific surface area of the sample 1 h was found to be higher (Figure 5-21). Ultimately, maximized adsorption can be achieved by combining a large number of well dispersed nano-particles within the structure and an optimal nano-particle size distribution. It was show that after the addition of 25 wt% gold, the H_2 storage capacity normalised by gold weight is increased by over two fold (between 77 K and 87 K). This can be attributed to the fact that, although the overall available specific surface area is lower, the number and size of the gold NPs acting on the surface to attract gases for the 5 h treated sample is greater. The hydrogen adsorption should be then considered as a function of the exposed gold surface area rather than of the total membrane specific surface area as the CNTs alone showed least ability to absorb gases. The atomic adsorption of hydrogen by gold has been has been reported [419] and found to be related to the recombination of protons on the atomic gold surface [420, 421]. Here, the volume of gas adsorbed is lowest for the non plating reference sample (Figure 5-32-B) confirming that the CNTs play a role of nano-particle growth support only and do not participate greatly into the adsorption or selectivity phenomenon.

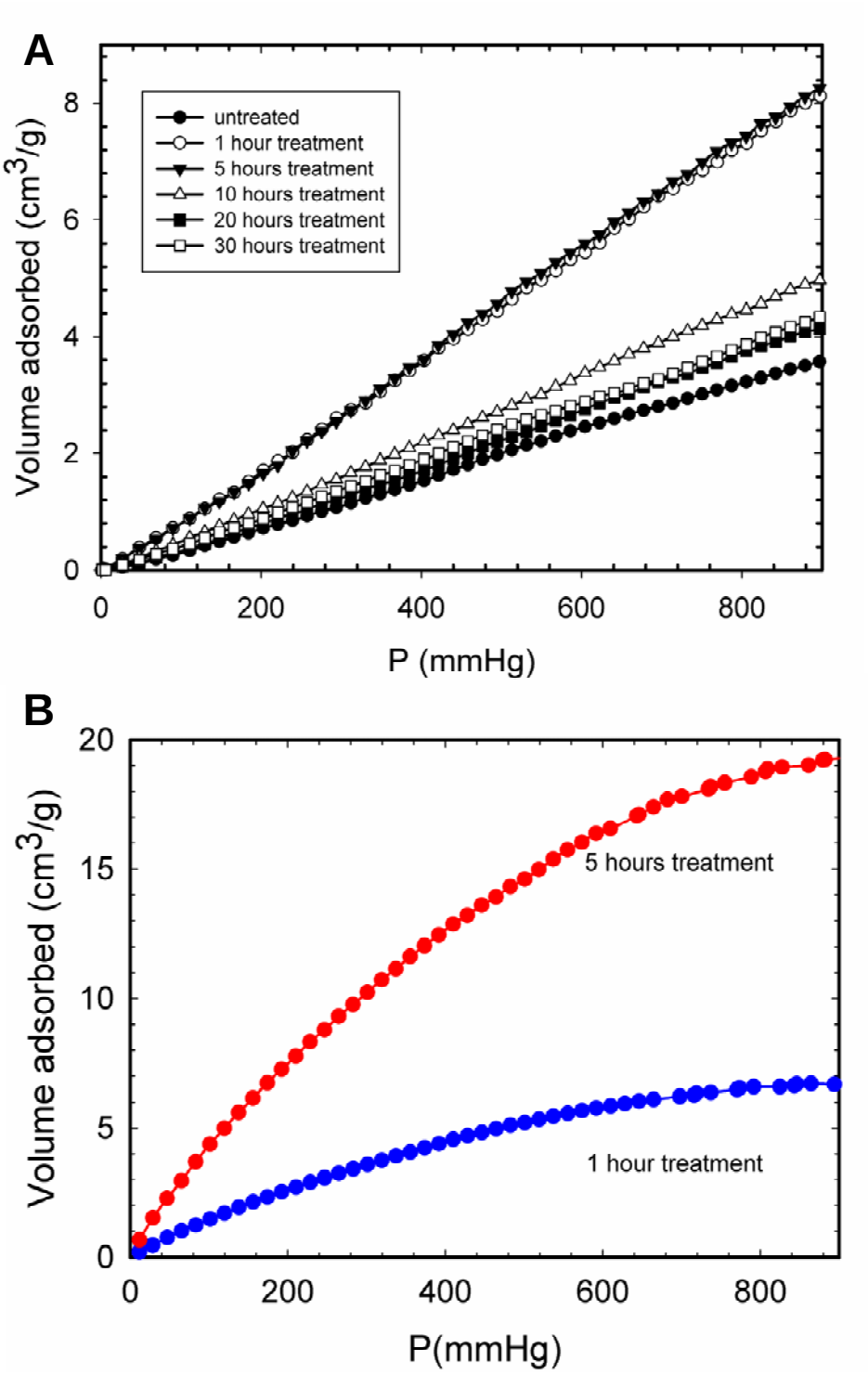

Figure 5-30 A: CO_2 adsorption (volume) on the series of samples; and B: H_2 volume adsorbed at 77 K for the 1 h and 5 h platted samples

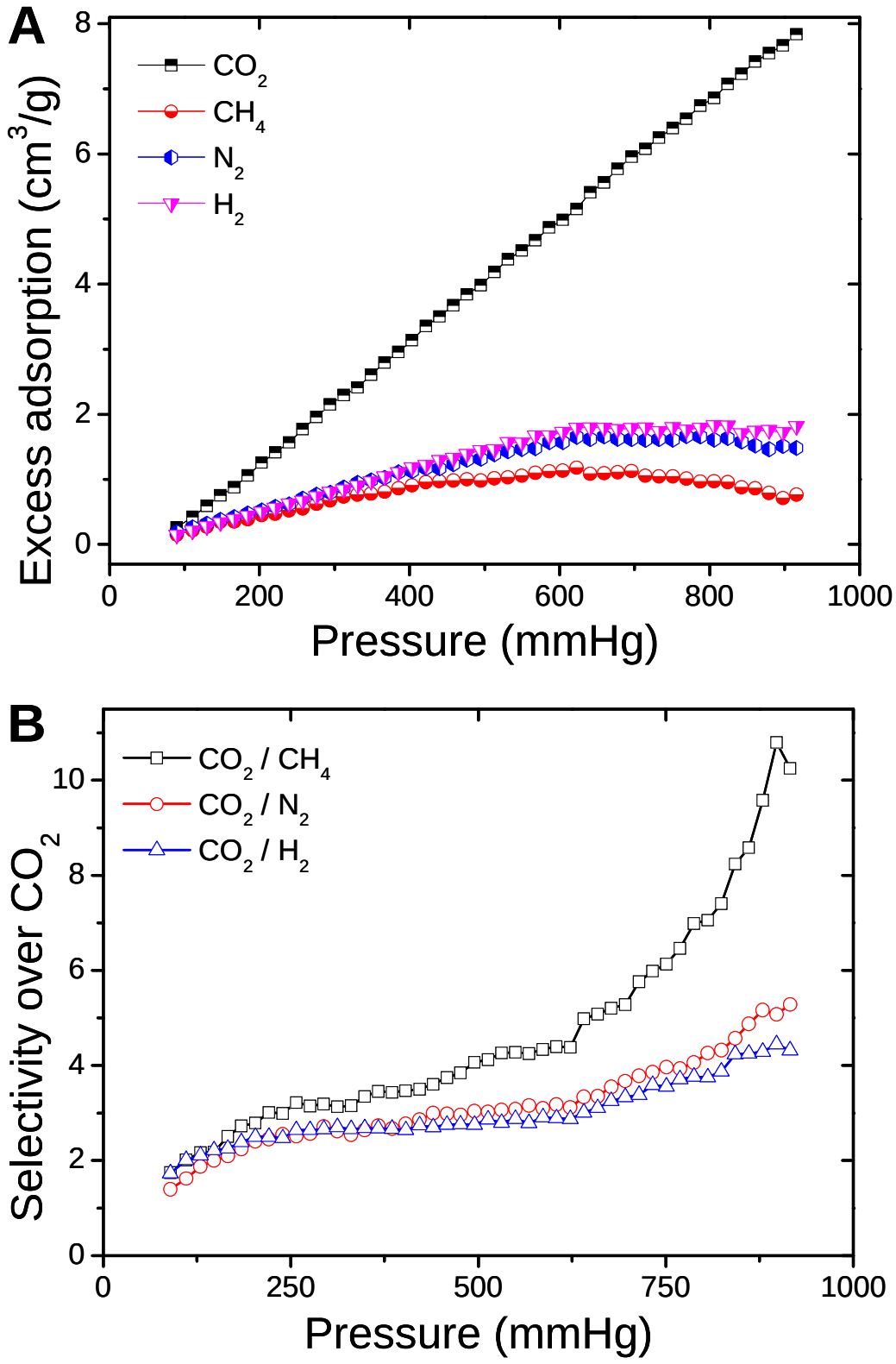

Figure 5-31 Gas excess adsorption (A) and relative selectivity over CO_2 (B) for the 5 h plated sample

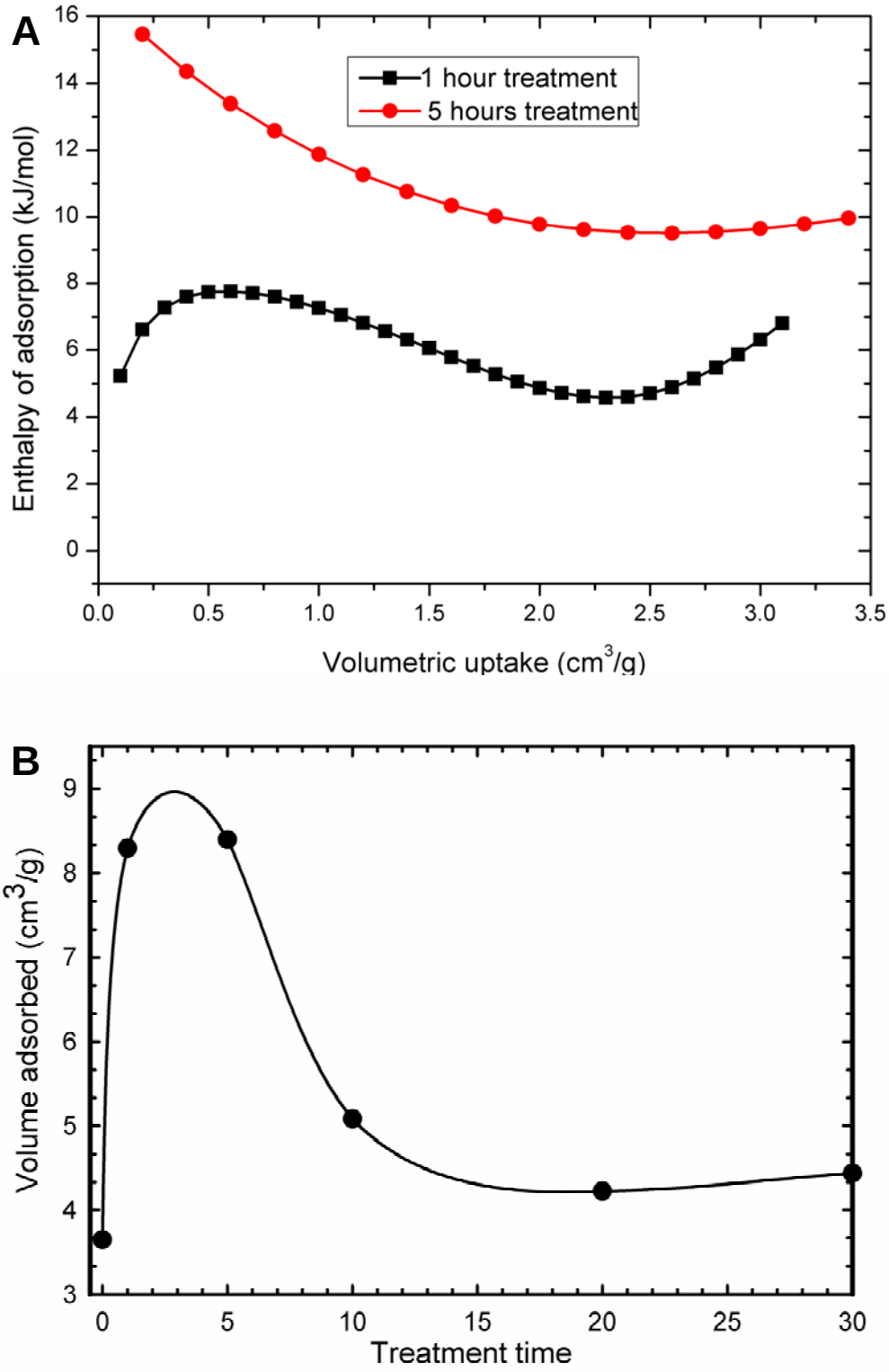

Figure 5-32 A: The 5h plated sample showed high enthalpy of adsorption of H_2 (A). The large surface of gold exposed led to important activation of the surface and of adsorption of CO_2 for the shorter plating times (B)

Gold was chosen in this study for its natural affinity with carbon, but cheaper metals, such as nickel, or metals exhibiting higher capacity for H_2 adsorption or catalytic capacity such as platinum or palladium might be plated. Furthermore, the nanotubes used in this study exhibited an average 8 to 10 walls in their structure. It is likely that replacing them with single walled CNTs (SWNTs) would first create a higher initial specific surface area available for nano-particle growth, thus offering opportunity for more homogeneous distribution and secondly improving the thermal stability and electrical conductivity of the structure thanks to the intrinsic properties of SWNTs.

Gold surfaces have been previously shown affinity for organics [422] and to be an adequate substrate for organic grafting [423]. A range of molecules could be attached to the gold via a thiol linkage, thereby modifying the membrane surfaces and pores with functional groups. The selective transport of permeate molecules could be controlled and enhanced with the immobilization of appropriate functional groups on the gold. Furthermore,longer plating times may lead to denser membranes with tighter pores applicable for nanofiltration and potentially for separation of organic gases.

BPs were successfully templated with gold nanoparticles to produce denser and less porous membranes. We demonstrated that even after 30 hours of plating they remained porous and no significant change in air permeation was noticeable. The change in electrical resistance of the BP strips was directly correlated to the amount of gold in the structure and this could be used for the design of improved sensors for toxic metals of organic compound detection. Electroless plating revealed to be an interesting method for plating nano-porous materials and expose metal nanoparticles offering catalytic or activation properties. However the control of the nanoparticle size and distribution is critical and understanding their role in the gas adsorption process, and how they affect the electrical resistance is critical.

In fact, the impact of the nano-particles size can be understood by considering the change in specific surface area generated from the particle diameter (Figure 5-33). Even a change of a few nanometers will drastically change the specific surface area. It is assumed that the structures offer a range of nano-particles sizes, due to the growth conditions and that the

amount and relative mass of small particles dominate the CO2 adsorption regime in the case of the 1 h and 5 h plated samples. Continuous plating over the CNTs at longer plating times certainly improved electrical and thermal conductivities but does not improve the adsorption performance.

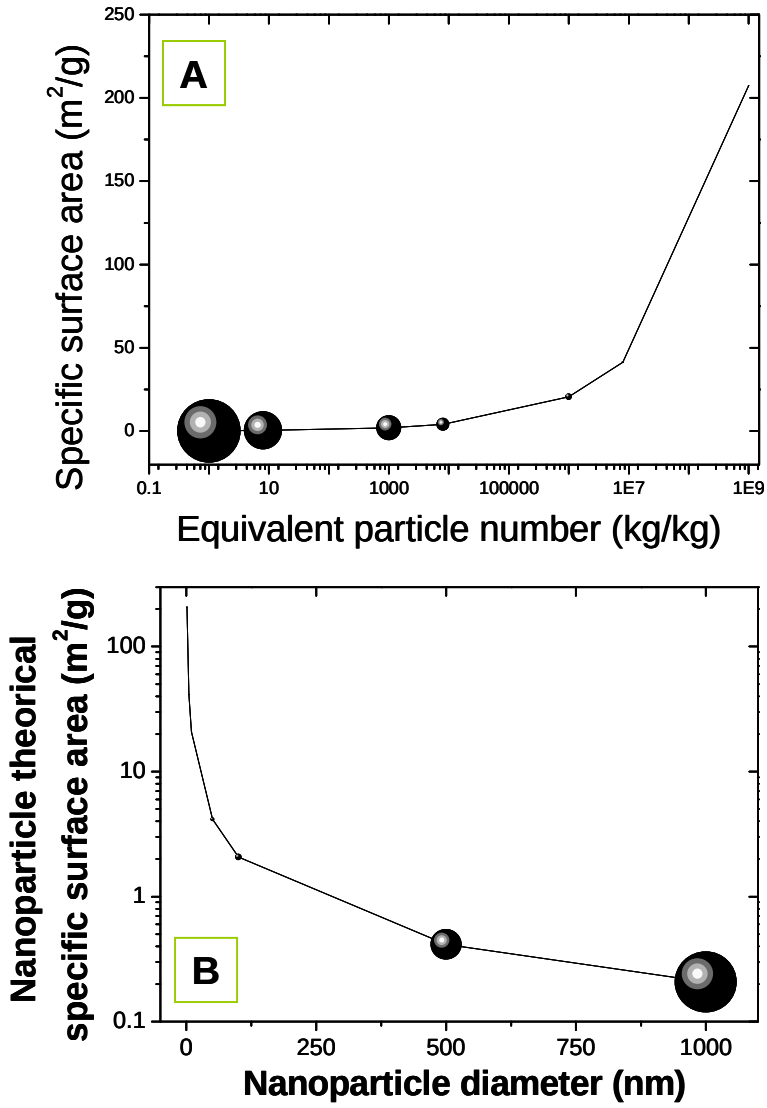

Figure 5-33 A: Specific surface area as a function of the particle number related to 1000 nm; B: nano-particle specific surface area as a function of the particle diameter

A simple and reproducible way to decorate carbon nanotube highly porous macro structures with size-controlled and homogeneous gold NPs was reported. We demonstrated that carbon nanotubes structures can be successfully and efficiently used for growth of NPs in a very confined space.

Nanoporous, thermally stable, electro active materials, with tuneable properties, were fabricated by using carbon nanotube bucky-paper as a template to grow both gold layers and nano-clusters, and expose large surface area of gold for gas adsorption. The distribution of the nanoparticles within the structure requires a thorough control for optimal formation of a continuous structure. These composites could lead to improved gas storage or CO_2 sequestration materials as their high adsorption properties were attributed to the combination of the gold activation with the optimal distribution and growth of nanoparticles within the confined space. Furthermore the conducting CNT structure combined with the gold presence could also be used in electro-catalysis application and within bio sensing applications. This work also offers new perspectives in advanced energy storage materials and the processing method maybe transposed to other and more catalytic efficient metals or other types of macro structures made of nanoparticles.

Furthermore, a range of molecules can be attached to the gold via a thiol linkage, thereby modifying the membrane surfaces and pores with functional groups. The selective transport of permeate molecules may be controlled and enhanced with the immobilization of appropriate functional groups on the gold. Longer plating times may lead to denser membranes with tighter pores applicable for nanofiltration and potentially for separation of organic gases.

5.4 General conclusions

In summary, a number of composite CNT membranes were processed from self-supporting BP membranes. We demonstrated that composite CNT membranes gave comparable and sometimes higher flux and permeability than PTFE membranes of similar pore size and consistently performed better than their self-supporting BP counterparts. In the “sandwiched BP” structure, the PP supports improved the membrane lifespan by a factor 10, with membranes lasting for up to 40 hours of continuous testing. The salt rejection efficiency of the composite structures was also improved with an average value of 95% for all of the membranes while reaching on average 98% for the alkoxysilane modified CNTs, 98.5% for some sandwiched structures, and 99% for PTFE coated samples.

The addition of alkoxysilane groups did greatly change the limit entry pressure of the structure without altering the membrane properties (pore size and porosity). The role of surface energy and hydrophobicity was clearly demonstrated through these experiments where the best performing membranes were the one membranes having the lowest surface energy to repel the liquid water from wicking and degrading the integrity of the structure.

Overall, the lifespan of the composite membranes was shown to be much higher than that of the self-supporting BPs. This improvement was necessary to get better statistical and averaged flux over time. The lifespan and performance of the membranes remains, however too low and it seems unlikely that the composite membranes could be used in the near future as membranes for membrane distillation.

The “Sandwiched BP”, the alkoxysilane modified CNT BPs and PTFE coated BPs composite membranes were found to be the most efficient of the structures investigated in this work, and represent novel ways to use carbon nanotubes and incorporate them into macro-structures.

Furthermore, interesting adsorption properties of BPs were also demonstrated through the testing of the gold nanoparticles / CNT BP composites. The role of the CNTs was to offer growth support to the gold

particles and benefit from the natural high porosity and specific surface area of the BP. The precision of the coating and the tuning of the pore size and porosity were clearly demonstrated thus making fabrication of these promising novel composite structures for various applications possible.

The metal reinforced structures could lead to improved gas storage or CO_2 sequestration materials as their high adsorption properties were attributed to the combination of the gold activation with the optimal distribution and growth of nanoparticles within the confined space. Furthermore, the conducting CNT structure combined with the gold presence could also be used in electro-catalysis applications and in bio sensing applications. This work also offers new perspectives in advanced energy storage materials and the processing methods can be transposed to other, more catalytic efficient metals or other type of macro structures made of nanoparticles.

Chapter 6

6 Discussion on the direct contact membrane distillation results

The DCMD permeability, salt rejection and lifespan results will be discussed in this chapter for the various structures tested over the scope of this PhD thesis. PTFE and PVDF commercial membranes will be used as benchmarks to compare the self-supporting and composite BP membranes used in chapter 4 and 5 in the DCMD set up. Comparison with simple water vapor diffusion models as well as estimation of some geometrical properties of the membranes that could not be experimentally determined will be presented and also discussed.

This chapter will be presented as a discussion and won't include any new experimental data. References to previous work, publications or chapter will, however, be used in order to discuss the work and results. First the benchmark and initial work on self-supporting BPs will be discussed. Then improved performance membranes, including work on mechanical reinforcement and surface energy change will be discussed. Eventually, the lifespan and salt rejection of the different membranes will be compared and global conclusions will be drawn.

"In the end…"

~ Chester Bennington – Linkin Park lead singer

Initial work: benchmarks and proofs of concept

In order to first evaluate the materials performance, the fluxes across self-supporting BP membranes were measured, as presented in Chapter 4. These membranes were solely composed of CNTs and did not include any reinforcement or backing material that could affect the permeation. This step was critical to assess if (i) BP were viable structures that could sustain the stress of the module and (ii) if their intrinsic properties were sufficient to desalinate water, which was the ultimate goal of the study. The permeability of these membranes was calculated by taking the gradient of the flux as a function of the water vapor pressure gradient across the membrane and dividing it by the membrane thickness. Permeability was found to be a fairer and more optimal way to compare membranes of different geometrical properties.

Effectively to compare the benchmark with previous works from literature, 3 types of PTFE membranes exhibiting different average pore size were tested (Chapter 4). The average pore size varied between 20 nm up to 450 nm. The studies found in the literature, as well as the first tests in pilot plants, used "large" pore size membranes with pores typically falling between 200 to 600 nm. For this reason, a comparison with similar membranes was first preferred to clearly rank the BPs versus commercially available PTFE membranes. However, since the self-supporting BP membranes showed permeabilities up to 2.5 times lower than the commercial PTFE 450 nm pore size membranes, another source of more morphology-similar membranes was sought to compare with. PTFE membranes, purchased from Pall and exhibiting similar pore size distributions (30 - 60 nm) were found to offer a more relevant comparison with the BP membranes since the geometrical variations between the different membranes were reduced. These membranes, as depicted in Chapter 4, exhibited similar pore size distributions with a slightly larger average pore size. The porosity of all the PTFE

membranes were measured to be lower by 20 to 25 % on average than the BP, while the thermal conductivity of the PTFE, known to be the lowest of most of the polymeric materials was found to be about 10 time times lower than the BPs.

Furthermore, several membrane geometrical parameters determined in Chapter 3 and 4, the average pore size, porosity and thickness were compiled and used to calculate the theoretical permeability of the membranes in three different regimes: Poiseuille, transition and Knüdsen regimes. These values were compared with the calculated permeabilities based on the membrane flux and process global pressure gradient following Equation 2 in Chapter 1. Large discrepancies between the theoretical and experimental values were found for both benchmark and self-supporting membranes.

Even though the theoretical permeability values calculated based on the transition regime, with a dominant Knüdsen term, gave the closest agreement with the experimental results, large differences between the calculated data and the experimental data remained. The mean free path for the BP membrane was calculated to be close to 1, which should lead the membrane to perform in a mixed Knüdsen and transition regime. In the Knüdsen transport regime, both pore size and porosity rule the diffusion regime since the permeability is directly proportional to the pore radius and porosity. The theoretical calculations predict the PTFE membrane permeability to be ~2 to 5 times greater than that of the BP membrane, largely due to the difference in pore size. This has also been observed by other groups and is likely due to system effects such as the impact of the temperature polarisation as well as the model assuming ideal cylindrical pores [99, 135], while the tested structures here reported were composed of a succession of cavities and gaps between the fibres composing the membrane.

To better fit the experimental permeability values a second modelling, only based on the geometrical parameters of the membranes, was undertaken following the procedure from Zhang et al. [144]. Values relatively close to the experimental values of porosities, pore size and measured

thickness were used to calculate the Knüdsen pre-factors P_{Kn} defined in Equation 1:

$$P_{Kn} = \frac{\varepsilon.r}{t.\tau} \qquad (6\text{-}1)$$

Where ε is the membrane porosity, r the average pore radius, t the membrane thickness and τ the membrane tortuosity.

Theoretical values of the tortuosities as described by Equation 6-2 and compiled in Table 6-1, were obtained by assuming a given CNT density packing in the membrane from the measured porosity values and by using the average CNT diameter, showed that these tortuosities are likely to be strongly underestimated in the case of the BPs as calculated with Equation 6-2. These values will be also used in the next section to compare the different membranes.

For a membrane unit thickness of 1, the equation is then simplified and the values of tortuosity can be calculated for different numbers of CNTs in cross sections. A CNT diameter value of 15 nm was used following the TEM observations depicted in Chapter 3. Further details on the tortuosity calculations are given in Appendix 6.

$$\tau = 1 + (\pi - 1) \times \frac{nD}{2} \qquad (6\text{-}2)$$

Where τ is the membrane tortuosity, D the CNT diameter, and n the number of CNTs per unit cross section.

Some areas on the TEM video presented in Chapter 4 showed that very few nanotubes were present while a larger number of CNTs were found in the nodes constituting the non-woven structure thereby indicating that the tortuosity varied across the membrane. It is more realistic to consider the real tortuosities to be around 1 to 3. Higher tortuosities as estimated by Equation 6-2 may greatly affect the predicted performance of the membrane as water vapor will be transported through the longer air-gap path length. In fact, theoretical calculations of the tortuosities that assumed a given CNT packing density in the membrane from the measured porosity values, and by using the

average CNT diameter likely underestimated the tortuosities values for the BPs. These values will be also used in the next section to compare the different membranes. The calculated tortuosity gave pre-factors values closer that of the PTFE20 reference.

Table 6-1 CNT BP tortuosity calculation for a 100 nm thick BP (Appendix 6)

CNT number	*Half perimeter of CNT cylinder nm*	*Total pathway nm*	*Tortuosity*
0	0	100	1
1	18.8	118.8	1.2
5	94.2	194.2	1.9
10	188.4	288.4	2.9

The values of the Knüdsen pre-factor were estimated by taking the experimentally determined geometrical values (pore, size, porosity and thickness) as well as the calculated value of tortuosity of the different membranes and normalizing it with that of the PTFE20 membrane. As seen from these calculations, a retro-estimation of the theoretical membrane properties was possible. To match the Knüdsen pre-factor ratios, the tortuosity, which was the main parameter assumed in previous work [144, 424], had to be decreased by about 40 % while the pore size was adjusted to around the average value obtained from the porometry study. This brought the theoretical permeance to a more realistic value, as shown in Table 6-2. These values were used in the next sections of this chapter to compare with experimentally determined permeabilities.

Table 6-2 Knudsen pre-factor estimated from Equation 2; BP corresponds to a self-supporting structure without any surface modifications, while the data for the PTFE correspond to the values experimentally and theoretically obtained for commercial Pall membranes as presented in Chapter 4 and 5

Membrane	Porosity	Pore size nm	Tortuosity	Thickness µm	Knudsen Pre-factor
PTFE20	0.65	57	1.15	20.00	1.00
PTFE220	0.65	220	1.22	50.00	2.13
PTFE450	0.65	450	1.25	55.50	3.75
BP	0.90	32	1.22	30.00	0.74

The calculations show that the impact of pore size is critical for membrane permeation and that larger pores clearly benefit diffusion. Although the BP porosity was much larger than that of PTFE membranes, water vapor diffusion across the membranes was still predicted to be at least 25% lower in the case of the BPs. The tortuosity of the membrane also plays an important role in the permeation.

The self supporting BPs exhibited large salt rejection values above 90%, with an average salt rejection of around 92 %. Despite that salt passage occurred through cracks formed by mechanical stress induced by the water streams, the self-supporting BPs resisted cracking during continuous testing for more than 3 hours. These encouraging results were used to engineer improved composite BPs which would present higher salt rejection, better stability over time and improved permeability.

Composite material BPs permeation: a higher performance

Several approaches were undertaken to modify the BPs and change their properties to achieve higher permeabilities more comparable with the PTFE membranes. The best permeabilities amongst the BP composites processed were obtained for the sandwiched, PTFE coated and alkoxysilane modified CNT composites. All these membranes exhibited both longer lifespan than the self-supporting membranes (6 to 13 times) while showing better salt rejection properties (from 95 up to 98 %). This enhanced salt

rejection demonstrated that much less cracking occurred for these structures. Furthermore, these composite membranes exhibited permeabilities only 50 % of that obtained for the control PTFE 450 nm pore size membranes [410], while offering up to 20 % more permeability than the PTFE 20 nm pore size membranes. This was promising, as PTFE membranes are amongst the best performing for MD.

A number of factors may contribute to the lower permeability measured for the composite CNT membranes compared to the PTFE 450 nm control. The variations in structure and surface energy were certainly amongst the main reasons for the permeability differences and the supremacy of the PTFE membranes. The differences between the membranes may firstly attributed to the BP membrane thermal conductivity, which is ~10 times greater than that of PTFE. The thermal conductivity is an important property for the membrane distillation process as it determines the amount of heat transfer through the membrane thus influencing both temperature gradient and vapor pressure difference across the membrane.

Secondly, the structure and pore shape of PTFE membranes were distinctly different from the BP non-woven structure. The BP pores consisted of an interconnected network of interstitial gaps between CNTs, while PTFE membranes pores were long and thin due to the stretching process used during their fabrication. The PTFE pores were also likely to be straighter, leading to a less tortuous path. The PTFE membranes tortuosity was estimated to be around 1.15, from previous calculations [425], calculations of the theoretical BP tortuosity may vary from 1 up to 2.9 as previously reported.

Furthermore, as demonstrated by the SEM images throughout this thesis, the average BP pore size was ~10 to 15 times smaller than that for PTFE 450 nm membranes. Knüdsen diffusion theory predicts that the molar flux should be proportional to the radius of the pores, making this an important property affecting flux [109]. This is illustrated in Figure 6-1 where the permeability clearly increases with larger pore size membranes. The permeability values of the membranes, either commercial PTFE20 or BP were very close to each other compared to that of the larger pore size commercial

PTFE membranes. This strongly agrees with Equation 6-1 as diffusion was considered directly proportional to the average membrane pore size.

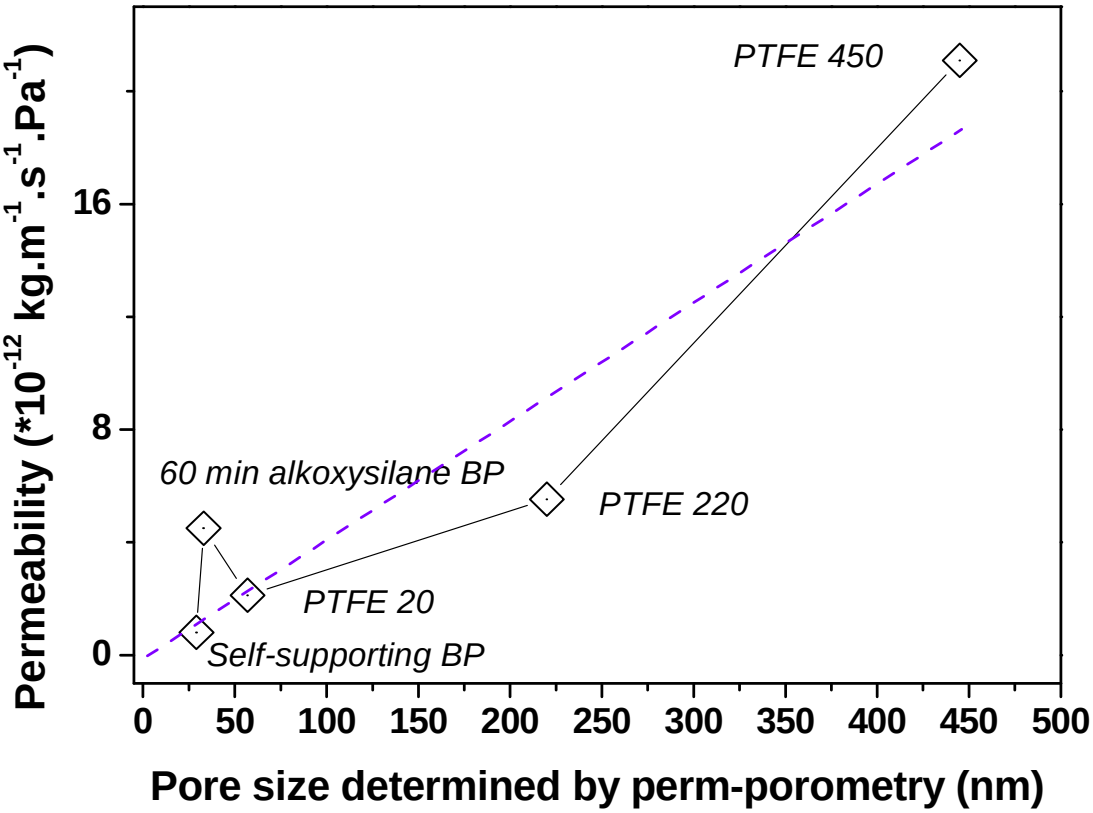

Figure 6-1 Permeability as a function of the average pore size of the membranes. The theoretical curve as a function of pore size is shown and was calculated from Equation 6-3 (dashed dark blue line)

The permeance across a membrane can be defined in direct contact membrane distillation by the empirically derived equation as defined in [424, 426]:

$$J = 7.81 \times \frac{\varepsilon . d}{t . \tau} \times \frac{MT^{1.072}}{\sqrt{2\pi RMT} + 4dR(P - P_A)} (P_{T1} - P_{T2}) \quad (6\text{-}3)$$

Where ε is the membrane porosity, d the average membrane pore size, t the membrane thickness, τ the tortuosity, R the gas constant, M the molecular mass of the gas (vapor in this case), T the temperature of the air gap in K, P

the pressure in the air gap, P_A the atmospheric pressure, P_{T1} the vapor pressure at the stream temperature T1 (hot) and P_{T2} the vapor pressure at the stream temperature T2 (cold).

It was shown that the P_{Kn} ratio [424], defined in Equation 6-1 can be a suitable way to compare structures of different geometries and predict their behaviour in DCMD. The P_{Kn} coefficients were calculate and are shown in Table 6-3 for the PTFE membranes and for different tortuosities and porosities of BPs in order to highlight the impact of these two parameters on the P_{Kn} values (i.e. the variation of BP porosity and tortuosity was theoretical and was not achieved experimentally). Furthermore, to better compare the membranes and set a benchmark for analysis, the P_{Kn} coefficients were normalized by dividing by the $P_{Kn(PTFE\ 20)}$ corresponding the the P_{Kn} value for the 20 nm pore size PTFE membrane.

The P_{Kn} ratios of the BPs were calculated and were all inferior to all that of the PTFE membranes. This was explained from the large difference in pore size and tortuosity between the BPs and PTFE membranes. However, as expected, the P_{Kn} ratio normalized with the PTFE 20 were found to increase linearly within the PTFE series since pore size was the only parameter that changed between the samples.

Interestingly, while this trend was respected when the permeabilities of the PTFE membranes were normalized with that of PTFE 20 (Table 6-4), large differences were obtained for the experimentally determined porosities of the BP composite membranes, although their respective pore sizes were very similar, as demonstrated in Table 6-3. In fact most of the BP samples, apart from the self-supporting samples and the PVDF infiltrated samples performed better than the PTFE 20 membranes. However, these trends for the theoretical P_{Kn} values and the experimentally determined permeabilities were not the same. The BP characteristics did not alter upon fabrication of the composite membranes so that similar P_{Kn} values were predicted for the composite membranes and the self-supporting membranes. These were predicted to be less than the PTFE 20 membranes. However, the permeabilities of the composite BPs were larger than the PTFE20 membranes. This was attributed to the fact that the large difference in porosity

was affecting the flux to a larger extent than expected and that the network of pores created by the non-woven structure led to improved permeabilities. This confirms that geometrical properties of the membranes are critical and that large pores and porosities are desired to achieve high permeation.

Table 6-3 Values of P_{Kn} calculated from Equation 6-1 and from experimentally obtained membrane parameters. The tortuosity was estimated from Table 6-1; BP 1 to BP 4 correspond to modelled BP structures where either porosity or tortuosity were adjusted to simulate different structures

	Pore size	Porosity	Tortuosity	Thickness	P_{Kn}	P_{Kn} / $P_{Kn\ PTFE\ 20}$
Modelled	µm	%		Mm		
BP1	0.032	0.9	1.2	60	0.00040	0.35
BP2	0.032	0.9	1.5	60	0.00032	0.28
BP3	0.032	0.9	1.8	60	0.00027	0.23
BP4	0.032	0.92	1.8	60	0.00027	0.24
PTFE 20	0.057	0.66	1.1	35	0.00098	1.00
PTFE 220	0.22	0.7	1.1	35	0.00400	3.51
PTFE 450	0.45	0.7	1.1	35	0.00818	7.18

Furthermore, the permeability obtained experimentally, was also normalized with regard to that of the self-supporting BP and of the PTFE 20 membranes. The experimentally determined permeabilities, as defined in Chapter 1, k was used to compare with the P_{Kn} values. k / k_{BP} values normalized by the ratio of the k_{BP} and individual membrane pore size, taken from Table 6-3, were calculated and are displayed in Table 6-4. Interestingly the largest ratios were found for the surface energy modified BPs (both PTFE coated and alkoxysilane modified CNTs), thus identifying a significant effect of surface hydrophobicity on permeability. This demonstrates that although large pores are critical to achieve high flux, surface energy of the membrane also significantly influences performance and this effect is unaccounted for in Equation 6-1.

The scattering of the permeabilities values is clearly shown in Figure Figure 6-2 where the experimental k / k PTFE20 ratios were plotted against the theoretical P_{Kn} / P_{Kn} (PTFE20) ratios. This clearly shows that although the PTFE membranes performed in the expected range, some modified BP

membranes displayed higher than expected performance, if only based on the experimentally determined geometrical parameters necessary to calculate P_{Kn}.

A number of geometrical parameters, not taken in account in classical DCMD modelling could also impart on permeation while being related to the changes therein observed. In fact, the surface topography or roughness was affected by the various coatings and treatments undertaken on the BPs and could explain the improved permeation of the alkoxysilane and PTFE coated samples. The addition of these hydrophobic functional groups or layers very likely had a dual effect due to the increased roughness that they generated on the BP surface, which as was previously demonstrated affects the vapour/liquid equilibrium, and by reducing heat transfers by better insulating the composite membrane. These two parameters were in the view of the authors critical and helped improving the performance of these membranes.

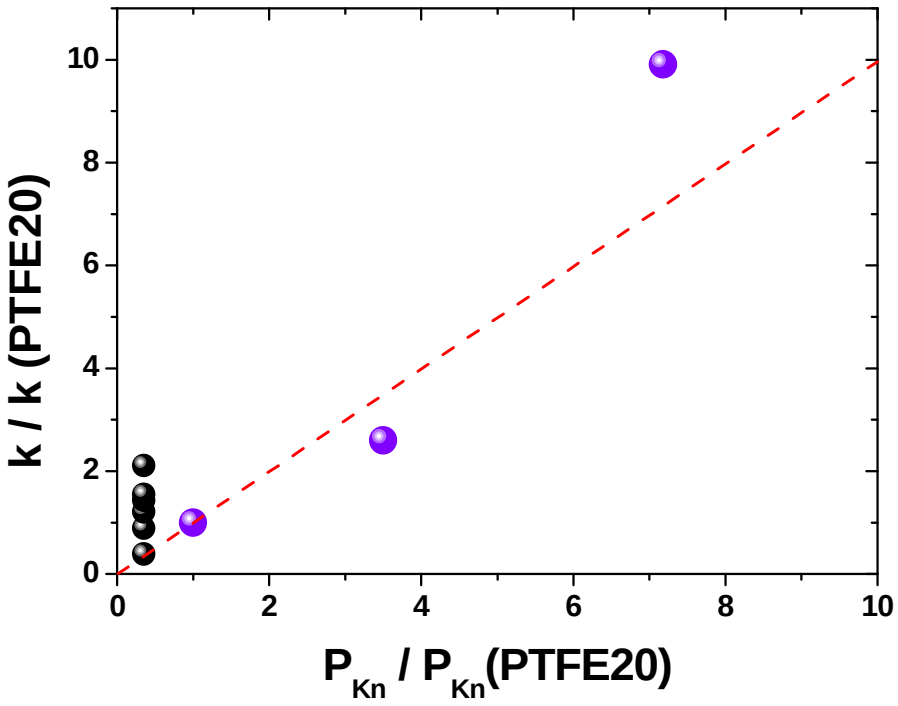

Figure 6-2 Relative position of the k(membrane) / k (PTFE20) values as a function of the theoretical values of P_{Kn} / P_{Kn} (PTFE20) calculated from the experimental geometrical parameters (pore size, porosity, thickness)

Table 6-4 Experimental permeabilities, k, and permeabilities normalization ratio with the PTFE 20 nm and the self-supporting BPs k value

Experimental	k *10^{-12} $kg.m^{-1}.s^{-1}.Pa^{-1}$	$k / k_{PTFE\ 20}$ Experimental	P_{Kn} / P_{Kn} (PTFE20) Theoretical	k / k_{BP} Experimental	k / k_{BP} Pore size normalized
Self-supporting BP	0.83	0.39	0.35	1	1
Sandwiched BP	3.31	1.55	-	3.99	3.99
PVDF infiltrated BP	1.89	0.89	-	2.28	2.28
PS infiltrated BP	2.57	1.21	-	3.10	3.1
60 min alkoxysilane BP	4.5	2.11	-	5.42	5.42
PTFE coated BP	3.05	1.43	-	3.67	3.67
PTFE 20 XP	2.13	1	1.00	2.57	1.48
PTFE 220 XP	5.53	2.60	3.51	6.66	0.99
PTFE 450 XP	21.1	9.91	7.18	25.42	1.86

The comparison between the sandwiched BPs and the polymer infiltrated BPs also showed clearly that the addition of matter within the BP pores, which reduced the membrane porosity, had a significant impact on the permeability and drastically reduced the transport performance. On the other hand, the little amount of polymer added on the PTFE coated BPs did not have such a drastic impact on the structure since these samples exhibited the largest permeabilities (Table 6-4).

It is interesting that the PTFE coated BP and the alkoxysilane modified CNT BP both exhibited higher permeabilities than their self-supporting BP counterparts (Table 6-3). This was attributed to the change in surface energy of the membrane. This parameter is not accounted in Equations 6-1 to 6-3 as Knudsen diffusion does not account for surface hydrophobicity. A lower surface energy will likely have two positive effects on the membrane performance. Super-hydrophobic surfaces might first create a thin film of air at the interface water / material as it has been shown to occur in the case of thin PTFE films [427-430]. The thin layer would isolate the membrane and reduce both thermal diffusion and pore wetting [431], known sources of reduced flux in MD. It might also help repelling water from wicking and entering into the

structure, thus preventing fast ageing and crack formation as shown to occur for self-supporting BPs in Chapter 4. The fact that the alkoxysilane modified CNT BPs exhibited the highest permeabilities and deviation from the calculated value might also be attributed to the addition of the aliphatic chains present in the GPTMS [336, 432]. These chains, by substituting to CNT/CNT contacts might reduce the thermal conductivity of the membrane and thus help limiting the temperature polarisation effect. This is supported by the trends shown in Figure 6-3, where the membrane permeability increases monotonically for the PTFE coated BPs with contact angle but the alkoxysilane modified BP had permeability above that of the PTFE coated BP trend line. The main distinction between these two structures is that the PTFE only coated the BP surface, so conduction through the bulk of the BPs was unaffected by the PTFE coated, while the alkoxysilane functionalisation was performed thoughout the BP and so may have reduced the bulk thermal conductivity as well as surface effects. This supports the hypothesis that the additional alkyl chains, probably reduced heat conduction between CNT fibres. This reduction acted to increase MD performance for the alkoxysilane modified CNT BP.

This clearly demonstrates the predominant role of hydrophobic forces in MD, and could lead the way to fabrication and use of even more hydrophobic membranes. The use of longer GPTMS chains, or of fluoro-polymers as reported in this thesis, could even further enhance the effect and thus increase the vapor permeation properties by sharply reducing sides effects such as temperature polarisation and pore wetting.

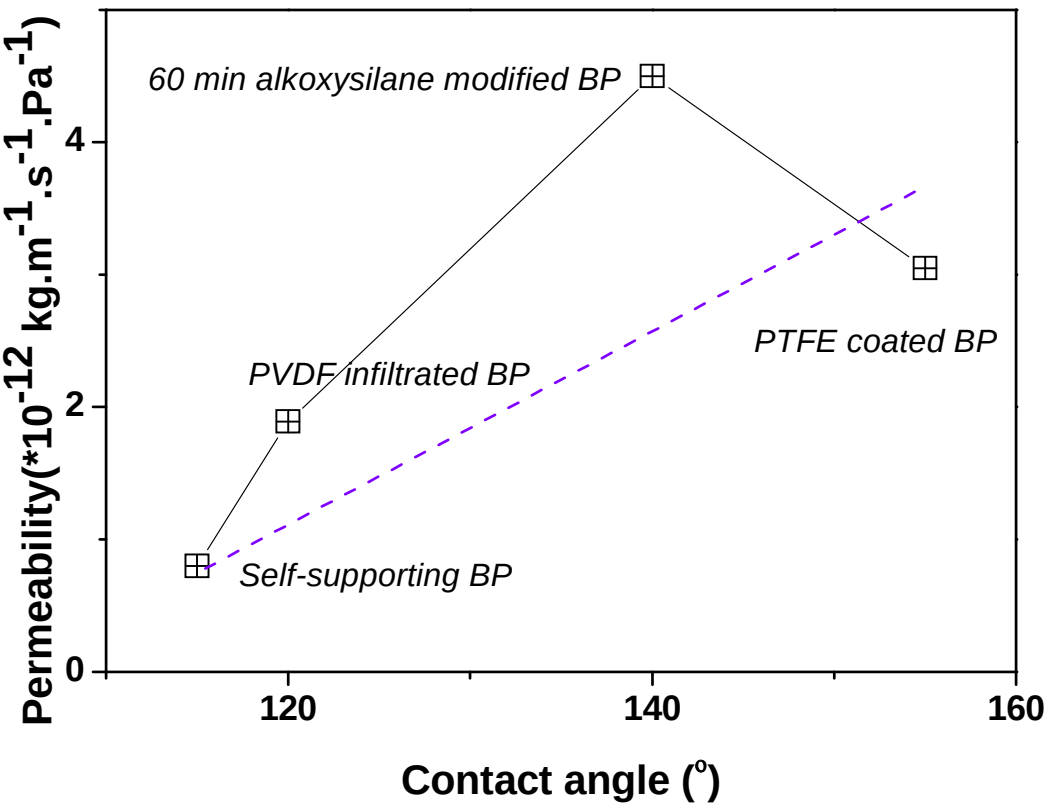

Figure 6-3 Permeability behaviour as a function of the contact angle measured on a goniometer for similar pore size membranes

Lifespan and salt rejection

All the membranes exhibited salt rejection of at least of 90 %. In fact, following the trend in permeation results, higher salt rejections were obtained for the improved lifespan and enhanced hydrophobicity membranes. Thus enhanced permeability performance also resulted in improved global membrane integrity.

As shown in **Error! Reference source not found.**, very little evidence of fouling was found on the used membranes even without back washing. A number of small salt crystals were found to adhere to the BP surface after DCMD testing showing very slight fouling after more than 15 h of testing. Furthermore, cross sections performed on the self-supporting BP after testing showed that salty water wicked only into the cracks since neither sodium nor

chloride were found elsewhere by EDS (top left insert in **Error! Reference source not found.**).

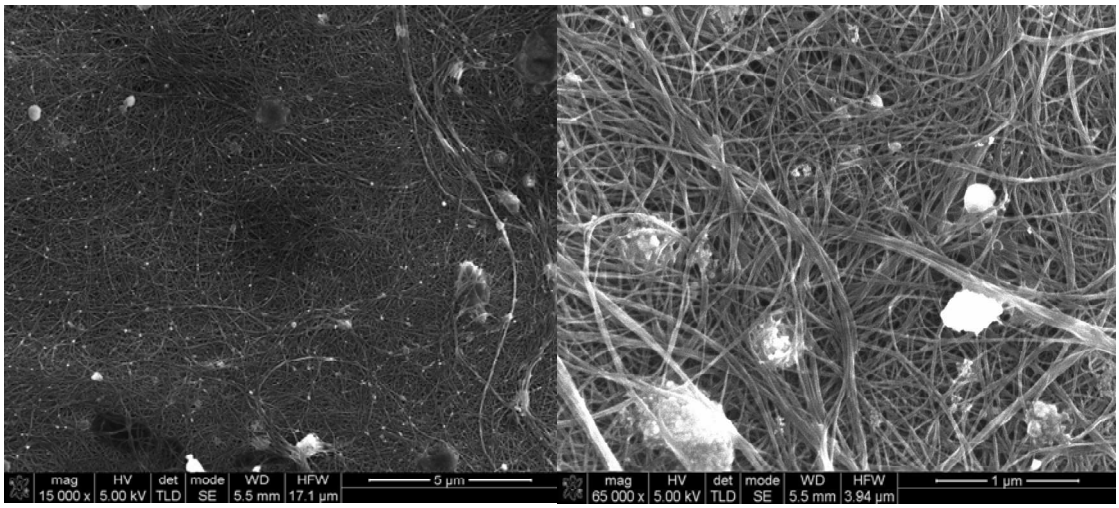

Figure 6-4 Fouling at the top surface of a BP

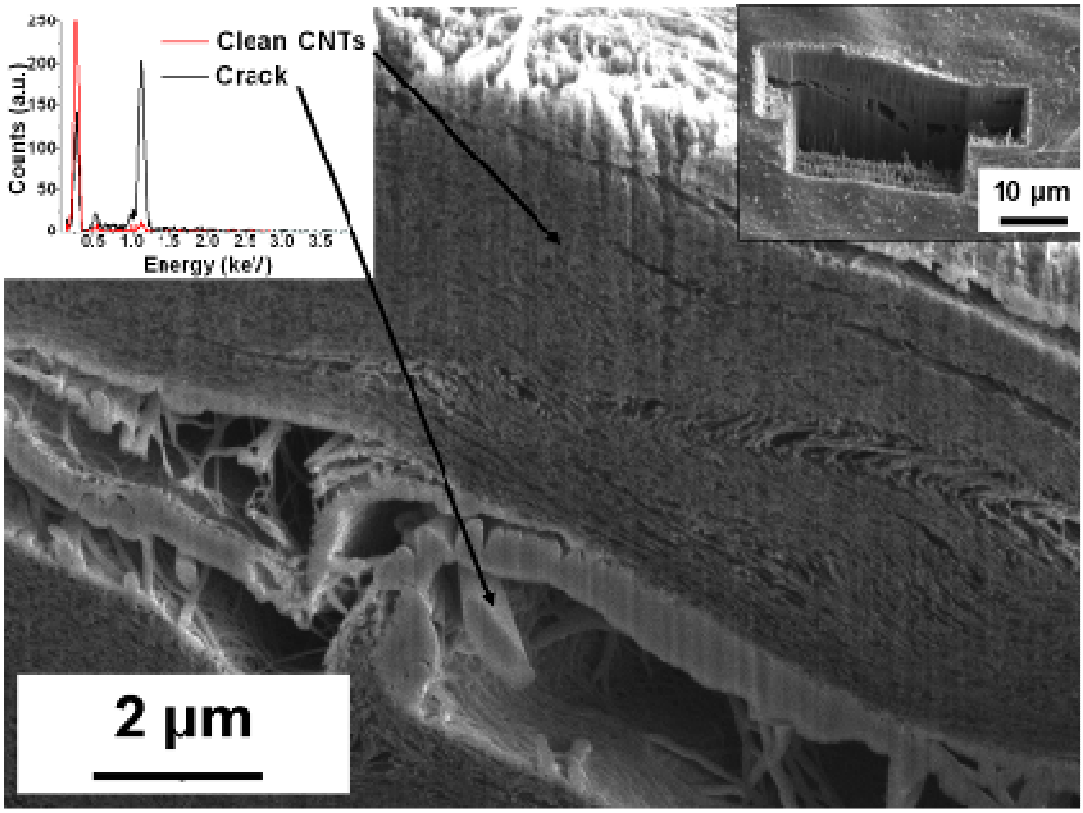

Figure 6-5 FIB cross section of a BP after testing

As BPs were intrinsically hydrophobic and porous, water cannot permeate as a liquid under low working pressures. The bubble point of the different membranes exceeded 700 kPa, which was above the transmembrane pressure applied in the module that was varied between 10 and 50 kPa depending on particular experiment. For this reason no wetting should have occurred and salt rejection should have been superior than 99 %. Unfortunately, as shown in this work, the average salt rejection of the membranes did not reach 99 %. This was attributed to crack formation, as presented in Chapter 4, and to integrity loss of the main active layer of the membrane: the bucky-paper. In addition, the membranes exhibiting the highest desalination capacity were also those that offered longer lifespan, thus clearly correlating salt rejection to integrity. In fact, as shown in Figure 6-6, the lifespan of the membrane appeared to be related to the average salt rejection. In this work, the lifespan was calculated as the time corresponding to desalination efficiency greater than 90 %. This in fact explains why the sandwiched membrane (green bar) performed longer than the other samples.

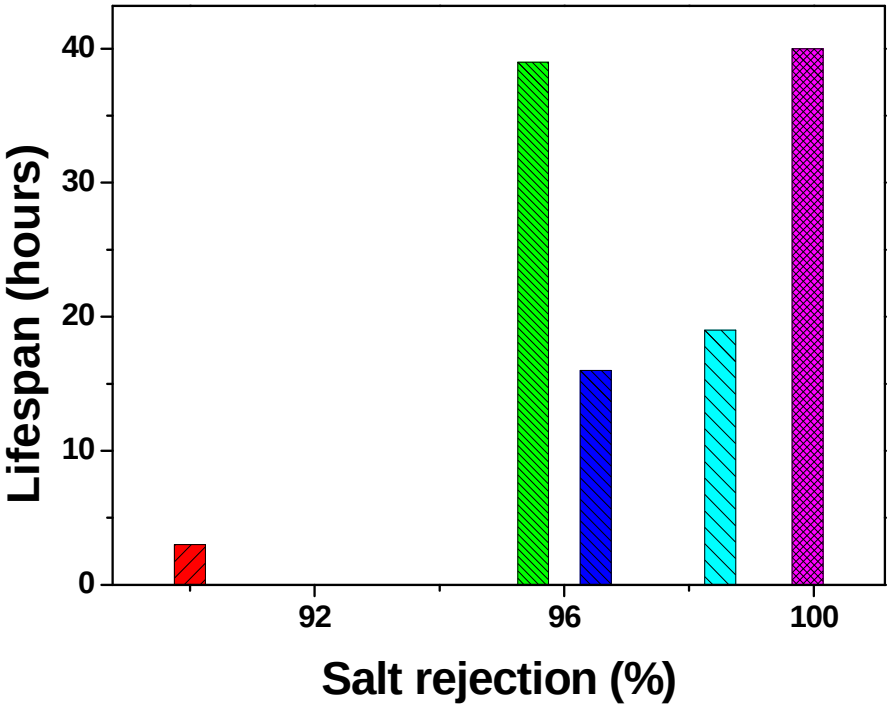

Figure 6-6 Lifespan for series of BP membranes as a function of salt rejection; from left to right: self-supporting membrane, sandwiched BP, PVDF infiltrated, PS infiltrated and PTFE BP coated

The best approach undertaken in order to enhance salt rejection and lifespan was also the one that enhanced water vapor transport and the membrane permeance. Changing the surface energy, or increasing the membrane surface hydrophobicity revealed to be the best option and the largest lifespan (40h) and salt rejection (>98 %) were obtained for the PTFE coated and alkoxysilane grafted CNT . It seems that the lifespan increased because of the simultaneous action of the mechanical reinforcement offered by the coating and of the enhanced hydrophobicity that prevented water wicking and thus crack formation.

In the case of surface coatings, the BP was used more as a support for a more hydrophobic layer than for its own properties, which was a technique that was also investigated in Chapter 5 when the CNT BPs were used to grow the gold nano-particles and not for their own catalytic or surface adsorption properties.

Conclusions of the discussion chapter

Are bucky-papers suitable for Membrane Distillation?

It is unlikely, due to the difference of permeability between the CNT BP and the PTFE benchmark membranes that BP will be industrially used in MD. This study demonstrated that their use was compromised unless large pore size modifications could be undertaken to further enhance the permeance of the membranes.

However, due to their ease of processing and reproducibility, BP will certainly become a commonly used CNT material in the future. Several outcomes of this work should be pointed out. First, this work contributed to improving the understanding of the fundamental knowledge of the BP properties. BPs allow exposure of large quantities of CNTs in a confined space which, as demonstrated through this work, can exhibit large specific surface area, high hydrophobicity and moderate mechanical stability. This work also demonstrated that CNT BP membranes could be used on larger scales than what was previously reported. In this work, CNTs were often used to build a porous template with large porosity rather than for their intrinsic properties. This shows a novel way to consider CNTs: as possible substrates where gas (or vapor) can or cannot adsorb and not only as nano-channels as previously demonstrated.

The specific structure of the BP and their pore interconnectivity certainly affected the DCMD performance. Several parameters were found to highly affect and influence the MD results. As presented, pore size, porosity and hydrophobicity were the main parameters that affected the flux and membrane performance. Large pores, of a few hundreds of nanometres should be preferred to obtain high flux membranes although a maximum pore size is determined by the liquid entry pressure of the membrane in order to avoid water wicking in the air-gap. BPs were found to be equal if not superior to commercial PTFE membranes exhibiting similar pore size, but as pore size

is one of the three critical parameter for achieving high flux, could not fully compete with larger pore size PTFE membranes.

The discussion presented in this chapter and based on the work presented in the previous sections of this thesis demonstrated that CNT BP composites can be efficiently used over a few dozen of hours as membranes for MD. They exhibited reasonable flux and very high salt rejection but their performance remained low compared with typical PTFE membranes.

Different approaches were undertaken to improve the performance of the self-supporting BPs. The study of the impact of the hydrophobicity clearly demonstrated that greater hydrophobicity lead to better vapor transport. This was likely to be related to the wetting of the membrane surface pores and possibly to a thin insulating air film on the surface. These effects were considered to reduce temperature polarisation. A thin nanometric sized layer of PTFE, or specific hydrophobic grafting on the CNTs surface were demonstrated to be simple ways to drastically change the BP surface energy and permeability. The fact that the hydrophobicity enhanced BP performed better than the PTFE membranes of similar pore size further demonstrates this point. In addition to this, it is likely that the addition of more hydrophobic compounds throughout the membranes also reduced the thermal conductivity of the membranes thus further enhancing the performance. This effect was not predicted by conventional MD theory which has focused on “easily” measurable geometrical parameters such as porosity, thickness and pore size. The permeation of water vapor is often assumed to be independent of the liquid water meniscus formation at the pore surface [433], although previous work on temperature polarisation [434, 435] clearly demonstrated that different trans-membrane pressures, stream velocities [148] or membrane material conductivity would lead to different permeation behaviours . Most of the time, modelling assumes cylindrical pores [146, 436], thus deeply simplifying both pore wetting and water vapor transport.

It could be expected that surface modifications on commercial PTFE membranes by grafting thin hydrophobic compounds may also help improve water permeation and further reduce the impact of pore wetting on their rough surface. Furthermore, the composite BP membrane exhibited highly enhanced lifespan compared to the non-reinforced self-supporting BPs. The

natural stiffness of the self-supporting BPs, provided only by the intertwined CNTs and van der Waals forces, was certainly not sufficient to offer membranes of long term stability. Polymer infiltration in the large BP porosity, simple BP sandwiching with a polymeric reinforcement material or surface coating were shown to greatly improve the mechanical stability.

These trends are summarized in the general graphical conclusion, displayed in Figure 6-7. The pore structure was simplistically modelled as a 4-CNT-interconnect where the degree of hydrophobicity of the system, also known as the surface energy of the surface, is shown as a red glow around the CNTs. The 4 main BP structures, (i) self-supporting BP, (ii) polymer reinforced BP, (iii) PTFE coated BP and (iv) alkoxysilane coated BP are presented and compared. As shown in Figure 6-7, and demonstrated across this chapter, the presence of the hydrophobic alkyl chains did improve both permeation and lifespan when compared with that of the self-supporting BP membranes. The enhanced stability and performance were related to the hydrophobicity throughout the membrane improved mechanical strength afforded by the coating and reduced thermal conductivity.

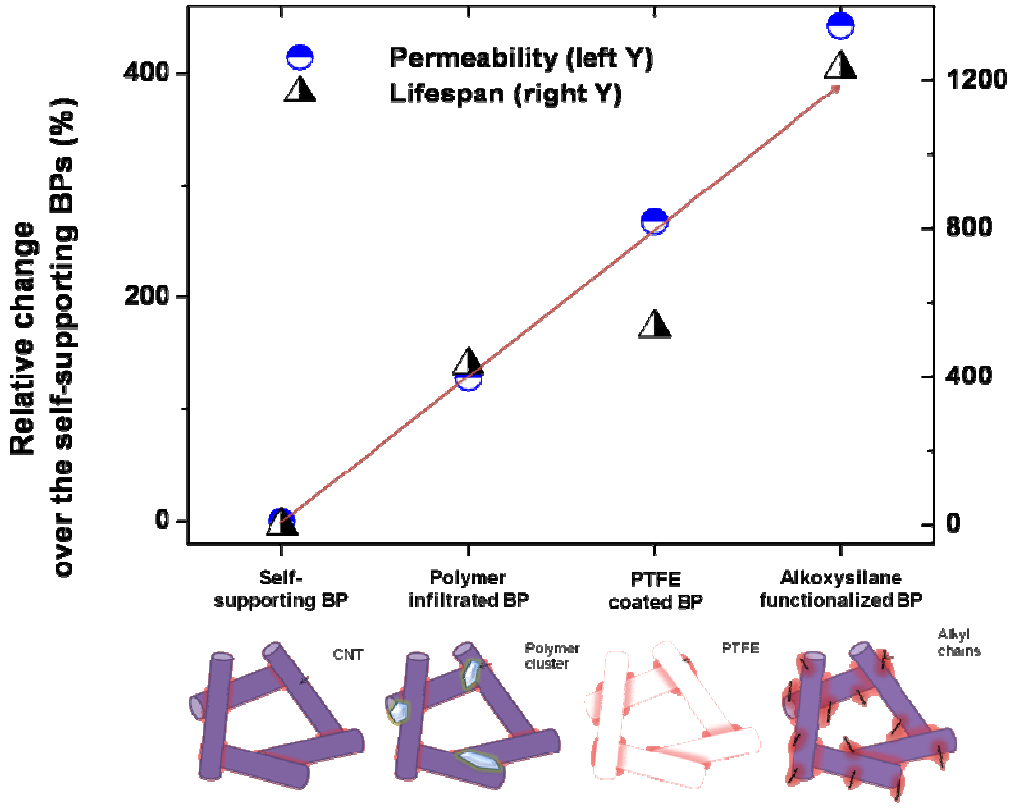

Figure 6-7 Graphical conclusion; the enhancement in surface energy is shown on the CNT drawings as a function of the red glowing. Values were calculated as a relative variation over the self-supporting BPs

7 General conclusions

On the outcomes of this work...

First of all, this work shows, as a proof of concept, that CNT BPs can be used in a practical application to desalinate water. The self-supporting BP membranes were processed, characterised and tested in gas permeation and DCMD to demonstrate the relevance of the concept and to identify points of improvements. These membranes exhibited interesting properties, such as very large porosities (> 90%), specific surface areas (> 200 $m^2.g^{-1}$), tensile modulus (>1 GPa) and low thermal conductivity compared to pure graphite. Furthermore we demonstrated that pore size could be tuned by mixing nanotubes of various diameters together.

The BPs exhibited similar properties compared with commercial membranes used in MD and performed successfully to desalinate water.

However, to improve both the mechanical stability and the membrane performance, several approaches were undertaken to fabricate composite membranes by using the BPs as a template. The resistance to ageing and membrane lifespan were increased, while performances were greatly improved. The lifespan of the composite membranes was brought up to more than 40 h compared with the initial 2 to 3 hours of the self-supporting membranes. Fluxes up to 15 $kg.m^{-2}.h^{-1}$ were reached for large water vapor pressure differences. Those fluxes were comparable, if not superior, to that of PVDF or PTFE membranes exhibiting similar pore size distributions.

This proved that the versatility of the BPs both chemical and mechanical should be investigated as a preferential way to handle and modify CNTs. BP are a simpler and safer way, than pristine powders or forests to handle and benefit from some of the CNT properties.

The lower performances of the composite BPs compared with the other PTFE membranes were directly attributed to the large difference in pore size.

The BPs exhibited pores 10 to 20 times smaller than the PTFE membranes, thus reducing the benefits from their large specific surface area and porosity. The difference in contact angle, or the hydrophobicity of the material, was also considered as a possible limitation of BPs over PTFE membranes.

To address these issues and target better performance membranes, work was performed to increase the surface hydrophobicity and the inner porosity of the BPs. We showed that increased hydrophobicity lead to improved performance, stability and lifespan membranes. The chemical functionalisation of the CNT sidewalls with alkoxy-silane chains as well as the thin PTFE coating lead to drastic changes in the membrane properties and behaviour. The LEP of the membranes was clearly increased without greatly altering the other membrane properties such as pore size, porosity or BET surface area.

This work demonstrated the major role of hydrophobicity as a clear way to decrease, for a given structure, the surface pore wetting which is a cause of flux decline and temperature polarisation in MD. Furthermore we showed that the modelling of water permeation across a BP during DCMD did not fully follow the Knüdsen regime. The succession of larger/narrower cavities as well as the complexity of the pore inter-connections may lead to an increased resistance to diffusion. A combination of Knüdsen and other regimes, such as entropic diffusion may better explain the diffusion process.

Another outcome of this work concerned the dispersion of the CNTs. Most of the dispersion techniques presented in the literature do lead to damaging the CNTs. A novel simple and non-aggressive dispersion process based on sonicating the CNTs in an alcohol solution at low temperature was performed to obtain well suspended CNTs. This phenomenon was not previously reported and opens the way for further studies on the impact of temperature on the preparation and processing of CNT macro-structures.

Two other side studies were performed to investigate the properties and performance in separation of the BP structures and find possible fields of applications. The point was to show that BPs were versatile structures that could be used in a large range of applications if properly tuned and modified.

Work was first carried out to better control the porosity of the BP by adding sacrificial polymeric beads within their pores. Post carbonization of the beads led to macro-voids within the BPs, thus potentially enhancing their separation and permeation behaviour. Enhanced specific surface area material was processed through this method that could be used for the adsorption of chemicals, organics or gas. These membranes did not lead to greater permeation because of residual carbon shells formation from amorphous carbon redepositing. The removal of the carbon shells might lead to very promising structures that could be post functionalised or filled up with very specific materials for enhanced selectivity. The large pores, on a nanoscale of the BPs do not make them highly exciting structures for nanofiltration but many simple ways, as demonstrated through this work, exist to modify the BPs and make them more suitable with many separation, sensing and storage applications.

Secondly, gold/CNT composites BP were processed by electroless deposition of gold within the pores of the BPs. This method led to highly controlled pore size and porosity composites exhibiting clearly improved adsorption of CO_2 and H_2 compared to the non plated BPs. This is a potential technique to modify CNTs with activated metal nanoparticles. This novel work showed that nanoparticles could be grown in very confined spaces on the surface of nanotubes to enhance their specific surface area and add of their properties to fabricate advanced nano-composites. However improvements and different approaches could be undertaken. Different deposition protocols might lead to a better control of the particle size and distribution across the samples while the use of other metal, cheaper such as nickel, or exhibiting better affinity for surface gas adsorption and sensing such as palladium or platinum, could be investigated.

This thesis showed that CNT in the form of a BP can be used as a template to fabricate more advanced and hybrid structures. Most of this work was focused on building effective membranes around the frame of the BPs to show that ways to benefit from the CNT properties are various: use the large range of

chemical reactions possible on graphene, use the high porosity and specific surface area of the BPs to grow specific nano-particles, use the thermal stability and low heat conductivity of the BP in applications where polymeric membrane cannot sustain temperature.

Current limitations and issues related to CNT use…

The up-scaling of BP processing to large quantities would likely raise several issues. First the dispersability of the CNTs in large concentrations is problematic. Most of the studies published show that if too concentrated, CNT suspensions become unstable and aggregation of CNTs occurs over a very short time frame. Better methods to disperse and stabilise CNTs in solutions are required before considering any up-scaled process. Furthermore, we have been allowed to use fairly pure CNTs grown at the CSIRO in this study. The quality and standards of commercial nanotubes is constantly improving but still remain inferior to that of laboratory produced CNTs. Consistency in CNTs processing conditions and in batch quality needs to be improved to generate large, reproducible quantities of CNTs. Furthermore, the price of carbon nano-materials and CNTs especially is still a limiting factor for their use even though it has sharply decreased during the past decade. It is likely that the improvements and up-scaling of CNT growth and production will lead to further price decreases, thus making CNTs more attractive and competitive with other materials. A company called Nanolab [397] has already commercialized BPs and propose different sizes showing that this structure is certainly of interest ot the broader community.

The reproducibility of the results and the number of samples tested is also a concern. Due to the small amounts of CNTs available for this study, a limited number of samples were prepared thus reducing the sense of a statistical analysis of the results. Getting better statistical data to better assess the study would require growing a larger amount of CNTs to provide more samples. This issue is certainly inherent to most of the cutting edge CNT projects where the quantity of material available for processing is low.

Eventually, the last main concern of using CNTs in water based applications regards the concept of nano-safety and prevention. Past experiences, where up-scaling and mass production of novel or nano-sized materials were prematurely undertaken and had dramatic outcomes for exposed workers and consumers. The issues related to asbestos, where the confinement of the fibres is critical for a safe use, or of additives in food or products with direct contact with skin have already created major health crises in the past. A number of studies [437, 438] refer to nanotubes as potential asbestos-like nanomaterials. Their aspect ratio, high affinity for organic matter and relative inert chemistry make them challenging particles to study from a toxicology point of view and potential hazards for health and membrane cell integrity. Their addition into membranes designed for water purification or desalination raises philosophical and ethical concerns if no complete clinical studies on the material toxicity were undertaken prior to use. Published research where bacteria or mice were exposed in various degrees to concentrated CNT sources have shown that CNTs can have a harmful impact on cell integrity and respiratory systems. More studies simulating the possible degradation of BPs over time and in different conditions would be required to assess of their use for health applications. Impurities present on the CNTs, such as metallic nano-particles, may also induce further damage. This is a serious concern and despite showing promising results in several separation applications, their impact on health should be properly investigated prior to any further large scale studies.

Identification of possible future areas of research…

Despite the fact that CNT BP were not shown to perform better than other polymeric materials regarding DCMD, this work has lead to a better understanding and perception of their intrinsic properties which could be applied in other separation areas. The main limitation of BPs over their PTFE counterparts was shown to be their pore size, falling on average a decade lower. Several approaches could be undertaken to change the BP pore size while still benefiting from the other properties of CNTs. A combination of various approaches undertaken in this work could lead to high performance

membranes. For example, lithography performed on the BP surface could lead to reproducible arrays of pores across the BP thickness. As shown during our FIB milling, the BP would certainly sustain a large number of pores thus allowing flexibility in the pore size distribution and pore density. Such modified BPs could then be sputtered with a very thin layer of PTFE which would then improve both lifespan and performance in DCMD of the membranes.

Furthermore, as demonstrated with the gold/CNT study, CNT BPs can be successfully used to grow metallic nanoparticles. The natural large porosity and specific surface area of the BP makes them promising candidates as supports for specific molecules or particles. Such composites could be used in applications such as adsorption, storage, sensing or catalysis. Due to the low adsorption capacity or catalytic properties of carbon, pure CNT BP would likely show average and limited performance, thus requiring specific functionalisation or active sites adsorbed on their surface. In the case of metal activated surface, electroless plating was shown to be successful and if applied to specific metals, such as nickel or palladium, and after optimizing the plating solution concentration and plating times, could lead to improved gas adsorption substrates. CNTs have already been shown to be very precise sensors and work has been carried out to graft metal particles on their surface to enhance their sensitivity to organics.

In fact, CNT based membranes may find an applications in niche areas where the CNT thermal or chemical stability would be beneficial. The variety of behaviours, which are directly related to the CNT number of defects or contaminants in their structure, or length may still lead to a number of breakthroughs in applications where polymeric materials cannot be used, such as the recovery of corrosive hot effluents in the mining industry, or where metallic alloys cannot be used such as in the case of very oxidative environments. The full spectrum of applications where CNTs have a future is still writing its own history.

In a nutshell...

This PhD covered a large range of characterisation and experimental methods, which was inherent to its goal: finding potential ways to process stable and reproducible membranes for water purification and gas separation. I have been honoured to be granted a CSIRO Materials Science and Engineering scholarship to perform this research and to be immersed within CMSE and the Institute for Sustainability and Innovation at Victoria University for these past 3 years. I learnt new skills and expertise in characterisation techniques, and engineering and material processing, and would like to thank once again all the people without whom this work would not have been possible.

A vous tous, merci.

"Live as if you were to die tomorrow. Learn as if you were to live forever."

~ Mahatma Gandhi

8 References

[1] S.P. library, Global water and air volume, in: S.P. library (Ed.), E055/330, 2009.

[2] Wikipedia, Water, in, 2010.

[3] U.S.B.o. Census, Total midyear world population 1950-2050, in, pp. Current Population Projections.

[4] N. Geographic, Water our thirsty world, National Geographic, 217 (2010).

[5] Wikipedia, Water crisis, in.

[6] U. Nations, World water crisis worsened by corruption, repression: UN report, in, 2006.

[7] Wikipedia, Peak Water, in, 2010.

[8] Wikipedia, Desalination, in, 2010.

[9] Wikipedia, Lockedland country, in, 2010.

[10] T. Barbari, Basic principles of membrane technology : Marcel Mulder (Ed.), Kluwer Academic Publishers, Dordrecht, The Netherlands, 1991; hardbound, Dfl. 200, ISBN 0-7923-0978-2; paperback, Dfl. 70, ISBN 0-7923-0979-0; 400 pp, Journal of Membrane Science, 72 (1992) 304-305.

[11] A. Kent Coleman, Optimization of a single effect, multi-stage flash distillation desalination system, Desalination, 9 (1971) 315-331.

[12] L.T. Fan, C.Y. Cheng, C.L. Hwang, I.E. Erickson, K.D. Kiang, Analysis and optimization of a multieffect multistage flash distillation system -- part II. Optimization, Desalination, 4 (1968) 361-388.

[13] O.A. Hamed, A.M. Zamamiri, S. Aly, N. Lior, Thermal performance and exergy analysis of a thermal vapor compression desalination system, Energy Conversion and Management, 37 (1996) 379-387.

[14] F. Al-Juwayhel, H. El-Dessouky, H. Ettouney, Analysis of single-effect evaporator desalination systems combined with vapor compression heat pumps, Desalination, 114 (1997) 253-275.

[15] H.T. El-Dessouky, H.M. Ettouney, F. Al-Juwayhel, Multiple Effect Evaporation--Vapour Compression Desalination Processes, Chemical Engineering Research and Design, 78 (2000) 662-676.

[16] J.M. Veza, MECHANICAL VAPOR COMPRESSION DESALINATION PLANTS - A CASE-STUDY, Desalination, 101 (1995) 1-10.
[17] A.C. Langmuir, The advantages of the multiple-effect distillation of glycerine and other products, Transactions of the American Institute of Chemical Engineers, 2 (1909) 274-279.
[18] M.K. Selcuk, DESIGN + PERFORMANCE EVALUATION OF MULTIPLE-EFFECT TILTED SOLAR DISTILLATION UNIT, Sol. Energy, 8 (1964) 23-&.
[19] J.C. Deronzier, MULTIPLE-EFFECT DISTILLATION PROCESS WITH HORIZONTAL TUBE EVAPORATORS, Desalination, 31 (1979) 115-124.
[20] E.E. Delyannis, STATUS OF SOLAR ASSISTED DESALINATION - A REVIEW, Desalination, 67 (1987) 3-19.
[21] L. Garcia-Rodriguez, Seawater desalination driven by renewable energies: a review, Desalination, 143 (2002) 103-113.
[22] E. Mathioulakis, V. Belessiotis, E. Delyannis, Desalination by using alternative energy: Review and state-of-the-art, Desalination, 203 (2007) 346-365.
[23] I.C. Karagiannis, P.G. Soldatos, Water desalination cost literature: review and assessment, Desalination, 223 (2008) 448-456.
[24] T. Matsuura, Progress in membrane science and technology for seawater desalination - a review, Desalination, 134 (2001) 47-54.
[25] L.F. Greenlee, D.F. Lawler, B.D. Freeman, B. Marrot, P. Moulin, Reverse osmosis desalination: Water sources, technology, and today's challenges, Water Research, 43 (2009) 2317-2348.
[26] M. Soltanieh, W.N. Gill, REVIEW OF REVERSE-OSMOSIS MEMBRANES AND TRANSPORT MODELS, Chemical Engineering Communications, 12 (1981) 279-363.
[27] R.J. Petersen, COMPOSITE REVERSE-OSMOSIS AND NANOFILTRATION MEMBRANES, Journal of Membrane Science, 83 (1993) 81-150.
[28] M. Elimelech, X.H. Zhu, A.E. Childress, S.K. Hong, Role of membrane surface morphology in colloidal fouling of cellulose acetate and composite aromatic polyamide reverse osmosis membranes, Journal of Membrane Science, 127 (1997) 101-109.

[29] C.H. Lee, THEORY OF REVERSE-OSMOSIS AND SOME OTHER MEMBRANE PERMEATION OPERATIONS, Journal of Applied Polymer Science, 19 (1975) 83-95.
[30] D.E. Potts, R.C. Ahlert, S.S. Wang, A CRITICAL-REVIEW OF FOULING OF REVERSE-OSMOSIS MEMBRANES, Desalination, 36 (1981) 235-264.
[31] E.M. Vrijenhoek, S. Hong, M. Elimelech, Influence of membrane surface properties on initial rate of colloidal fouling of reverse osmosis and nanofiltration membranes, Journal of Membrane Science, 188 (2001) 115-128.
[32] A.E. Childress, M. Elimelech, Effect of solution chemistry on the surface charge of polymeric reverse osmosis and nanofiltration membranes, Journal of Membrane Science, 119 (1996) 253-268.
[33] D. Prats, M.F. Chillon-Arias, M. Rodriguez-Pastor, Analysis of the influence of pH and pressure on the elimination of boron in reverse osmosis, Desalination, 128 (2000) 269-273.
[34] M. Kang, M. Kawasaki, S. Tamada, T. Kamei, Y. Magara, Effect of pH on the removal of arsenic and antimony using reverse osmosis membranes, Desalination, 131 (2000) 293-298.
[35] B.A. Winfield, TREATMENT OF SEWAGE EFFLUENTS BY REVERSE-OSMOSIS - PH BASED STUDIES OF THE FOULING LAYER AND ITS REMOVAL, Water Research, 13 (1979) 561-564.
[36] M. Kumar, S.S. Adham, W.R. Pearce, Investigation of seawater reverse osmosis fouling and its relationship to pretreatment type, Environmental Science & Technology, 40 (2006) 2037-2044.
[37] S. van Hoof, A. Hashim, A.J. Kordes, The effect of ultrafiltration as pretreatment to reverse osmosis in wastewater reuse and seawater desalination applications, Desalination, 124 (1999) 231-242.
[38] M.W. Hickey, R.D. Hill, B.R. Smith, INVESTIGATIONS INTO THE ULTRAFILTRATION AND REVERSE-OSMOSIS OF WHEYS .1. THE EFFECTS OF CERTAIN PRETREATMENTS, New Zealand Journal of Dairy Science and Technology, 15 (1980) 109-121.
[39] K.K. Sirkar, Membrane separation technologies: Current developments, Chemical Engineering Communications, 157 (1997) 145-184.

[40] E. Korin, I. Ladizhensky, E. Korngold, Hydrophilic hollow fiber membranes for water desalination by the pervaporation method, Chemical Engineering and Processing, 35 (1996) 451-457.
[41] J.-H. Choi, J. Jegal, W.-N. Kim, H.-S. Choi, Incorporation of multiwalled carbon nanotubes into poly(vinyl alcohol) membranes for use in the pervaporation of water/ethanol mixtures, Journal of Applied Polymer Science, 111 (2009) 2186-2193.
[42] J.C. Farmer, D.V. Fix, G.V. Mack, R.W. Pekala, J.F. Poco, Capacitive deionization of NaCl and NaNO3 solutions with carbon aerogel electrodes, Journal of the Electrochemical Society, 143 (1996) 159-169.
[43] J.C. Farmer, D.V. Fix, G.V. Mack, R.W. Pekala, J.F. Poco, Capacitive deionization of NH4ClO4 solutions with carbon aerogel electrodes, Journal of Applied Electrochemistry, 26 (1996) 1007-1018.
[44] K. Dermentzis, K. Ouzounis, Continuous capacitive deionization-electrodialysis reversal through electrostatic shielding for desalination and deionization of water, Electrochimica Acta, 53 (2008) 7123-7130.
[45] M. Hoang, B. Bolto, T. Tran, Desalination by Capacitive Deionisation, Water, February 2009 (2009) 63-66.
[46] L. Pan, X. Wang, Y. Gao, Y. Zhang, Y. Chen, Z. Sun, Electrosorption of anions with carbon nanotube and nanofibre composite film electrodes, Desalination, 244 (2009) 139-143.
[47] H. Li, Y. Gao, L. Pan, Y. Zhang, Y. Chen, Z. Sun, Electrosorptive desalination by carbon nanotubes and nanofibres electrodes and ion-exchange membranes, Water Research, 42 (2008) 4923-4928.
[48] Y.-x. Jia, H.-l. Li, M. Wang, L.-y. Wu, Y.-d. Hu, Carbon Nanotube: Possible Candidate for Forward Osmosis, Separation and Purification Technology, In Press, Accepted Manuscript.
[49] S. Chou, L. Shi, R. Wang, C.Y. Tang, C. Qiu, A.G. Fane, Characteristics and potential applications of a novel forward osmosis hollow fiber membrane, Desalination, In Press, Corrected Proof.
[50] R. Wang, L. Shi, C.Y. Tang, S. Chou, C. Qiu, A.G. Fane, Characterization of novel forward osmosis hollow fiber membranes, Journal of Membrane Science, 355 158-167.

[51] J.R. McCutcheon, R.L. McGinnis, M. Elimelech, Desalination by ammonia-carbon dioxide forward osmosis: Influence of draw and feed solution concentrations on process performance, Journal of Membrane Science, 278 (2006) 114-123.
[52] J.O. Kessler, C.D. Moody, Drinking water from sea water by forward osmosis, Desalination, 18 (1976) 297-306.
[53] A. Achilli, T.Y. Cath, E.A. Marchand, A.E. Childress, The forward osmosis membrane bioreactor: A low fouling alternative to MBR processes, Desalination, 239 (2009) 10-21.
[54] C.R. Martinetti, A.E. Childress, T.Y. Cath, High recovery of concentrated RO brines using forward osmosis and membrane distillation, Journal of Membrane Science, 331 (2009) 31-39.
[55] J.H. Hanemaaijer, J. van Medevoort, A.E. Jansen, C. Dotremont, E. van Sonsbeek, T. Yuan, L. De Ryck, Memstill membrane distillation - a future desalination technology, Desalination, 199 (2006) 175-176.
[56] C. Charcosset, A review of membrane processes and renewable energies for desalination, Desalination, 245 (2009) 214-231.
[57] A. Pak, T. Mohammadi, Wastewater treatment of desalting units, Desalination, 222 (2008) 249-254.
[58] K.W. Lawson, D.R. Lloyd, Membrane distillation. II. Direct contact MD, Journal of Membrane Science, 120 (1996) 123-133.
[59] K.W. Lawson, D.R. Lloyd, Membrane distillation, Journal of Membrane Science, 124 (1997) 1-25.
[60] K.W. Lawson, D.R. Lloyd, Membrane distillation .1. Module design and performance evaluation using vacuum membrane distillation, Journal of Membrane Science, 120 (1996) 111-121.
[61] K. Smolders, A.C.M. Franken, Terminology for Membrane Distillation, Desalination, 72 (1989) 249-262.
[62] K. Bélafi-Bakó, B. Koroknai, Enhanced water flux in fruit juice concentration: Coupled operation of osmotic evaporation and membrane distillation, Journal of Membrane Science, 269 (2006) 187-193.
[63] S. Gunka, S. Verbych, M. Bryk, N. Hilal, Concentration of apple juice using direct contact membrane distillation, Desalination, 190 (2006) 117-124.

[64] R. Broseus, J. Cigana, B. Barbeau, C. Daines-Martinez, H. Suty, Removal of total dissolved solids, nitrates and ammonium ions from drinking water using charge-barrier capacitive deionisation, Desalination, 249 (2009) 217-223.
[65] Y. Fujii, S. Kigoshi, H. Iwatani, M. Aoyama, Selectivity and characteristics of direct contact membrane distillation type experiment. I. Permeability and selectivity through dried hydrophobic fine porous membranes, Journal of Membrane Science, 72 (1992) 53-72.
[66] Y. Fujii, S. Kigoshi, H. Iwatani, M. Aoyama, Y. Fusaoka, Selectivity and characteristics of direct contact membrane distillation type experiment. II. Membrane treatment and selectivity increase, Journal of Membrane Science, 72 (1992) 73-89.
[67] M.C. García-Payo, M.A. Izquierdo-Gil, C. Fernández-Pineda, Air gap membrane distillation of aqueous alcohol solutions, Journal of Membrane Science, 169 (2000) 61-80.
[68] F. Peng, C. Hu, Z. Jiang, Novel ploy(vinyl alcohol)/carbon nanotube hybrid membranes for pervaporation separation of benzene/cyclohexane mixtures, Journal of Membrane Science, 297 (2007) 236-242.
[69] A. Criscuoli, E. Drioli, A. Capuano, B. Memoli, V.E. Andreucci, Human plasma ultrafiltrate purification by membrane distillation: process optimisation and evaluation of its possible application on-line, Desalination, 147 (2002) 147-148.
[70] S. Al-Obaidani, E. Curcio, F. Macedonio, G. Di Profio, H. Al-Hinai, E. Drioli, Potential of membrane distillation in seawater desalination: Thermal efficiency, sensitivity study and cost estimation, Journal of Membrane Science, 323 (2008) 85-98.
[71] F. Banat, R. Jumah, M. Garaibeh, Exploitation of solar energy collected by solar stills for desalination by membrane distillation, Renewable Energy, 25 (2002) 293-305.
[72] J. Blanco Gálvez, L. García-Rodríguez, I. Martín-Mateos, Seawater desalination by an innovative solar-powered membrane distillation system: the MEDESOL project, Desalination, 246 (2009) 567-576.

[73] L. Dumée, K. Sears, J. Schütz, N. Finn, M. Duke, S. Gray, Design and Characterisation of Carbon Nanotube Bucky-Paper Membranes for Membrane Distillation, in: ICOM08, Honolulu - Hawaii, USA, 2008.
[74] L. Dumée, K. Sears, J. Schütz, N. Finn, M. Duke, S. Gray, Carbon nanotube based composite membranes for water desalination by membrane distillation, DESALINATION AND WATER TREATMENT, (2010).
[75] L.F. Dumée, K. Sears, J. Schütz, N. Finn, C. Huynh, S. Hawkins, M. Duke, S. Gray, Characterization and evaluation of carbon nanotube Bucky-Paper membranes for direct contact membrane distillation, Journal of Membrane Science, 351 (2010) 36-43.
[76] C. Feng, K.C. Khulbe, T. Matsuura, R. Gopal, S. Kaur, S. Ramakrishna, M. Khayet, Production of drinking water from saline water by air-gap membrane distillation using polyvinylidene fluoride nanofiber membrane, Journal of Membrane Science, 311 (2008) 1-6.
[77] M. Khayet, J.I. Mengual, T. Matsuura, Porous hydrophobic/hydrophilic composite membranes - Application in desalination using direct contact membrane distillation, Journal of Membrane Science, 252 (2005) 101-113.
[78] J. Koschikowski, M. Wieghaus, M. Rommel, Solar thermal-driven desalination plants based on membrane distillation, Desalination, 156 (2003) 295-304.
[79] L. Song, Z. Ma, X. Liao, P.B. Kosaraju, J.R. Irish, K.K. Sirkar, Pilot plant studies of novel membranes and devices for direct contact membrane distillation-based desalination, Journal of Membrane Science, 323 (2008) 257-270.
[80] H.J. Zwijnenberg, G.H. Koops, M. Wessling, Solar driven membrane pervaporation for desalination processes, Journal of Membrane Science, 250 (2005) 235-246.
[81] A. Bessieres, M. Meireles, R. Coratger, J. Beauvillain, V. Sanchez, Investigations of surface properties of polymeric membranes by near field microscopy, Journal of Membrane Science, 109 (1996) 13.
[82] C. Cabassud, D. Wirth, Membrane distillation for water desalination: how to chose an appropriate membrane?, in: Conference on Desalination and the Environment - Fresh Water for All, Elsevier Science Bv, Malta, Italy, 2003, pp. 307-314.

[83] E. Drioli, Y.L. Wu, MEMBRANE DISTILLATION - AN EXPERIMENTAL-STUDY, Desalination, 53 (1985) 339-346.
[84] M.S. El-Bourawi, Z. Ding, R. Ma, M. Khayet, A framework for better understanding membrane distillation separation process, Journal of Membrane Science, 285 (2006) 4-29.
[85] C. Gostoli, G.C. Sarti, SEPARATION OF LIQUID-MIXTURES BY MEMBRANE DISTILLATION, Journal of Membrane Science, 41 (1989) 211-224.
[86] L. Martínez, F.J. Florido-Díaz, A. Hernández, P. Prádanos, Characterisation of three hydrophobic porous membranes used in membrane distillation: Modelling and evaluation of their water vapour permeabilities, Journal of Membrane Science, 203 (2002) 15-27.
[87] M. Khayet, K.C. Khulbe, T. Matsuura, Characterization of membranes for membrane distillation by atomic force microscopy and estimation of their water vapor transfer coefficients in vacuum membrane distillation process, Journal of Membrane Science, 238 (2004) 199-211.
[88] S. Cerneaux, I. Struzynska, W.M. Kujawski, M. Persin, A. Larbot, Comparison of various membrane distillation methods for desalination using hydrophobic ceramic membranes, Journal of Membrane Science, 337 (2009) 55-60.
[89] M.C. García-Payo, M. Essalhi, M. Khayet, Effects of PVDF-HFP concentration on membrane distillation performance and structural morphology of hollow fiber membranes, Journal of Membrane Science, In Press, Corrected Proof.
[90] M.A. Izquierdo-Gil, G. Jonsson, Factors affecting flux and ethanol separation performance in vacuum membrane distillation (VMD), Journal of Membrane Science, 214 (2003) 113-130.
[91] A. Hernández, J.I. Calvo, P. Prádanos, F. Tejerina, Pore Size Distributions in Microporous Membranes. A Critical Analysis of the Bubble Point Extended Method, J. Membr. Sci., 112 (1996) 1-12.
[92] M. Qtaishat, D. Rana, M. Khayet, T. Matsuura, Preparation and characterization of novel hydrophobic/hydrophilic polyetherimide composite membranes for desalination by direct contact membrane distillation, Journal of Membrane Science, 327 (2009) 264-273.

[93] D. Li, M.W. Frey, Y.L. Joo, Characterization of nanofibrous membranes with capillary flow porometry, Journal of Membrane Science, 286 (2006) 104-114.
[94] J.I. Calvo, A. Hernández, P. Prádanos, L. MartInez, W.R. Bowen, Pore Size Distributions in Microporous Membranes II. Bulk Characterization of Track-Etched Filters by Air Porometry and Mercury Porosimetry, Journal of Colloid and Interface Science, 176 (1995) 467-478.
[95] A. Hernández, J.I. Calvo, P. Prádanos, F. Tejerina, Pore size distributions in microporous membranes. A critical analysis of the bubble point extended method, Journal of Membrane Science, 112 (1996) 1-12.
[96] M. Mietton-Peuchot, C. Condat, T. Courtois, Use of gas-liquid porometry measurements for selection of microfiltration membranes, Journal of Membrane Science, 133 (1997) 73-82.
[97] M. Qtaishat, M. Khayet, T. Matsuura, Guidelines for preparation of higher flux hydrophobic/hydrophilic composite membranes for membrane distillation, Journal of Membrane Science, 329 (2009) 193-200.
[98] J.R. Oppenheimer, A.G. Martin, L.P. Walker, Measurements of air-filled porosity in unsaturated organic matrices using a pycnometer, Bioresource Technology, 59 241-247.
[99] J. Phattaranawik, R. Jiraratananon, A.G. Fane, Effect of pore size distribution and air flux on mass transport in direct contact membrane distillation, Journal of Membrane Science, 215 (2003) 75-85.
[100] R.W. Schofield, A.G. Fane, C.J.D. Fell, Gas and vapour transport through microporous membranes. II. Membrane distillation, Journal of Membrane Science, 53 (1990) 173-185.
[101] R. Smajda, A. Kukovecz, B. Hopp, M. Mohl, Z. Kónya, I. Kiricsi, Morphology and N_2 Permeability of Multi-wall Carbon Nanotube-Teflon Membranes, J. Nanosci. Nanotechnol., 7 (2007) 1604-1610.
[102] R. Smajda, A. Kukovecz, Z. Konya, I. Kiricsi, Structure and gas permeability of multi-wall carbon nanotube buckypapers, Carbon, 45 (2007) 1176-1184.
[103] C. Fernández-Pineda, M.A. Izquierdo-Gil, M.C. García-Payo, Gas permeation and direct contact membrane distillation experiments and their

analysis using different models, Journal of Membrane Science, 198 (2002) 33-49.
[104] S. Srisurichan, R. Jiraratananon, A.G. Fane, Mass transfer mechanisms and transport resistances in direct contact membrane distillation process, Journal of Membrane Science, 277 (2006) 186-194.
[105] M. Tomaszewska, M. Gryta, A.W. Morawski, Mass transfer of HCl and H2O across the hydrophobic membrane during membrane distillation, Journal of Membrane Science, 166 (2000) 149-157.
[106] A.M. Alklaibi, N. Lior, Transport analysis of air-gap membrane distillation, Journal of Membrane Science, 255 (2005) 239-253.
[107] S.C. Xu, Y.X. Wang, S.C. Wang, Transport mode of membrane distillation process and the VMD method to determine the membrane configurational number, Journal of Membrane Science, 97 (1994) 1-6.
[108] D. Wirth, C. Cabassud, Water desalination using membrane distillation: comparison between inside/out and outside/in permeation, Desalination, 147 (2002) 139-145.
[109] A. Burgoyne, M.M. Vahdati, Direct Contact Membrane Distillation, Separation Science and Technology, 35 (2000) 1257 - 1284.
[110] P. Peng, A.G. Fane, X.D. Li, Desalination by membrane distillation adopting a hydrophilic membrane, Desalination, 173 (2005) 45-54.
[111] M. Khayet, T. Matsuura, J.I. Mengual, M. Qtaishat, Design of novel direct contact membrane distillation membranes, Desalination, 192 (2006) 105-111.
[112] S. Bonyadi, T.S. Chung, Flux enhancement in membrane distillation by fabrication of dual layer hydrophilic-hydrophobic hollow fiber membranes, Journal of Membrane Science, 306 (2007) 134-146.
[113] M. Gryta, Fouling in direct contact membrane distillation process, Journal of Membrane Science, 325 (2008) 383-394.
[114] A.C.M. Franken, J.A.M. Nolten, M.H.V. Mulder, D. Bargeman, C.A. Smolders, WETTING CRITERIA FOR THE APPLICABILITY OF MEMBRANE DISTILLATION, Journal of Membrane Science, 33 (1987) 315-328.
[115] Hollow fibres PVDF, in.
[116] Flat sheet chapter.
[117] hollow fibre module.

[118] T.Y. Cath, V.D. Adams, A.E. Childress, Experimental study of desalination using direct contact membrane distillation: a new approach to flux enhancement, Journal of Membrane Science, 228 (2004) 5-16.
[119] T.-C. Chen, C.-D. Ho, H.-M. Yeh, Theoretical modeling and experimental analysis of direct contact membrane distillation, Journal of Membrane Science, 330 (2009) 279-287.
[120] M. Khayet, P. Godino, J.I. Mengual, Theory and experiments on sweeping gas membrane distillation, Journal of Membrane Science, 165 (2000) 261-272.
[121] M. Khayet, P. Godino, J.I. Mengual, Nature of flow on sweeping gas membrane distillation, Journal of Membrane Science, 170 (2000) 243-255.
[122] C.H. Lee, W.H. Hong, Effect of operating variables on the flux and selectivity in sweep gas membrane distillation for dilute aqueous isopropanol, Journal of Membrane Science, 188 (2001) 79-86.
[123] C.A. Rivier, M.C. Garcia-Payo, I.W. Marison, U. von Stockar, Separation of binary mixtures by thermostatic sweeping gas membrane distillation I. Theory and simulations, Journal of Membrane Science, 201 (2002) 1-16.
[124] S. Bandini, C. Gostoli, G.C. Sarti, Separation efficiency in vacuum membrane distillation, Journal of Membrane Science, 73 (1992) 217-229.
[125] S. Bandini, A. Saavedra, G.C. Sarti, Vacuum membrane distillation: Experiments and modeling, Aiche Journal, 43 (1997) 398-408.
[126] S. Bonyadi, T.-S. Chung, Highly porous and macrovoid-free PVDF hollow fiber membranes for membrane distillation by a solvent-dope solution co-extrusion approach, Journal of Membrane Science, 331 (2009) 66-74.
[127] G.C. Sarti, C. Gostoli, S. Bandini, Extraction of organic components from aqueous streams by vacuum membrane distillation, Journal of Membrane Science, 80 (1993) 21-33.
[128] G.C. Sarti, C. Gostoli, S. Bandini, EXTRACTION OF ORGANIC-COMPONENTS FROM AQUEOUS STREAMS BY VACUUM MEMBRANE DISTILLATION, in: International Conf on Engineering of Membrane Processes, Garmisch Partenkir, Germany, 1992, pp. 21-33.
[129] M. Tomaszewska, Concentration of the extraction fluid from sulfuric acid treatment of phosphogypsum by membrane distillation, Journal of Membrane Science, 78 (1993) 277-282.

[130] L. Dumée, K. Sears, J. Schütz, N. Finn, M. Duke, S. Gray., Design and Characterisation of Carbon Nanotube Bucky-Paper Membranes for Membrane Distillation, DESALINATION AND WATER TREATMENT, (2009) Submitted.
[131] E. Curcio, E. Drioli, Membrane Distillation and Related Operationsâ€”A Review, Separation & Purification Reviews, 34 (2005) 35 - 86.
[132] M. Gryta, M. Tomaszewska, K. Karakulski, Wastewater treatment by membrane distillation, Desalination, 198 (2006) 67-73.
[133] B.R. Babu, N.K. Rastogi, K.S.M.S. Raghavarao, Mass transfer in osmotic membrane distillation of phycocyanin colorant and sweet-lime juice, Journal of Membrane Science, 272 (2006) 58-69.
[134] V. Calabro, B.L. Jiao, E. Drioli, THEORETICAL AND EXPERIMENTAL-STUDY ON MEMBRANE DISTILLATION IN THE CONCENTRATION OF ORANGE JUICE, Industrial & Engineering Chemistry Research, 33 (1994) 1803-1808.
[135] M. Gryta, M. Tomaszewska, Heat transport in the membrane distillation process, Journal of Membrane Science, 144 (1998) 211-222.
[136] A.M. Alklaibi, N. Lior, Heat and mass transfer resistance analysis of membrane distillation, Journal of Membrane Science, 282 (2006) 362-369.
[137] S. Bouguecha, R. Chouikh, M. Dhahbi, Numerical study of the coupled heat and mass transfer in membrane distillation, Desalination, 152 (2003) 245-252.
[138] M. Gryta, M. Tomaszewska, W. Morawski, Heat transfer in membrane distillation, Inzynieria Chemiczna I Procesowa, 17 (1996) 159-173.
[139] J. Phattaranawik, R. Jiraratananon, A.G. Fane, Effects of net-type spacers on heat and mass transfer in direct contact membrane distillation and comparison with ultrafiltration studies, Journal of Membrane Science, 217 (2003) 193-206.
[140] J. Phattaranawik, R. Jiraratananon, A.G. Fane, Heat transport and membrane distillation coefficients in direct contact membrane distillation, Journal of Membrane Science, 212 (2003) 177-193.
[141] G. Ramon, Y. Agnon, C. Dosoretz, Heat transfer in vacuum membrane distillation: Effect of velocity slip, Journal of Membrane Science, 331 (2009) 117-125.

[142] R.W. Schofield, A.G. Fane, C.J.D. Fell, HEAT AND MASS-TRANSFER IN MEMBRANE DISTILLATION, Journal of Membrane Science, 33 (1987) 299-313.
[143] P. Termpiyakul, R. Jiraratananon, S. Srisurichan, Heat and mass transfer characteristics of a direct contact membrane distillation process for desalination, Desalination, 177 (2005) 133-141.
[144] J. Zhang, N. Dow, M. Duke, E. Ostarcevic, J.-d. Li, S. Gray, Identification of material and physical features of membrane distillation membranes for high performance desalination, Journal of membrane science, (2010).
[145] J. Zhang, J.-D. Li, M. Duke, Z. Xie, S. Gray, Performance of asymmetric hollow fibre membranes in membrane distillation under various configurations and vacuum enhancement, Journal of Membrane Science, 362 517-528.
[146] S.P. Agashichev, D.V. Falalejev, Modeling temperature polarization phenomena for longitudinal shell-side flow in membrane distillation process, Desalination, 108 (1997) 99-103.
[147] R.W. Schofield, A.G. Fane, C.J.D. Fell, R. Macoun, Factors Affecting Flux in Membrane Distillation, Desalination, 77 (1990) 279-294.
[148] M.N. Chernyshov, G.W. Meindersma, A.B. de Haan, Modelling temperature and salt concentration distribution in membrane distillation feed channel, Desalination, 157 (2003) 315-324.
[149] M. Courel, M. Dornier, G.M. Rios, M. Reynes, Modelling of water transport in osmotic distillation using asymmetric membrane, Journal of Membrane Science, 173 (2000) 107-122.
[150] F. Lagana, G. Barbieri, E. Drioli, Direct contact membrane distillation: modelling and concentration experiments, Journal of Membrane Science, 166 (2000) 1-11.
[151] L. Mariah, C.A. Buckley, C.J. Brouckaert, E. Curcio, E. Drioli, D. Jaganyi, D. Ramjugernath, Membrane distillation of concentrated brines--Role of water activities in the evaluation of driving force, Journal of Membrane Science, 280 (2006) 937-947.
[152] R.B. Bird, W.E. Stewart, E.N. Lightfoot, Transport Phenomena, Revised 2nd Edition, John Wiley & Sons, Inc, New Yor/Chichester/Weinheim/Brisbane/Singapore/Toronto, 2006.

[153] D. Basmadjian, Mass transfer: principles and applications, 2004.
[154] S.P. Agashichev, A.V. Sivakov, MODELING AND CALCULATION OF TEMPERATURE-CONCENTRATION POLARIZATION IN THE MEMBRANE DISTILLATION PROCESS (MD), Desalination, 93 (1993) 245-258.
[155] M. Celere, C. Gostoli, Heat and mass transfer in osmotic distillation with brines, glycerol and glycerol-salt mixtures, Journal of Membrane Science, 257 (2005) 99-110.
[156] H. Susanto, Towards practical implementations of membrane distillation, Chemical Engineering and Processing: Process Intensification, 50 (2011) 139-150.
[157] L. Dumée, J.L. Campbell, K. Sears, J. Schütz, N. Finn, M. Duke, S. Gray, The impact of hydrophobic coating on the performance of carbon nanotube bucky-paper membranes in membrane distillation, Desalination, In Press, Corrected Proof.
[158] L. Dumée, V. Germain, K. Sears, J. Schütz, N. Finn, M. Duke, S. Cerneaux, D. Cornu, S. Gray, Enhanced durability and hydrophobicity of carbon nanotube bucky paper membranes in membrane distillation, Journal of Membrane Science, 376 (2011) 241-246.
[159] Y. Wu, Y. Kong, X. Lin, W. Liu, J. Xu, Surface-modified hydrophilic membranes in membrane distillation, Journal of Membrane Science, 72 (1992) 189-196.
[160] M. Qtaishat, M. Khayet, T. Matsuura, Novel porous composite hydrophobic/hydrophilic polysulfone membranes for desalination by direct contact membrane distillation, Journal of Membrane Science, 341 (2009) 139-148.
[161] M. Khayet, T. Matsuura, Application of surface modifying macromolecules for the preparation of membranes for membrane distillation, Desalination, 158 (2003) 51-56.
[162] D.E. Suk, T. Matsuura, H.B. Park, Y.M. Lee, Synthesis of a new type of surface modifying macromolecules (nSMM) and characterization and testing of nSMM blended membranes for membrane distillation, Journal of Membrane Science, 277 (2006) 177-185.

[163] Z.D. Hendren, J. Brant, M.R. Wiesner, Surface modification of nanostructured ceramic membranes for direct contact membrane distillation, Journal of Membrane Science, 331 (2009) 1-10.
[164] M. Gryta, J. Grzechulska-Damszel, A. Markowska, K. Karakulski, The influence of polypropylene degradation on the membrane wettability during membrane distillation, Journal of Membrane Science, 326 (2009) 493-502.
[165] M. Gryta, Long-term performance of membrane distillation process, Journal of Membrane Science, 265 (2005) 153-159.
[166] P. Peng, A.G. Fane, X. Li, Desalination by membrane distillation adopting a hydrophilic membrane, Desalination, 173 (2005) 45-54.
[167] M. Khayet, T. Matsuura, Preparation and Characterization of Polyvinylidene Fluoride Membranes for Membrane Distillation, Industrial & Engineering Chemistry Research, 40 (2001) 5710-5718.
[168] M. Khayet, J.I. Mengual, T. Matsuura, Porous hydrophobic/hydrophilic composite membranes: Application in desalination using direct contact membrane distillation, Journal of Membrane Science, 252 (2005) 101-113.
[169] J.T.F. Keurentjes, J.G. Harbrecht, D. Brinkman, J.H. Hanemaaijer, M.A. Cohen Stuart, K. van't Riet, Hydrophobicity measurements of microfiltration and ultrafiltration membranes, Journal of Membrane Science, 47 (1989) 333-344.
[170] BSI, PAS71 - Vocabulary - Nanoparticles, in, 2005.
[171] D.T. Colbert, R.E. Smalley, Fullerene nanobutes for molecular electronics, Trends in Biotechnology, 17 (1999) 46-50.
[172] S. Iijima, Helical microtubules of graphitic carbon, Nature, 354 (1991) 56-58.
[173] M.d.F. Daenen, R.D., B. Hamers, P.G.A. Janssen, K. Schouteden, M.A.J. Veld, Wondruous wolrd of Carbon nanotubes, in, 2003.
[174] S. Matsumoto, L. Pan, H. Tokumoto, Y. Nakayama, Selective growth of single-walled carbon nanotubes by chemical vapor deposition, Physica B: Condensed Matter, 323 (2002) 275-276.
[175] C.P. Huynh, S.C. Hawkins, Understanding the synthesis of directly spinnable carbon nanotube forests, Carbon, 48 1105-1115.

[176] J. Bernholc, D. Brenner, M. Buongiorno Nardelli, V. Meunier, C. Roland, Mechanical and electrical properties of nanotubes, Annual Review of Materials Research, 32 (2002) 28.
[177] M. Daenen, R.D. de Fouw, B. Hamers, P.G.A. Janssen, K. Schouteden, M.A.J. Veld, Wondruous wolrd of Carbon nanotubes, in, 2003.
[178] Tong Lin, Vardhan Bajpai, Tao Ji, Liming Dai, Chemistry of Carbon Nanotubes, ChemInform, 34 (2003).
[179] C.H. Lee, M. Xie, V. Kayastha, J. Wang, Y.K. Yap, Patterned Growth of Boron Nitride Nanotubes by Catalytic Chemical Vapor Deposition, Chemistry of Materials, 22 1782-1787.
[180] V. Nirmala, P. Kolandaivel, Structure and electronic properties of armchair boron nitride nanotubes, Journal of Molecular Structure: THEOCHEM, 817 (2007) 137-145.
[181] L. Li, C.P. Li, Y. Chen, Synthesis of boron nitride nanotubes, bamboos and nanowires, Physica E: Low-dimensional Systems and Nanostructures, 40 (2008) 2513-2516.
[182] K. Özdogan, S. Berber, Optimizing the hydrogen storage in boron nitride nanotubes by defect engineering, International Journal of Hydrogen Energy, 34 (2009) 5213-5217.
[183] J.W. Kang, et al., Structures of ultrathin copper nanotubes, Journal of Physics: Condensed Matter, 14 (2002) 8997.
[184] G. Xie, X. Li, H. Jiao, Template-Synthesized Copper Nanotubes via Electroless Plating, Journal of Dispersion Science and Technology, 29 (2008) 120 - 123.
[185] L. Velleman, J.G. Shapter, D. Losic, Gold nanotube membranes functionalised with fluorinated thiols for selective molecular transport, Journal of Membrane Science, 328 (2009) 121-126.
[186] P.K. Panigrahi, A. Pathak, Microwave-assisted synthesis of WS 2 nanowires through tetrathiotungstate precursors, Science and Technology of Advanced Materials, 9 (2008) 045008.
[187] I.G.-. IsraCast, Nano-Armor: Protecting the Soldiers of Tomorrow, in, 2005.
[188] Wikipedia, Tungsten(IV) sulfide, in, 2010.

[189] X.-y. Liu, J.-h. Zeng, S.-y. Zhang, R.-b. Zheng, X.-m. Liu, Y.-t. Qian, Novel bismuth nanotube arrays synthesized by solvothermal method, Chem. Phys. Lett., 374 (2003) 348-352.
[190] C. Su, et al., Bismuth nanotubes: potential semiconducting nanomaterials, Nanotechnology, 13 (2002) 746.
[191] Y. Tian, Y. He, Y. Zhu, Low temperature synthesis and characterization of molybdenum disulfide nanotubes and nanorods, Materials Chemistry and Physics, 87 (2004) 87-90.
[192] W.K. Hsu, B.H. Chang, Y.Q. Zhu, W.Q. Han, H. Terrones, M. Terrones, N. Grobert, A.K. Cheetham, H.W. Kroto, D.R.M. Walton, An Alternative Route to Molybdenum Disulfide Nanotubes, Journal of the American Chemical Society, 122 (2000) 10155-10158.
[193] X. Chen, M. Schriver, T. Suen, S.S. Mao, Fabrication of 10 nm diameter TiO2 nanotube arrays by titanium anodization, Thin Solid Films, 515 (2007) 8511-8514.
[194] M. Qamar, C.R. Yoon, H.J. Oh, N.H. Lee, K. Park, D.H. Kim, K.S. Lee, W.J. Lee, S.J. Kim, Preparation and photocatalytic activity of nanotubes obtained from titanium dioxide, Catalysis Today, 131 (2008) 3-14.
[195] O.K. Varghese, D. Gong, M. Paulose, K.G. Ong, C.A. Grimes, Hydrogen sensing using titania nanotubes, Sensors and Actuators B: Chemical, 93 (2003) 338-344.
[196] E. Sennik, Z. Çolak, N. KılInç, Z.Z. Öztürk, Synthesis of highly-ordered TiO2 nanotubes for a hydrogen sensor, International Journal of Hydrogen Energy, 35 4420-4427.
[197] T. Rattanavoravipa, T. Sagawa, S. Yoshikawa, Photovoltaic performance of hybrid solar cell with TiO2 nanotubes arrays fabricated through liquid deposition using ZnO template, in, 2008, pp. 1445-1449.
[198] Z. Liu, B. Pesic, K.S. Raja, R.R. Rangaraju, M. Misra, Hydrogen generation under sunlight by self ordered TiO2 nanotube arrays, International Journal of Hydrogen Energy, 34 (2009) 3250-3257.
[199] P. Castrucci, M. Scarselli, M. De Crescenzi, M. Diociaiuti, P.S. Chaudhari, C. Balasubramanian, T.M. Bhave, S.V. Bhoraskar, Silicon nanotubes: Synthesis and characterization, Thin Solid Films, 508 (2006) 226-230.

[200] Dmitrii F. Perepichka, F. Rosei, Silicon Nanotubes, Small, 2 (2006) 22-25.
[201] C. Mu, Q. Zhao, D. Xu, Q. Zhuang, Y. Shao, Silicon Nanotube Array/Gold Electrode for Direct Electrochemistry of Cytochrome c, The Journal of Physical Chemistry B, 111 (2007) 1491-1495.
[202] O. Michael Graham Richard, Canada, Li-Ion Battery Breakthrough: Silicon Nanotubes Boost Capacity 10x, in, 2009.
[203] S.C. Hawkins, J.M. Poole, C.P. Huynh, Catalyst Distribution and Carbon Nanotube Morphology in Multilayer Forests by Mixed CVD Processes, The Journal of Physical Chemistry C, 113 (2009) 12976-12982.
[204] C. Huynh, S. Hawkins, Understanding the synthesis of directly spinnable carbon nanotube forests, Submitted to Carbon, (2009).
[205] C. Huynh, S. Hawkins, Understanding the Synthesis of Directly Spinnable Carbon Nanotube Forests., Submitted to Carbon, (2009).
[206] Y.H. Yun, V. Shanov, Y. Tu, S. Subramaniam, M.J. Schulz, Growth mechanism of long aligned multiwall carbon nanotube arrays by water-assisted chemical vapor deposition, Journal of Physical Chemistry B, 110 (2006) 23920-23925.
[207] S. Daniel, T.P. Rao, K.S. Rao, S.U. Rani, G.R.K. Naidu, H.Y. Lee, T. Kawai, A review of DNA functionalized/grafted carbon nanotubes and their characterization, Sens. Actuator B-Chem., 122 (2007) 672-682.
[208] A.E. Aliev, C. Guthy, M. Zhang, S. Fang, A.A. Zakhidov, J.E. Fischer, R.H. Baughman, Thermal transport in MWCNT sheets and yarns, Carbon, 45 (2007) 2880-2888.
[209] B. Fugetsu, E. Sano, M. Sunada, Y. Sambongi, T. Shibuya, X. Wang, T. Hiraki, Electrical conductivity and electromagnetic interference shielding efficiency of carbon nanotube/cellulose composite paper, Carbon, 46 (2008) 1256-1258.
[210] Q.-m. Gong, Z. Li, X.-d. Bai, D. Li, Y. Zhao, J. Liang, Thermal properties of aligned carbon nanotube/carbon nanocomposites, Materials Science and Engineering A, 384 (2004) 209-214.
[211] M. Grujicic, W.C. Bell, L.L. Thompson, K.L. Koudela, B.A. Cheeseman, Ballistic-protection performance of carbon-nanotube-doped poly-vinyl-ester-

epoxy matrix composite armor reinforced with E-glass fiber mats, Materials Science & Engineering A, 479 (2008) 10-22.
[212] Y.W. Ju, G.R. Choi, H.R. Jung, W.J. Lee, Electrochemical properties of electrospun PAN/MWCNT carbon nanofibers electrodes coated with polypyrrole, Electrochimica Acta, 53 (2008) 5796-5803.
[213] P.C. Ma, J.-K. Kim, B.Z. Tang, Functionalization of carbon nanotubes using a silane coupling agent, Carbon, 44 (2006) 3232-3238.
[214] L.M. Sherman, Carbon Nanotubes Lots of Potential—If the Price is Right in, 2009.
[215] Nanogloss, How Much Do Nanotubes Cost?, in, October 2009.
[216] J. Hone, M.C. Llaguno, N.M. Nemes, A.T. Johnson, J.E. Fischer, D.A. Walters, M.J. Casavant, J. Schmidt, R.E. Smalley, Electrical and thermal transport properties of magnetically aligned single wall carbon nanotube films, Applied Physics Letters, 77 (2000) 666-668.
[217] M. Akoshima, K. Hata, D.N. Futaba, K. Mizuno, T. Baba, M. Yumura, Thermal Diffusivity of Single-Walled Carbon Nanotube Forest Measured by Laser Flash Method, in: 1st International Symposium on Thermal Design and Themophysical Property for Electronics, Inst Pure Applied Physics, Tsukuba, JAPAN, 2008.
[218] J. Che, T. Cagin, W.A.G. Iii, Thermal conductivity of carbon nanotubes, Nanotechnology, 11 (2000) 65-69.
[219] K.R. Atkinson, S.C. Hawkins, C. Huynh, C. Skourtis, J. Dai, M. Zhang, S. Fang, A.A. Zakhidov, S.B. Lee, A.E. Aliev, C.D. Williams, R.H. Baughman, Multifunctional carbon nanotube yarns and transparent sheets: Fabrication, properties, and applications, Physica B: Condensed Matter, 394 (2007) 339-343.
[220] S.V. Ahir, Y.Y. Huang, E.M. Terentjev, Polymers with aligned carbon nanotubes: Active composite materials, Polymer, 49 (2008) 3841-3854.
[221] J.N. Coleman, U. Khan, W.J. Blau, Y.K. Gun'ko, Small but strong: A review of the mechanical properties of carbon nanotube-polymer composites, Carbon, 44 (2006) 1624-1652.
[222] C. Li, E.T. Thostenson, T.-W. Chou, Sensors and actuators based on carbon nanotubes and their composites: A review, Composites Science and Technology, 68 (2008) 1227-1249.

[223] K. Sears, L. Dumée, J. Schütz, M. She, C. Huynh, S. Hawkins, M. Duke, S. Gray, Recent Developments in Carbon Nanotube Membranes for Water Purification and Gas Separation, Materials, 3 (2009) 127-149.
[224] D. Suppiger, S. Busato, P. Ermanni, Characterization of Single-Walled Carbon Nanotube Mats and their Performance as Electromechanical Actuators, Carbon, 46 (2008) 1085-1090.
[225] U. Vohrer, I. Kolaric, M.H. Haque, S. Roth, U. Detlaff-Weglikowska, Carbon Nanotube Sheets for the use as Artificial Muscles, Carbon, 42 (2004) 1159-1164.
[226] J.H. Rouse, Polymer-Assisted Dispersion of Single-Walled Carbon Nanotubes in Alcohols and Applicability toward Carbon Nanotube/Sol-Gel Composite Formation, Langmuir, 21 (2005) 1055-1061.
[227] S. Bandow, S. Asaka, X. Zhao, Y. Ando, Purification and Magnetic Properties of Carbon Nanotubes, Appl. Phys. A: Mater. Sci. Process., 67 (1998) 23-27.
[228] A.C. Dillon, T. Gennett, K.M. Jones, J.L. Alleman, P.A. Parilla, M.J. Heben, A Simple and Complete Purification of Single-Walled Carbon Nanotube Materials, Adv. Mater., 11 (1999) 1354-1358.
[229] M. Cinke, J. Li, B. Chen, A. Cassell, L. Delzeit, J. Han, M. Meyyappan, Pore Structure of Raw and Purified HiPco Single-Walled Carbon Nanotubes, Chem. Phys. Lett., 365 (2002) 69-74.
[230] J.G. Park, S. Li, X. Fan, C. Zhang, B. Wang, The High Current-Carrying Capacity of Various Carbon Nanotube-Based Buckypapers, Nanotechnology, 19 (2008) 185710-(185711-185717).
[231] Y.-Q. Xu, H. Peng, R.H. Hauge, R.E. Smalley, Controlled Multistep Purification of Single-Walled Carbon Nanotubes, Nano Lett., 5 (2005) 163-168.
[232] H. Hu, B. Zhao, M.E. Itkis, R.C. Haddon, Nitric Acid Purification of Single-Walled Carbon Nanotubes, J. Phys. Chem. B, 107 (2003) 13838-13842.
[233] K.J. Ziegler, Z. Gu, H. Peng, E.L. Flor, R.H. Hauge, R.E. Smalley, Controlled Oxidative Cutting of Single-Walled Carbon Nanotubes, J. Am. Chem. Soc., 127 (2005) 1541-1547.

[234] Z. Sun, V. Nicolosi, D. Rickard, S.D. Bergin, D. Aherne, J.N. Coleman, Quantitative Evaluation of Surfactant-Stabilised Single-Walled Carbon Nanotubes:Dispersion Quality and its Correlation with Zeta Potential, J. Phys. Chem. C, 112 (2008) 10692-10699.
[235] L. Vaisman, H.D. Wagner, G. Marom, The Role of Surfactants in Dispersion of Carbon Nanotubes, Adv. Colloid Interface Sci., 128-130 (2006) 37-46.
[236] T. Lin, V. Bajapi, T. Ji, L. Dai, Chemistry of Carbon Nanotubes, Aust. J. Chem., 56 (2003) 635-651.
[237] M.S.P. Shaffer, X. Fan, A.H. Windle, Dispersion and Packing of Carbon Nanotubes, Carbon, 36 (1998) 1603-1612.
[238] J. Yu, N. Grossiord, C.E. Koning, J. Loos, Controlling the Dispersion of Multi-wall Carbon Nanotubes in Aqueous Surfactant Solution, Carbon, 45 (2007) 618-623.
[239] B.R. Priya, H.J. Byrne, Investigation of Sodium Dodecyl Benzene Sulfonate Assisted Dispersion and Debundling of Single-Walled Carbon Nanotubes, J. Phys. Chem. B, 112 (2008) 332-337.
[240] Y. Wang, L. Gao, J. Sun, Y. Liu, S. Zheng, H. Kajiura, Y. Li, K. Noda, An Integrated Route for Purification, Cutting and Dispersion of Single-Walled Carbon Nanotubes, Chem. Phys. Lett., 432 (2006) 205-208.
[241] A. Nish, J.-J. Hwang, J. Doig, R.J. Nicholas, Highly Selective Dispersion of Single-Walled Carbon Nanotubes using Aromatic Polymers, Nature, 2 (2007) 640-646.
[242] M. Zheng, A. Jagota, E.D. Semke, B.A. Diner, R.S. Mclean, S.R. Lustig, R.E. Richardson, N.G. Tassis, DNA-Assisted Dispersion and Separation of Carbon Nanotubes, Nature, 2 (2003) 338-342.
[243] E.V. Blagov, G.L. Klimchitskaya, V.M. Mostepanenko, van der Waals interaction between a microparticle and a single-walled carbon nanotube, Physical Review B, 75 (2007) 235413.
[244] V.A. Parsegian, Van der Waals Forces: A Handbook for Biologists, Chemists, Engineers, and Physicists, Cambridge University Press, 2005.
[245] C. Wei, D. Srivastava, K. Cho, Thermal Expansion and Diffusion Coefficients of Carbon Nanotube-Polymer Composites, Nano Letters, 2 (2002) 647-650.

[246] Q. Cheng, S. Debnath, E. Gregan, H.J. Byrne, Effect of Solvent Solubility Parameters on the Dispersion of Single-Walled Carbon Nanotubes, J. Phys. Chem. C, 112 (2008) 20154-20158.
[247] Jihua Gou, Single-walled nanotube bucky paper and nanocomposite, Polymer International, 55 (2006) 1283-1288.
[248] J.U. Lee, J. Huh, K.H. Kim, C. Park, W.H. Jo, Aqueous suspension of carbon nanotubes via non-covalent functionalization with oligothiophene-terminated poly(ethylene glycol), Carbon, 45 (2007) 1051-1057.
[249] C. Li, J. Liu, X. Qu, B. Guo, Z. Yang, Polymer-modified halloysite composite nanotubes, Journal of Applied Polymer Science, 110 (2008) 3638-3646.
[250] Z. Spitalsky, D. Tasis, K. Papagelis, C. Galiotis, Carbon nanotube-polymer composites: Chemistry, processing, mechanical and electrical properties, Progress in Polymer Science, In Press, Corrected Proof.
[251] M. Majumder, N. Chopra, B.J. Hinds, Effect of Tip Functionalization on Transport through Vertically Oriented Carbon Nanotube Membranes, J. Am. Chem. Soc., 127 (2005) 9062-9070.
[252] M. Majumder, A. Stinchcomb, B.J. Hinds, Towards mimicking natural protein channels with aligned carbon nanotube membranes for active drug delivery, Life Sciences, 86 563-568.
[253] B.J. Hinds, N. Chopra, T. Rantell, R. Andrews, V. Gavalas, L.G. Bachas, Aligned multiwalled carbon nanotube membranes, Science, 303 (2004) 62-65.
[254] K.-Y. Lin, W.-T. Tsai, T.-J. Yang, Effect of Ni nanoparticle distribution on hydrogen uptake in carbon nanotubes, Journal of Power Sources, In Press, Corrected Proof.
[255] N. Alexeyeva, J. Kozlova, V. Sammelselg, P. Ritslaid, H. Mändar, K. Tammeveski, Electrochemical and surface characterisation of gold nanoparticle decorated multi-walled carbon nanotubes, Applied Surface Science, 256 3040-3046.
[256] J. Kim, M.M. Rabbani, D. Kim, M. Ree, J.H. Yeum, C.H. Ko, Y. Kim, J.-S. Bae, W. Oh, Structural and electrochemical properties of gold-deposited carbon nanotube composites, Current Applied Physics, 10 S201-S205.

[257] J. Manso, M.L. Mena, P. Yáñez-Sedeño, J. Pingarrón, Electrochemical biosensors based on colloidal gold-carbon nanotubes composite electrodes, Journal of Electroanalytical Chemistry, 603 (2007) 1-7.
[258] X. Su, J. Wu, B.J. Hinds, Catalytic activity of ultrathin Pt films on aligned carbon nanotube arrays, Carbon, In Press, Corrected Proof.
[259] S. Agrawal, M.S. Raghuveer, H. Li, G. Ramanath, Defect-induced electrical conductivity increase in individual multiwalled carbon nanotubes, Applied Physics Letters, 90 (2007) 193104-193104-193103.
[260] M.-L. Sham, J.-K. Kim, Surface functionalities of multi-wall carbon nanotubes after UV/Ozone and TETA treatments, Carbon, 44 (2006) 768-777.
[261] K.K.S. Lau, J. Bico, K.B.K. Teo, M. Chhowalla, G.A.J. Amaratunga, W.I. Milne, G.H. McKinley, K.K. Gleason, Superhydrophobic carbon nanotube forests, Nano Letters, 3 (2003) 1701-1705.
[262] V. Pichot, P. Launois, M. Pinault, M. Mayne-L'Hermite, C. Reynaud, Evidence of strong nanotube alignment and for iron preferential growth axis in multiwalled carbon nanotube carpets, Applied Physics Letters, 85 (2004) 473-475.
[263] O.A. Louchev, T. Laude, Y. Sato, H. Kanda, Diffusion-controlled kinetics of carbon nanotube forest growth by chemical vapor deposition, Journal of Chemical Physics, 118 (2003) 7622-7634.
[264] M. Zhang, K.R. Atkinson, R.H. Baughman, Multifunctional carbon nanotube yarns by downsizing an ancient technology, Science, 306 (2004) 1358-1361.
[265] B.Y.A. Kim, H. Muramatsu, T. Hayashi, M. Endo, M. Terrones, M.S. Dresselhaus, Fabrication of High Purity, Double-Walled Carbon Nanotube Buckypaper, Chem. Vap. Deposition, 12 (2006) 327-330.
[266] Á. Kukovecz, R. Smajda, Z. Kónya, I. Kiricsi, Controlling the Pore Diameter Distribution of Multi-Wall Carbon Nanotube Buckypapers, Carbon, 45 (2007) 1696-1716.
[267] S.H. Ng, J. Wang, Z.P. Guo, J. Chen, G.X. Wang, H.K. Liu, Single wall carbon nanotube paper as anode for lithium-ion battery, Electrochimica Acta, 51 (2005) 23-28.

[268] X. Sun, R. Li, B. Stansfield, J.P. Dodelet, S. DÃƒÃƒsilets, 3D carbon nanotube network based on a hierarchical structure grown on carbon paper backing, Chem. Phys. Lett., 394 (2004) 266-270.
[269] Y. Yun, Z. Dong, V.N. Shanov, A. Doepke, W.R. Heineman, H.B. Halsall, A. Bhattacharya, D.K.Y. Wong, M.J. Schulz, Fabrication and characterization of carbon nanotube array electrodes with gold nanoparticle tips, Sensors and Actuators B: Chemical, 133 (2008) 208-212.
[270] N. Bendiab, R. Almairac, J.L. Sauvajol, S. Rols, E. Elkaim, Orientation of single-walled carbon nanotubes by uniaxial pressure, Journal of Applied Physics, 93 (2003) 1769-1773.
[271] L.F. Dumée, K. Sears, J. Schütz, N. Finn, C. Huynh, S. Hawkins, M. Duke, S. Gray, Characterization and evaluation of carbon nanotube Bucky-Paper membranes for direct contact membrane distillation, Journal of Membrane Science, In Press, Corrected Proof (2010).
[272] M. Endo, H. Muramatsu, T. Hayashi, Y.A. Kim, M. Terrones, M.S. Dresselhaus, 'Buckypaper' from Coaxial Nanotubes, Nature, 433 (2005) 476.
[273] R. Smajda, Á. Kukovecz, Z. Kónya, I. Kiricsi, Structure and Gas Permeability of Multi-Wall Carbon Nanotube Buckypapers, Carbon, 45 (2007) 1176-1184.
[274] R.L.D. Whitby, T. Fukuda, T. Maekawa, S.L. James, S.V. Mikhalovsky, Geometric Control and Tuneable Pore Size Distribution of Buckypaper and Buckydiscs, Carbon, 46 (2008) 949-956.
[275] P.G. Whitten, G.M. Spinks, G.G. Wallace, Mechanical properties of carbon nanotube paper in ionic liquid and aqueous electrolytes, Carbon, 43 (2005) 1891-1896.
[276] M.T. Byrne, Y.K. Gun'ko, Recent Advances in Research on Carbon Nanotube–Polymer Composites, in, WILEY-VCH Verlag, pp. 1672-1688.
[277] S.M. Cooper, H.F. Chuang, M. Cinke, B.A. Cruden, M. Meyyappan, Gas Permeability of a Buckypaper Membrane, Nano Lett., 3 (2003) 189-192.
[278] L. Dumée, K. Sears, J. Schutz, N. Finn, M. Duke, S. Gray, Carbon nanotube based composite membranes for water desalination by membrane distillation, Desalination and Water treatment, 17 (2010) 72-79.
[279] P. Gonnet, Z. Liang, E.S. Choi, R.S. Kadambala, C. Zhang, J.S. Brooks, B. Wang, L. Kramer, Thermal conductivity of magnetically aligned carbon

nanotube buckypapers and nanocomposites, Current Applied Physics, 6 (2006) 119-122.
[280] J. Gou, Z.Y. Liang, B. Wang, Experimental Design and Optimization of Dispersion Process for Single-Walled Carbon Nanotube Bucky Paper, International Journal of Nanoscience, 3 (2004) 14.
[281] H. Muramatsu, T. Hayashi, Y.A. Kim, D. Shimamoto, Y.J. Kim, K. Tantrakarn, M. Endo, M. Terrones, M.S. Dresselhaus, Pore structure and oxidation stability of double-walled carbon nanotube-derived bucky paper, Chem. Phys. Lett., 414 (2005) 444-448.
[282] A. Salmi, E. Haeggstrom, K. Arstila, K. Nordlund, J. Keinonen, Increasing the Stiffness of SWCNT Bucky Paper by Heavy Ion Irradiation, in: REVIEW OF PROGRESS IN QUANTITATIVE NONDESTRUCTIVE EVALUATION, AIP, Portland, Oregon (USA), 2007, pp. 1183-1188.
[283] U. Voher, N.P. Zschoerper, Y. Koehne, S. Langowski, C. Oehr, Plasma modification of carbon nanotubes and Bucky papers, Plasma Processes Polym., 4 (2007) S871-S877.
[284] Z. Wang, Z. Liang, B. Wang, C. Zhang, L. Kramer, Processing and property investigation of single-walled carbon nanotube (SWNT) buckypaper/epoxy resin matrix nanocomposites, Composites Part A, 35 (2004) 1225-1232.
[285] R.L.D. Whitby, T. Fukuda, T. Maekawa, S.L. James, S.V. Mikhalovsky, Geometric control and tuneable pore size distribution of buckypaper and buckydiscs, Carbon, 46 (2008) 949-956.
[286] G. Broza, Thermoplastic elastomers with multi-walled carbon nanotubes: Influence of dispersion methods on morphology, Composites Science and Technology, 70 1006-1010.
[287] H. Cong, J. Zhang, M. Radosz, Y. Shen, Carbon Nanotube Composite Membranes of Brominated Poly(2,6-diphenyl-1,4-phenylene oxide) for Gas Separation, J. Membr. Sci., 294 (2007) 178-185.
[288] S. Yun, J. Kim, Z. Ounaies, TECHNICAL NOTE: Single-walled carbon nanotube/polyaniline coated cellulose based electro-active paper (EAPap) as hybrid actuator, Smart Materials and Structures, 15 (2006) N61-N65.

[289] Q. He, Y. Cui, S. Ai, Y. Tian, J. Li, Self-assembly of composite nanotubes and their applications, Current Opinion in Colloid & Interface Science, 14 (2009) 115-125.
[290] A. Hernández-Pérez, F. Avilés, A. May-Pat, A. Valadez-González, P.J. Herrera-Franco, P. Bartolo-Pérez, Effective properties of multiwalled carbon nanotube/epoxy composites using two different tubes, Composites Science and Technology, 68 (2008) 1422-1431.
[291] S. Musso, J.-M. Tulliani, G. Ferro, A. Tagliaferro, Influence of carbon nanotubes structure on the mechanical behavior of cement composites, Composites Science and Technology, 69 (2009) 1985-1990.
[292] B.J. Landi, S.L. Castro, H.J. Ruf, C.M. Evans, S.G. Bailey, R.P. Raffaelle, CdSe quantum dot-single wall carbon nanotube complexes for polymeric solar cells, Solar Energy Materials and Solar Cells, 87 (2005) 733-746.
[293] K.-M. Lee, C.-W. Hu, H.-W. Chen, K.-C. Ho, Incorporating carbon nanotube in a low-temperature fabrication process for dye-sensitized TiO2 solar cells, Solar Energy Materials and Solar Cells, 92 (2008) 1628-1633.
[294] S. Uk Lee, W. Seok Choi, B. Hong, A comparative study of dye-sensitized solar cells added carbon nanotubes to electrolyte and counter electrodes, Solar Energy Materials and Solar Cells, 94 680-685.
[295] G. Viswanathan, D.B. Kane, P.J. Lipowicz, High Efficiency Fine Particulate Filtration using Carbon Nanotube Coatings, Adv. Mater., 16 (2004) 2045-2049.
[296] L. Ci, S.M. Manikoth, X. Li, R. Vajtai, P.M. Ajayan, Ultrathick Freestanding Aligned Carbon Nanotube Films, Advanced Materials, 19 (2007) 3300-3303.
[297] Y.C. Hong, D.H. Shin, S.C. Cho, H.S. Uhm, Surface transformation of carbon nanotube powder into super-hydrophobic and measurement of wettability, Chem. Phys. Lett., 427 (2006) 390-393.
[298] A.S. Brady-Esétvez, S. Kang, M. Elimelech, A Single-Walled-Carbon-Nanotube Filter for Removal of Viral and Bacterial Pathogens, Small, 4 (2008) 481-484.
[299] V.K.K. Upadhyayula, V. Gadhamshetty, Appreciating the role of carbon nanotube composites in preventing biofouling and promoting biofilms on

material surfaces in environmental engineering: A review, Biotechnology Advances, 28 802-816.
[300] T. Akasaka, F. Watari, Capture of bacteria by flexible carbon nanotubes, Acta Biomaterialia, 5 (2009) 607-612.
[301] F. Peng, F. Pan, H. Sun, L. Lu, Z. Jiang, Novel Nanocomposite Pervaporation Membranes composed of Poly(vinyl alcohol) and Chitosan-Wrapped Carbon Nanotubes, J. Membr. Sci., 300 (2007) 13-19.
[302] O. Balcajin, A. Noy, F. Fornasiero, C.P. Grigoropoulos, J.K. Holt, J.B. In, S. Kim, H.G. Park, S. Nora, D. Mamadou, D. Jeremiah, S. Anita, S. Richard, Nanofluidic Carbon Nanotube Membranes: Applications for Water Purification and Desalination, in: Nanotechnology Applications for Clean Water, William Andrew Publishing, Boston, 2009, pp. 77-93.
[303] M. Majumder, P.M. Ajayan, D. Enrico, G. Lidietta, Carbon Nanotube Membranes: A New Frontier in Membrane Science, in: Comprehensive Membrane Science and Engineering, Elsevier, Oxford, pp. 291-310.
[304] B. Corry, Designing Carbon Nanotube Membranes for Efficient Water Desalination, J. Phys. Chem. B, 112 (2008) 1427-1434.
[305] E.M. Kotsalis, J.H. Walther, P. Koumoutsakos, Multiphase water flow inside carbon nanotubes, International Journal of Multiphase Flow, 30 995-1010.
[306] J.A. Thomas, A.J.H. McGaughey, O. Kuter-Arnebeck, Pressure-driven water flow through carbon nanotubes: Insights from molecular dynamics simulation, International Journal of Thermal Sciences, 49 281-289.
[307] J.A. Thomas, J.H. McGaughey, Reassessing Fast Water Transport Through Carbon Nanotubes, Nano Lett., 8 (2008) 2788-2793.
[308] T.A. Beu, Simulation of the flow of aqueous solutions through carbon nanotubes, Computer Physics Communications, In Press, Corrected Proof.
[309] A. Subramani, M. Badruzzaman, J. Oppenheimer, J.G. Jacangelo, Energy Minimization Strategies and Renewable Energy Utilization for Desalination: A Review, Water Research, In Press, Accepted Manuscript.
[310] A. Noy, H.G. Park, F. Fornasiero, J.K. Holt, C.P. Grigoropoulos, O. Bakajin, Nanofluidics in Carbon Nanotubes, Nanotoday, 2 (2007) 22-29.
[311] G. Hummer, J.C. Rasalah, J.P. Noworyta, Water Conduction through the Hydrophobic Channel of a Carbon Nanotube, Nature, 414 (2001) 188-190.

[312] A. Waghe, J.C. Rasaiah, G. Hummer, Filling and Emptying Kinetics of Carbon Nanotubes in Water, J. Chem. Phys., 117 (2002) 10789-10795.
[313] A. Kalra, S. Garde, G. Hummer, Osmotic Water Transport through Carbon Nanotube Membranes, Proc. Natl. Acad. Sci. U. S. A., 100 (2003) 10175-10180.
[314] G. Hummer, Water, proton, and ion transport: from nanotubes to proteins, Molecular Physics, 105 (2007) 201-207.
[315] M. Majumder, N. Chopra, R. Andrews, B.J. Hinds, Enhanced Flow in Carbon Nanotubes, Nature, 438 (2005) 44.
[316] J.K. Holt, A. Noy, T. Huser, D. Eaglesham, O. Bakajin, Fabrication of a Carbon Nanotube-Embedded Silicon Nitride Membrane for Studies of Nanometer-Scale Mass Transport, Nano Lett., 4 (2004) 2245-2250.
[317] J.K. Holt, H.G. Park, Y.M. Wang, M. Stadermann, A.B. Artyukhin, C.P. Grigoropoulos, A. Noy, O. Bakajin, Fast mass transport through sub-2-nanometer carbon nanotubes, Science, 312 (2006) 1034-1037.
[318] J. Holt, Fast transport through carbon nanotubes and implications for water treatment, in: Innovative technical solutions for water management in Australia, University of Adelaide, South Australia, 2006.
[319] J.K. Holt, H.G. Park, Y. Wang, M. Staderman, A.B. Artyukhin, C.P. Grigoropoulos, A. Noy, O. Bakajin, Fast Mass Transport Through Sub-2-Nanometer Carbon Nanotubes, Science, 312 (2006) 1034-1037.
[320] F. Fornasiero, H.G. Park, J.K. Holt, M. Stadermann, C.P. Grigoropoulos, A. Noy, O. Bakajin, Ion exclusion by sub-2-nm carbon nanotube pores, Proc. Natl. Acad. Sci. U. S. A., 105 (2008) 17250-17255.
[321] F. Fornasiero, H.G. Park, J.K. Holt, M. Stadermann, C.P. Grigoropoulos, A. Noy, O. Bakajin, Ion Exclusion by Sub-2-nm Carbon Nanotube Pores, Proc. Natl. Acad. Sci. U. S. A., 0710437105 (2008) 1-6.
[322] B. Hinds, D. Liming, Aligned carbon nanotube membranes, in: Carbon Nanotechnology, Elsevier, Amsterdam, 2006, pp. 491-523.
[323] W. Mi, Y.S. Lin, Y. Li, Vertically Aligned Carbon Nanotube Membranes on Macroporous Alumina Supports, J. Membr. Sci., 304 (2007) 1-7.
[324] S. Kim, J.R. Jinschek, H. Chen, D.S. Sholl, E. Marand, Scalable Fabrication of Carbon Nanotube/Polymer Nanocomposite Membranes for High Flux Gas Transport, Nano Lett., 7 (2007) 2806-2811.

[325] L.S.K. Pang, J.D. Saxby, S.P. Chatfield, Thermogravimetric analysis of carbon nanotubes and nanoparticles, The Journal of Physical Chemistry, 97 (1993) 6941-6942.
[326] J.D. Harris, R.P. Raffaelle, T. Gennett, B.J. Landi, A.F. Hepp, Growth of multi-walled carbon nanotubes by injection CVD using cyclopentadienyliron dicarbonyl dimer and cyclooctatetraene iron tricarbonyl, Materials Science and Engineering B, 116 (2005) 369-374.
[327] B.L. Allen, P.D. Kichambare, P. Gou, I.I. Vlasova, A.A. Kapralov, N. Konduru, V.E. Kagan, A. Star, Biodegradation of Single-Walled Carbon Nanotubes through Enzymatic Catalysis, Nano Letters, 8 (2008) 3899-3903.
[328] S.R. Brownlow, A.P. Moravsky, N.G. Kalugin, B.S. Majumdar, Probing deformation of double-walled carbon nanotube (DWNT)/epoxy composites using FTIR and Raman techniques, Composites Science and Technology, 70 1460-1468.
[329] E. Titus, N. Ali, G. Cabral, J. Gracio, P. Ramesh Babu, M. Jackson, Chemically functionalized carbon nanotubes and their characterization using thermogravimetric analysis, fourier transform infrared, and raman spectroscopy, Journal of Materials Engineering and Performance, 15 (2006) 182-186.
[330] L. Stobinski, B. Lesiak, L. Kövér, J. Tóth, S. Biniak, G. Trykowski, J. Judek, Multiwall carbon nanotubes purification and oxidation by nitric acid studied by the FTIR and electron spectroscopy methods, Journal of Alloys and Compounds, 501 77-84.
[331] S. Lefrant, M. Baibarac, I. Baltog, J.Y. Mevellec, C. Godon, O. Chauvet, Functionalization of single-walled carbon nanotubes with conducting polymers evidenced by Raman and FTIR spectroscopy, Diamond and Related Materials, 14 867-872.
[332] S.H. Jeong, K.K. Kim, S.J. Jeong, K.H. An, S.H. Lee, Y.H. Lee, Optical absorption spectroscopy for determining carbon nanotube concentration in solution, Synthetic Metals, 157 (2007) 570-574.
[333] G.A. Rance, D.H. Marsh, R.J. Nicholas, A.N. Khlobystov, UV-vis absorption spectroscopy of carbon nanotubes: Relationship between the [pi]-electron plasmon and nanotube diameter, Chem. Phys. Lett., 493 19-23.

[334] A. Schierz, H. Zänker, Aqueous suspensions of carbon nanotubes: Surface oxidation, colloidal stability and uranium sorption, Environmental Pollution, 157 (2009) 1088-1094.
[335] R. Tantra, P. Schulze, P. Quincey, Effect of nanoparticle concentration on zeta-potential measurement results and reproducibility, Particuology, 8 279-285.
[336] P.C. Ma, J.-K. Kim, B.Z. Tang, Effects of silane functionalization on the properties of carbon nanotube/epoxy nanocomposites, Composites Science and Technology, 67 (2007) 2965-2972.
[337] H.T. Ham, Y.S. Choi, I.J. Chung, An Explanation of Dispersion States of Single-Walled Carbon Nanotubes in Solvents and Aqueous Surfactant Solutions using Solubility Parameters, J. Colloid Interface Sci., 286 (2005) 216-223.
[338] M.D. Clark, S. Subramanian, R. Krishnamoorti, Understanding surfactant aided aqueous dispersion of multi-walled carbon nanotubes, Journal of Colloid and Interface Science, 354 144-151.
[339] R. Rastogi, R. Kaushal, S.K. Tripathi, A.L. Sharma, I. Kaur, L.M. Bharadwaj, Comparative study of carbon nanotube dispersion using surfactants, Journal of Colloid and Interface Science, 328 (2008) 421-428.
[340] H. Xu, H. Abe, M. Naito, Y. Fukumori, H. Ichikawa, S. Endoh, K. Hata, Efficient dispersing and shortening of super-growth carbon nanotubes by ultrasonic treatment with ceramic balls and surfactants, Advanced Powder Technology, 21 551-555.
[341] A. Lucas, C.c. Zakri, M. Maugey, M. Pasquali, P.v.d. Schoot, P. Poulin, Kinetics of Nanotube and Microfiber Scission under Sonication, The Journal of Physical Chemistry C, 113 (2009) 20599-20605.
[342] C. Park, Z. Ounaies, K.A. Watson, R.E. Crooks, J. Smith, S.E. Lowther, J.W. Connell, E.J. Siochi, J.S. Harrison, T.L.S. Clair, Dispersion of single wall carbon nanotubes by in situ polymerization under sonication, Chem. Phys. Lett., 364 (2002) 303-308.
[343] J. Doak, R.K. Gupta, K. Manivannan, K. Ghosh, P.K. Kahol, Effect of particle size distributions on absorbance spectra of gold nanoparticles, Physica E: Low-dimensional Systems and Nanostructures, 42 1605-1609.

[344] C.F. Bohren, D.R. Huffman, Extinction, in Absorption and Scattering of Light by Small Particles, 2007.
[345] K.C. Etika, M.A. Cox, J.C. Grunlan, Tailored dispersion of carbon nanotubes in water with pH-responsive polymers, Polymer, 51 1761-1770.
[346] K.C. Etika, F.D. Jochum, P. Theato, J.C. Grunlan, Temperature Controlled Dispersion of Carbon Nanotubes in Water with Pyrene-Functionalized Poly(N-cyclopropylacrylamide), Journal of the American Chemical Society, 131 (2009) 13598-+.
[347] A.I. Zhbanov, E.G. Pogorelov, Y.-C. Chang, Van der Waals Interaction between Two Crossed Carbon Nanotubes, ACS Nano, 4 5937-5945.
[348] L. Zarkova, U. Hohm, Effective (n-6) Lennard-Jones Potentials with Temperature-Dependent Parameters Introduced for Accurate Calculation of Equilibrium and Transport Properties of Ethene, Propene, Butene, and Cyclopropaneâ€ Journal of Chemical & Engineering Data, 54 (2009) 1648-1655.
[349] J.E. Jones, On the Determination of Molecular Fields. II. From the Equation of State of a Gas, Proceedings of the Royal Society of London. Series A, 106 (1924) 463-477.
[350] A.M.K. Esawi, M.M. Farag, Carbon nanotube reinforced composites: Potential and current challenges, Materials & Design, 28 (2007) 2394-2401.
[351] M. O'Connell, J., Carbon Nanotubes: Properties and Applications, in, Taylor & Francis Group, Boca Raton, USA, 2006.
[352] G.A. Rance, D.H. Marsh, S.J. Bourne, T.J. Reade, A.N. Khlobystov, van der Waals Interactions between Nanotubes and Nanoparticles for Controlled Assembly of Composite Nanostructures, ACS Nano, 4 4920-4928.
[353] S.V. Rotkin, K. Hess, Many-Body Terms in van der Waals Cohesion Energy of Nanotubes, Journal of Computational Electronics, 1 (2002) 323-326.
[354] W.B. Lu, B. Liu, J. Wu, J. Xiao, K.C. Hwang, S.Y. Fu, Y. Huang, Continuum modeling of van der Waals interactions between carbon nanotube walls, Applied Physics Letters, 94 (2009) 101917-101913.
[355] A. Urbina, et al., Dynamics of functionalized single wall carbon nanotubes in solution studied by incoherent neutron scattering experiments, Journal of Physics: Condensed Matter, 20 (2008) 104208.

[356] L. Zheng, S. Li, J.P. Brody, P.J. Burke, Manipulating Nanoparticles in Solution with Electrically Contacted Nanotubes Using Dielectrophoresis, Langmuir, 20 (2004) 8612-8619.
[357] P.J. Pauzauskie, A. Jamshidi, J.K. Valley, J.J.H. Satcher, M.C. Wu, Parallel trapping of multiwalled carbon nanotubes with optoelectronic tweezers, Applied Physics Letters, 95 (2009) 113104-113103.
[358] M.P. Rossi, H. Ye, Y. Gogotsi, S. Babu, P. Ndungu, J.-C. Bradley, Environmental Scanning Electron Microscopy Study of Water in Carbon Nanopipes, Nano Lett., 4 (2004) 989-993.
[359] A. Checco, T. Hofmann, E. DiMasi, C.T. Black, B.M. Ocko, Morphology of Air Nanobubbles Trapped at Hydrophobic Nanopatterned Surfaces, Nano Letters, 10 1354-1358.
[360] G. Papastavrou, et al., Interactions between hydrophilic and hydrophobic surfaces on microscopic scale and the influence of air bubbles as observed by scanning force microscopy in aqueous and alcoholic mediums, EPL (Europhysics Letters), 52 (2000) 551.
[361] M. Krasowska, J. Zawala, K. Malysa, Air at hydrophobic surfaces and kinetics of three phase contact formation, Advances in Colloid and Interface Science, 147-148 155-169.
[362] R.H. Yoon, J.L. Yordan, The critical rupture thickness of thin water films on hydrophobic surfaces, Journal of Colloid and Interface Science, 146 (1991) 565-572.
[363] G.S. Rosengarten, C. Kwok, F., Superinsulating heat transfer surfaces for microfluidic channels, International Journal Transport Phenomena, 10 (2008) 293-306.
[364] R.A. Pushkarova, R.G. Horn, Surface forces measured between an air bubble and a solid surface in water, Colloids and Surfaces A: Physicochemical and Engineering Aspects, 261 (2005) 147-152.
[365] B. Corry, Designing Carbon Nanotube Membranes for Efficient Water Desalination, The Journal of Physical Chemistry B, 112 (2008) 1427-1434.
[366] H. Muramatsu, T. Hayashi, Y.A. Kim, D. Shimamoto, Y.J. Kim, K. Tantrakarn, M. Endo, M. Terrones, M.S. Dresselhaus, Pore Structure and Oxidation Stability of Double-Walled Carbon Nanotube-Derived Bucky Paper, Chem. Phys. Lett., 414 (2005) 444-448.

[367] S. Inoue, N. Ichikuni, T. Suzuki, T. Uematsu, K. Kaneko, Capillary Condensation of N_2 on Multiwall Carbon Nanotubes, J. Phys. Chem. B, 102 (1998) 4689-4692.
[368] G. Onyestyák, J. Valyon, K. Hernádi, I. Kiricsi, L.V.C. Rees, Equilibrium and Dynamics of Acetylene Sorption in Multiwalled Carbon Nanotubes, Carbon, 41 (2003) 1241-1248.
[369] S.M. Cooper, H.F. Chuang, M. Cinke, B.A. Cruden, M. Meyyappan, Gas Permeability of a Buckypaper Membrane, Nano Letters, 3 (2003) 189-192.
[370] J.M. Rodríguez-Maroto, L. Martínez, Bulk and measured temperatures in direct contact membrane distillation, Journal of Membrane Science, 250 (2005) 141-149.
[371] A. Å iber, Phonons and specific heat of linear dense phases of atoms physisorbed in the grooves of carbon nanotube bundles, Physical Review B, 66 (2002) 235414.
[372] G.A. Jorge, V. Bekeris, C. Acha, M.M. Escobar, S. Goyanes, D. Zilli, A.L. Cukierman, R.J. Candal, Effects of phonon dimensionality in the specific heat of multiwall carbon nanotubes at low temperatures, Journal of Physics: Conference Series, 167 (2009) 012008.
[373] J.C. Lasjaunias, K. BiljakoviÄ‡, Z. Benes, J.E. Fischer, P. Monceau, Low-temperature specific heat of single-wall carbon nanotubes, Physical Review B, 65 (2002) 113409.
[374] C. Masarapu, L.L. Henry, B. Wei, Specific heat of aligned multiwalled carbon nanotubes, Nanotechnology, 16 (2005) 1490-1494.
[375] V.N. Popov, Low-temperature specific heat of nanotube systems, Physical Review B, 66 (2002) 153408.
[376] A. Andreescu, A. Savin, R. Steigmann, N. Iftimie, E. Mamut, R. Grimberg, Model for thermal conductivity of composites with carbon nanotubes, Journal of Thermal Analysis and Calorimetry, 94 (2008) 349-353.
[377] P. Kim, L. Shi, A. Majumdar, P.L. McEuen, Thermal transport measurements of individual multiwalled nanotubes, Physical Review Letters, 87 (2001) 4.
[378] Q. Li, C. Liu, X. Wang, S. Fan, Measuring the thermal conductivity of individual carbon nanotubes by the Raman shift method, Nanotechnology, 20 (2009) 145702-145702.

[379] S.L. Shinde, J. Goela, Unusually high thermal conductivity of carbon nanotubes, in: Springer (Ed.) High Thermal Conductivity Materials, 2004, pp. 40.
[380] R. Prasher, Thermal boundary resistance and thermal conductivity of multiwalled carbon nanotubes, Physical Review B, 77 (2008) 11.
[381] D.J. Yang, Q. Zhang, G. Chen, S.F. Yoon, J. Ahn, S.G. Wang, Q. Zhou, Q. Wang, J.Q. Li, Thermal conductivity of multiwalled carbon nanotubes, Physical Review B, 66 (2002) 6.
[382] C.H. Yu, L. Shi, Z. Yao, D.Y. Li, A. Majumdar, Thermal conductance and thermopower of an individual single-wall carbon nanotube, Nano Letters, 5 (2005) 1842-1846.
[383] W. Nunes dos Santos, P. Mummery, A. Wallwork, Thermal diffusivity of polymers by the laser flash technique, Polym. Test, 24 (2005) 628-634.
[384] K. Ueberreiter, J. Naghizadeh, Thermal diffusivity of polymers, Colloid & Polymer Science, 250 (1972) 927-931.
[385] M. Hattori, Thermal diffusivity of some linear polymers, Colloid & Polymer Science, 202 (1965) 11-14.
[386] H. Xie, A. Cai, X. Wang, Thermal diffusivity and conductivity of multiwalled carbon nanotube arrays, Physics Letters A, 369 (2007) 120-123.
[387] J. Zhao, D.W. Schaefer, D. Shi, J. Lian, J. Brown, G. Beaucage, L. Wang, R.C. Ewing, How Does Surface Modification Aid in the Dispersion of Carbon Nanofibers?, The Journal of Physical Chemistry B, 109 (2005) 23351-23357.
[388] J.J. Hernández, M.C. García-Gutiérrez, A. Nogales, D.R. Rueda, T.A. Ezquerra, Small-angle X-ray scattering of single-wall carbon nanotubes dispersed in molten poly(ethylene terephthalate), Composites Science and Technology, 66 (2006) 2629-2632.
[389] B.N. Wang, R.D. Bennett, E. Verploegen, A.J. Hart, R.E. Cohen, Characterizing the Morphologies of Mechanically Manipulated Multiwall Carbon Nanotube Films by Small-Angle X-ray Scatteringâ€ The Journal of Physical Chemistry C, 111 (2007) 17933-17940.
[390] B.N. Wang, R.D. Bennett, E. Verploegen, A.J. Hart, R.E. Cohen, Quantitative Characterization of the Morphology of Multiwall Carbon Nanotube

Films by Small-Angle X-ray Scattering, The Journal of Physical Chemistry C, 111 (2007) 5859-5865.
[391] G. Beaucage, D.W. Schaefer, Structural studies of complex systems using small-angle scattering: a unified Guinier/power-law approach, Journal of Non-Crystalline Solids, 172-174 (1994) 797-805.
[392] F. Laganà, G. Barbieri, E. Drioli, Direct contact membrane distillation: modelling and concentration experiments, Journal of Membrane Science, 166 (2000) 1-11.
[393] K.W. Lawson, M.S. Hall, D.R. Lloyd, Compaction of microporous membranes used in membrane distillation. I. Effect on gas permeability, Journal of Membrane Science, 101 (1995) 99-108.
[394] L. Martinez-Diez, M.I. Vazquez-Gonzalez, Temperature and concentration polarization in membrane distillation of aqueous salt solutions, Journal of Membrane Science, 156 (1999) 265-273.
[395] D. Chandler, Interfaces and the driving force of hydrophobic assembly, Nature, 437 (2005) 640-647.
[396] H. Lee, et al., Comparison of frictional forces on graphene and graphite, Nanotechnology, 20 (2009) 325701.
[397] BP commercial products- Nanolab, in.
[398] Large sheet of nanotube BP, in.
[399] D.P. Instruments, Solid surface energy data (SFE) for common polymers, in, 2007.
[400] S. Carabineiro, B. Nieuwenhuys, Adsorption of small molecules on gold single crystal surfaces, Gold Bulletin, 42 (2009) 288-301.
[401] P. Jensen, X. Blase, P. Ordejón, First principles study of gold adsorption and diffusion on graphite, Surface Science, 564 (2004) 173-178.
[402] H. Sakurai, S. Tsubota, M. Haruta, Hydrogenation of CO2 over gold supported on metal oxides, Applied Catalysis A: General, 102 (1993) 125-136.
[403] M. Kaempgen, M. Lebert, N. Nicoloso, S. Roth, Multifunctional carbon nanotube networks for fuel cells, Applied Physics Letters, 92 (2008) 3.
[404] C.-Y. Chen, K.-Y. Lin, W.-T. Tsai, J.-K. Chang, C.-M. Tseng, Electroless deposition of Ni nanoparticles on carbon nanotubes with the aid of

supercritical CO2 fluid and a synergistic hydrogen storage property of the composite, International Journal of Hydrogen Energy, 35 5490-5497.
[405] D. Yuan, Y. Liu, Electroless deposition of Cu on multiwalled carbon nanotubes, Rare Metals, 25 (2006) 237-240.
[406] C. Kartusch, J.A. Van Bokhoven, Hydrogenation over gold catalysts: The interaction of gold with hydrogen, Gold Bulletin, Volume 42 (2009).
[407] L. Dumée, L. Velleman, K. Sears, M. Hill, J. Schütz, N. Finn, M. Duke, S. Gray, Control of porosity and pore size of metal reinforced carbon nanotube membranes, Membranes, Submitted (2010).
[408] V.P. Menon, and Martin, C.R., Fabrication and Evaluation of Nanoelectrode Ensembles, Anal. Chem., 67 (1995) 1920- 1928.
[409] L. Dumee, L. Velleman, K. Sears, M. Hill, J. Schutz, N. Finn, M. Duke, S. Gray, Control of Porosity and Pore Size of Metal Reinforced Carbon Nanotube Membranes, Membranes, 1 (2010) 25-36.
[410] L. Dumée, K. Sears, J. Schütz, N. Finn, M. Duke, S. Gray, Characterization and evaluation of carbon nanotube bucky-paper membranes for direct contact membrane distillation, Journal of Membrane Science, (Submitted on the 25th of July 2009 - being reviewed).
[411] M. Sakai, T. Yanagisawa, A. Nakajima, Y. Kameshima, K. Okada, Effect of Surface Structure on the Sustainability of an Air Layer on Superhydrophobic Coatings in a Waterâ'Ethanol Mixture, Langmuir, 25 (2008) 13-16.
[412] W. Barthlott, T. Schimmel, S. Wiersch, K. Koch, M. Brede, M. Barczewski, S. Walheim, A. Weis, A. Kaltenmaier, A. Leder, H.F. Bohn, The Salvinia Paradox: Superhydrophobic Surfaces with Hydrophilic Pins for Air Retention Under Water, Advanced Materials, 22 2325-2328.
[413] J.L. Campbell, M. Breedon, K. Latham, K. Kalantar-zadeh, Electrowetting of Superhydrophobic ZnO Nanorods, Langmuir, 24 (2008) 5091-5098.
[414] L. Martínez, F.J. Florido-Díaz, A. Hernández, P. Prádanos, Estimation of vapor transfer coefficient of hydrophobic porous membranes for applications in membrane distillation, Separation and Purification Technology, 33 (2003) 45-55.

[415] Catalytic conversion of water and carbon dioxide to low cost energy, hydrogen, carbon monoxide, oxygen and hydrocarbons, in, 5516742, United States Patent
[416] S.-S. Nam, H. Kim, G. Kishan, M.-J. Choi, K.-W. Lee, Catalytic conversion of carbon dioxide into hydrocarbons over iron supported on alkali ion-exchanged Y-zeolite catalysts, Applied Catalysis A: General, 179 (1999) 155-163.
[417] Y. Zhang, J. Fei, Y. Yu, X. Zheng, Study of CO2 Hydrogenation to Methanol over Cu-V/[gamma]-Al2O3 Catalyst, Journal of Natural Gas Chemistry, 16 (2007) 12-15.
[418] I. Melián-Cabrera, M. López Granados, P. Terreros, J.L.G. Fierro, CO2 hydrogenation over Pd-modified methanol synthesis catalysts, Catalysis Today, 45 (1998) 251-256.
[419] S.J. Holden, D.R. Rossington, Hydrogen Adsorption on Silver, Gold, and Aluminum. Studies of Parahydrogen Conversion, The Journal of Physical Chemistry, 68 (1964) 1061-1067.
[420] L. Stobinski, R. Dus, Atomic hydrogen adsorption on thin gold films, Surface Science, 269-270 (1992) 383-388.
[421] L. Stobinski, R. Nowakowski, R. Dus, Atomic hydrogen adsorption on thin discontinuous and continuous gold films - Similarities and differences, Vacuum, 48 (1997) 203-207.
[422] X. Liu, M. Zhu, S. Chen, M. Yuan, Y. Guo, Y. Song, H. Liu, Y. Li, Organicâˆ’Inorganic Nanohybrids via Directly Grafting Gold Nanoparticles onto Conjugated Copolymers through the Dielsâˆ’Alder Reaction, Langmuir, 24 (2008) 11967-11974.
[423] J. Haccoun, C. Vautrin-Ul, A. Chaussé, A. Adenier, Electrochemical grafting of organic coating onto gold surfaces: Influence of the electrochemical conditions on the grafting of nitrobenzene diazonium salt, Progress in Organic Coatings, 63 (2008) 18-24.
[424] J. Zhang, J.-D. Li, S. Gray, Effect of applied pressure on performance of PTFE membrane in DCMD, Journal of Membrane Science, 369 (2011) 514-525.
[425] C.-C. Ho, A.L. Zydney, Measurement of membrane pore interconnectivity, Journal of Membrane Science, 170 (2000) 101-112.

[426] J. Zhang, J.-D. Li, M. Duke, Z. Xie, S. Gray, Performance of asymmetric hollow fibre membranes in membrane distillation under various configurations and vacuum enhancement, Journal of Membrane Science, 362 (2010) 517-528.
[427] J. Li, L. Wang, W. Jiang, Super-hydrophobic surface of bulk carbon nanotubes compacted by spark plasma sintering followed by modification with polytetrofluorethylene, Carbon, 48 (2010) 2668-2671.
[428] H.J. Ensikat, A.J. Schulte, K. Koch, W. Barthlott, Droplets on Superhydrophobic Surfaces: Visualization of the Contact Area by Cryo-Scanning Electron Microscopy, Langmuir, 25 (2009) 13077-13083.
[429] X. Sheng, J. Zhang, Air layer on superhydrophobic surface underwater, Colloids and Surfaces A: Physicochemical and Engineering Aspects, 377 (2011) 374-378.
[430] Y. Wu, N. Saito, F.A. Nae, Y. Inoue, O. Takai, Water droplets interaction with super-hydrophobic surfaces, Surface Science
Berlin, Germany: 4-9 September 2005, Proceedings of the 23th European Conference on Surface Science, 600 (2006) 3710-3714.
[431] H. Asanuma, H. Noguchi, K. Uosaki, H.-Z. Yu, Water Structure at Superhydrophobic Quartz/Water Interfaces: A Vibrational Sum Frequency Generation Spectroscopy Study, The Journal of Physical Chemistry C, 113 (2009) 21155-21161.
[432] Z. Ma, Y. Hong, L. Ma, M. Su, Superhydrophobic Membranes with Ordered Arrays of Nanospiked Microchannels for Water Desalination, Langmuir, 25 (2009) 5446-5450.
[433] V.A. Bui, L.T.T. Vu, M.H. Nguyen, Modelling the simultaneous heat and mass transfer of direct contact membrane distillation in hollow fibre modules, Journal of Membrane Science, 353 (2010) 85-93.
[434] L. Martínez-Díez, M.I. Vázquez-González, Temperature and concentration polarization in membrane distillation of aqueous salt solutions, Journal of Membrane Science, 156 (1999) 265-273.
[435] A. Velazquez, J.I. Mengual, Temperature Polarization Coefficients in Membrane Distillation, Industrial & Engineering Chemistry Research, 34 (1995) 585-590.

[436] M. Khayet, Membranes and theoretical modeling of membrane distillation: A review, Advances in Colloid and Interface Science, In Press, Corrected Proof.
[437] P. Wick, P. Manser, L.K. Limbach, U. Dettlaff-Weglikowska, F. Krumeich, S. Roth, W.J. Stark, A. Bruinink, The degree and kind of agglomeration affect carbon nanotube cytotoxicity, Toxicology Letters, 168 (2007) 121-131.
[438] A Review of Carbon Nanotube Toxicity and Assessment of Potential Occupational and Environmental Health Risks, Critical Reviews in Toxicology, 36 (2006) 189-217.
[439] E.R. Meshot, M. Bedewy, K.M. Lyons, A.R. Woll, K.A. Juggernauth, S. Tawfick, A.J. Hart, Measuring the lengthening kinetics of aligned nanostructures by spatiotemporal correlation of height and orientation, Nanoscale, 2 896-900.
[440] H. Kobayashi, M. Shioya, T. Tanaka, T. Irisawa, Synchrotron radiation small-angle X-ray scattering study on fracture process of carbon nanotube/poly(ethylene terephthalate) composite films, Composites Science and Technology, 67 (2007) 3209-3218.
[441] Z. Xiong, C.K. Yong, G. Wu, P. Chen, W. Shaw, A. Karkamkar, T. Autrey, M.O. Jones, S.R. Johnson, P.P. Edwards, W.I.F. David, High-capacity hydrogen storage in lithium and sodium amidoboranes, Nat Mater, 7 (2008) 138-141.
[442] E. Poirier, Thermodynamics of hydrogen adsorption in MOF-177 at low temperatures: measurements and modelling, NANOTECHNOLOGY, 20 (2009).
[443] E. Poirier, A. Dailly, Investigation of the Hydrogen State in IRMOF-1 from Measurements and Modeling of Adsorption Isotherms at High Gas Densities, The Journal of Physical Chemistry C, 112 (2008) 13047-13052.
[444] C. Liu, Y.Y. Fan, M. Liu, H.T. Cong, H.M. Cheng, M.S. Dresselhaus, Hydrogen Storage in Single-Walled Carbon Nanotubes at Room Temperature, Science, 286 (1999) 1127-1129.
[445] Y. Ralph T, Hydrogen storage by alkali-doped carbon nanotubes–revisited, Carbon, 38 (2000) 623-626.
[446] D.o.E.-. USA, in, 2011.

Chapter 9

9 Appendix 1 to 6

A series of complimentary information is given for the curiosity of the reader in the following section. The appendixes are referred in the text in their appropriate chapter.

9.1 Appendix 1 - Dispersion and CNT/solvent interaction

9.1.1 Collapse of CNT forest under the influence of solvent evaporation

The CNT affinity for the solvent was shown across this work to be critical. As shown in the optical micrographs in Figure 9-1 CNT forests exposed to specific solvents and dried in STP conditions present various degrees of collapsing. Several solvents were used to condense CNT-forests into honey-comb like structures.

Propan-2-ol, which was used in the dispersion of the CNTs presented the highest viscosity and the lowest surface tension of the tested solvents. This might explain its high affinity with the CNTs and its dispersion capacity.

Table 9-1 Selected solvent properties at 20 ºC

Solvents	Viscosity	Surface tension	Vapor pressure	Wet CNTs?
	mPa.s	mN/m	kPa	
Acetone	**0.306**	25.2	30.8	Yes
Propan-2-ol	**2.038**	**23**	6.02	Yes
DI Water	0.89	**72.8**	3.17	No
DMF	0.794	35.74	**0.439**	Yes but slowly
DMC	0.413	27.2	**58.2**	Yes
Xylene	0.48	28	1.7	Yes
Acetonitrile	0.369	28.66	11.9	Yes
THF	0.456	26.4	21.6	Yes spreads fast

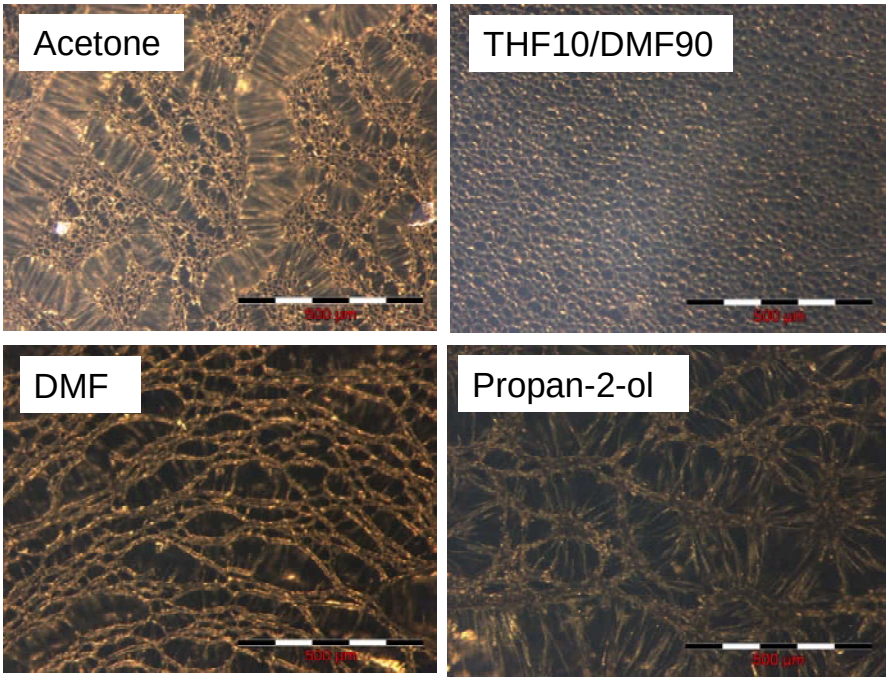

Figure 9-1 CNT forest collapse under solvent influence

The CNTs collapsed under the influence of the evaporating solvent to form dense walls as shown in the schematic in Figure 9-2. The patterns were reproducible and the geometries of the pores formed by the collapse were very well defined and consistent across a sample. This was confirmed by SEM analysis as shown in Figure 9-3. A schematic showing the solvent infiltration procedure is given in Figure 9-2.

This work was carried out in order to better understand the relationship between the solvent and the pattern obtained after evaporation. Unfortunately to process large surface areas of porous membranes, a large number of CNT forests were required and the study was not continued. This however shows another way to manipulate CNTs to form porous structures.

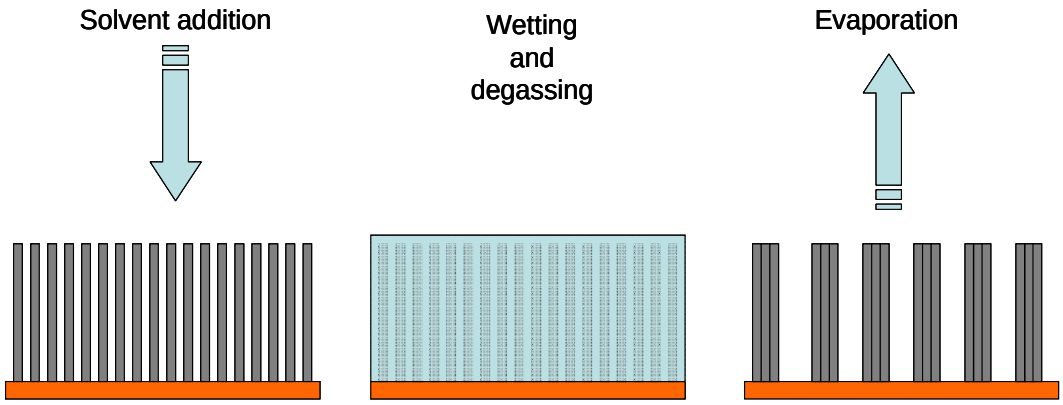

Figure 9-2 Schematic of the condensation process at room temperature

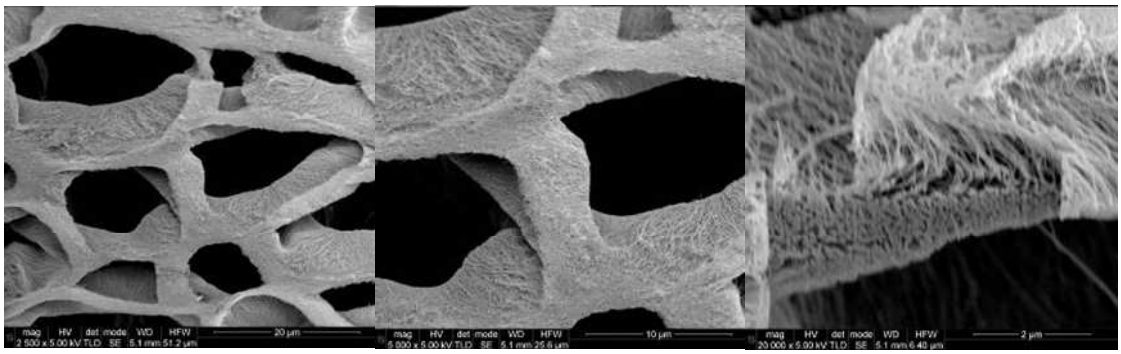

Figure 9-3 SEM of a forest condensed with acetone; a cross section of the right hand side shows the density of the wall

As shown in Figure 9-4 the patterns were regular on large scales (up to a few millimetres) and their geometries (pentagon shaped in general) was consistent with aligned vertical CNTs (Figure 9-5).

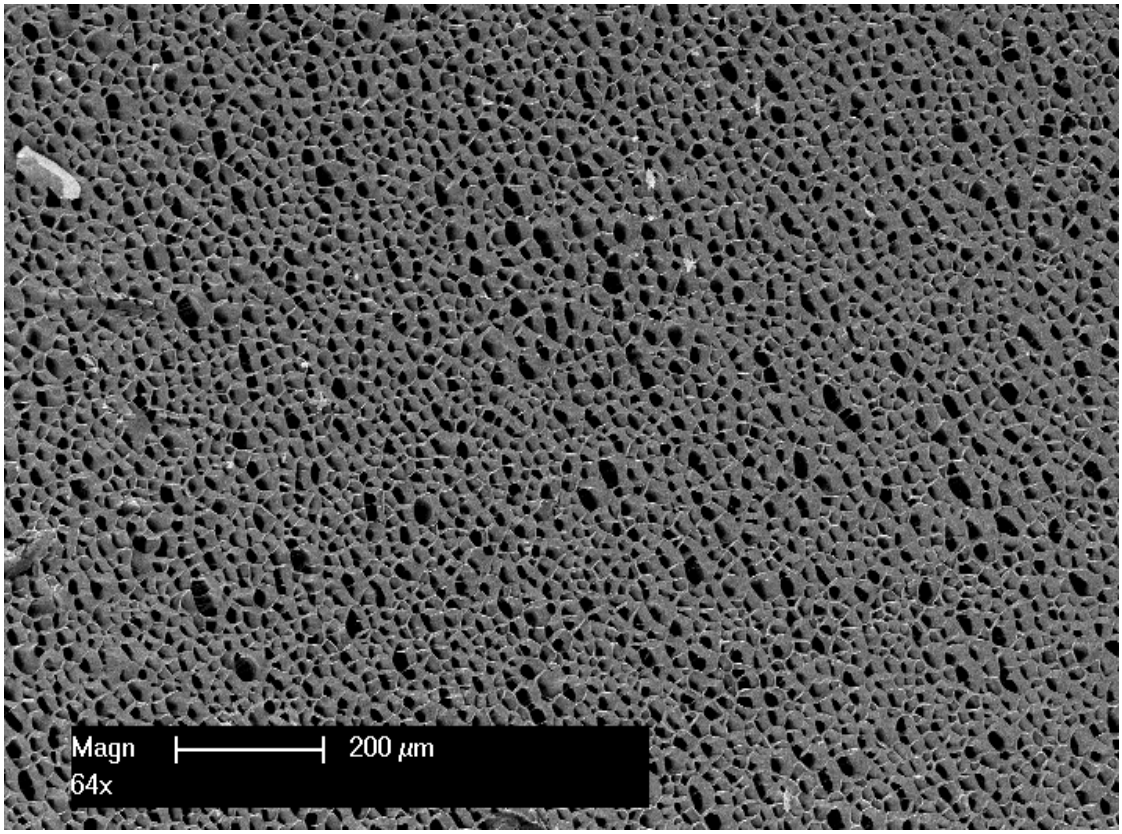

Figure 9-4 THF/DMF densified forest

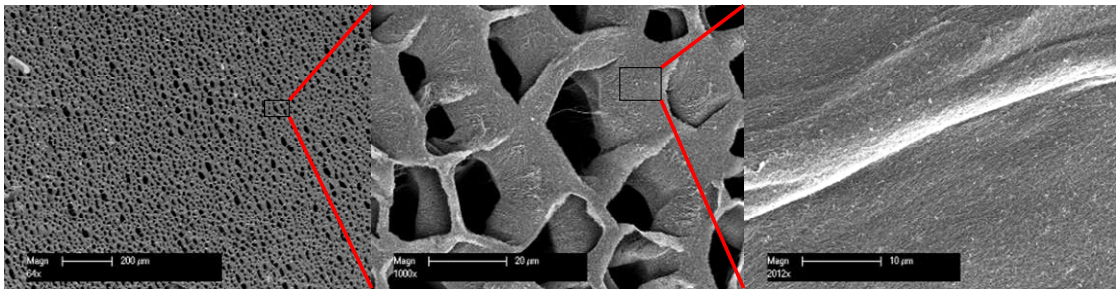

Figure 9-5 pore geometries and CNT alignment in the condensed forests after exposure to a THF/DMF solution

9.1.2 Spectro UV/visible spectroscopy results for the CVD dispersion

The spectra for CVD-A and CVD-B were not consistent with each other and it was not possible to replicate the measurement twice. This was attributed to the large concentrations and number wide bundle size distribution of CNTs (Figure 9-6 and Figure 9-7).

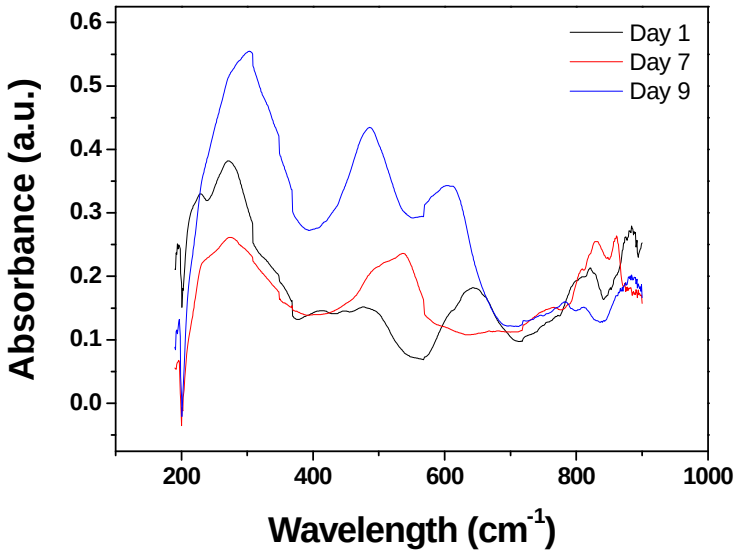

Figure 9-6 Absorbance CVD - B after 1, 7 and 9 days of sonication

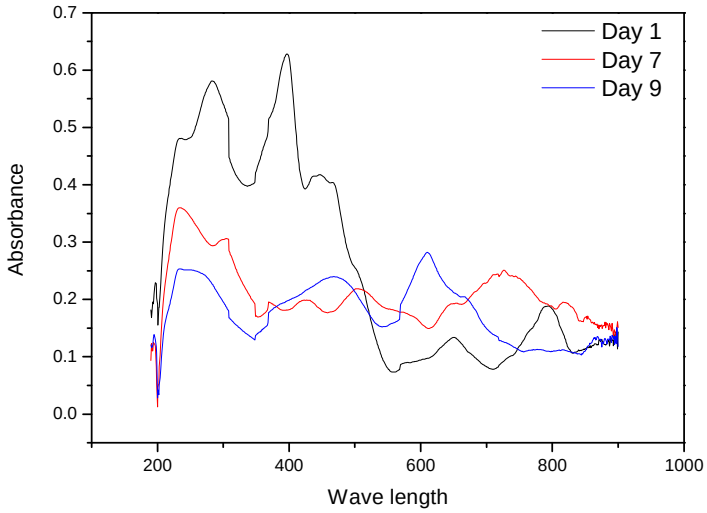

Figure 9-7 Absorbance CVD - A after 1, 7 and 9 days of sonication

9.1.3 Zeta sizer data

The spectrum for the IPA is given in Figure 9-8. It is clearly different from the CNT/propan-2-ol solutions.

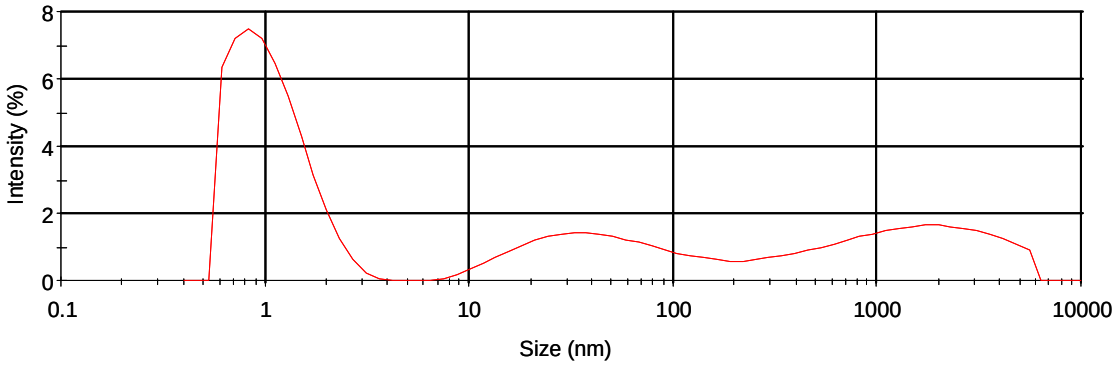

Figure 9-8 Zeta sizer spectrum for the propan-2-ol alone.. The intensity was much lower compared to suspensions in which CNTs were present and noise was visible all across the range of particle sizes.

As shown in Figure 9-9 the size of the macro-bundles visible for the Zeta sizer tended to decrease after several freezing – sonication cycles.

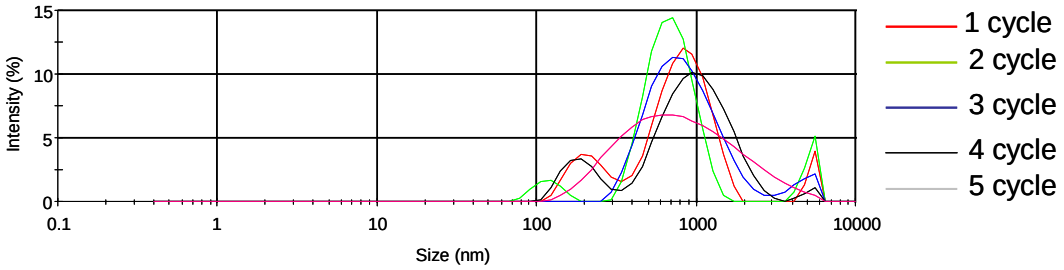

Figure 9-9 CVD impact of repeated sonication

The bundling kinetics of the CCI CNTs is visible in Figure 9-10. The average bundle size progressively increases over short periods of time (10 min).

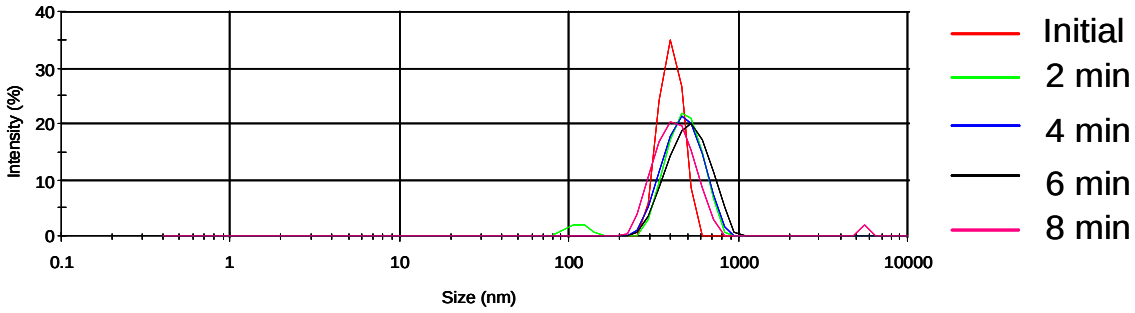

Figure 9-10 CCI bundling kinetics; the sample was first sonicated 5 min and then tested every 2 min

Similar tests were also performed with single walled CNTs suspensions. The concentrations were kept low (less than 50 mg / L) for these tests. Here again the impact of several freezing-sonication cycles is visible. The average bundle size slides progressively down from about 700 nm to 150 nm (Figure 9-11).

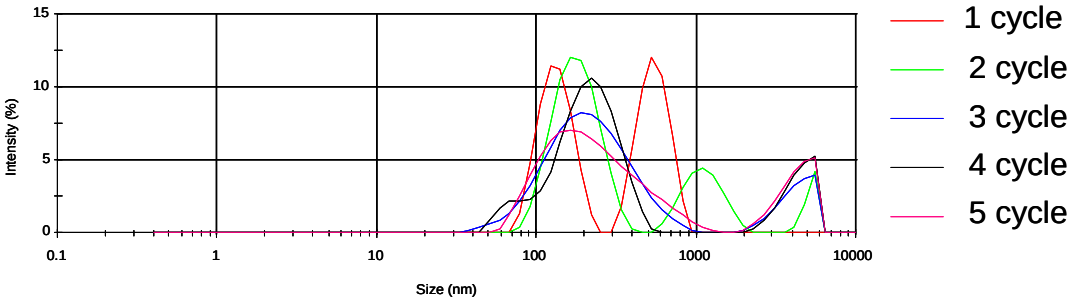

Figure 9-11 SWNT bundling kinetics

9.1.4 E-SEM images and air bubble presence on the CCI CNTs in solution

As seen in Figure 9-12 air bubbles were present under water drops being formed at the surface of the BP. The archs in Figure 9-12-A and B clearly show that air is penetrating under the droplet. Furthermore measurements made on the CNT diameters visible in the drops in Figure 9-12-C and D showed a slight increase of between 12 and 16 % of the original diameter. This was consistent over all the CNTs examined. These measures were precise at 1 pixel after treating the image to increase the contrast at its

maximum to better visualize the CNTs. This corresponded to a global diameter increase of ~ 7 nm (3.5 on each side of the nanotube) [364]. That was ascribed to the presence of an air-gap between the CNTs and the water.

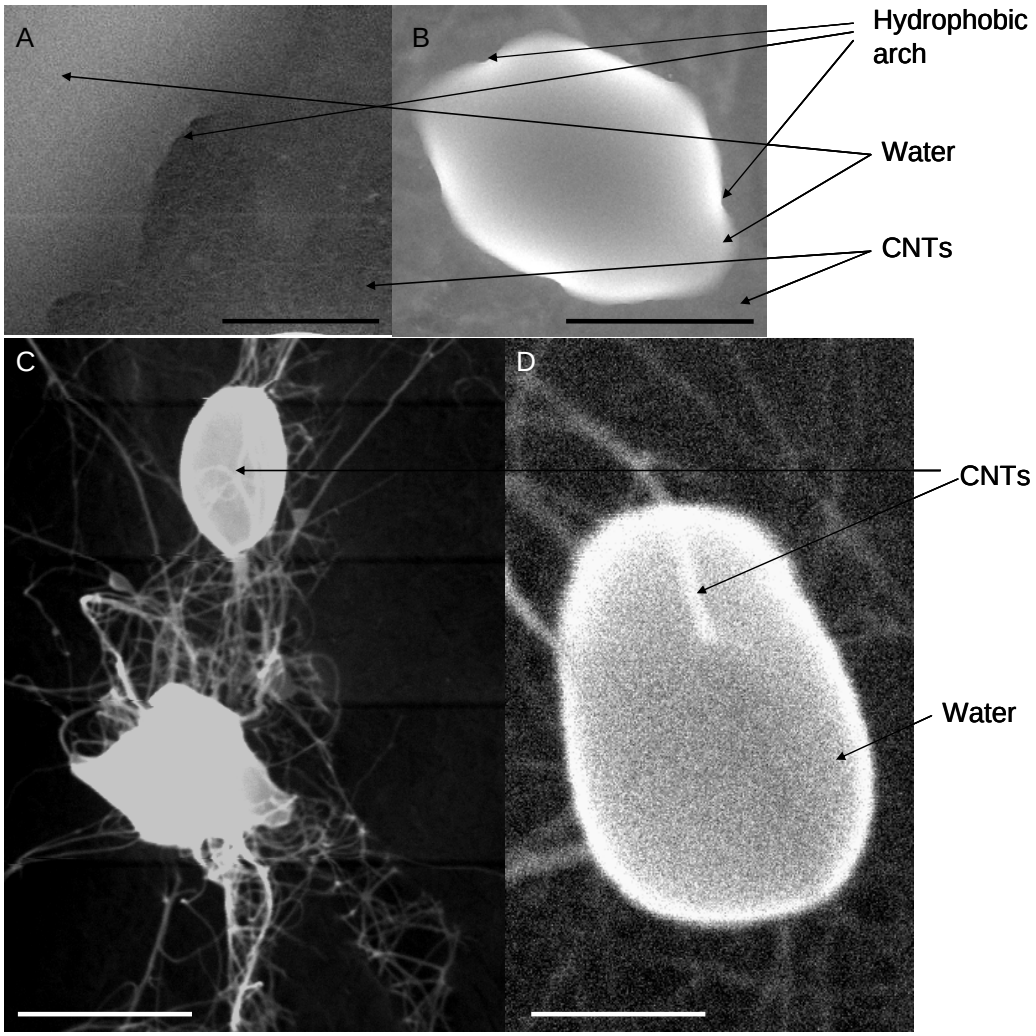

Figure 9-12 Presence of air bubbles - E-SEMs at 1 kPa of water vapor atmosphere; the scale bars on A, B, C and D correspond respectively to 50, 10 , 5 and 1 μm

9.2 Appendix 2 - Pore characterisation by SEM analysis

9.2.1 Pore size

CNTs Bucky papers were processed from CCI and CVD CNTs at different mixing ratios. The samples for images were taken on the edge but the images were focused as far as possible from the edge. The image analysis was performed on ISIS software from the SEM FEG series. Three examples will be given in the following sections CPD100, CCI50 and CCI100. Histograms of pore size distribution are also given as indication of the pore characteristics of each BP. Each colour on the SEM images corresponds to a pore class (Figure 9-13, Figure 9-14, Figure 9-15, Figure 9-16).

The weight percent ratio between CCI and CVD CNTs as well as the samples names and eccentricities calculated from the image analysis are given in Table 9-2.

The eccentricities were calculated from equation 8-1:

$$e = \sqrt{1 - \left(\frac{R_{\min}}{R_{\max}}\right)^2} \qquad (9\text{-}1)$$

Where R_{min} and R_{max} are respectively the minimum and maximum diameters calculated from the Feret's analysis.

Table 9-2 Sample designation

Sample name	w%CCI	Eccentricity
CPD100	0%	0.76
CCI10	10	0.72
CCI20	20	0.75
CCI40	40	0.75
CCI50	50	0.80
CCI60	60	0.82
CCI80	80	0.70
CCI100	100	0.69

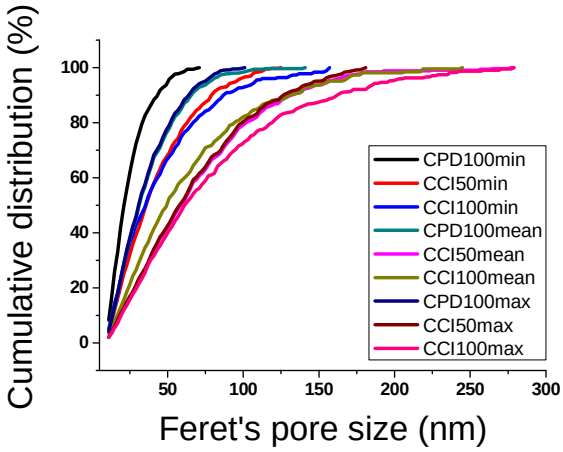

Figure 9-13 Feret's pore size distribution for all the samples analysed

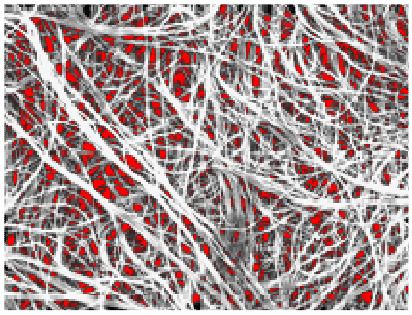

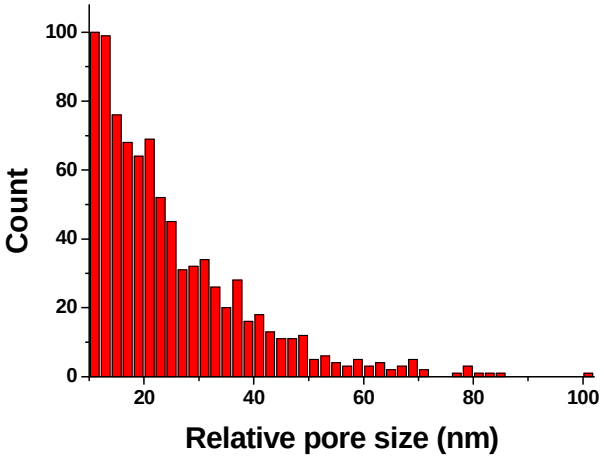

Figure 9-14 SEM of a CPD100 BP (top) with histogram of pore size distribution (right)

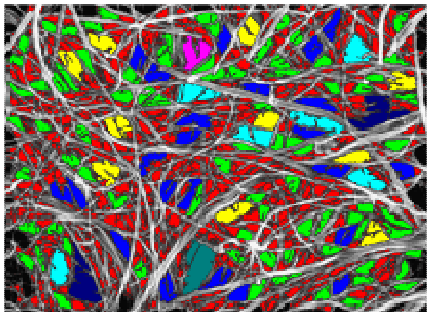

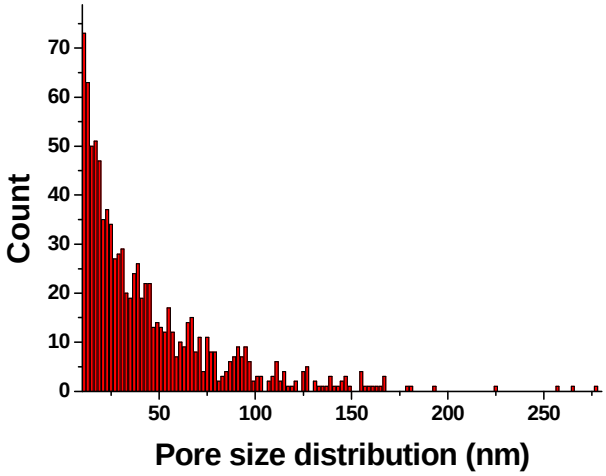

Figure 9-15 SEM of a CCI50 BP (top) with histogram of pore size distribution (right)

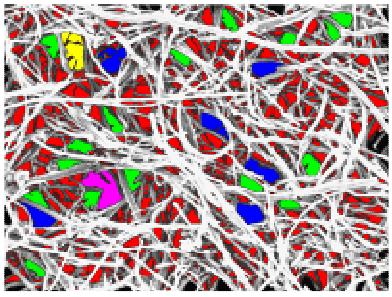

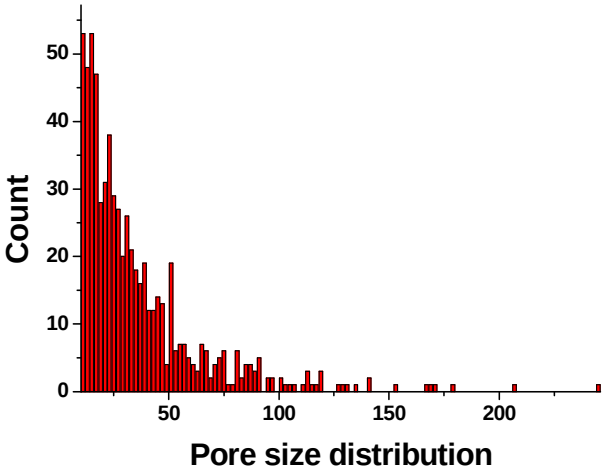

Figure 9-16 SEM of a CCI100 BP (top) with histogram of pore size distribution (right)

9.2.2 Surface roughness

The surface roughness and thickness were shown to vary randomly on the surface according to the presence of macro-bundles in the structure. The surface of the BP was mapped by reconstructing the surface from scan lines as shown in Figure 9-17. Controlling accurately the thickness was critical to processing reproducible composites and to test with a high degree of accuracy their mechanical properties. Local thickness variations were minor and generally limited to a window of 8-10 % of the nominal thickness (Figure 9-17).

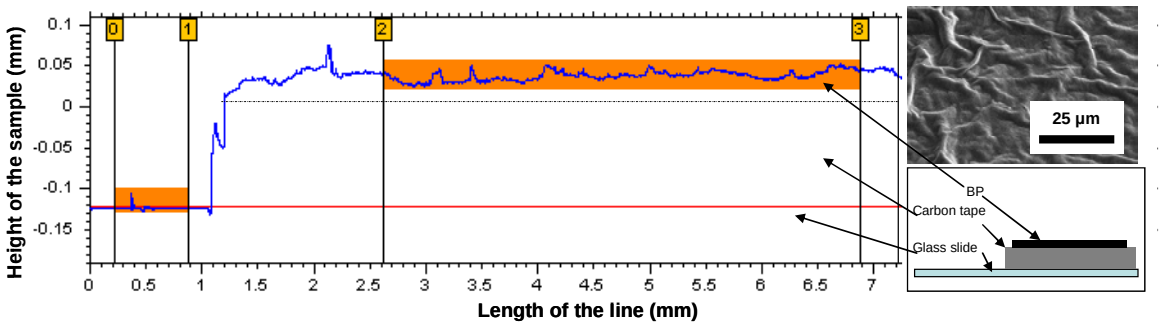

Figure 9-17 Altisurf measurement of a BP thickness. The sample was stuck on carbon tape, and on a glass slide used as a reference. The resolution of the light beam was of 20 nm.

C) Porometer test – typical wet up / dry up test

The test consisted of two separate steps. The sample was first wetted by a solvent and pressurized with gas until all the liquid entered the BP before a second step exposed the BP to pure gas only (Figure 9-18).

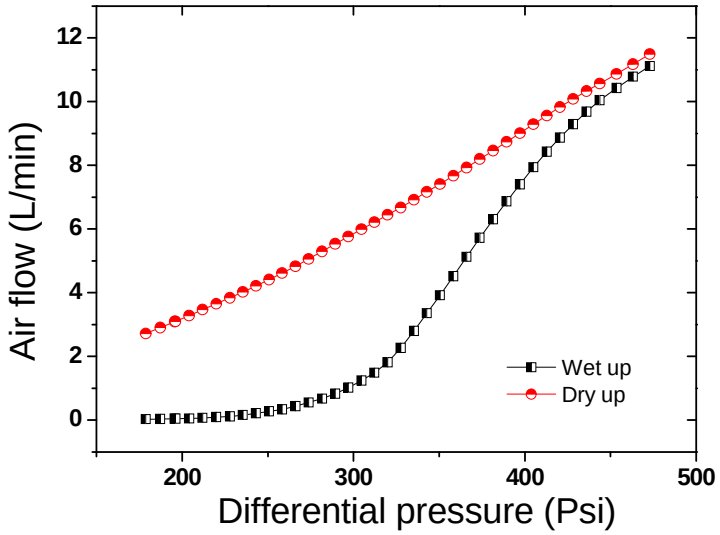

Figure 9-18 Wet up / dry up typical test

9.3 Appendix 3 – DCMD

9.3.1 PTFE and PVDF membranes – general facts

Polyvinylidene Fluoride (PVDF) is a highly non-reactive and stable thermoplastic fluoropolymer. Compared to other fluoro-polymers, it has a lower melting point of around 177℃ and can be dissolved in solvent to be cast or extruded. It has a low density (1.78) and low cost compared to other fluoro-polymers.

Poly(tetra-fluoro ethylene) (PTFE) is a fluorocarbon entirely composed of carbon and fluorine. PTFE can be difficult to wet by water or oil-containing substances, as fluorocarbons demonstrate mitigated London dispersion forces due to the high electronegativity of fluorine thus preventing hydrogen or strong surface bond formation. PTFE has one of the lowest coefficients of friction and has a density of about 2.2 and a melting point of 327 ℃. It however starts degrading above 260 ℃ (Figure 9-19) .

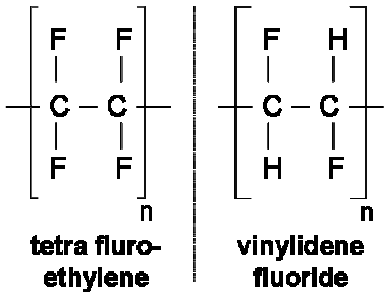

Figure 9-19 Chemical formulae of the two polymers; left: poly(tetra-fluoro ethylene) and right: poly(vinylidene fluoride)

In the case of the PVDF membranes, the pores where composed of series of interconnected spherical cavities. This was due to the phase inversion process used to fabricate them. The cavity size and depth were consistent across thick layers of polymers. The pore size, measured by SEM and porometry, varied between 200 and 450 nm while the porosity, as measured by pycnometer tests was ~65%. The PVDF membranes were

supported on poly(ethylene) (PE) non-woven fabric offering larger pore size than the membrane (around 200 µm) but lower porosity (50%). The thickness of the active layer was between 40 and 50 µm for a porosity of 65-70% (Table 9-1).

The PTFE membranes had a different morphology due to their processing method and conditions. PTFE films are cast from acid solutions and stretched to provoke splitting of ligamer chains. This processing method leads to a succession of interconnected dense nodes and thin PTFE fibres. The pores were composed of the interstitial gaps between the fibres (Chapter 4). This structure had similar features to the Bucky-papers. The membranes were supported either on PE non-woven fabric having similar properties as the PVDF supports or on PE grids similar to those shown in Figure 9-20. These grids were also used to sandwich BP in Chapter 6. The porosity of the grid was comprised between 55 and 60% and the pores where much larger than those of the average active layer membrane, thus not affecting the selectivity and wetting. The thickness of the PTFE active layer was measured and found to lie between 30 and 40 µm, while its porosity was measured by pycnometer tests to be around 65-70 %.

Table 9-3 PVDF and PTFE main properties

Membrane	*Material*	*Pore size*	*Pore size*	*Porosity*	*Thickness*	*Company*
		Manufacturer	Measured		Support layer	
		nm	nm	%	um	
PVDF02	PVDF	200	220	70	40-50	GE
PVDF04	PVDF	400	415	70	40-50	GE
PTFE-P002	PTFE	20	57	65-70	30-40	Pall
PTFE-P02	PTFE	200	273	65-70	30-40	Pall
PTFE-P045	PTFE	450	321	65-70	30-40	Pall
PTFE-M045	PTFE	450	405	65-70	30-40	Millipore
PTFE-M1	PTFE	1000	2190	65-70	35-45	Millipore

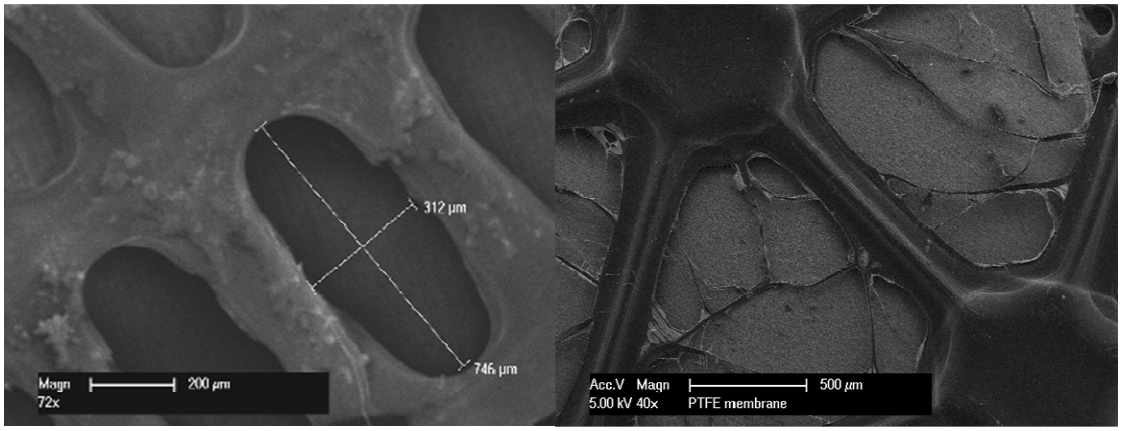

Figure 9-20 Typical PE support grid

9.3.2 PVDF DCMD results

A 0.45 µm pore size PVDF membrane was tested under various hot feed temperatures (25, 45, 65, 85 and 95 ºC) in the DCMD rig. The cold permeate temperature was kept constant at 5ºC. The flux was shown to increase linearly with the variation of water vapor pressure, which follows the established theory for DCMD. Furthermore the fluxes of the PVDF membranes were comparable with that of the BP at similar vapor pressure differences. It was greater only by about 10 % on average.

This is interesting since the PVDF pores were about 10 times larger than the BP pores. The difference with the PTFE membranes was attributed to the large difference in surface energy. The contact angle with deionised water of the PVDF membrane was found to be around 90 º (Figure 9-22).

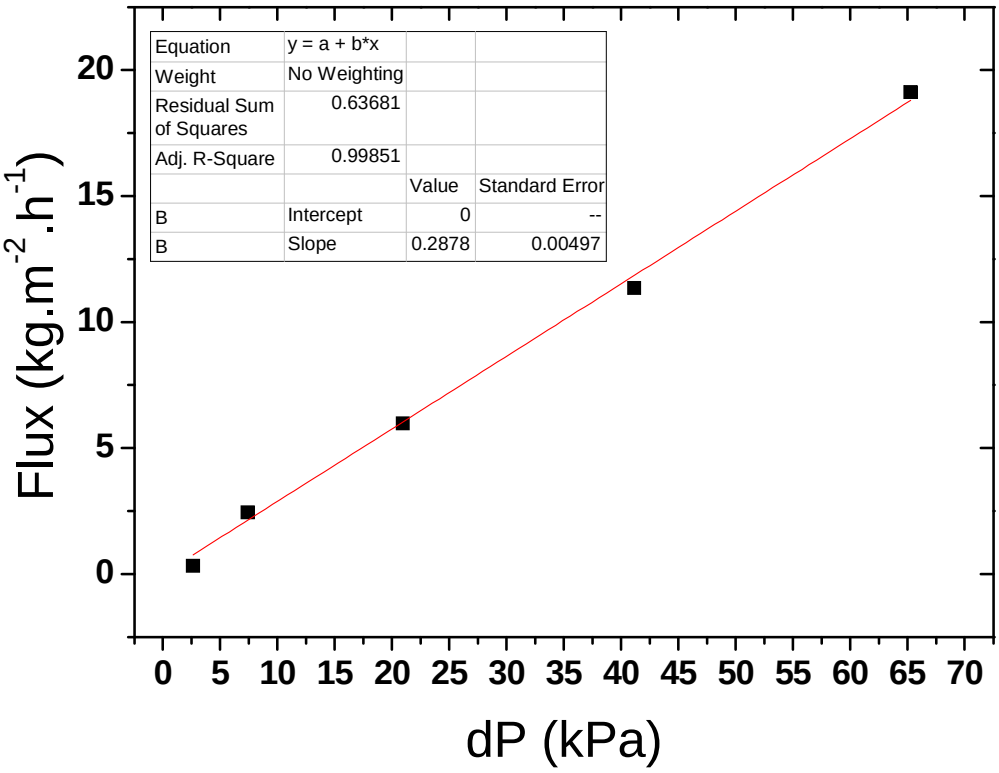

Figure 9-21 Flux as a function of water vapor pressure for the 0.22 µm pore size PVDF membrane

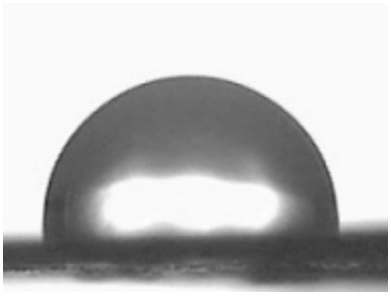

Figure 9-22 Contact angle on a 0.45 µm PVDF membrane with deionised water

The pore size distributions of the two tested PVDF membranes are shown in Figure 9-23. The bubble point pressure of the 0.22 and 0.45 pore size membranes were found to be respectively 86.46 and 95.61 kPa.

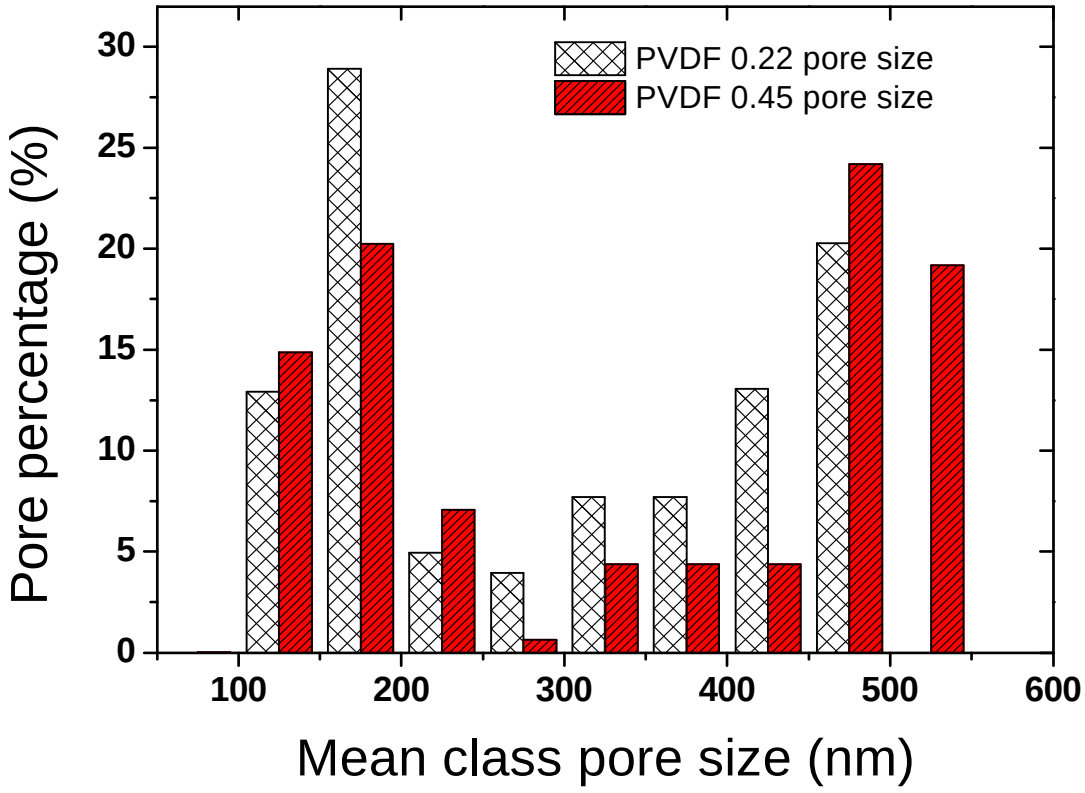

Figure 9-23 Pore size distributions of the PVDF membranes

9.3.3 Examples of solution conductivity rise after BP failure

As shown in Figure 9-24 the failure of a membrane was easily detectable because of the fast conductivity rise. Displayed in Figure 9-25 are typical conductivity curves for a PTFE coated BP, a sandwich BP and a PTFE membrane (0.45 μm pore size). A very slight increase was detectable over a few hours of testing.

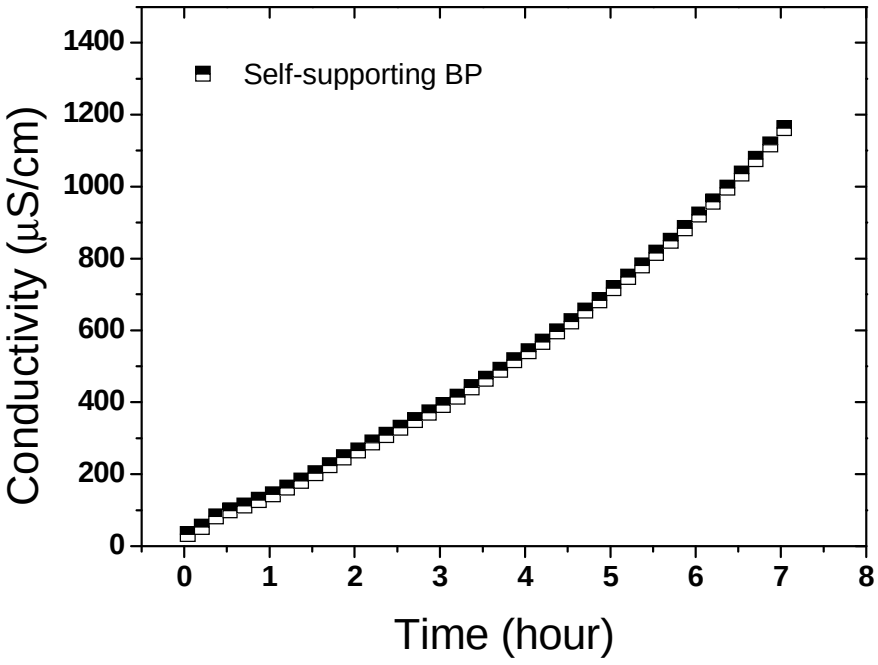

Figure 9-24 Conductivity rise for a self-supporting BP after failure

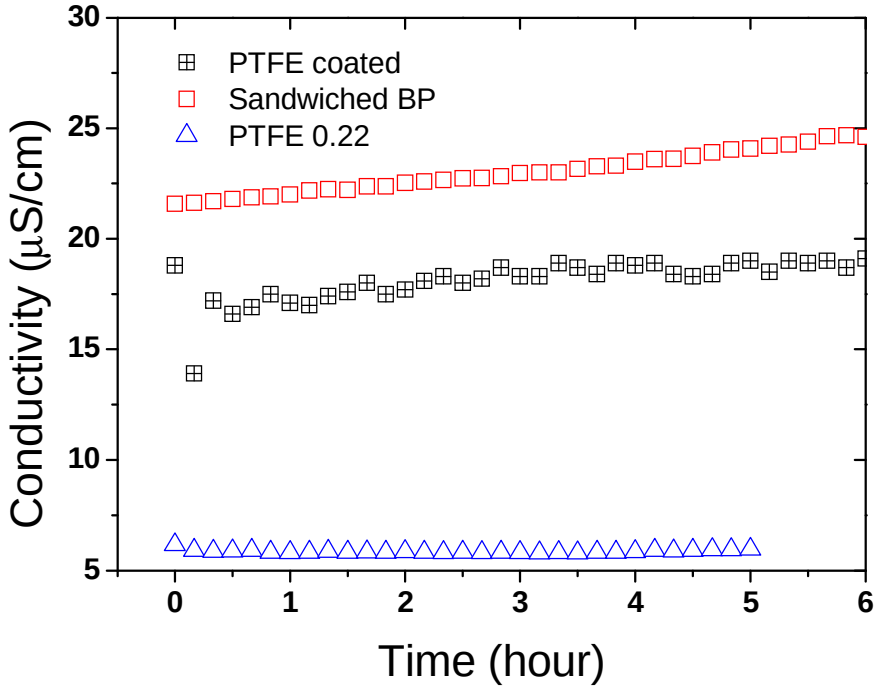

Figure 9-25 Conductivity rise for 2 BP composite membranes (PTFE coated and sandwiched) and a PTFE membrane (0.45 µm pore size)

9.3.4 Theorical calculations of Knüdsen diffusion pre-factors

Here are listed a few examples of pre-factors calculated for different geometrical configurations.

Table 9-4 Pre-factors values for a modelled polymeric membrane

Porosity	Pore size nm	Tortuosity	Thickness µm	Coefficient Knüdsen
0.7	30	1.1	30	0.64
0.7	200	1.1	30	4.24
0.7	450	1.1	30	9.55
0.7	30	1.1	50	0.38
0.7	200	1.1	50	2.55
0.7	450	1.1	50	5.73
0.7	30	1.3	30	0.54
0.7	200	1.3	30	3.59
0.7	450	1.3	30	8.08
0.7	30	1.3	50	0.32
0.7	200	1.3	50	2.15
0.7	450	1.3	50	4.85

Table 9-5 Pre-factor values for a modelled BP

Porosity	Pore size nm	Tortuosity	Thickness µm	Coefficient Knüdsen
0.9	20	1.2	30	0.50
0.9	20	1.4	30	0.43
0.9	20	1.6	30	0.38
0.9	20	1.8	30	0.33
0.9	20	2	30	0.30
0.9	20	1.2	50	0.30
0.9	20	1.4	50	0.26
0.9	20	1.6	50	0.23
0.9	20	1.8	50	0.20
0.9	20	2	50	0.18

0.9	25	1.2	30	0.63
0.9	25	1.4	30	0.54
0.9	25	1.6	30	0.47
0.9	25	1.8	30	0.42
0.9	25	2	30	0.38
0.9	25	1.2	50	0.38
0.9	25	1.4	50	0.32
0.9	25	1.6	50	0.28
0.9	25	1.8	50	0.25
0.9	25	2	50	0.23

9.4 Appendix 4 – BP thermal properties

9.4.1 Previous work on the thermal properties of CNT structures

Table 9-6 Thermal properties from scientific literature

at 293K	CNT type	Growth method	Structure	Specific heat	Thermal conductivity	Thermal diffusivity	Thermal expansion
Unit				J/g*K	W/m*K	*10-5 m2/s	*10-4 m/m*K
Literature graphite			planar	0.71	720	10.25	0.26
Yi-1999	MWNT	CVD	**forest**	0.495	25	3.8	
Aliev-2007	MWNT	dry state technique	**sheet**		50	82	
Aliev-2008	MWNT	dry state technique	**yarn**	0.7	26	620	
Hone-2002	SWNT	MD simulation	**bundle**	0.65	220		
Popov-2002	MWNT	MD simulation	**single CNT**	~0.7			
Lasjaunias-2002	SWNT	laser ablation	bundle	~0.7			
Yang-2004	MWNT	CVD	forest		12-17	0.7-10	
Berber-2000	SWNT	MD simulation	isolated CNT		6600		
Pipes-2002	SWNT	MD simulation	bundles				0.5-2.5
Bandow-1997	MWNT	arc discharge	forest				29
Maniwa-2001	SWNT	laser ablation	bundles				42
Composites…							
Kim-2007	MWNT	CVD	dispersed in PLLA		0.15/0.4		
Wei-2002	SWNT	MD simulation	dispersed in PE			0.7*10-4	4.5
Gong-2004	MWNT	CVD	aligned in PAN		~70		

Figure 9-26 shows a typical heat response to the laser induced heat stimulus. Half time to reach a maximum intensity of ~ 0.5 s were usually detected on the CNT samples. As shown in Figure 9-27 the presence of the CNTs greatly improved the conductivity of the capton tape. The highest diffusivities were found to be achieved with the CNT forest. In this configuration the CNTs were aligned with the heat wave direction and less phonon dispersions were likely. It was however not possible to directly compare the value of these samples with those of the BPs since the BP did not require sandwiching.

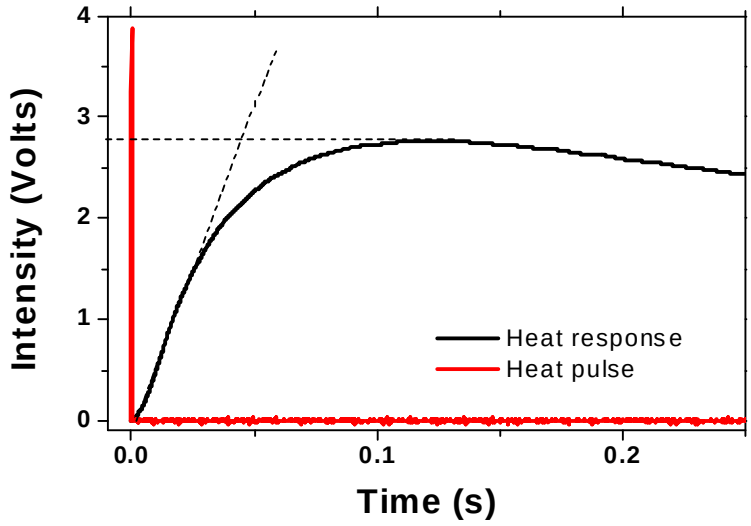

Figure 9-26 Heat response of a BP after the laser heat pulse

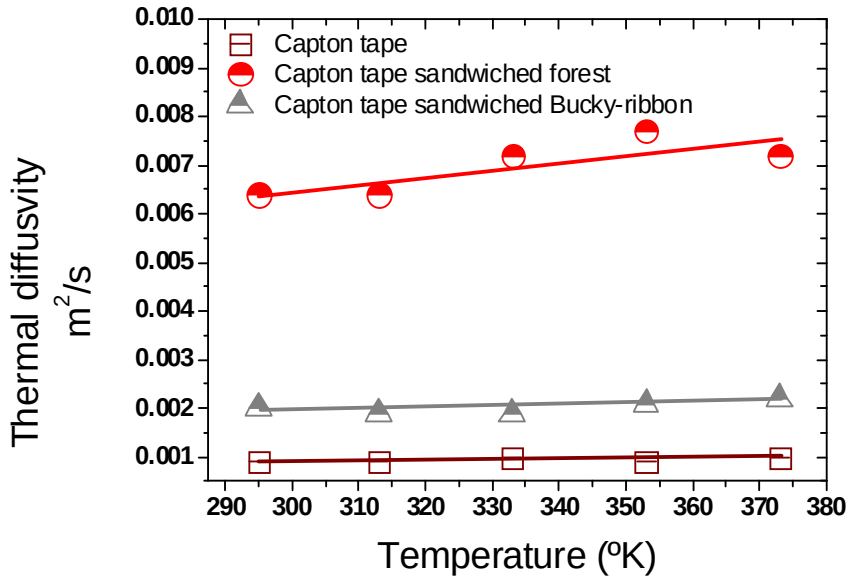

Figure 9-27 Thermal diffusivity calculated for other sandwiched materials (forest and bucky-ribbon); capton tape was used as a reference

9.5 Appendix 5 – SAXS analysis

The main papers and their corresponding test parameters used for this analysis are given in Table 9-7.

Table 9-7 SAXS literature review

Experiment	*Reference*	*Properties*	*Sample*	*Wavelength (nm) and distance (mm)*	*Energy (keV)*
Lengthening kinetics of CNTs	[439]	True CNT length	Forest	-	10
SWNT dispersed in PET	[388]	Bundling CNT/polymer	BP	0.15 nm	
CNT dispersed in elastomers	[286]	Interface CNT polymer matrix	BP	-	8
Fracture process of carbon nanotube/poly(ethylene terephthalate)	[440]	Increased toughness nano-composite	Dispersed CNTs in matrix	0.15 nm 2100 mm	-
Morphologies of Mechanically Manipulated of MWNT	[389]	Deformed CNTs by uniaxial pressure	Forest	0.1239 / 0.1371 nm 1789 mm	-
Morphology of MWNT Films	[390]	Alignment determination	Forest	0.1239 nm 1435.1 mm	45

Thermal expansion was found to behave differently in the case of the PS/CNT composite sample up to 240 – 250 ºC (Figure 9-28). This was attributed to the fact that PS was reducing the BP thermal contraction up to its melting point. Above this point, both surface tension of the molten polymer and the effect of the PS thermal expansion lead to less dense samples. Furthermore, in the case of the solvent densified BPs, where a BP was exposed to the evaporation of acetone prior to the test, no clear trend was found which was attributed to the already compacted structure allowing less

CNT free movement (Figure 9-29). As previously demonstrated (Chapter 3 and Appendix 1) the evaporation of solvent tended to increase bundling by condensing CNTs into denser bundles.

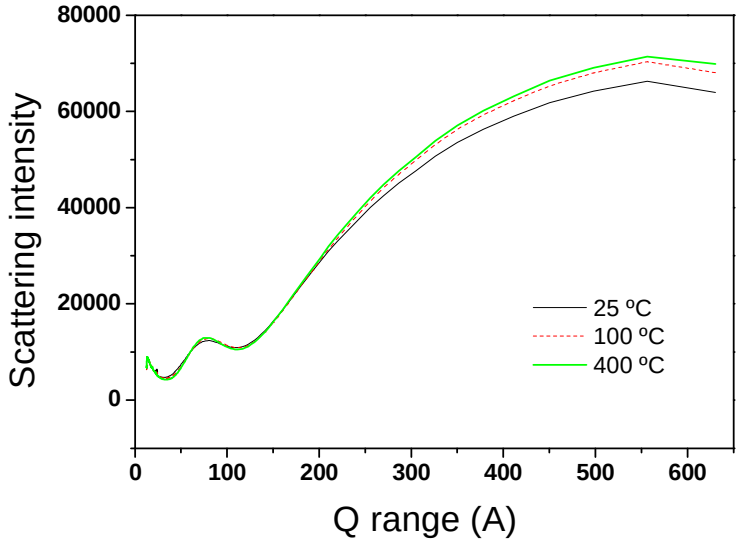

Figure 9-28 Scattering intensity for the PS/BP composite

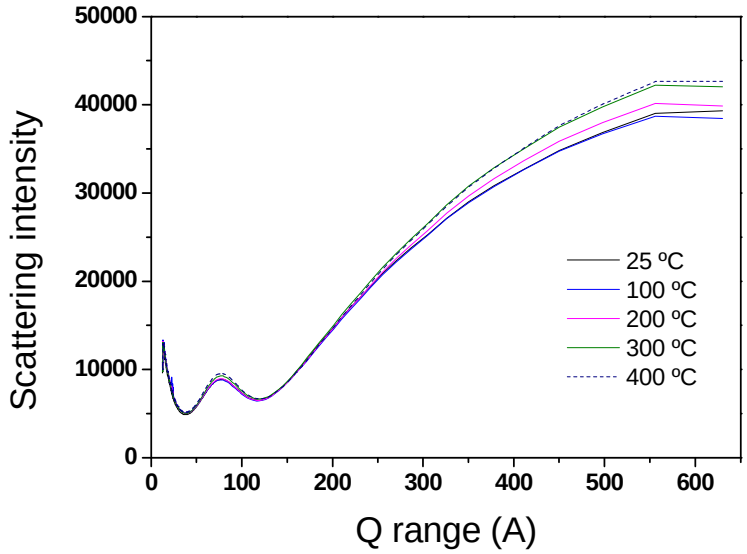

Figure 9-29 Scattering intensity for the acetone condensed BP

As shown in Figure 9-30 and Figure 9-31 the radius of gyration and the Guinier scattering radius do change as a function of temperature. A clear drop in the gyration radius is visible above 250 ºC corresponding to the formation of

larger features. As predicted by the theory, the Guinier scattering radius increases with increasing radius of gyration (Figure 9-32) [387, 391].

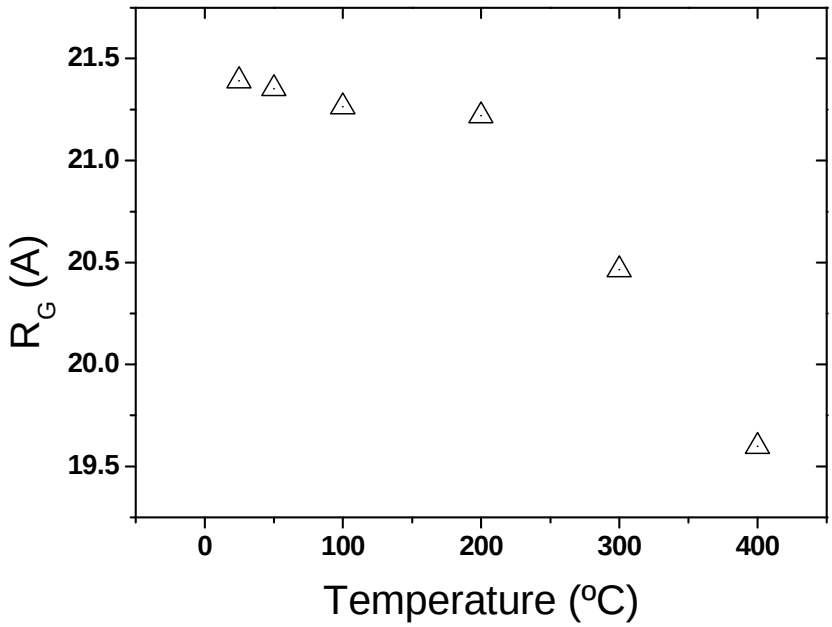

Figure 9-30 Radius of gyration as a function of temperature for a BP self-supporting sample

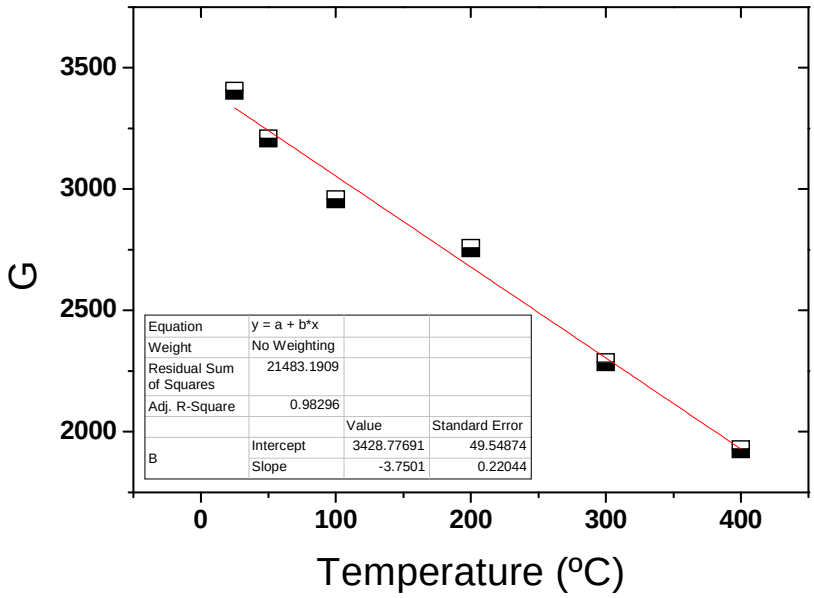

Figure 9-31 Guinier scattering radius as a function of temperature for a self-supporting BP

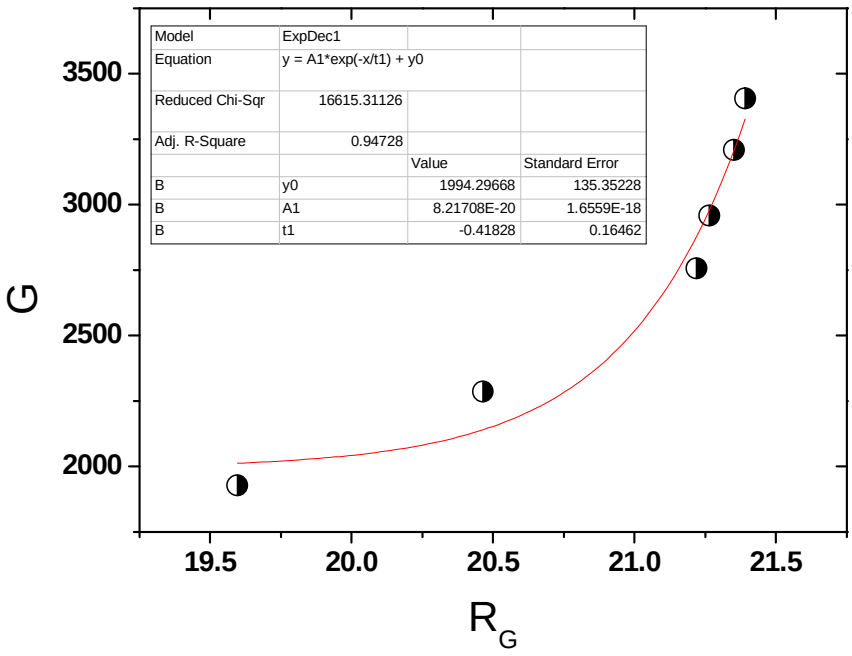

Figure 9-32 Size of the features as a function of the radius of gyration

9.6 Appendix 6 - Tortuosity calculations

The membrane tortuosity is defined across a **t** thick membrane as the true path for gas or liquid molecules to travel within its pores. This path is defined as the minimum pathway divided by the membrane thickness.

For an idea membrane where pores are perfectly straight across the membrane thickness, the tortuosity is minimized down to a value of 1 while, in real case scenarios it is always considered greater than 1, due to possible blockages, deviations or particles present along the pore way.

Furthermore, in the case of packed materials, a porosity of 0.X corresponds to a packing density of (1-0.X). This values correlates to the number of bodies along the way within the membrane porosity, *n*. Therefore, if there is n bodies in the unit volume, then

$$(1-0.X) = n \times V_{individualbody} \quad (9\text{-}2)$$

Where $V_{individualbody}$ is the volume of each particle in the way.

The total pathway across a membrane made of cylindrical bodies corresponds to the sum of two values:

- The free path between the bodies
- The n times the half-perimeters of the bodies n*(pi*D)/2

The total pathway across a **t** thick membrane is then:

$$T_{path} = t - n \times D + n\pi \times D/2 \quad (9\text{-}3)$$

Where T_{path} is the total path across the membrane for a gas molecule to travel from one side to the other, and D is the particle diameter.

Thus the tortuosity is equal to:

$$\tau = \frac{T_{path}}{t} = 1 - + \frac{(\pi - 1)nD}{2t} \qquad (9\text{-}4)$$

If **t** is a unit membrane thickness (assumed as a unit in the membrane), then Tau becomes:

$$\tau = 1 - + \frac{(\pi - 1)nD}{2} \qquad (9\text{-}5)$$

Note: (9-5) is purely based upon geometrical assumptions on the membrane morphology and CNT diameters, membrane porosity and thickness obtained experimentally. According to the TEM video presented in Chapter 3, porosity of 0.9 or more was found to ne credible.

9.7 Appendix 7 – Comparison of the capacity of gold coated CNT BP with other materials

In fact when compared to adsorption capacity of previous publications (Table 9-8), this work (up to 0.075 w%) is about 73 times lower than the U.S. Department of Energy (U.S.) targets and most of the high adsorption materials developed to date. These preliminary results are however encouraging as they demonstrate the potential of decorated nanotubes if optimized. As routes to further enhance their adsorption capacity, we propose to use single walled nanotubes (SWNT) to further increase the available surface area for NP growth and therefore enhance the amount of gold adsorbed and therefore the fuel cells properties. The steady CNTs price decrease experienced over the past 5 years is expected to continue while CNT quality and purity will very likely keep improving leading to further potential developments for CNTs in day-to-day usage. CNTs could therefore become in a close future valuable low cost substrates for high gas adsorption materials growth and nucleation. Furthermore while gold is considered as an expensive metal, the ease of coating on relatively cheaper CNTs, and the viability of using other lower cost metals such as nickel, could lead to cost advantages of our proposed material. Future work will consider these approaches.

Table 89-8 Comparison of the maximum hydrogen adsorption with previous works and structures at 77K, at pressures above 1 atm

Samples	**Hydrogen adsorption**	**Enthalpy**	**Reference**
	wt%	$kJ.mol^{-1}$	
Metal organic framework	1	- 3.3	[442]
Metal organic framework	1.8	-3.7	[443]
SWNT - non HCl purified	2	-	[444]
SWNT - partially purified	2.5	-	[444]
SWNT - fully purified	4.2	-	[444]
Lithium doped MWNT	2.5	-	[445]
Potassium doped MWNT	1.8	-	[445]
DOE target 2015	5.5	-	[446]
5h Gold decorated MWNT	0.075	-9.8	This work